
Holocene sea-ice and ice-sheet variability on the Northeast Greenland continental shelf

Kumulative Dissertation

zur Erlangung des akademischen Grades
eines Doktors der Naturwissenschaften

-Dr. rer. nat.-

am Fachbereich Geowissenschaften
der Universität Bremen

vorgelegt von

Nicole Syring

Bremerhaven, 2020

Gutachter der Dissertation:

Prof. Dr. Rüdiger Stein

Prof. Dr. Ralph Schneider

Ph.D. Colloquium

Breaking the ice – A Holocene Northeast Greenland sea-ice and ice-sheet history

01.10.2020

Versicherung an Eides Statt / *Affirmation in lieu of an oath* gem. § 5 Abs. 5 der Promotionsordnung vom 18.06.2018 /

according to § 5 (5) of the Doctoral Degree Rules and Regulations of 18 June, 2018

Ich / I, Nicole Syring, Mathildenstraße 91, 28203 Bremen, 2340187

(Vorname / *First Name*, Name / *Name*, Anschrift / *Address*, ggf. Matr.-Nr. / *student ID no.*, *if applicable*)

versichere an Eides Statt durch meine Unterschrift, dass ich die vorliegende Dissertation selbständig und ohne fremde Hilfe angefertigt und alle Stellen, die ich wörtlich dem Sinne nach aus Veröffentlichungen entnommen habe, als solche kenntlich gemacht habe, mich auch keiner anderen als der angegebenen Literatur oder sonstiger Hilfsmittel bedient habe und die zu Prüfungszwecken beigelegte elektronische Version (PDF) der Dissertation mit der abgegebenen gedruckten Version identisch ist. / *With my signature I affirm in lieu of an oath that I prepared the submitted dissertation independently and without illicit assistance from third parties, that I appropriately referenced any text or content from other sources, that I used only literature and resources listed in the dissertation, and that the electronic (PDF) and printed versions of the dissertation are identical.*

Ich versichere an Eides Statt, dass ich die vorgenannten Angaben nach bestem Wissen und Gewissen gemacht habe und dass die Angaben der Wahrheit entsprechen und ich nichts verschwiegen habe. / *I affirm in lieu of an oath that the information provided herein to the best of my knowledge is true and complete.*

Die Strafbarkeit einer falschen eidesstattlichen Versicherung ist mir bekannt, namentlich die Strafandrohung gemäß § 156 StGB bis zu drei Jahren Freiheitsstrafe oder Geldstrafe bei vorsätzlicher Begehung der Tat bzw. gemäß § 161 Abs. 1 StGB bis zu einem Jahr Freiheitsstrafe oder Geldstrafe bei fahrlässiger Begehung. / *I am aware that a false affidavit is a criminal offence which is punishable by law in accordance with § 156 of the German Criminal Code (StGB) with up to three years imprisonment or a fine in case of intention, or in accordance with § 161 (1) of the German Criminal Code with up to one year imprisonment or a fine in case of negligence.*

Ort / *Place*, Datum / *Date*

Unterschrift / *Signature*

“And the day came when the risk to remain tight in a bud
was more painful than the risk it took to blossom.”

– Anaïs Nin –

TABLE OF CONTENT

Abbreviations

| | |
|-----------------|-----|
| Abstract | I |
| Zusammenfassung | III |
| Danksagung | VII |

Chapter 1

| | |
|--|----|
| 1. Introduction | 1 |
| 1.1 Modern Arctic physiography and oceanography | 1 |
| 1.2 Study area – Fram Strait and Northeast Greenland continental shelf | 4 |
| 1.3 The role of Arctic sea ice in the climate system | 5 |
| 1.4 Ongoing anthropogenic climate change – a future perspective | 10 |
| 1.5 From an ancient to a modern Arctic Ocean | 16 |
| 1.6 Common past climate proxies in the Arctic environment | 21 |

Chapter 2

| | |
|--|----|
| 2.1 Motivation | 29 |
| 2.2 Thesis Outline and declaration of Authors contribution | 32 |

Chapter 3

| | |
|---|----|
| 3.1 Data set & material and methods | 35 |
| 3.2 Data acquisition | 35 |
| 3.3 Organic-geochemical methods – Proxies used for past climate reconstructions | 39 |

Chapter 4

Holocene changes in sea-ice cover and polynya formation along the eastern North Greenland shelf: New insights from biomarker records

| | |
|---|----|
| 4.1 Introduction | 46 |
| 4.1.1 Background | 46 |
| 4.1.2 Regional Setting | 48 |
| 4.2 Material and methods | 50 |
| 4.2.1 Sediment material | 50 |
| 4.2.2 Methods | 50 |
| 4.2.2.1 Chronology | 50 |
| 4.2.2.2 Organic bulk sediment parameters | 52 |
| 4.2.2.3 Extraction and analysis of lipid biomarkers | 52 |
| 4.2.2.4 Statistical analysis | 54 |
| 4.3. Results | 54 |
| 4.3.1 Organic/inorganic bulk parameters | 54 |
| 4.3.2 Biomarker | 55 |
| 4.4 Discussion | 56 |
| 4.4.1 Proxies used for past sea-ice reconstructions on the eastern North Greenland shelf: some general aspects | 56 |
| 4.4.2 Sea-ice variability off eastern North Greenland during the Holocene | 59 |
| 4.4.3 Short-term cyclic variability in Holocene environmental conditions | 65 |
| 4.5. Conclusions | 66 |

Holocene interactions between glacier retreat, sea-ice formation and Atlantic Water advection at the inner Northeast Greenland continental shelf

| | |
|---|----|
| 5.1 Introduction and regional setting | 68 |
| 5.1.1 Aim of study | 71 |
| 5.2 Material and methods | 72 |
| 5.2.1 Material | 72 |
| 5.2.2 Methods | 72 |
| 5.3 Results | 76 |
| 5.3.1 Age model of Core PS100/100 and sedimentation rates | 76 |
| 5.3.2 Lithofacies and bulk organic parameters | 77 |
| 5.3.3 Biomarkers | 79 |
| 5.3.4 Foraminifers | 80 |
| 5.4 Discussion | 82 |
| 5.4.1 Late Weichselian initial deglaciation (>10 ka) | 82 |
| 5.4.2 Early Holocene (~10 to 9.6 ka) | 83 |
| 5.4.3 Late early Holocene (9.6 to 7.9 ka) | 86 |
| 5.4.4 Mid to late Holocene (7.9 ka to present) | 89 |
| 5.5 Conclusion | 92 |

Chapter 6**95**

Sea-ice biomarker proxies in surface and subsurface sediments from the Northeast Greenland Shelf - Signals for (paleo) environmental conditions and diagenetic degradation

| | |
|--|-----|
| 6.1 Introduction and regional setting | 96 |
| 6.2 Background information of lipid biomarkers and organic bulk parameters | 98 |
| 6.3 Material and methods | 100 |
| 6.3.1 Material | 100 |
| 6.3.2 Methods | 101 |
| 6.4 Results | 102 |
| 6.4.1 Surface samples | 103 |
| 6.4.2 Subsurface samples | 104 |
| 6.5 Discussion | 106 |
| 6.5.1 Modern sea-ice distribution | 107 |
| 6.5.2 Past climate reconstructions | 109 |
| 6.5.3 Diagenetic degradation vs. primary signal | 111 |
| 6.6 Conclusion | 115 |

Chapter 7**117**

| | |
|----------------|-----|
| 7.1 Conclusion | 117 |
| 7.2 Outlook | 119 |
| References | 121 |
| Appendix | 145 |

Abbreviations

| | |
|--------------------|---|
| AA | Arctic Amplification |
| ACEX | Arctic Coring Expedition |
| AMS | Accelerator Mass Spectrometry |
| AMOC | Atlantic Meridional Overturning Circulation |
| AO | Arctic Oscillation |
| AW | Atlantic Water |
| BG | Beaufort Gyre |
| BSTFA | Bis-trimethylsilyl-TriFluoroacet-Amide |
| CaCO ₃ | Calcium Carbonate |
| C/N | Ratio of Carbon and Nitrogen |
| δ ¹³ C | Stable Carbon Isotopes |
| δ ¹⁸ O | Stable Oxygen Isotopes |
| EGC | East Greenland Current |
| GC-MS | Gas Chromatography – Mass Spectrometry |
| GHG | Greenhouse Gas |
| GIS | Greenland Ice Sheet |
| HBI | Highly-Branched Isoprenoid |
| HBI II | Di-unsaturated HBI lipid |
| HBI III | Tri-unsaturated HBI lipid |
| HTM | Holocene Thermal Maximum |
| IODP | Integrated Ocean Drilling Program |
| IPCC | Intergovernmental Panel on Climate Change |
| IP ₂₅ | Ice Proxy with 25 carbon atoms |
| IPSO ₂₅ | Ice Proxy with 25 carbon atoms for the Southern Ocean |
| IRD | Ice Rafted Debris |
| ka | Thousand years before present |
| LGM | Last Glacial Maximum |
| LF | Lithofacies |
| MIS | Marine Isotope Stage |
| MIZ | Marginal Ice Zone |
| MS | Magnetic Susceptibility |
| MTOG | Marine Terminating Outlet Glacier |
| MUC | Multicorer |
| MYI | Multiyear Ice |
| NADW | North Atlantic Deep Water Formation |

| | |
|-------------------|--------------------------------------|
| NAO | North Atlantic Oscillation |
| NC | Norwegian Current |
| NEEM | North Greenland Eemian Ice Drilling |
| NEG | Northeast Greenland |
| NEGCC | Northeast Greenland Coastal Current |
| NEGIS | Northeast Greenland Ice Stream |
| NEW Polynya | Northeast Water Polynya |
| NØIB | Norske Øer Ice Barrier |
| PETM | Paleocene Eocene Thermal Maximum |
| PIP ₂₅ | Phytoplankton-IP ₂₅ index |
| PS | Research Vessel <i>Polarstern</i> |
| PW | Polar Water |
| SIM | Selected Ion Mode |
| SpSIC | Spring Sea Ice Concentrations |
| SST | Sea surface Temperatures |
| RAW | Recirculating Atlantic Water |
| TC | Total Carbon |
| TIC | Total Inorganic Carbon |
| TN | Total Nitrogen |
| TOC | Total Organic Carbon |
| TPD | Transpolar Drift |
| WDB | Wet Bulk Density |
| WSC | West Spitsbergen Current |
| ZI | Zachariae Isstrøm |
| 79NG | Nioghalvfjærdsbræ/79°Glacier |
| ¹⁴ C | Radiocarbon |

Abstract

When will all the Arctic sea ice in summer be gone? The rapid decline in average sea-ice extent by more than one-third during the last 3 to 4 decades leaves a sad note in terms of climate model projections. Dramatic Arctic sea-ice loss generally appears faster than climate models have forecasted. Nowadays, rapidly changing environmental conditions in the Fram Strait, the passage between Greenland and Spitsbergen, are of particular concern. Sea-ice loss here is rising and the Northeast Greenland Ice Sheet is thinning. During past decades, the amount of drift ice export has increased through Fram Strait, contributing with a significant number to the freshwater budget of the Nordic seas and global ocean circulation.

Here our analysis of the Northeast Greenland continental shelf located in the western Fram Strait, uniquely records past climate changes in a highly versatile environmental system of the Arctic Ocean. Multivariate analysis of molecular highly branched isoprenoids (HBIs), specific sterols, foraminifers and organic/inorganic bulk parameters were carried out on selected downcore records and surface samples from the Northeast Greenland continental shelf. These proxies allow reconstructions of past changes in sea-ice cover, primary production, terrigenous input as well as ice-sheet extent.

The first manuscript provides insights into past sea-ice variability on the outer Northeast Greenland continental shelf and the seasonal formation of the Northeast Water Polynya since the onset of the Holocene to present-day. This outer shelf regime is highly influenced by drift ice and cold water from the central Arctic Ocean and annually occurring local sea-ice formation. Interactive sea-ice and ocean dynamics regulate the regional climate and biology on the marginal shelf. Continuous seasonal sea-ice presence throughout the Holocene within three prominent stages mark relatively abrupt shifts at ~9 ka and ~1 ka. A reduced to variable sea-ice cover with an overall high primary productivity most likely driven by maximum solar insolation was observed during the early Holocene. Sea-ice melt and the intensified inflow of warmer recirculating Atlantic Water favored intensive planktic blooms and fluxes of both marine and terrigenous organic matter. Environmental conditions changed towards seasonal sea-ice conditions and a stronger drift ice signal rather than local one, evidenced by terrigenous biomarkers and IRD content during the mid Holocene. Finally, a stable seasonal sea-ice margin within a fully developed polynya environment occurred during the late Holocene and highlights the last 1 ka.

To understand ocean – sea ice – ice sheet interactions, a second study focuses on the inner Northeast Greenland continental shelf where marine terminating outlet glaciers of the Northeast Greenland Ice Stream are bounded by a near permanent lastfast ice barrier named Norske Øer. A downcore record that fronts the 79°Glacier embayment and includes sedimentological, micropaleontological and organic-geochemical data sets, provides fundamental insights into the detailed initial late Weichselian deglacial to Holocene sea-ice and ice sheet history. In contrast to the outer shelf, drift ice is rather trivial while the local ice barrier plays a fundamental role by preventing glaciers from calving due to the buttressing effect. A reconstruction of the waxing/waning 79°Glacier and changes in the Norske Øer ice barrier

during this specific interval was generated, showing the timing of 79°Glacier retreat and disintegration, accompanied by the intensification in sea-ice conditions. Distinct lithofacies types represent the transition from deglacial conditions with a grounded 79°Glacier through a proximal to a distal glaciomarine environment displaying the onset of the 79°Glacier retreat and total disintegration of the ice shelf at 7.9 ka. Our biomarker and foraminiferal proxy records reflect local sea-ice conditions that changed from a stable sea-ice margin and high productivity system during the early Holocene Thermal Maximum (~10.6 to 9.6 ka) to prolonged seasonal sea-ice conditions in the late early Holocene (9.6 to 7.9 ka) and near perennial sea-ice conditions in the mid to late Holocene (7.9 ka to present). These changes are strongly triggered by Atlantic Water inflow decreasing from early to late Holocene times. The intrusion of warmer Atlantic Water towards the Northeast Greenland continental shelf and changes in the solar insolation supposed to be the main climate drivers.

A third study addresses ways of possible diagenetic alteration on organic bulk parameters and biomarkers in recent and sub-recent samples from the Northeast Greenland continental shelf in comparison with other Arctic records. Multicorer records may be altered by near-surface degradation processes, suggested from the extremely high concentration values in the surface sediments sharply decreasing to minimum values within the uppermost about ~5 cm. Downcore records, however, predominately still reflect a primary signal.

In summary, our high-resolution records fill the gap of past climate conditions from the western Fram Strait and show detailed changes sea-ice behavior, primary productivity, terrigenous supply and ice-sheet dynamics during the past ~10.2 ka on the Northeast Greenland continental shelf. Environmental conditions and climate reacted partly abrupt during specific time intervals e.g. early Holocene, but does not clearly reflect a Neoglacial Cooling trend in contrast to the eastern Fram Strait during the mid to late Holocene. Future studies are needed to understand how closely ice shelves and sea ice interact with each other, especially in this highly versatile area where ice sheet loss of 79°Glacier could make a difference in 1 m sea level. Another important aspect of future studies is to discuss and quantify biomarker degradation that may have influenced down-core biomarker variability. Finally, these paleo records from Greenland and Spitsbergen would complete the overall picture in sea-ice history of the Fram Strait and its driving mechanisms and help to understand changes in their critical key climate components.

Zusammenfassung

Wann wird das gesamte arktische Meereis im Sommer verschwunden sein? Der rapide Rückgang der durchschnittlichen Meereisausdehnung um mehr als ein Drittel während der letzten 3 bis 4 Jahrzehnte hinterlässt in den Klimamodellprojektionen eine traurige Nachricht. Der dramatische Meereisverlust in der Arktis scheint im Allgemeinen schneller einzutreten, als die Klimamodelle vorhergesagt haben. Heutzutage sind die sich rasch ändernden Umweltbedingungen in der Framstraße, der Passage zwischen Grönland und Spitzbergen, besonders besorgniserregend. Der Meereisverlust verstärkt sich, und das nordostgrönländische Inlandeis wird dünner. In den letzten Jahrzehnten hat der Treibeisexport über die Framstraße zugenommen und trägt mit einer beträchtlichen Zahl zum Süßwasserhaushalt der nordischen Meere und zur globalen Ozeanzirkulation bei.

Hier zeichnet unsere Analyse des nordostgrönländischen Kontinentalschelfs in der westlichen Framstraße in einzigartiger Weise vergangene Klimaänderungen in einem äußerst vielseitigen Umweltsystem des Arktischen Ozeans auf. Multivariate Analysen von molekularen hochverzweigten Isoprenoiden (HBI), spezifischen Sterolen, Foraminiferen und organisch/anorganischen Bulk-Parametern wurden an ausgewählten marinen Sedimentkernen und Oberflächenproben vom nordostgrönländischen Kontinentalschelf durchgeführt. Diese Proxies ermöglichen Rekonstruktionen vergangener Veränderungen der Meereisbedeckung, der Primärproduktion, des terrigenen Eintrags sowie der Ausdehnung des Grönland-Eisschildes.

Das erste Manuskript gibt Einblicke in die vergangene Meereisvariabilität auf dem äußeren nordostgrönländischen Kontinentalschelf und die jahreszeitliche Bildung der Nordost Wasserpolynja seit Beginn des Holozäns bis heute. Dieses äußere Schelfregime wird stark von Treibeis, kaltem Wasser aus dem zentralen Arktischen Ozean und der jährlich auftretenden lokalen Meereisbildung beeinflusst. Interaktive Meereis- und Ozeandynamiken regulieren das regionale Klima und die Biologie auf dem marginalen Schelf. Kontinuierliche saisonale Meereisvorkommen während des Holozäns innerhalb dreier markanter Stadien markieren relativ abrupte Veränderungen bei ~9 ka und ~1 ka. Während des frühen Holozäns wurde eine reduzierte bis variable Meereisbedeckung mit einer insgesamt hohen Primärproduktivität beobachtet, die höchstwahrscheinlich auf die maximale Sonneneinstrahlung zurückzuführen ist. Die Meereisschmelze und der verstärkte Zufluss von wärmerem, rezirkulierendem Atlantikwasser begünstigten intensive Planktonblüten und die Ablagerung von sowohl mariner als auch terrigener organischer Substanz. Die Umweltbedingungen änderten sich in Richtung saisonaler Meereisbedingungen und eines verstärkten Treibeissignals, was durch terrigene Biomarker und IRD-Gehalt während des mittleren Holozäns belegt wird. Schließlich trat während des späten Holozäns ein stabiler saisonaler Meereisrand innerhalb einer voll entwickelten Polynya-Umgebung auf und hebt insbesondere die letzten 1 ka hervor.

Um die Wechselwirkungen zwischen Ozean – Meereis – Eisschild zu verstehen, konzentriert sich eine zweite Studie auf den inneren nordostgrönländischen Kontinentalschelf, wo die marinen

Auslassgletscher des nordostgrönländischen Eisstroms durch eine nahezu permanente Eisbarriere namens Norske Øer begrenzt werden. Die Kernlokation befindet sich vor der 79°Gletscherbucht, und die Studie umfasst sedimentologische, mikropaläontologische und organisch-geochemische Datensätze, die grundlegende Einblicke in die detaillierte anfängliche spätweichselzeitliche bis holozäne Meereis- und Eisschildgeschichte liefern. Im Gegensatz zum äußeren Schelf ist das Treibeis eher von sekundärer Bedeutung, während hier die lokale Eisbarriere eine fundamentale Rolle spielt, indem sie Gletscher daran hindert, aufgrund des Stützeffekts zu kalben. Es wurde eine Rekonstruktion des wachsenden/schwindenden 79°Gletschers und der Veränderungen der Norske Øer Eisbarriere während dieses spezifischen Intervalls erstellt, die den Zeitpunkt des Rückzugs und des Zerfalls des 79°Gletschers zeigt, begleitet von der Intensivierung der Meereisbedeckung. Verschiedene Lithofaziestypen stellen den Übergang von deglazialen Bedingungen mit einem auf dem Schelf liegenden 79°Gletscher über eine proximale bis hin zu einer distalen glaziomarinen Umgebung dar, die den Beginn des Rückzugs des 79°Gletschers und den vollständigen Zerfall des Schelfeises bei 7.9 ka zeigen. Unsere Biomarker- und Foraminiferen-Proxy-Rekonstruktionen spiegeln die lokalen Meereisbedingungen wider, die sich von einem stabilen Meereisrand und einem System hoher Produktivität während des frühen Holozänen Thermischen Maximums (~10.6 bis 9.6 ka) zu ausgedehnten saisonalen Meereisbedingungen im späten frühen Holozän (9.6 bis 7.9 ka) und fast permanenten Meereisbedingungen im mittleren bis späten Holozän (7.9 ka bis heute) veränderten. Diese Veränderungen werden stark durch den Rückgang des Atlantikwassereinstroms vom frühen bis zum späten Holozän ausgelöst. Das Eindringen von wärmerem Atlantikwasser in Richtung des nordostgrönländischen Kontinentalschelfs und Veränderungen in der Sonneneinstrahlung waren höchstwahrscheinlich die treibenden Klimafaktoren.

Eine dritte Studie befasst sich mit der möglichen diagenetischen Veränderung organischer Bulkparameter und Biomarker in rezenten und subrezentem Proben vom nordostgrönländischen Kontinentalschelf im Vergleich mit anderen arktischen Lokationen. Die Multicorer-Daten weisen auf oberflächennahe diagenetische Abbauprozesse hin, was sich in den extrem hohen Biomarker Konzentrationen in den Oberflächensedimenten, die drastisch in den oberen ~5cm zu Minimalwerten abnehmen, widerspiegelt. Unterhalb von ~5 cm bleibt jedoch überwiegend das Primärsignal erhalten. Zusammenfassend lässt sich sagen, dass unsere hochauflösenden Aufzeichnungen aus der westlichen Fram Straße detaillierte Einblicke in die Meereisausdehnung, die Primärproduktivität, den terrigene Eintrag und in die Eisschichtdynamik während der vergangenen ~10.2 ka auf dem nordostgrönländischen Kontinentalschelf zeigen. Umweltbedingungen und Klima reagierten teilweise recht abrupt in bestimmten Intervallen, z.B. im frühen Holozän, spiegeln aber im Gegensatz dazu nicht eindeutig einen neoglazialen Abkühlungstrend im Vergleich zur östlichen Framstraße während des mittleren bis spätes Holozän wider. Zukünftige Studien sind notwendig, um zu verstehen, wie eng Schelfeis und Meereis miteinander interagieren, insbesondere in diesem sehr vielseitigen Gebiet, wo ein Eisschildverlust von 79°Gletscher einen Unterschied von 1 m Meeresspiegelanstieg ausmachen könnte.

Ein weiterer wichtiger Aspekt zukünftiger Studien ist die Diskussion der Degradation von Biomarkern. Übergeordnet würden diese Paläoaufzeichnungen von Grönland bis zu Spitzbergen das Gesamtbild der Meereisgeschichte in der Framstraße vervollständigen, antreibende Mechanismen hervorheben und zum allgemeinen Verständnis der Veränderungen in ihren kritischen Schlüsselkomponenten des Klimas beitragen.

Danksagung

Lieber Rudy (Prof. Dr. Ruediger Stein), liebe Kirsten (Dr. Kirsten Fahl) DANKE für ALLES. Durch eure intensive Unterstützung und Betreuung hat diese Arbeit ihre wertvolle Form erhalten. Danke für all die anregenden und spannenden Diskussionen, Perspektivenwechsel, wissenschaftlichen Freiheiten und euer immenses Vertrauen in mich. Neben den wissenschaftlichen Werten und ehrlichen Worten, gebt ihr dieser Arbeitsgruppe zusätzlich einen familiären Touch, welcher die gemeinsame Zusammenarbeit immer besonders schön gestaltet hat. Ich durfte so viel von euch lernen: bessere Betreuer hätte ich nicht an meiner Seite wissen können, die sich so viel Zeit nehmen und jederzeit für mich ins Feuer springen würden. Die Expeditionen in die Arktis werde ich für immer mit großer Freude in meinem Herzen tragen. Jetzt geht diese Reise weiter...

Bei Prof. Dr. Ralph Schneider bedanke ich mich für die Übernahme der Zweitbegutachtung.

Mit Walter Luttmann im Labor konnte nichts schiefgehen – mit mir manchmal schon; danke für die Erklärungen und deine Geduld. Gerne philosophierten wir übers Leben, lachten viel, tauschten Anekdoten aus; langweilig wurde es nie. Rita Fröhlking, Susanne Wiebe, Valea Schumacher, Wirda Susanti, Norbert Lensch, Jens Matthiessen, Frank Niessen danke ich für die Unterstützung bei relevanten technischen Geräteeinführungen und bei den Messungen und Expeditionsvorbereitungen.

Ein riesiges Dankeschön geht an meine lieben Bürokollegen Kevin Küssner (alias Kev Kev), Nachrichtenbeauftragter und Patenonkel von Bürokind Elfriede; Nele Lamping als Mitglied der Klappradgang; Denise Dieckstahl die gute Seele. Ich werde unsere lauten Musikeskapaden und all die guten Gespräche im Büro vermissen. Mein Dank gilt auch den anderen lieben Kollegen Dr. Anne Kremer, Dr. Henriette Kolling, Dr. Thomas Ronge, Wenig-si Chao, Elena Vorrath, Julia Hagemann, Dr. Marc Wengler, Shuzhuang Wu, Jeetendra Saini, Junjie Wu und Defang You.

Maximilian Vahlenkamp danke ich, dass er mich ein großes Stück auf meinem Weg bis zum Anfang der Doktorzeit begleitet hat und mir zeigte, wie ich mein verflixtes erstes Paper strukturiere.

Danke auch an meine Corona-Buddies Catharina Haug und Jos Maalderink, ein Anfang von etwas Neuem!

Ladies-Stammtisch: Patrizia Geprägs, Jenny Wendt, Gesche und Lavinia Permien. Treue Seelen die mein Leben in jeglicher Hinsicht bereichern und mich immer so nehmen wie ich bin. Danke, ihr seid einfach klasse Menschen mit viel Herz, Humor und offenen Armen, wenn ich sie gebraucht habe.

Viva mis amigos internacionales & AWI friends! Thanks to all these lovely people for being a great part of my life: Madda(lena) Bayer-Giraldi, Emma(bear) Smith, Sebastian Hinck, Miguel(ito) Andrés-Martínez, Dami(ano) Della Lunga, Rebecca Karbauer, Jen(ny) Roberts, Rob(ert) Green, Sophie Berger, Gorgia Micha, Stylianos Kritsotalaks. Always better together and party until the sun rises up again.

Was wäre mein Leben ohne meine Familie: Ich danke von ganzen Herzen meinen wundervollen Eltern, die stets mein Fels in der Brandung sind. Ihr glaubt an mich, wenn ich es nicht kann, begleitet mich durch alle Höhen und Tiefen und zeigt mir wie wichtig es ist Träume zu leben! Ich danke auch meinen lieben Großeltern (die Kerze bei der Madonna hat geholfen), meinen Geschwistern Pascal und Susan für all ihre aufmunternden Worte, den Jungs von Casa Hellwege, Tante Ulle und alle die noch dazugehören.

Chapter 1

1. Introduction

1.1 Modern Arctic physiography and oceanography

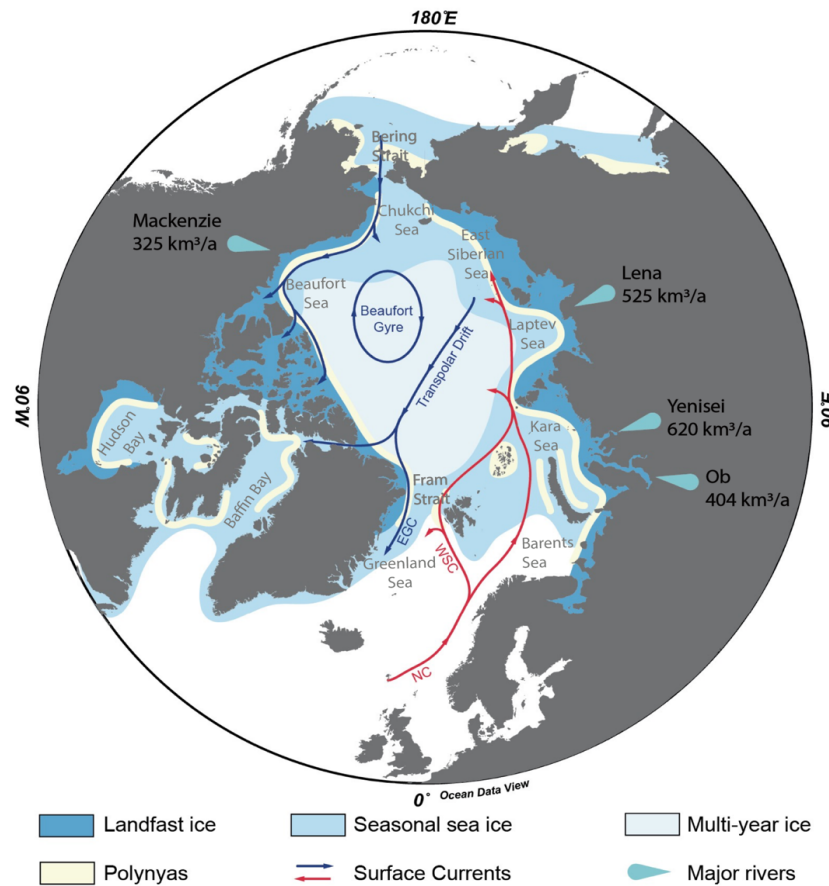


Figure 1.1: Map of the Arctic Ocean showing main surface currents carrying warm North Atlantic Waters into the Arctic via the Norwegian Current (NC) and West Spitsbergen Current (WSC) and cold fresh waters out of the Arctic via the East Greenland Current (EGC). Wind-driven ocean circulation are the Beaufort Gyre and Transpolar Drift (Nørgaard-Pedersen et al., 2007; MacDonald et al., 2004). Color shaded area indicate landfast ice, polynyas and the average extent of seasonal and perennial sea ice of 1981–2010 (<http://nsidc.org>, accessed in March 2018). Blue pointers show the input of the largest Arctic rivers transporting enormous amounts of freshwater to the shallow marginal seas (Gordeev et al., 1996; MacDonald et al., 1998; Millot et al., 2003; figure modified after Kremer et al., 2018).

The Arctic Ocean is the smallest and shallowest of the world's five major oceans. It is distributed between $\sim 70^\circ\text{N}$ (Amerasian side) and $\sim 65^\circ\text{N}$ (Eurasian side) and covers an area of ~ 14 million km^2 (2.6% total area of the world's ocean, less than 1% of volume; Jakobsson 2002; Jakobsson et al., 2012). Besides its surrounding waters, the Arctic Ocean is bordered by the landmasses of North America, Greenland, Canada, Iceland, Norway, Alaska and Russia (Fig. 1.1). The Lomonosov Ridge (Fig. 1.2) divides the Arctic Ocean into two major basins, the Amerasian Basin and Eurasian basins. The Amerasian Basin is subdivided into the Canada Basin and Makarov Basin by the Alpha-Mendeleyev Ridge and the Eurasian Basin into the Amundsen Basin and Nansen Basin by the Gakkel Ridge (Fig. 1.2).

Water mass exchange between the Arctic Ocean and world oceans is regulated by two major ocean gateways. Low salinity Pacific Water unidirectionally enter the Arctic Ocean via the narrow and shallow Bering Strait. The Fram Strait (water depths of up to 2545 m) passage is the only deep-water connection between the Arctic Ocean and Atlantic Ocean and controls the inflow of warm Atlantic Waters (Fig. 1.1, 1.2). Shallow waterways also occur in the Canadian Arctic Archipelago and Barents Sea. Due to the limited exchange conditions the Arctic Ocean basin resembles the “Mediterranean Sea”.

Marginal seas of the Arctic Ocean include the Beaufort Sea, Chukchi Sea, East Siberian Sea, Laptev Sea, Kara Sea, Greenland Sea and the adjacent seas in the Hudson Bay and Baffin Bay (Fig. 1.1). These seas comprise the world’s broadest and shallowest shelves (area from coastline to shelf break), covering approximately 52.7% of the total area of Arctic Ocean and their size and depth vary regionally (Fig. 1.2; Stein, 2008; Williams and Carmack, 2015). The East Siberian shelf for examples stretches up to 1500 km offshore and is the largest continental shelf of the Earth. The largest Arctic rivers are named Ob, Yenisei, Lena (1500 km^3) and originate from the Eurasian continent and the Mackenzie river (325 km^3) from the Canadian Archipelago (Fig. 1.1). They flow out onto these shelves and fed the Arctic Ocean with freshwater that dominates the stratification at the surface (Aagaard and Carmack, 1989, Proshutinsky et al., 2015). Suspended terrigenous particles are transported by these rivers, playing a crucial role for the Arctic Ocean Carbon budget and marginal shelf productivity due to nutrients and dissolved carbon supply.

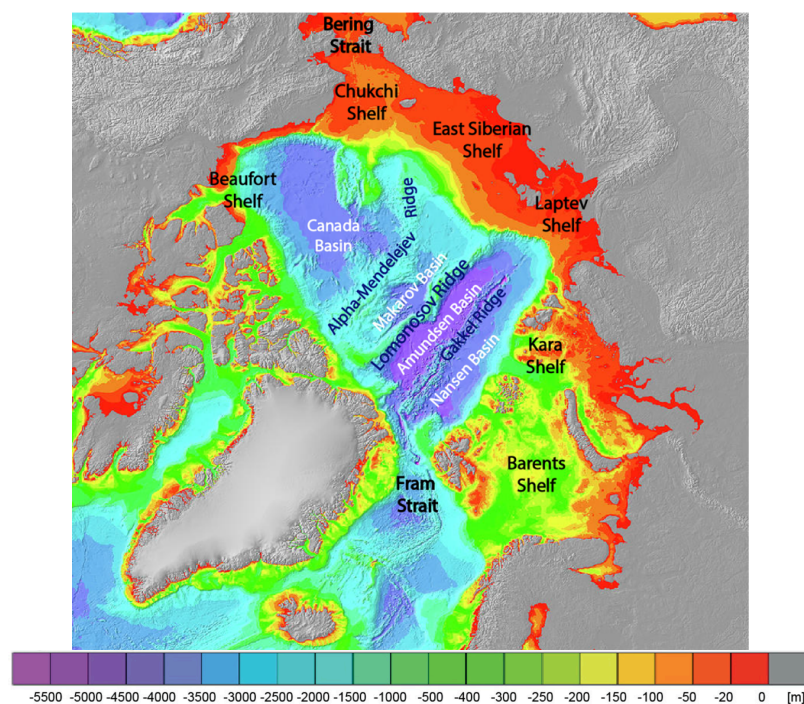


Figure 1.2: Bathymetric map of the Arctic Ocean and its shelf areas, submarine ridges, major basins and gateways to other oceans. Colored scale below indicates the bathymetric and topographic tints (Source: Jakobsson et al., 2012, International Bathymetric Chart of the Arctic Ocean, IBACO).

All waters of the Arctic Ocean are relatively cold and variations in the density are controlled by changes in salinity. Roughly, there are three main water masses, the surface water masses, the intermediate waters (Atlantic Layer), and the deep waters (Fig. 1.3). A thin, less dense and lower temperature surface layer at the top separates the underlying saltier, denser deep ocean waters by the so-called Arctic halocline ranging between 30–50 m, in which both temperature and salinity rise with increasing ocean depth (Aagaard et al., 1985; Coachman et al., 1969). Next to the Arctic halocline, the low saline Polar Mixed Layer (PML) occurs, keeping sea surface temperatures close to the freezing point caused by river runoff. Hydrography of the upper most variable and heterogenous surface layer (0–200 m, Fig. 1.3) is characterized by local mixing through latent heat of freezing and thawing, brine rejections during sea-ice formation in winter while in summer, ice melt and precipitation, variations in the incoming solar radiation, and the energy fluxes through sea ice produce a stratified, fresher surface layer. These surface waters are steered by two dominant wind driven ocean currents, the clockwise flowing Beaufort Gyre (BG) in the Canadian Arctic and the Transpolar Drift (TPD) that streams parallel to the Lomonosov Ridge towards Fram Strait (Fig. 1.1).

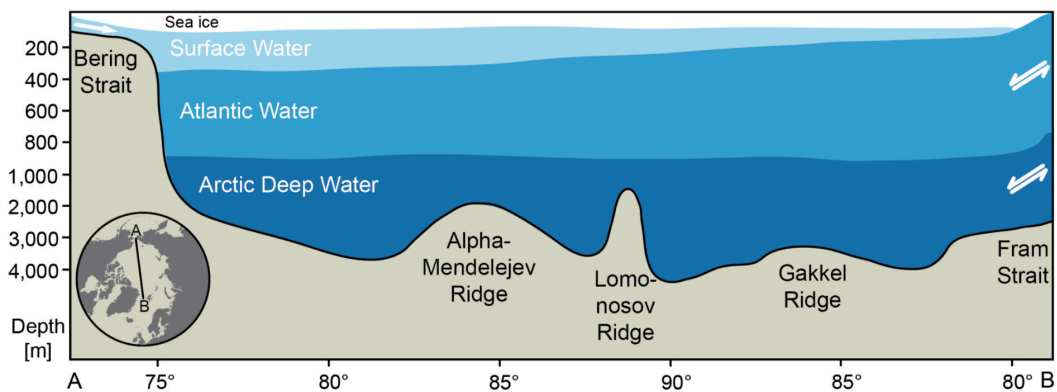


Figure 1.3: Schematic cross section of the Arctic oceanographic structure following the transect starting in the Bering Strait across the central Arctic Ocean towards the Fram Strait (Source: Kremer, 2018 modified after MacDonald et al., 2004). Exchange of water masses in the Fram Strait with neighboring oceans are marked by white arrows.

The Arctic intermediate water is a warmer Atlantic layer ($\sim 0^\circ\text{C}$ isotherm) found between the first 200 to 800 m and regulate the heat budget for the Arctic Ocean and the Nordic Seas and is, due to its strong gradient, sensitive to climate changes (Fig. 1.3; Schauer et al., 2004; Telesiński et al., 2014). In the eastern part of the Fram Strait, warm and saline North Atlantic Water ($T \sim 6\text{--}11^\circ\text{C}$, $S > 35$) enters the Arctic Ocean via the Norwegian Current (NC) and West Spitsbergen Current (WSC, Fig. 1.1, 1.4). Part of this water recirculates westward to the Northeast Greenland shelf as Recirculating Atlantic Water (Fig. 1.1, 1.4; Coachman, 1963; Coachman and Aagaard, 1974; Aagaard et al., 1987; Rudels et al., 2004). Below 800 m water depth, the Arctic Deep Water of higher salinities extends beneath the Atlantic layer to the seafloor and represents $\sim 60\%$ of the total volume (Fig. 1.3). This phenomenon results from a lateral exchange between the Nordic Seas and Arctic shelves during brine formation (Coachman and Aagaard, 1974).

1.2 Study area – Fram Strait and Northeast Greenland continental shelf

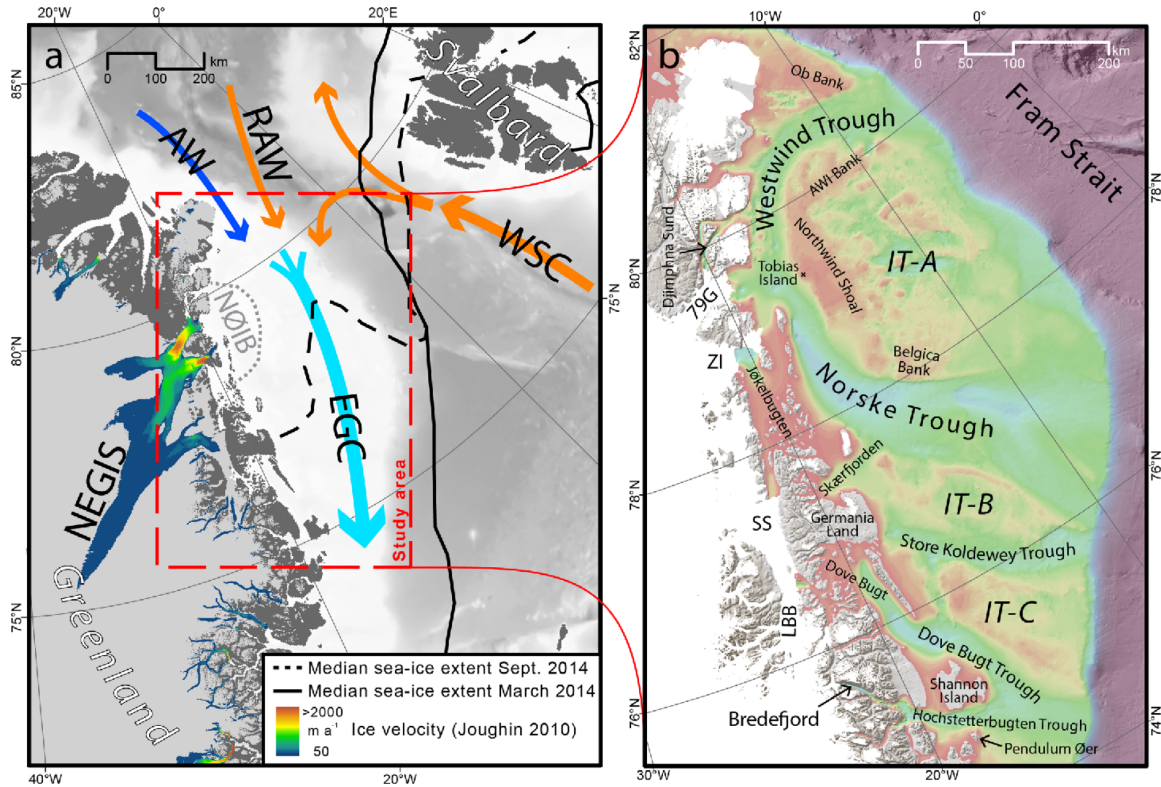


Figure 1.4: Location maps of the Fram Strait and Northeast Greenland continental shelf display the median sea-ice extent for winter (March 2014) and autumn (September 2014), ice-sheet velocities of NEGIS from Joughin et al. (2010), relevant ocean surface currents and the bathymetry to the right. NEGIS = Northeast Greenland Ice Stream, NØIB = Norske Øer Ice Barrier, AW = Arctic Water, RAW = Recirculating Atlantic Water, WSC = West Spitsbergen Current, and EGC = East Greenland Current. (b) Geographical names mentioned in the text; 79G = 79°N Glacier, ZI = Zachariae Isstrøm, SS = Storstrømmen, LBB = L. Bistrup Bræ, and IT = inter-trough areas (Source: Arndt et al., 2015).

Our main research area, the Northeast Greenland (NEG) continental shelf (76°N and 81°N) in the western Fram Strait is bounded by Greenland's coastline, fjords, islands and marine-terminating outlet glaciers to the left, the abyssal plain in its center and the eastern Fram Strait (Yermak Plateau and Spitsbergen) to the right (Fig. 1.4). As one of the broadest of Greenland's shelf areas it is extending more than 300 km offshore. The cold, fresh East Greenland Current (EGC, $T - 1^{\circ}\text{C}$, $S < 34.4$) flows with enormous amounts of drift ice southward along the NEG continental margin towards Iceland (Fig. 1.4; Aagaard et al., 1968; Hopkins, 1991; Rudels et al., 1999). In addition to the drift ice, the EGC also carries low salinity Arctic Water (AW), intermediate and deep waters from the interior of the central Arctic Ocean, as well as Recirculating Atlantic Water (RAW) from the eastern Fram Strait. Dense waters of the EGC contribute to the Denmark overflow and the North Atlantic Deep Water formation (NADW) and therefore may strengthen or weaken the Atlantic Meridional Overturning Circulation (AMOC; Rudels et al., 2002).

The reverse slopes of the Westwind Trough in the north and the Norske Trough in the south cross the entire shelf parallel and are deeper (200–500 m in depth) than the surrounding shallow banks and shoals

in the middle (AWI Bank, Belgica Bank and the Northwind Shoal, Fig. 1.4). These trough systems cover more than 40% of the NEG continental shelf and converge with their deepest sections in front of the 79° Glacier (79NG, Fig. 1.4; Reeh et al., 2001; Arndt et al., 2015). Length of the Westwind Trough is 300 km with a median width of 40 km, it curves roughly in a northeast direction. Typical characteristics of the Westwind Trough are ridges and banks at either side, a maximum water depth of 900 m underneath the 79NG and 300 m at the shelf edge. Norske Trough is 350 km long with an average width of 35 km, striking southeastwards and has a maximum water depth of 560 m. The Norske and Westwind Trough systems act as ideal water mass pathways and direct warmer recirculating Atlantic Water into the ice-shelf cavities. Elongated depressions filled with several km-thick sediments were mapped on the middle and outer NEG continental shelf (Benn and Evans, 2010; Arndt et al., 2015). A detailed overview of further geological features for example sills, hammocks and the zone of salt diapirs and the bathymetry, is given by Arndt et al. (2015, 2017).

Nioghalfjerdsbræ (79NG), Zachariae Isstrøm (ZI) and Storstrømmen are the three major fast flowing marine-terminating outlet glaciers at the coast and part of the Northeast Greenland Ice Stream (NEGIS), that extends 700 km inwards with a fast flow of 20 m per year (Fig. 1.4, Joughin et al., 2010, Rignot, 2011). The Greenland Ice Sheet drains ~12% via NEGIS and supplies an extensive amount of freshwater to the NEG continental shelf (Fig. 1.4; Zwally et al., 2012). These outlet glaciers are enclosed in a semi-permanent fast-ice barrier, named Norske Øer Ice Barrier (NØIB, ice thicker than 2 m above sea level), which covers an extensive area of the shelf between 78°N–80°N and stretches approximately 75–150 km from the coast eastward towards a series of islands (Fig. 1.4; Reeh et al., 2001; Hughes et al., 2011; Sneed et al., 2016). Further, it plays a fundamental role by preventing iceberg discharge from calving glacier fronts of 79NG and ZI and tidewater ice streams (Sneed et al., 2016). NØIB builds the southern tip of the seasonally and highly productive Northeast Water Polynya (NEW Polynya) and is bounded by drift ice outflow from the central Arctic Ocean to the east (Budèus and Schneider, 1995). Both vary annually in size and horizontal extent (Budèus and Schneider, 1995). Centered over two shallow banks (Ob and Belgica Bank), the NEW Polynya seasonally appears between April to September (Schneider and Budèus, 1994). It mostly controls the local ecosystem and exports carbon to deeper areas of the Greenland Sea (Hirche et al., 1994). Additional detailed description of the research area is given in the three investigated manuscripts (chapter 4, 5 and 6).

1.3 The role of Arctic sea ice in the climate system

Sea ice, as a part of the cryosphere, covers 7% of the Earth's surface and about 15% of the world's ocean (Wadhams, 2003; Weeks, 2010; Shokr and Sinha, 2015). Due to its low density, it floats on the ocean surface. At the onset of sea-ice formation, small ice crystals form at the ocean surface and transform into larger ice sheets, depending on the temperature, salinity, wind and waves. Salt ions are expelled to the underlying waters during this process, producing brines (Thomas and Dieckmann, 2008).

These enriched, dense brines are present both in cavities and channels in the sea ice itself, but can sink to the ocean bottom and contribute to the formation of deep-water, driving thermohaline circulation (Wadhams et al., 1981; Rudels and Quadfasel, 1991; Dieckmann and Hellmer, 2003). Areas of extensive freshwater input by rivers and/or glaciers often create extended stratified low salinity layers at the ocean surface, favouring the formation of sea ice.

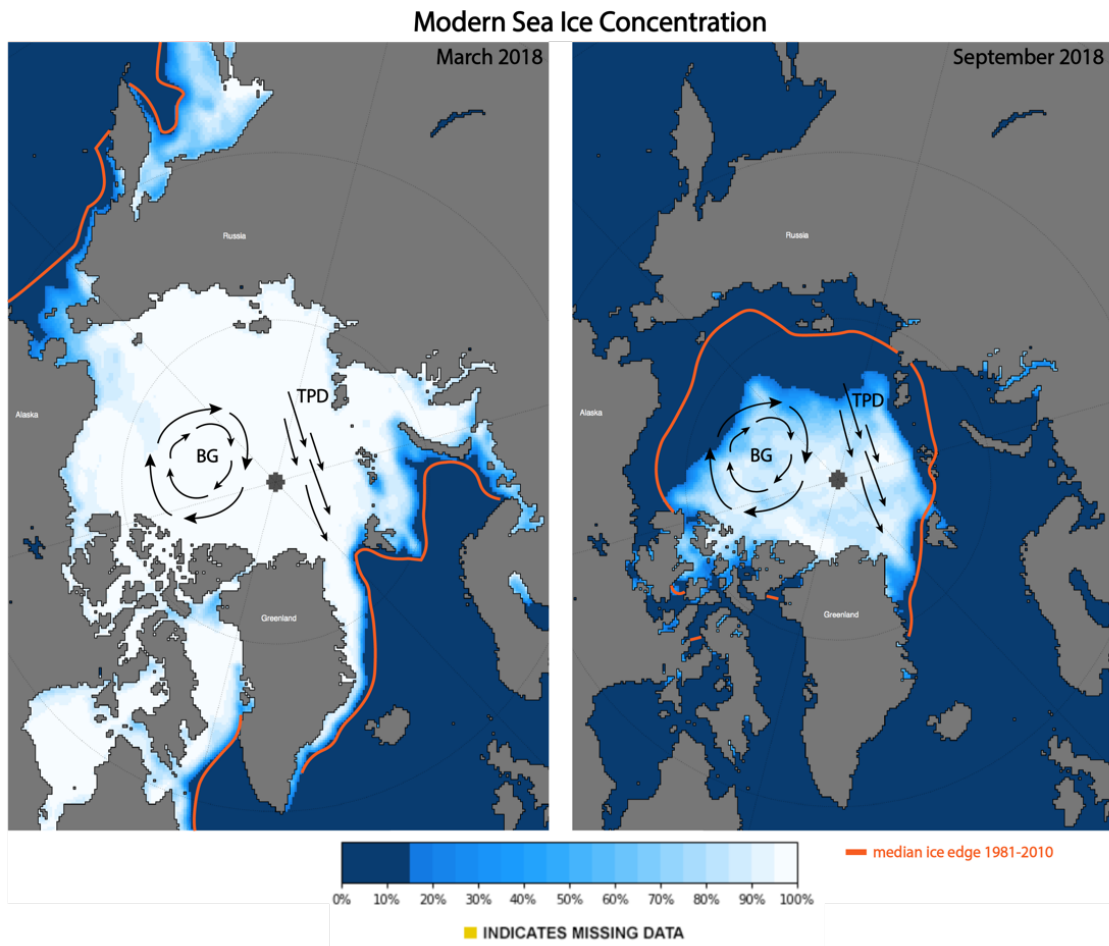


Figure 1.5: Satellite-derived sea-ice extent of the Arctic Ocean for March and September in 2018 relative to the median ice edge from 1981–2010 (Source: <https://nsidc.org/>, accessed in March 2020, Fetterer et al., 2017). Black arrows show the wind-driven Beaufort Gyre (BG) and Transpolar Drift (TPD).

Based on satellite observations (since 1979), Arctic sea reaches its maximum extent in winter (March), covering an area of approximately 14–15 million km² and retreats in summer (September) to <5–7 million km², but does not disappear completely (Fig. 1.5 and 1.6; <https://nsidc.org/>). Arctic sea ice as one of the most extreme Arctic oscillations experiences seasonal variations that annually differ in time and magnitude (Wang et al., 2000). In particular, first year-ice has a strong seasonal variation, most parts of it melt during the summer and it primarily forms in the surrounding marginal (shelf) areas and ranges between a few centimetres up to 1 m, even up to 2.5 m in the high Arctic during winter (Johannessen et al., 2004; Dieckmann and Thomas, 2010). Seasonal sea ice that survives the summer melt season may last for years and become multiyear ice (perennial sea ice) and is characteristic for the central Arctic Ocean with a thickness up to ~3–4 m (without ridges, Wadhams, 1992).

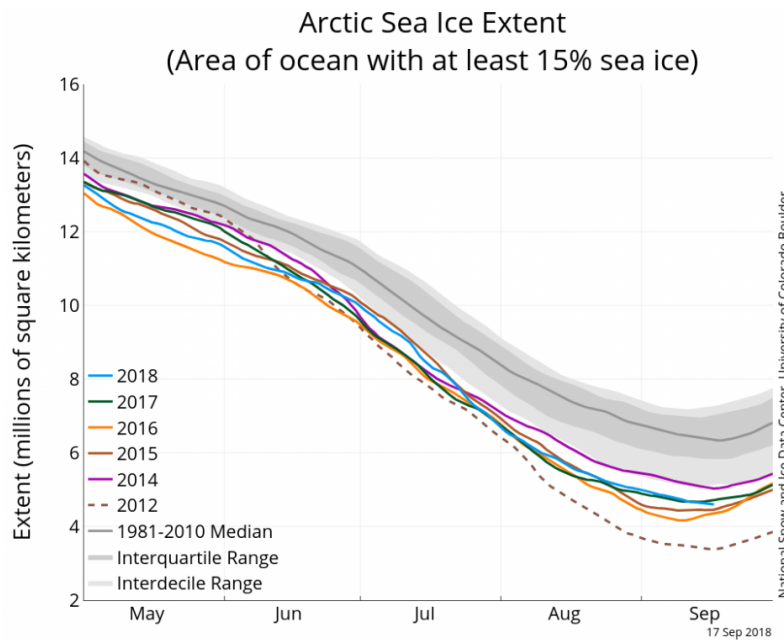


Figure 1.6: Arctic sea-ice extent in May to September 2018 in comparison with the daily extent of the four previous years and the record low year 2012. Median between 1981 to 2010 are represented by a dark grey line while the grey shaded area shows the interquartile and interdecile ranges of the data (Source: <https://nsidc.org/>, accessed in March 2020).

Most of the Arctic Ocean and its marginal seas are covered by sea ice during winter, except for the Barents Sea, which remains ice-free all year round because they are influenced by the warm, saline Atlantic Waters that enters the Arctic Ocean via the NC/WSC (Aagaard et al., 1987; <https://nsidc.org/>). During the winter times, the extension of sea ice even reaches other seas much further south of the Arctic Ocean, e.g. the Sea of Okhotsk, Baffin Bay, Bering Sea, Hudson Bay, the Greenland Sea, and the Labrador Sea (Fig. 1.5).

Another important type of sea ice is the landfast ice over shallow continental margins and shelves, that is immovably anchored to the shore or ocean bottom, even under wind or current activity (Gally et al., 2012). Pack ice (drift ice), on the other hand, is dynamic, drifting with the wind and currents and may due to collision with other pack ice become even thicker (Campbell, 1965).

Wind and ocean currents ensure that sea ice is constantly in motion. Two wind-driven ocean currents are located in the Arctic Ocean. A high-pressure system that spawns over North of Alaska and Canada builds the clockwise circulating Beaufort Gyre (Fig. 1.5) and traps sea ice for several years in the Amerasian Basin. In the Eurasian Basin, the linear structured Transpolar Drift occurs (Fig. 1.5). This gyre transport newly formed sea ice within one to three years from the East Siberian and Laptev sea shelves to the North Pole and Franz Joseph Land (mean drift ice velocity is 2 cm/s), through the Fram Strait and southward along NEG continental shelf (drift velocities up to 10 cm/s; Kaur et al., 2018). Arctic sea-ice movement is important to the climate system as it transports entrained climate-relevant gases, macro-nutrients, iron, organic matter, terrigenous particles and pollutants into different sectors of the Arctic (Rigor et al., 1997; Dethleff et al., 2000; Eicken et al., 2005; Damm et al., 2018; Peeken et al., 2018).

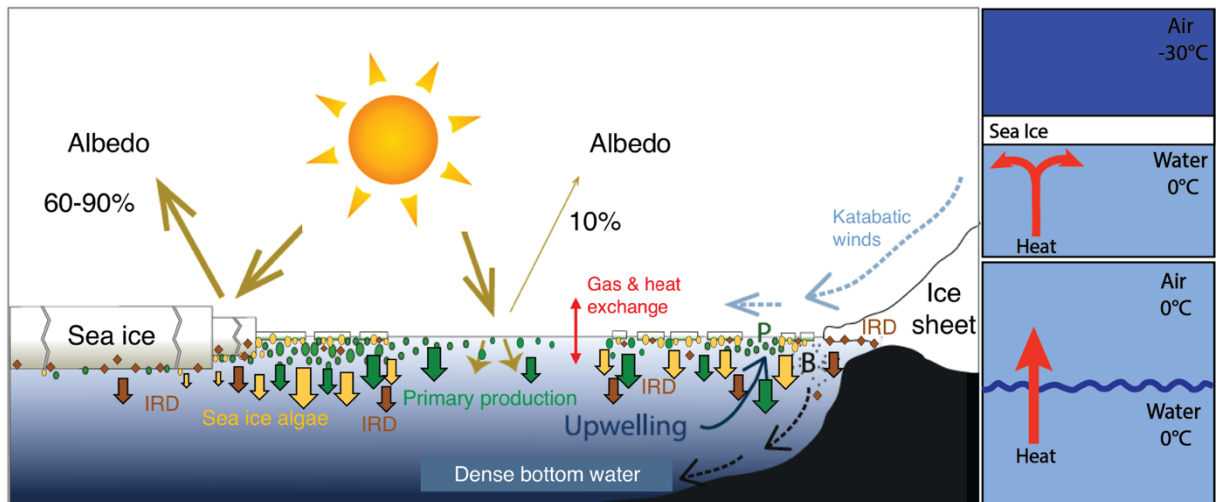


Figure 1.7: Simplified schematic illustration of sea-ice related processes e.g. albedo effect and absorption of incoming solar radiation (yellow arrows), heat and gas exchange between the ocean and atmosphere (red arrows), supply of material via sea-ice melt (downfacing arrows), upwelling, primary productivity (green arrows), brine and polynya formation and ice-sheet dynamics in the Arctic Ocean (Source: Stein, 2019; modified after de Vernal, et al., 2013 and Ruddiman, 2001, supplemented).

The seasonal formation of Arctic sea ice profoundly influences and protects the polar environment by regulating ocean and atmospheric circulation, primary productivity, albedo and the hydrological cycle (Fig. 1.7; Curry et al., 1995; Barry, 1996; Rudels et al., 1996; Sakshaug, 2004; Dieckmann and Thomas, 2010; Sévellec et al., 2017). Landfast ice along shores restricts wind and wave action near coastline ensuring less coastal erosion and protecting the ice shelves through the buttressing effect (for further details please see chapter 1.2, Reeh et al., 2001). The sea-ice covered or open-ocean areas determine the reflection and/or absorption of the solar incoming radiation. When a sea-ice cover exists nearly 80% is scattered back into space due to its bright surface (high albedo) and only 10% is absorbed (Fig. 1.7). Seasonal melting of sea ice from May to September exposes large areas of the ocean, allowing the absorption of sunlight during the warm season up to 90% (low albedo, Fig. 1.7; Pistone et al., 2014; Kashiwase et al., 2017). Sea ice also acts as an insulating cap and regulates the heat exchange between the ocean and atmosphere by reducing evaporation and heat loss to the atmosphere (Fig. 1.7; Jayne et al., 1999). Polar regions covered by sea-ice tends to be colder and drier than areas with without ice (Overland and Wang, 2010; Stroeve et al., 2012). The close relationship between sea ice, atmospheric and ocean temperatures, and sea-level pressure are shown in Fig. 1.8 (for further explanation see chapter 1.2).

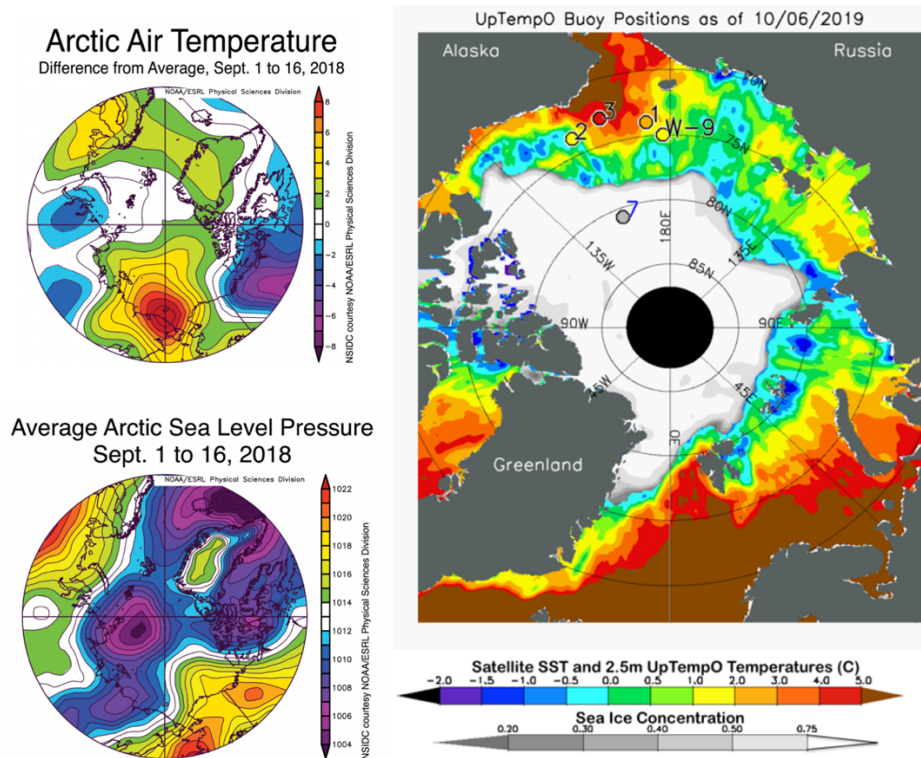


Figure 1.8: The Arctic Air Temperature (upper left corner) includes the differences from average air temperatures in the Arctic (at 925 hPa level in °C) for September 1 to 16 in 2018. Highest temperatures are red and colder ones are indicated by blues and purples. Average Arctic sea-level pressures (below) are in millibars (hPa) for September 1 to 16 in 2018. High pressure areas occur over land and a low pressure over the ocean. Satellite-derived sea surface temperatures (SST, to the right) and sea-ice concentration in September 2018 show temperatures ranging mostly between -1 and +1°C (ship travelling through the ice) and up to +4°C in open waters (Source: <https://nsidc.org/>, accessed in March 2020).

Moreover, two natural climate phenomena, that highly influence European and US winter weather occur in the Arctic; the Arctic Oscillation (AO) and the North Atlantic Oscillation (NAO; Wallace and Gutzler, 1981; Hurrell, 1995). Usually these large-scale counter clockwise circulation patterns (55°N) are synchronous and exhibit a positive and negative climate mode (Jones et al., 1997; Darby et al., 2012). Changes in sea-ice extent alters the wind-patterns over the Arctic and therefore influences the AO/NAO. During a positive AO/NAO, the polar vortex remains strong, meaning a low atmospheric pressure in the Arctic and high atmospheric pressures over the subtropics. With the northward shift of the Jet Stream, colder air masses and storms are kept around the North Pole and climate in the US is drier and warmer over Europe milder and wetter (Fig. 1.9; Ambaum et al., 2001; Wanner et al., 2001). In a negative mode, the Jet Stream moves south, transporting colder air masses, storms and winter weather to Europe (Fig. 1.9; Stroeve et al., 2011). In this negative mode, a stronger Beaufort Gyre causes an enhanced transport of sea ice towards the Siberian shelves and favours the build-up of thicker sea ice. In contrast, during a strong positive AO/NAO mode, sea ice is pushed out of the Arctic and tends to be younger and thinner, which is prone to melt after winter (Fig. 1.9; Darby et al., 2012).

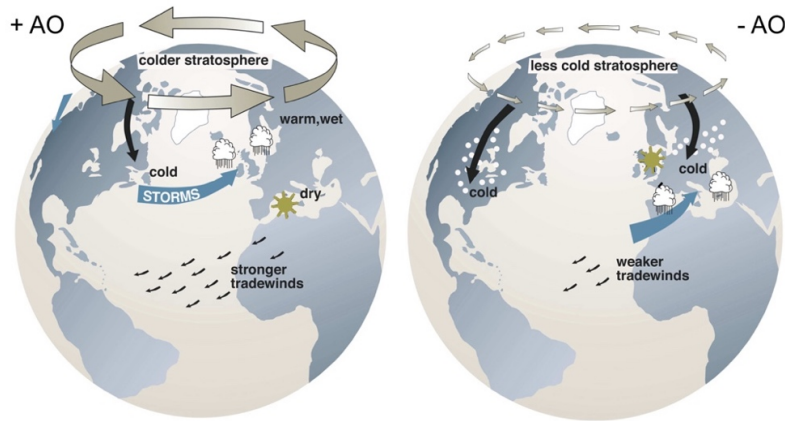


Figure 1.9: Schematic of the Arctic Oscillation (AO) and North Atlantic Oscillation (NAO) and its effects on weather and climate a) positive mode b) negative mode (after AMAP, 2017). (Source: <https://nsidc.org/>, accessed in March 2020).

Sea ice also impacts marine ecosystems, including fish, birds, marine mammals and the macro- and microorganisms that live in higher latitudes (Rudels et al., 1996; Dieckmann and Hellmer, 2008). When sea ice starts to melt, nutrients and terrigenous particles are released to water column and stimulate (in combination with sunlight) the growth of phytoplankton. These phytoplankton blooms form the heart of the Arctic marine food web. However, phytoplankton blooms have also been found on the underside of Arctic sea ice (Arrigo et al., 2011, 2012).

1.4 Ongoing anthropogenic climate change – a future perspective

With the beginning of the pre-industrial time our global pCO₂ level ranged from 275 to 284 ppm, today we have reached a level of 416.2 ppm (<https://co2.earth>, April 2020). This recent state is currently higher than the last 2.1 million years and comparable to the Pliocene epoch with global temperatures 3 to 4°C warmer than pre-industrial times (Zhang et al., 2014). An increase of global atmospheric temperatures by 0.87°C between 2006 to 2015 shows a significantly higher increase to the years 1850 to 1900. Ongoing rising pCO₂ emissions with today's pace encourage an increase of future global temperatures up to 1.5°C to 2°C in 2030 and 2052 and a pCO₂ up to 600 ppm (Szulejko et al., 2017). Due to the Arctic Amplification mentioned before, the Arctic is particularly sensitive to climatic variability and leads us to question the extent that recent trends in Arctic climate variability can be attributed to human-caused climate change, and what are the mechanisms behind (Francis et al., 2017). Arctic sea ice responds exceptionally fast and sensitively to environmental changes in the climate system. An example of the sensitivity of the Arctic to climate variability is that nearly 50% of summer sea-ice extent and 60% of its volume has disappeared within a generation. During this time, the smallest areal extent of sea-ice cover within the last 1400 years was recorded (Kinnard et al., 2011; Meier et al., 2014), and the surface melt area of the Greenland Ice Sheet (GIS) has increased by 45% since 2010 (Fig. 1.10; Tedesco et al., 2011).

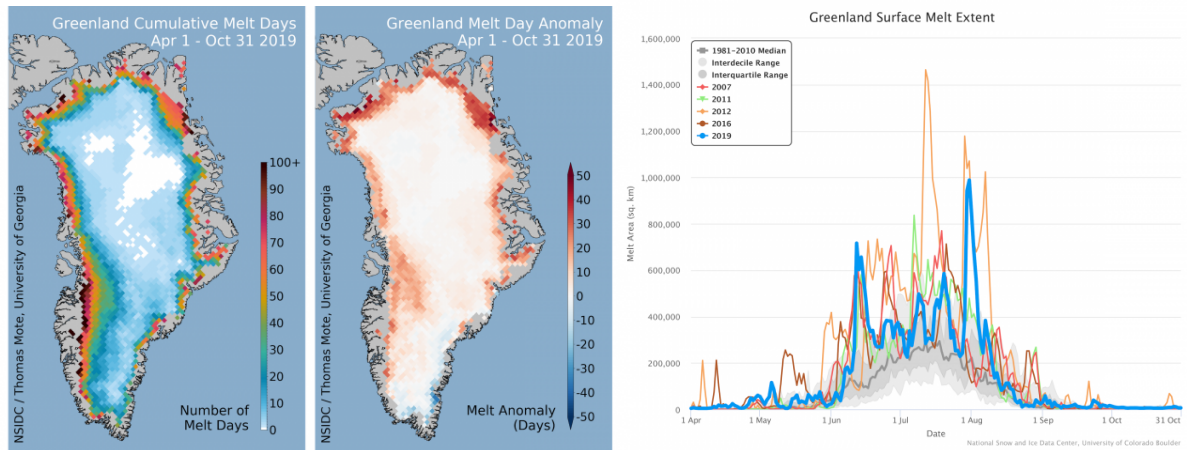


Figure 1.10: Maps to the left show (i) days of Greenland ice-sheet melt during the summer season, and (ii) the difference between 2019 total melt days and the 1981 to 2010 average number of melt days. The graph to the right shows the daily area of surface melting for 2019 and other years (Source: <https://nsidc.org/>, accessed in March 2020).

Sea-ice extent

Satellite observations of Arctic sea-ice extent show a strong downward trend in all months, during winter sea-ice loss has accelerated of approximately -2.4% per decade between 1979 to 1999 to -3.4% per decade from 2000 to present (Notz and Stroeve, 2016, 2018; Stroeve and Notz, 2018). Based on the 1981 to 2010 reference period, sea-ice loss was significantly during autumn, winter and spring than during summer in the last two years (Stroeve and Notz, 2018). The most extreme lows in Arctic sea-ice extent occurred in the years 2007, 2012 and 2019 (Cavalieri and Parkinson, 2012; Stroeve et al., 2014; <https://nsidc.org>, September 2019). Average sea-ice extent in September years 2007 and 2012 was 4.27 and 3.57 million km²; this is a reduction of 2.14 and 2.84 million km² from the 1981–2010 average (<https://nsidc.org>, 2018). Observations by Notz and Stroeve (2018) implies a sea-ice loss of 3 ± 0.3 m² of September sea-ice area per metric ton of CO₂ emission, which means seasonal summer sea will be lost for an additional 100 GT of CO₂ emissions (Fig. 1.11).

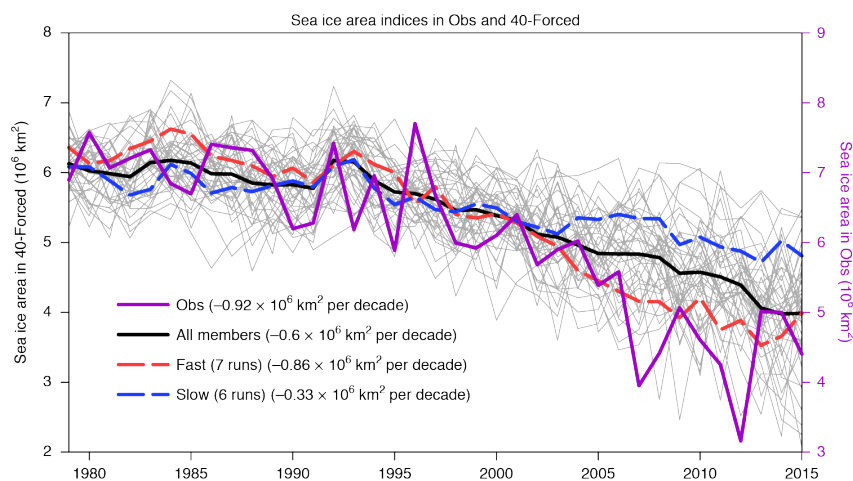


Figure 1.11: Observed and simulated total area of September sea-ice extent in 40-forced (grey line) and satellite observations by NSIDC (purple line, million km²). Black line shows all 40 members and the red and blue lines the average fastest/slowest melting groups. Note that observed sea-ice trends indicate a much stronger overall sea-ice decline compared to all simulated sea-ice models (Source: Ding et al., 2019).

Arctic sea-ice extent has already undergone drastic changes due to rising air temperatures, wind and radiative forcings, and oceanic heat fluxes (Fig. 1.12). These decisive parameters are all subject to natural variability and therefore the reconstruction and interpretation of past climate data is essential to assess future scenarios (Rigor et al. 2002; Shimada et al. 2006; Francis and Hunter 2007; Perovich et al. 2008; Ogi et al. 2010; Kay et al., 2011; Polyakov et al. 2011; SWIPA 2011; Rogers et al., 2015; Kapsch et al. 2016).

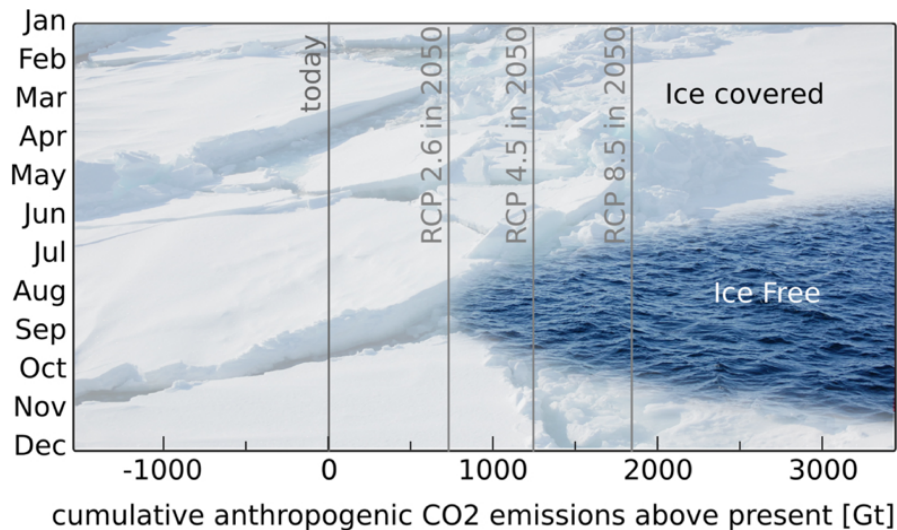


Figure 1.12: Predicted seasonality of Arctic sea ice as a function of ongoing outflow of CO₂ emissions. Present-day CO₂ emissions of 1600 Gt (since 1850) with an annual rate of ~40 Gt per year (Source: Stroeve and Notz, 2018).

Age and thickness of Arctic sea ice

The decline in seasonal sea-ice extent is not the only observable effect of a changing Arctic climate system, drastic alterations were observed in the reduced export of newly formed sea ice from the shallow Siberian shelves accompanied with the loss of multiyear sea ice (Fig. 1.13; Comiso, 2008; Kwok and Untersteiner, 2011; Kwok, 2018). First year ice barely survives the summer months (-15% per decade). This first year ice is important for two reasons, (i) it serves the TPD with sediment-laden sea ice, and (ii) it usually turns into multiyear ice (MYI) afterwards. The drastic decline of the central Arctic perennial sea-ice cover is shown by satellite images of the age and thickness of sea ice (Fig. 1.13). The oldest and thickest multiyear ice packs, containing 3–4 or + 4-years-old ice have essentially disappeared and 58% of the MYI are now consists of relatively young 2–3-year-old ice (Fig. 1.13; Maslanik et al., 2007). Furthermore, first-year ice extensively melted before could be included in the Transpolar Drift system (Krumpfen et al. 2019). Consequently, a long-term cut-off of transported material towards Northeast Greenland and the Fram Strait and a higher sediment release by nearly 24% ($4.8 \times 10^6 \text{ t y}^{-1}$) in the MIZ and the central Arctic Ocean may significantly influence overall sedimentary budgets, the biochemical cycle and ecosystems (Krumpfen et al., 2019).

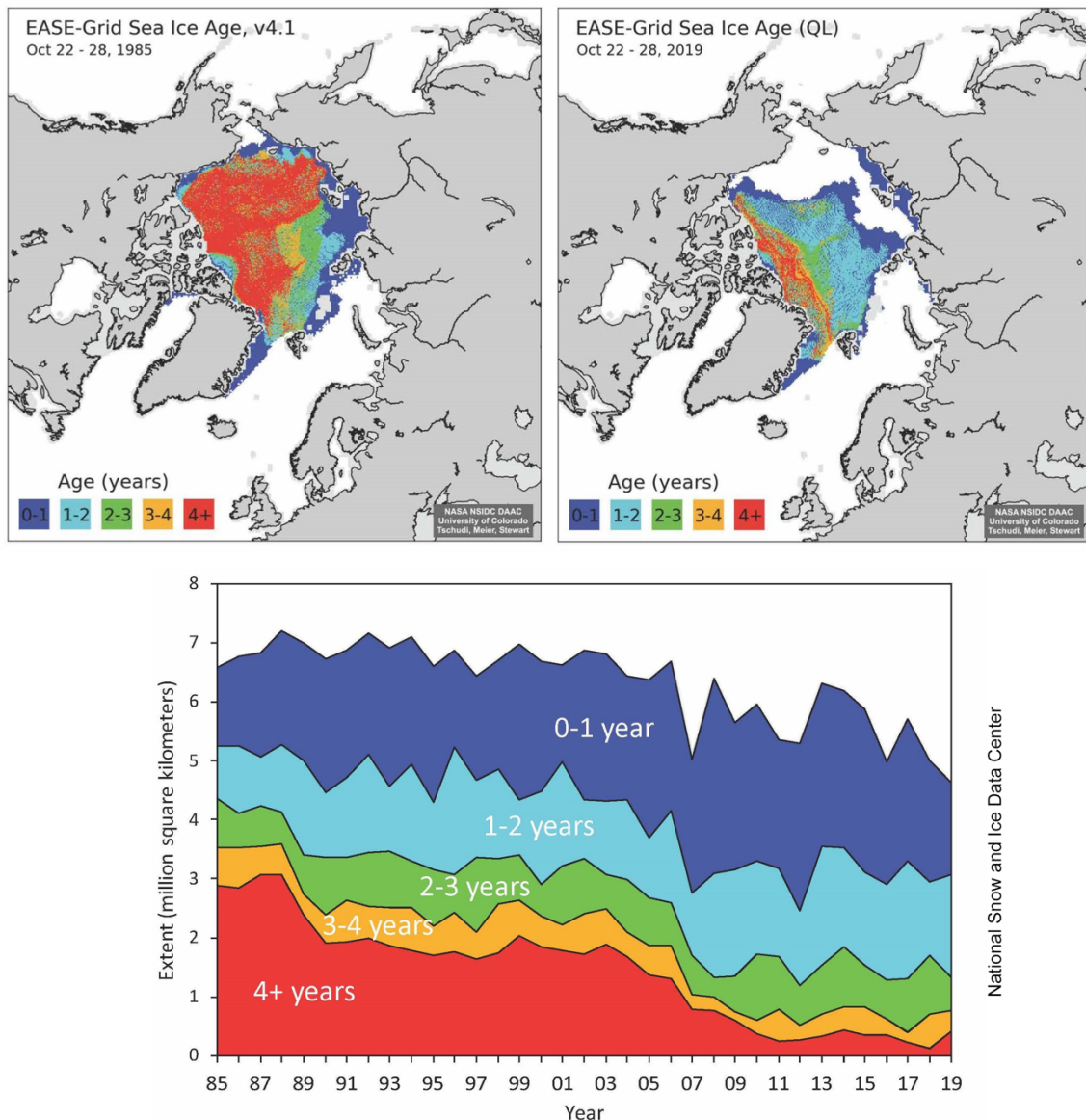


Figure 1.13: Upper maps shows the age of sea ice in the Arctic during the 22 to 28 October week in 1895 and 2019. The lower graph shows a time series of sea-ice age for the same week for the same time period (Source: NSIDC EASE-Grid Sea Ice Age, Version 4, <https://nsidc.org>).

Positive albedo feedback

A key driving force of the seasonal ocean-atmosphere heat budget is temperature, which is highly regulated by sea-ice extent in the Arctic Ocean and surrounding areas and its positive/negative albedo feedback (Fig. 1.14, 1.15; Manabe and Stouffer, 1980). Future model projections with rising air temperatures over the 21st century resolved strongest effects of the Arctic Amplification over the Arctic Ocean during the cold seasons (Fig. 1.14; Miller et al., 2010; Thackeray et al., 2019). Initial warming would lead to an earlier spring melt of the seasonal sea ice, causing a prolonged time period of open water areas (low albedo) and a higher absorption of solar radiation, accelerating the positive albedo feedback-loop (Fig. 1.15). Sensible heat will be stored in the upper mixed surface layers of the Arctic Ocean, favouring further ice melt and exposing even larger areas of dark open water to absorb heat (Fig. 1.15).

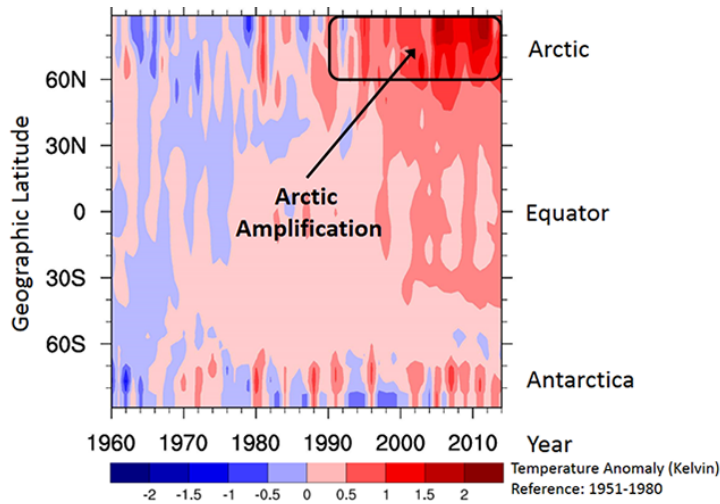


Figure 1.14: Zonally averaged near-surface air temperature anomaly shows strongest increase in the Arctic (Source: Wendisch et al., 2017).

By comparison, the response of thermodynamic processes and vertical heat flux in the summer months are actually rather small, because most of the incoming solar radiation is absorbed anyway (Miller et al., 2010). However, differences appear in the larger vertical extension of the heat storage of the mixed surface layers (~50 m) of the Arctic Ocean. This results in more heat is released back to the atmosphere in late autumn/early winter, which would weaken and delay the formation of sea-ice during the colder periods. These processes are consistent with recent observations of increasing autumn and winter air temperatures (Serreze et al., 2009).

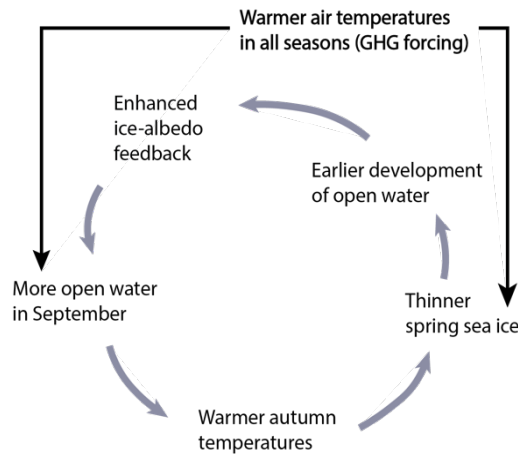


Figure 1.15: Feedback loop explains that extensive open water in recent September will lead to the formation of only thin first year ice, vulnerable to melting out the summer and hampers the build-up of MYI (Source: Stroeve et al., 2012).

Atlantic Meridional Overturning Circulation

Climate model outputs by Sévellec et al. (2017) show that the drastic loss of the Arctic sea-ice cover may hamper the formation of deep-waters and therefore weakens the AMOC (Fig. 1.16). The abnormal exposure of surface heat and freshwater fluxes cause positive buoyancy anomalies preventing deep-water formation. This results in a slowing down of AMOC (rate 0.4 Sv yr^{-1}) (Sévellec et al., 2017). A doubling of global ocean temperatures by 2100 (under future CO_2 emission scenarios) is predicted to result in further slow-down of the AMOC, weakening of the poleward heat transport, increases the ocean heat uptake and cause rising air temperatures over Northeast Greenland (Fig. 1.16; Yin et al., 2011; Cheng et al., 2013; AMAP, 2017).

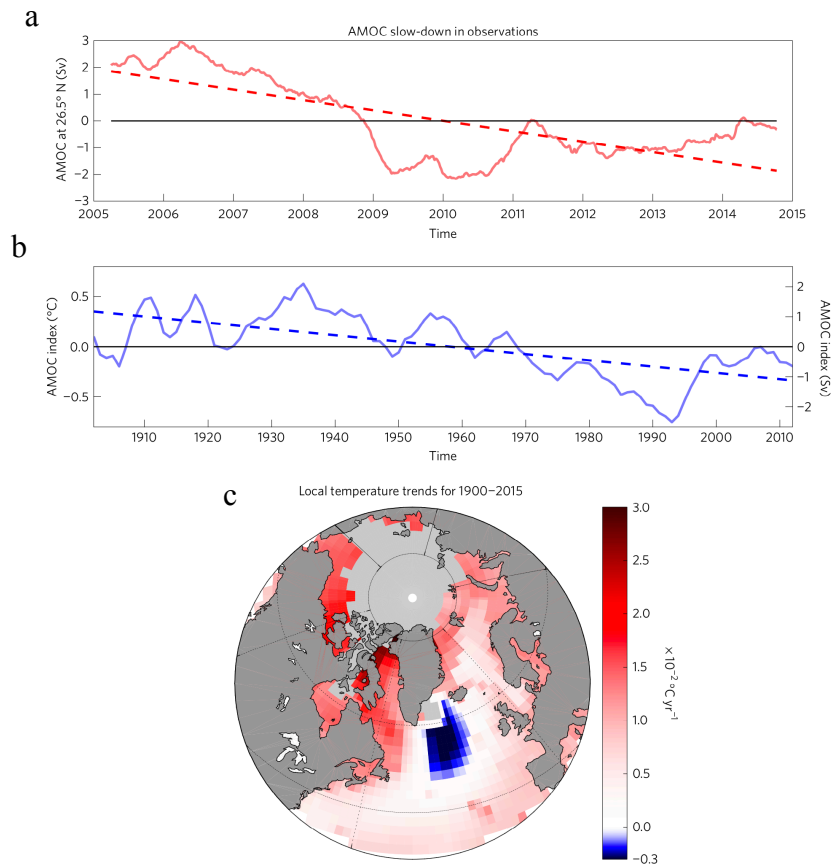


Figure 1.16: a) Graph shows the strength of the AMOC at 26.5°N (red curve), exposing a weakening during the last decade. b) AMOC index (°C) is defined by the surface air temperature between the subpolar North Atlantic and the Arctic, showing a negative AMOC intensity trend over the past century. c) Local averaged surface air temperature trends between 1900 to 2015 shows that the AMOC slow-down was caused by the so-called Warming Hole occurring the subpolar North Atlantic, especially between 50° and 60°N (Source: Sévellec et al., 2017).

This amplifies ice-sheet and sea-ice loss on the NEG continental shelf. A larger meltwater supply by 79NG and ZI into the North Atlantic promotes widespread ocean stratification with colder, fresher water overlying saltier water masses. This stratification may trigger a further weakening of the AMOC, promoting increased storm events over Europe (Sigman et al., 2004; Sévellec et al., 2017).

Jet Stream regulates the positive/negative AO/NAO

The continued loss of Arctic sea ice and mass volume of NEGIS, the rapid declining early summer snow covers on the Northern Hemisphere continents and the persistent rapid Arctic warming relative to the mid-latitudes cause widespread global climate changes referred to the Arctic Amplification (Liu et al., 2012; Tedesco et al., 2013; Simmonds, 2015). The AO/NAO modes are dictated by the Jet Stream and an increasing Arctic Amplification depress the poleward temperature gradient, the fundamental driver of the Jet Stream (Fig. 1.9; Wallace and Hobbs, 1977). A weakened, wavier jet stream is generated by Arctic warming and strong heat exchange between ocean and atmosphere. Thus, these high-amplitude patterns support a negative AO/NAO mode and unusual weather conditions over Europe during winter and summer (Fig. 1.9; Thompson and Wallace, 2001; Francis et al., 2015).

1.5 From an ancient to a modern Arctic Ocean

Arctic climate evolution

The long term-climate evolution of the Arctic Ocean has undergone drastic change throughout Earth's history and is characterized by warm greenhouse and cold icehouse phases. These changes have occurred gradually in some cases and more abrupt in others, but large-scale climate changes are mainly controlled by changing e.g. CO₂ concentrations, plate tectonic, opening and closure of Arctic ocean gateways (isolation from the world oceans), uplift of mountain ranges and plateaus, and orbital parameters (Milankovitch Cycles) (e.g. Stein et al. 2019 and references therein). So far, only limited, still fragmentary multiproxy-based records exist for the Cenozoic time interval, especially from the IODP-ACEX drilling campaign in 2004 on the Lomonosov Ridge (Fig. 1.17; Backman et al., 2008; Stein, 2019).

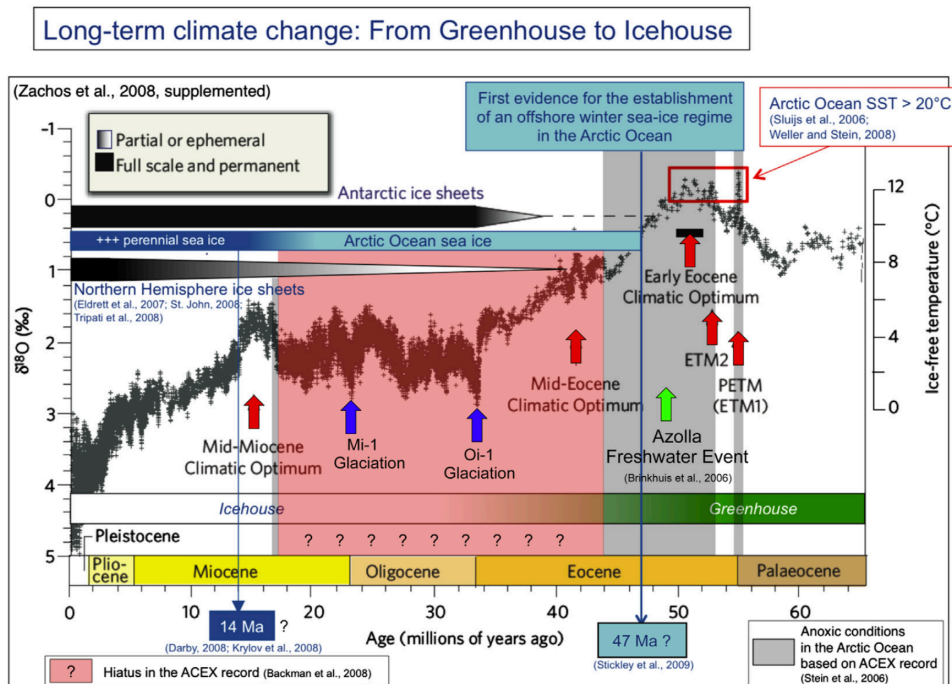


Figure 1.17: Global climate records show the past ~66 Ma Greenhouse-Icehouse transition, including the $\delta^{18}\text{O}$ curve (Zachos et al., 2008; supplemented), related Northern and Southern Hemisphere glaciations and sea-ice evolution. Black arrows show main Arctic Ocean gateway openings. Abbreviations: PETM = Paleocene-Eocene Thermal Maximum; EECO = Early Eocene Climatic Optimum; Oi-1 = Major Oligocene Glaciation Event; Mi-1 = Miocene Glaciation (Source: Stein, 2014 and references therein).

The Cenozoic climate (past 66 Ma) is primarily driven by (i) atmospheric CO₂, (ii) tectonics on long timescales and (iii) astronomical cycles on shorter timescales and is defined by frequent peak warm intervals (high pCO₂, negative $\delta^{18}\text{O}$, SST 23–27°C) e.g. PETM, Early Eocene Thermal Maximum and Mid-Miocene Climate Optimum (Fig. 1.17; Zachos et al., 2001, 2008; Tripathi et al., 2005; Moran et al., 2006; Sluijs et al., 2008, 2009; Stein et al., 2014). Palaeocene and early Eocene climate conditions correspond to similar trends like in the mid to late Cretaceous with distinctively higher greenhouse gas

concentrations and deep-water temperatures of 10°C (Zachos et al., 2001, 2008). pCO₂ emissions up to 1500 ppm and bottom water temperatures up to 12°C higher than today, peaked during the Early Eocene Climatic Optimum 52 to 50 Ma ago, but also showed incredibly high Arctic summer temperatures of up to 25°C (Zachos et al., 2001, 2008; Sluijs et al., 2006, 2008; Liu et al., 2009). The middle Eocene towards the Eocene-Oligocene boundary marks the transition from a greenhouse towards an icehouse conditions with a distinct decrease of pCO₂, massive southern hemisphere glaciation (34 Ma) and drift ice at both poles (pCO₂ 500 to 1000 ppm, SST <17°C) (Fig. 1.17; Moran et al., 2006; Tripathi et al., 2008; Liu et al., 2009; Stein et al., 2014; Heures and Rickaby, 2015).

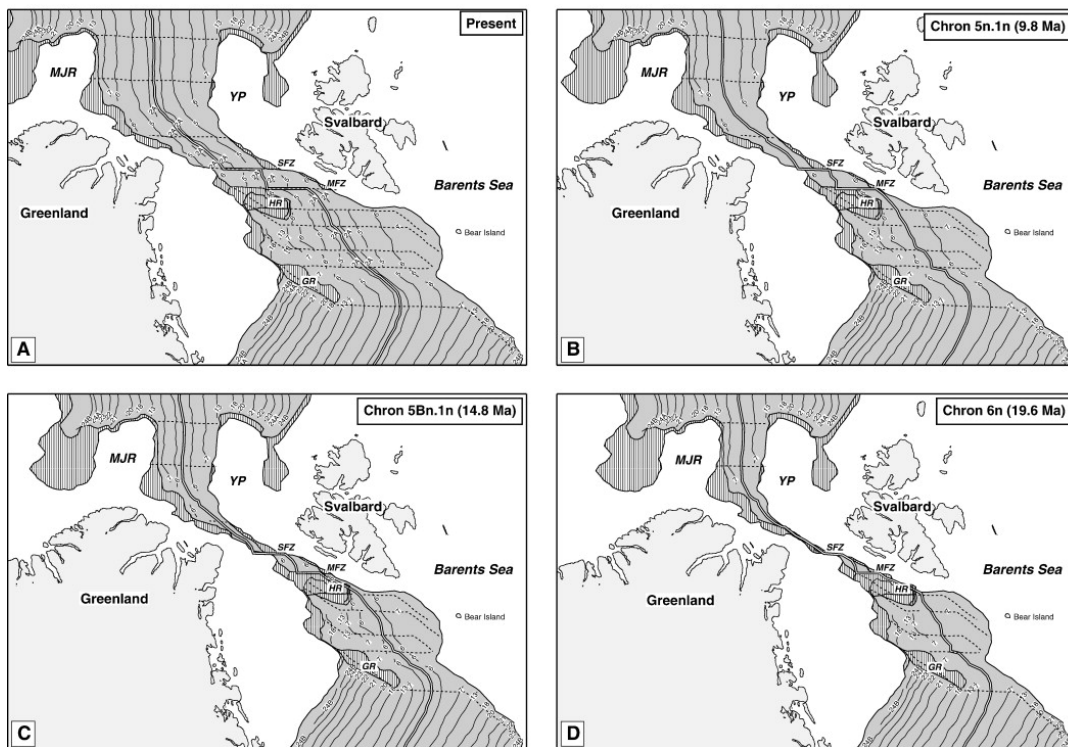


Figure 1.18: Opening of the Fram Strait shown in a plate tectonic reconstruction by Engen et al. (2008).

Isolated from the world's ocean during the early Cenozoic, the Arctic Ocean was characterized by low salinity, euxinic conditions in the well-stratified water column and the deposition of organic-rich sediments (e.g. Stein et al., 2006, 2008; Engen et al., 2008; Ehlers and Jokat, 2013). Modern-type oxygen-rich deep-water conditions from the North Atlantic established after the opening of the Fram Strait during the Oligocene or mid-Miocene (the timing of this distinct change is still under discussion; cf. Stein et al., 2019), followed by first major ice sheet growth on Svalbard 15 Ma ago (Fig. 1.17, 1.18; Jakobsson et al., 2007; Knies and Gaina, 2008). Seasonal sea ice and infrequently perennial ice formation are largely present during the Miocene (e.g. Moran et al., 2006; Darby et al., 2008; Stein et al., 2016a). The Bering Strait opening ~4.8 ka ago created a further high latitudinal gateway between the Pacific and Arctic Ocean (Marincovich and Gladenkov, 1999) and ensured a strong halocline and sea-ice formation due to the inflow of fresh Pacific Waters (Matthiesen et al., 2009).

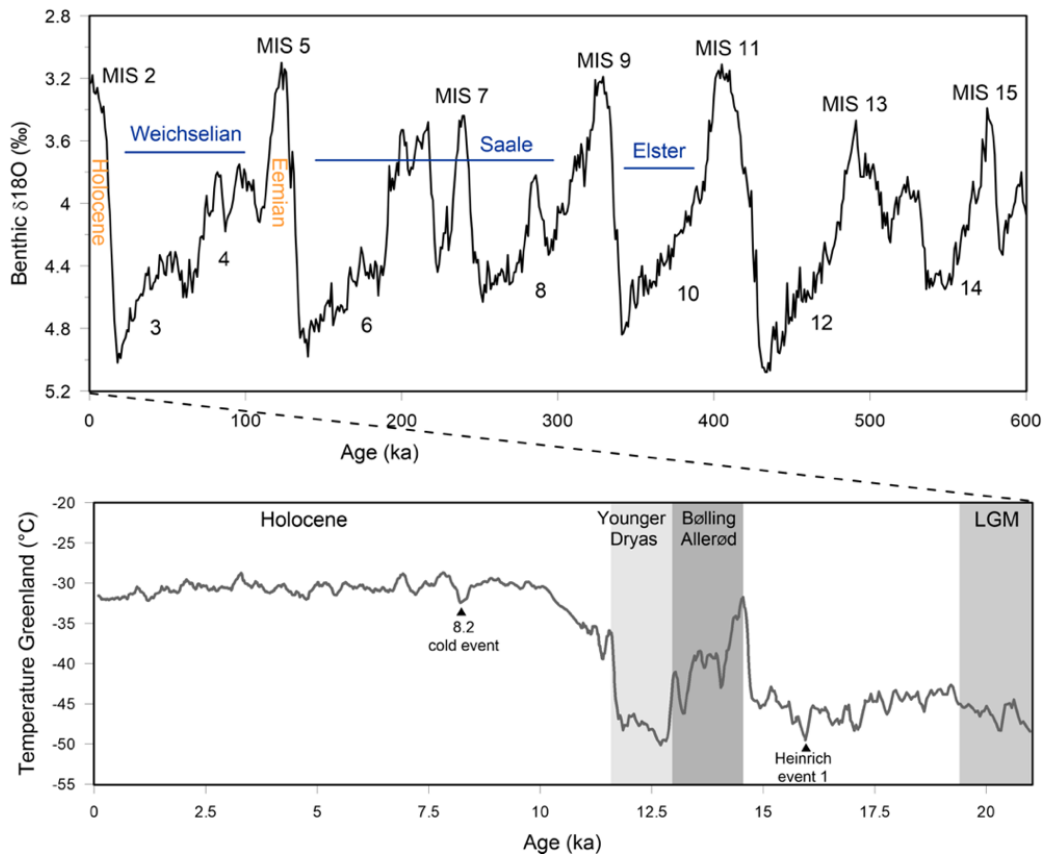


Figure 1.19: Benthic $\delta^{18}\text{O}$ stack (Lisiecki and Raymo, 2005) with its typical seesaw pattern shows the last main three glaciations (blue text), last two interglacials (orange text) and marine oxygen isotope stages (MIS) of the past 600 ka. Below is a Greenland temperature record (GISP2; Alley, 2004) of the last ~20 ka beginning with the LGM, followed by the Deglacial between 20 ka to 11.7 ka and the recent interglacial Holocene (11.7 ka to present). Most prominent deglacial cooling events of the Northern Hemisphere are Heinrich Event 1 (~17.5 to 16 ka), Younger Dryas (~12.9 to 11.7 ka) and 8.2 events and warm event Bölling Allerød (~14.7 to 12.9 ka; Shakun et al., 2010; Young et al., 2012).

With the onset of the Quaternary at 2.6 Ma, Earth's climate fluctuated between warm and cold stages emphasized by glacial and interglacial cycles with their typical seesaw pattern in marine oxygen isotope records and ice cores (Fig. 1.19; Lisiecki and Raymo, 2005). In total there are 1 to 104 MIS, but MIS 2, 6, 12 and 16 mark the largest glaciations with a colder, drier climate and enormous ice sheets. Most prominent interglacials with least global ice tend to occur during peak solar insolation in the Northern Hemisphere summer at the MIS stages 1, 5, 9 and 11 (e.g. Jakobsson et al., 2014; Nørgaard-Pedersen et al., 2007; Stein et al., 2012). A significant reorganization of the Arctic Ocean is reflected by waxing ice-sheets towards the marginal shelves at 1.6 Ma and a strong freshwater supply facilitating enhanced sea-ice formation (Matthiessen et al., 2009; Knies et al., 2009; Polyak et al., 2010). The Laurentide Ice Sheet and Eurasian Ice Sheet were the prominent features of the Pleistocene while their melting caused major disruptions in the deep-water formation and hampered the AMOC (Fig. 1.20; Fairbanks et al., 1989; Wickert et al., 2019).

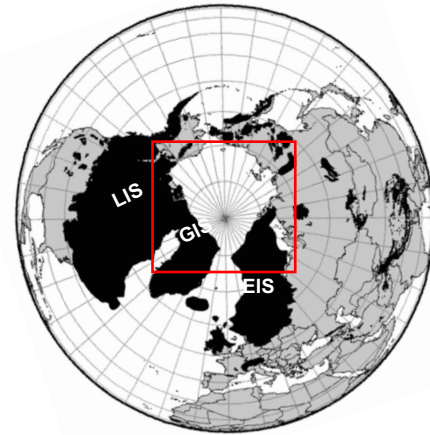
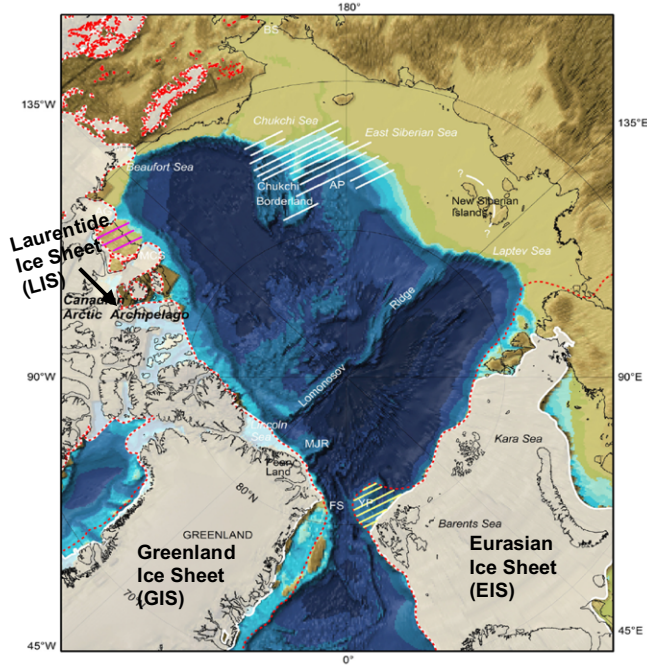


Figure 1.20: Extent of ice-sheets during the LGM (light shaded areas) and Quaternary (red dashed lines) on the Northern Hemisphere (Source: Jakobsson et al., 2014; Ehlers and Gibbard, 2007)

Last Glacial Maximum (LGM) sea level was approximately 120 m lower than nowadays, storing much of the freshwater in growing ice sheets (Fairbanks, 1989; Jakobsson et al., 2014). Most of the shallow Arctic shelves were exposed during the LGM and became stepwise, but fully flooded during the early Holocene ice melt and resulted in regional uplift and subsidence of coastal zones (Fig. 1.21; Ehlers and Gibbard, 2007; Blaschek and Renssen, 2013; Niessen et al., 2013; Jakobsson et al., 2014).

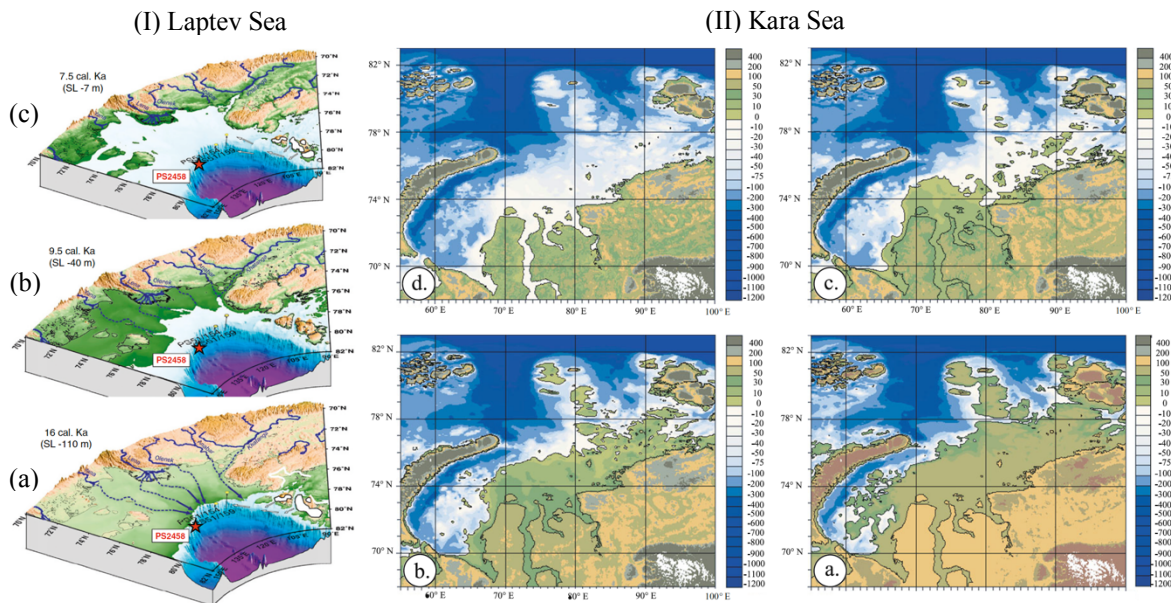


Figure 1.21: Reconstructed sea level rise from a glacial-like (LGM) towards a modern-like environment in the Laptev Sea and Kara Sea. (I) Laptev Sea a) LGM (-110 m), b) 9.5 ago (-40 m) and c) since 7 ka modern environment with the re-growth of ice-caps. (II) Kara Sea a) 18 ka ago (-100 m), b) 11 ka ago (-50 m), c) 9 ka ago (-30 m) and d) modern situation. (Sources: Stein and Fahl, 2004; Fahl and Stein, 2012).

The Holocene (11 ka to present)

Focus of this study is the recent interglacial the Holocene (11.7 ka ago to present) and will be explained in more detail in the following. Overall, the database of reliable Holocene high-resolution paleoclimate records from the northern North Atlantic region and Arctic (based on ice cores, lake sediments, pollen analysis, peat sequences, coastal and marine deep-sea sediments) is growing and provides information on extreme climate fluctuations under natural forcings (Briner et al., 2016). However, Holocene climate variations occurred larger and more frequently than expected and are closely linked to Earth's orbital variations and solar variability (Kaufman et al., 2016). Although these Holocene climate changes have a weaker amplitude compared to the LGM–Deglacial period, with boundary conditions closely related to our present-day situation, these records may be perfectly used for testing and approving our predictive climate models (Mayewski et al., 2004; Kaufman et al., 2016).

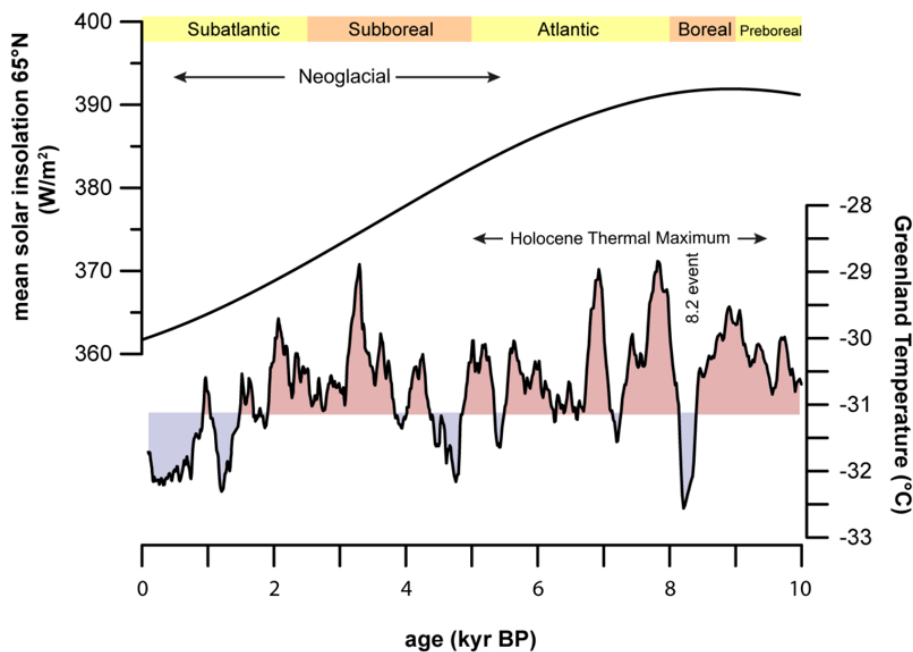


Figure 1.22: Holocene Greenland temperature (°C) record from the GISP ice core (based on $\delta^{18}\text{O}$; Alley et al., 2010) next to the Northern Hemisphere solar insolation curve (Source: Kolling, 2017; Laskar et al., 2004).

With the termination of the Younger Dryas cold event at the end of the late Weichselian Deglacial, the onset of the Holocene began with an abrupt rise in $\delta^{18}\text{O}$ recorded from Greenland ice cores (Fig. 1.19; Stuiver and Grootes, 2000; NGRIP-Members, 2004; Rasmussen et al., 2006; Alley et al., 2007, 2010). In consonance with several studies from the Fram Strait and other high Northern Hemisphere areas, the Holocene can be divided into three main intervals, 1) the early Holocene (11.7 ka to 9 ka), including the early Holocene Thermal Maximum and correlating with the ‘Proboreal’ and ‘Boreal’ chrozones, 2) the mid Holocene (9 ka to 5 ka) coinciding with the ‘Atlantic’ chronozones and 3) the late Holocene (5 ka to present) initiating the onset of the Neoglacial Cooling and linked to the ‘Subboreal’ and ‘Subatlantic’ chronozones (Fig. 1.22; Koç et al., 1993; Nesje and Dahl, 1993; Andersen et al., 2004; Alley et al., 2007, 2010; Rasmussen et al., 2007; Wanner et al., 2008; Andrews et al., 2010; Jennings et al., 2011).

Past climate records of the North Atlantic region show warmer conditions during the Early Holocene with temperatures possibly similar to or exceeding modern temperatures (Briner et al., 2016; Pendleton et al., 2019). Solar insolation reached its maximum peak during the early Holocene Thermal Maximum and gradually decreased to minimum values by the end of the late Holocene (Fig. 1.22; Laskar et al., 2004). Spatial and temporal response of the HTM in the climate system appeared regionally different. The HTM was often delayed by several thousand years relative to the summer insolation maximum despite it being orbitally forced (Fig. 1.22; Jansen et al., 2007; Renssen et al., 2009; Blaschek and Renssen, 2013a). Characteristic for this warm interval are abrupt, multidecadal to centennial-scale cooling events (most prominent ones are 9.3 and 8.2 ka) and the waning of Laurentide and Greenland ice-sheets, supplying huge amounts of freshwater into the adjacent seas and thereby altered the behaviour of AMOC (Alley et al., 1997; Barber et al., 1999; Kaufman et al., 2004; Kaplan and Wolfe, 2006; Renssen et al., 2009; Yu et al., 2010; Young et al., 2020). Finally, the mid to late Holocene marks the transition from warmer to cooler sea surface conditions accompanied by the start of the Neoglacial Cooling at 5 ka (Wanner et al., 2008).

1.6 Common past climate proxies in the Arctic environment

Paleoenvironmental climate reconstructions in the current study are originating from a number of climate proxies. Based on these proxies, certain environmental information about paleo sea-ice cover, primary productivity, supply of terrigenous material, meltwater input, glacier advance/readvance and water-mass characteristics can be traced and contextualized. Fundamental to these reconstructions is a robust stratigraphic framework, in our case radiocarbon (^{14}C) dating.

Micropaleontological and sedimentological proxies

Microfossils are derived from photo- and heterotrophic unicellular protists and crustaceans thriving in various water depths and bloom during particular seasons of the annual cycle. These microfossils are either composed of calcium carbonate polymorphs, opal silica or biopolymeric substances (Mortyn and Martinez-Botí, 2008; Hopkinson et al., 2011; Not et al., 2012; de Vernal et al., 2013). Planktic and benthic foraminifera for example secrete their fragile structure on a rigid calcite or aragonate shell (or test) while ostracodes are small microscopic crustaceans and build a calcium carbonate exoskeleton (Kucera, 2007; Cronin et al., 2010, 2013). The most dominant algae group in the global oceans are represented by silica-walled diatoms, while ~10–20% are encompassed by dinoflagellates that are highly resistant to mechanical alteration (taphonomy) and dissolution (Bogus et al., 2012; Miettinen et al., 2013; Miettinen, 2018). Highest primary productivity and flux rates of microorganisms are depending on their seasonal blooming cycle. Diatoms bloom in spring whereas dinoflagellates and calcareous-walled organisms are mainly produced during summer and autumn (Wassmann et al., 1999; Quillfeldt, 2000; Signorini and McClain, 2009; Hopkins et al., 2015; Skirbekk et al., 2016).

Settled down to the seafloor after death and preserved in the ocean sediments, they serve as useful proxies for reconstruction of different (paleo-) environments due to their well-known and limited environmental ranges. Distinctive physical properties (e.g. shelf morphology) and census data (e.g. presence/absence, relative abundance and biodiversity) of microfossils in combination with mathematical transfer functions provide all necessary information for reliable past climate reconstructions e.g. sea-surface and subsurface temperatures, sea-ice concentration (Koç et al., 1993; Matthiessen et al., 2001; Sarnthein et al., 2003; Polyak et al., 2010; de Vernal & Rochon, 2011, 2013; Cronin et al., 2013; de Vernal and Gersonde, et al., 2013; Seidenkrantz, 2013; Mietthinen et al., 2018; Limoges et al., 2018). Dinoflagellate cyst assemblages were used as tracers of past sea-surface conditions and sea-ice cover in the Arctic Ocean (de Vernal et al., 2012, 2013; Limoges et al., 2018). The use of percentage share and isotopic records of planktic and benthic foraminifera allows estimates of warm water advection (Polar Water vs. Atlantic Water), bioproductivity and upper and lower water mass properties (e.g. temperature, salinity and ventilation) (e.g. Bauch et al., 2001; Ebbesen and Hald, 2004; Ravelo and Hillaire-Marcel, 2007; Bakke et al., 2009; Jessen et al., 2010; Knies et al., 2018; Zehnich et al., 2020).

However, the preservation of these fragile microfossils is partly challenging or simply missing due to extreme Arctic environmental conditions and thus might limit their applicability (Steinsund and Hald, 1994; Schlüter et al., 2000; Matthiesen et al., 2001). Advantages using microfossil proxies are their semi-quantitative transfer function estimates, their wide and global temperature ranges and water masses-based census data, diverse population in different environmental settings, core top calibrations for quantitative estimates of e.g. sea surface and subsurface water temperatures, productivity, salinity. Disadvantages and limitations of these proxies are risk of dissolution, poor preservation under harsh conditions, diagenetic alteration (Köseoğlu, 2019, and references therein).

Ice-rafted Debris (IRD) terrigenous particles entrained in dirty sea ice and/or icebergs, often consisting of clay minerals, quartz, feldspars, heavy minerals, and specific Fe oxide grains and later released during ice melt to the seafloor. IRD is often used as proxy for identifying source areas and transport pathways and for reconstruction of ice-sheet and sea-ice history (Andrews, 2000; Polyak et al., 2010; Stuart and Long, 2011; Stein, 2019).

Biomarker proxies

The main approach of this thesis was to validate and undertake the application of biomarker climate proxies off the NEG continental shelf. In order to identify the likely source of sea-ice, phytoplankton and terrigenous biomarkers and to study their spatial and temporal variability, a number of sediment cores and surface samples were collected. The sites selected on the outer and inner NEG continental shelf have been proven, to be in previous studies, sites sensitive to climate changes driven by Arctic Ocean and the North Atlantic Ocean influences and its sediments contain unique high-resolution sequences deposited during the late Weichselian deglaciation and Holocene to present. A detailed

interpretation of investigated lipid biomarkers used in this study, including HBIs and specific sterols are described in more detail in the following chapters 4, 5 and 6.

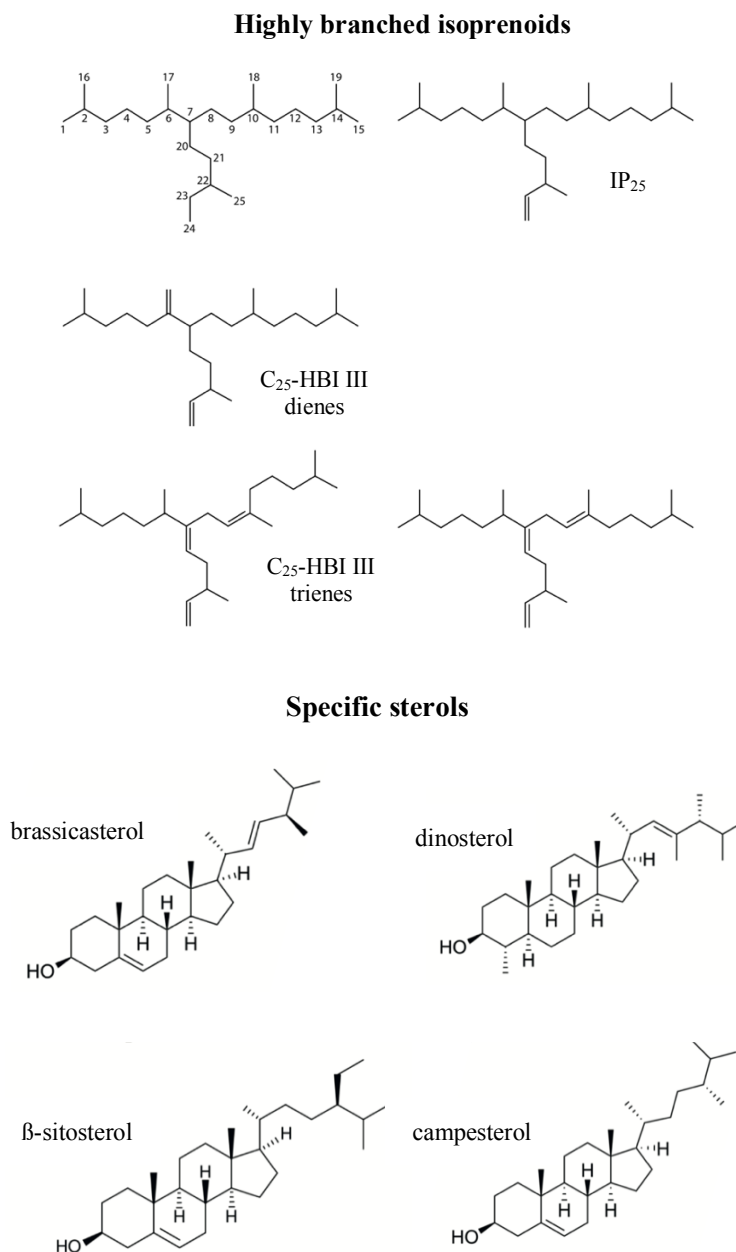


Figure 1.23: Chemical structure of common highly-branched isoprenoids and of specific sterols.

(a) Sea ice

Over the last decade, certain source-specific highly branched isoprenoids (HBIs), which are only biosynthesized by a relatively small number of diatom genera and preserved in marine sediments has opened a new field of past sea-ice reconstructions in the high Arctic environment (Belt et al., 2000; Belt et al., 2007; Rowland and Robson, 1990). Often these HBIs contain 20, 25, and 30 carbon atoms, where C₂₅ HBIs (haslenes, Fig. 1.23) with 2–5 carbon-carbon double bonds are the most common among them

(Belt et al., 1996, 2000). HBIs in marine sediments were first identified by Gearing et al. (1976), but Robson and Rowland (1986) dealt with the characterisation of the HBIs skeleton and their unsaturated analogues. Since then many investigations on (individual) marine and freshwater diatoms as HBI producers, their habitat, environmental parameters (e.g. salinity, temperature) and global/local distribution were made and explained by many authors (e.g. Wraige et al., 1998; Volkman et al., 1994; Belt et al., 2000, 2001b; Belt, 2018). Cultivated laboratory experiments showed that the degree of unsaturation (number of double bonds) of haslenes increases with their increasing diatom growth rate temperature (Belt et al., 2000; Rowland et al., 2001). In the Canadian Archipelago and Hudson Bay region, the mono-unsaturated C_{25} sea-ice proxy, termed as IP_{25} was first discovered by Belt et al. (2007) (Fig. 1.23). A comprehensive, comparative study on the IP_{25} extraction procedure, identification and quantification have been implemented within laboratories worldwide to assure data accuracy and due to its source-specificity and stability it shows the great potential of an ideal sea-ice proxy for the Arctic Ocean (Belt et al., 2012a; 2014). IP_{25} is produced by only three to four sea-ice associated diatoms; *Pleurosigma stuxbergii* var. *rhomboides* (Cleve in Cleve & Grunow) Cleve, *Haslea kjellmanii* (Cleve) Simonsen, *H. crucigeroides* (Hustedt) Simonsen, and/or *H. spicula* (Hickie) Lange-Bertalot (Fig. 1.23; Brown et al., 2014c). The insolation-driven ice-algae bloom is important in supporting the higher trophic food web and in the deposition of sea-ice derived organic matter in the water column and marine sediments (Fig. 1.24). It usually begins in May and June before the blooms of pelagic phytoplankton biomarkers starts (Fig. 1.24; Belt et al., 2014; Dieckmann and Hellmer, 2010; Leu et al., 2011). The sea-ice diatoms that produce IP_{25} preferentially inhabit the bottom few cm of Arctic sea ice within the interstitial brine channels with a volume fraction of $>5\%$ (Smith et al., 1993; Golden et al., 2007; Lee et al., 2011; Brown et al., 2014c).

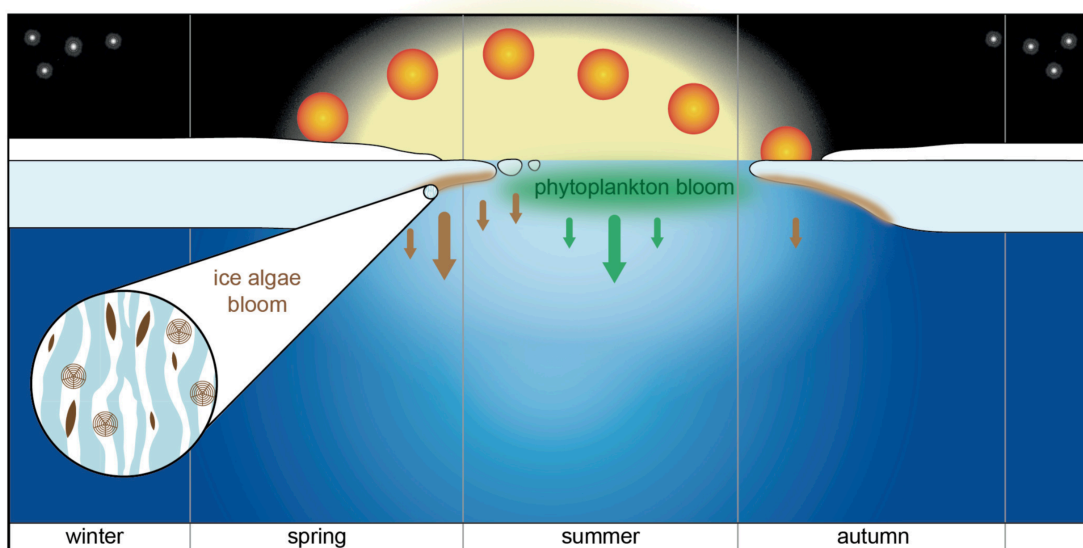


Figure 1.24: Seasonal production of sea-ice algae (brown) and open-water phytoplankton biomarker (green). Zoomed circle presents sea-ice algae colonisation living in the brine channels of the Arctic sea ice (Source: Kremer, 2018; modified after Wassmann, 2011 and Stein et al., 2012).

Sediment traps deployed at the southern Lomonosov Ridge showed increased IP₂₅ concentrations during the summer months (Fahl and Stein, 2012). However, accumulation of IP₂₅ does not occur during winter or is below detection limit. Therefore, IP₂₅ is interpreted to reflect spring/summer sea-ice cover (Fig. 1.23, Belt et al., 2007; Fahl and Stein, 2012).

Analysis of surface samples spanning the entire Arctic Ocean clearly indicate the ubiquitous presence of IP₂₅ in seasonally ice-covered areas and absence in open waters, supporting the occurrence in seasonal sea ice (Fig. 1.24; Navarro-Rodriguez et al., 2013; Weckström et al., 2013; Xiao et al., 2013, 2015a; Belt et al., 2015). Meanwhile IP₂₅ has been successfully reconstructed in many seasonally ice-covered areas across the sub-Arctic and Arctic regions, but also from the Lomonosov Ridge located in the central Arctic Ocean with perennial sea-ice conditions (for overviews, see Stein et al., 2012; Belt and Müller, 2013; Belt, 2018). Moreover, its stable molecular structure allows past sea-ice reconstruction over timescales of several million years back into the late Miocene (Stein et al., 2016). Therefore, it seems that IP₂₅ is quite resistant to diagenetic alteration by photodegradation, autoxidation and clay-induced isomerisation and remains relatively unaltered while settling (cf., Rontani et al., 2011; 2014a,b). Additionally, to the IP₂₅, another di-unsaturated molecule (HBI II) with two double bonds has been introduced as further biomarker for sea-ice reconstruction in the Arctic and Antarctic realm (Belt, 2018). Its co-occurrence with IP₂₅, their highly correlation and similarly enriched $\delta^{13}\text{C}$ values implied a sea-ice associated source; unfortunately HBI II was also traced in temperate freshwater systems, making it less source-specific (Brown et al., 2014b, c; Cabedo-Sanz et al., 2013; Xiao et al., 2013; He et al., 2016).

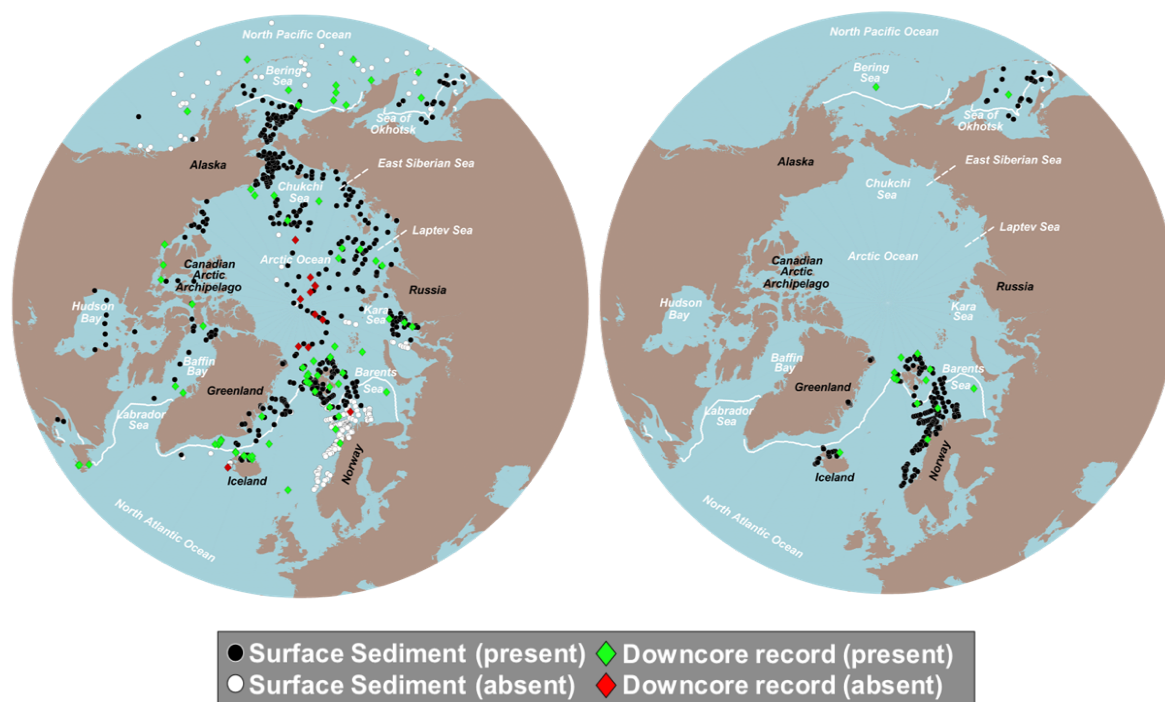


Figure 1.25: Right map shows distribution of surface samples and downcore records of IP₂₅ and the left one of HBI III (E and Z-isomer). The white line shows the median April sea-ice extent from 1981-2010 (Source: Köseoğlu et al., 2018; Fetterer et al., 2017).

Furthermore, Belt et al. (2016) identified a counterpart for the Antarctic, the so-called IPSO₂₅ (sea-ice proxy for the Southern Ocean with C₂₅), produced by sympagic diatom species *Berkeleya adeliensis* (Medlin) as source for HBI II (Fig. 1.23; Belt et al., 2016).

A challenge, however, is that IP₂₅ is absent under permanent-ice with limited nutrients and light penetration and under ice-free conditions where no ice-algae lives (Fig. 1.24, 1.26; Belt et al., 2007; Müller et al., 2011; Navarro-Rodriguez et al., 2013). Müller et al. (2011) established a useful combination between IP₂₅ and open water phytoplankton biomarkers (i.e., brassicasterol, dinosterol) to distinguish between these two end-members cases, the so-called PIP₂₅ (Phytoplankton-IP₂₅) index (for calculation see chapter 4 and 5). High phytoplankton markers and low IP₂₅ are indicative of reduced sea-ice to ice-free conditions (PIP₂₅<0.5, Fig. 1.26). On the other hand, enhanced IP₂₅ and phytoplankton values reflect marginal sea-ice conditions (intermediate PIP₂₅ between 0.5 and 0.75), and high IP₂₅ and minimum phytoplankton marker concentrations display an extensive sea-ice formation (PIP₂₅>0.75, Fig. 1.26; Müller et al., 2011). A uniform scale ranging between 0 to 1 ensured a more straightforward comparison of PIP₂₅ records among different regions Arctic Ocean, especially in areas where sea-ice settings are alike (e.g. Xiao et al., 2015a). Combined biomarker profiles, e.g. PIP₂₅ indices and x-y plots are still highly debated within the science community (Belt, 2018). The review paper by Belt (2018) highlights the limitations, advantages and disadvantages, and missing identification of boundary conditions of these proxies.

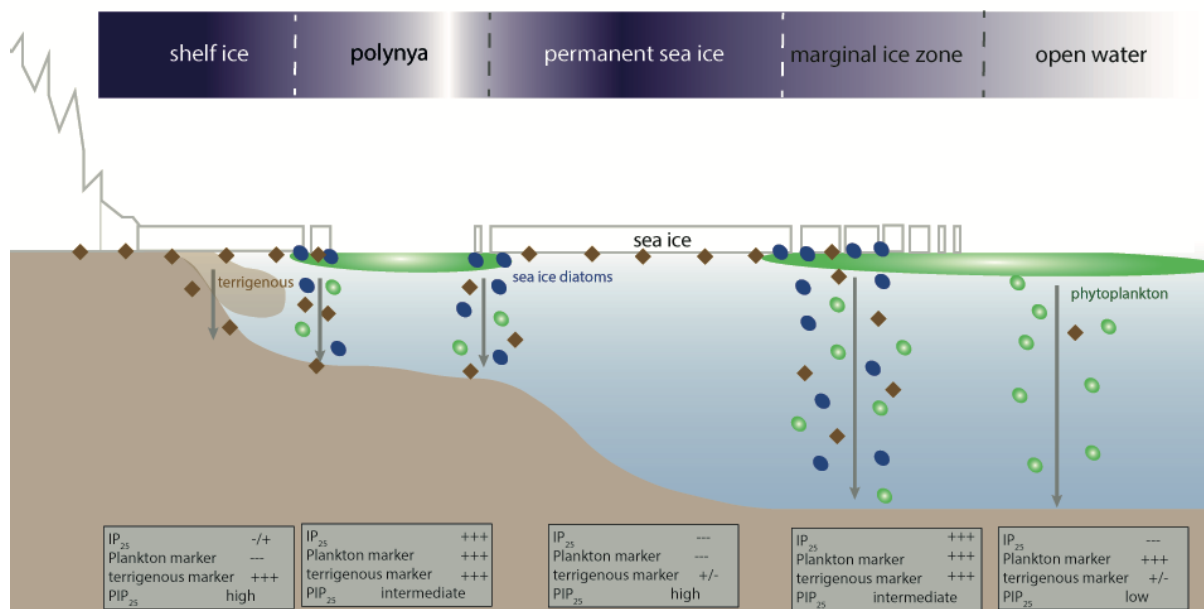


Figure 1.26: Generalized overview of different sea-ice scenarios shown in a Greenland's shelf cross-section, showing sea-ice algae (blue) and phytoplankton biomarker productivity (green) and terrigenous supply (brown). Below are the related PIP₂₅ indices (Source: Kolling, 2017; modified after Müller et al. (2011) and Stein et al. (2016)).

(b) Productivity

A HBI that is closely attributed to open-water (pelagic) conditions in the Arctic and Antarctic spring marginal-ice zone (MIZ), is named HBI III (Fig. 1.23, with E- and Z-isomers) and biosynthesized by *Rhizosolenia* spp. diatoms (e.g. Massé et al., 2011; Collins et al., 2013; Smik et al., 2016a, 2016b; Belt, 2018; Köseoğlu et al., 2018). The combination of IP₂₅ and HBI III, i.e., similar to the PIP₂₅ approach described above (see chapter 4 for details) supposed to provide a greater nuance to past sea-ice reconstructions (Fig. 1.27). The strong correlation of pelagically produced HBI III to receding spring MIZ enables HBI III to be used as an open-water counterpart to IP₂₅ and IPSO₂₅ (Belt et al., 2015; Smik et al., 2016a, 2016b; Köseoğlu et al., 2018; Belt et al., 2019). Further, the close relationship between HBI III E- and Z-isomers to spring chlorophyll concentrations (chl *a*) may indicate that this biomarker index (HBI-T₂₅) can be used to trace spring phytoplankton blooms, at least from studies in the Barents Sea and surrounding areas (Belt et al., 2019).

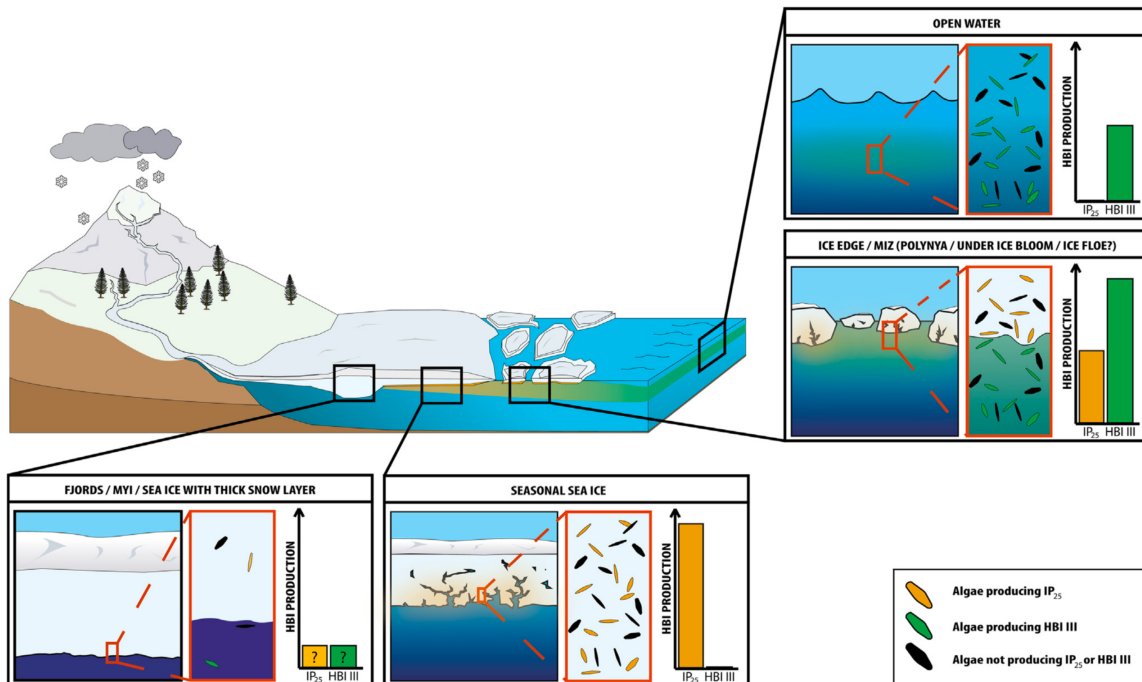


Figure 1.27: Schematic illustration shows the relative abundance of IP₂₅ and HBI III in different sea-ice settings or under ice-free conditions (Belt, 2018). The scenario of open-water indicates absent IP₂₅ and higher concentrations of phytoplankton biomarker HBI III (same occurs for brassicasterol and dinosterol = high values). The MIZ, including polynya-like conditions, are characterised by highest HBI III and intermediate IP₂₅ concentrations. Seasonal sea-ice formation is reflected by highest IP₂₅ values and zero HBI III values. Under a permanent/thick ice cover both biomarkers display reduced values (Source: Belt, 2018).

Additionally, this study uses the phytoplankton biomarkers brassicasterol and dinosterol to reflect changes in the open-water primary productivity (Fig. 1.23). Brassicasterol is biosynthesized by a broad marine/fluviat algae group. Dinosterol is predominately biosynthesized by dinoflagellates but also minorly by sea-ice diatoms (*Navicula* spp.; Yunker et al., 1995; Volkman et al., 1998; 2008). The application of brassicasterol as open-water phytoplankton has to be interpreted with caution, because its

partly biosynthesized by riverine freshwater diatoms like in the Kara and Laptev Sea and sea-ice diatoms (Yunker et al., 1995; Fahl and Stein, 1999; Fahl et al., 2003; Belt et al., 2013; Hörner et al., 2016).

(c) Terrigenous input

The terrigenous biomarkers β -sitosterol and campesterol are derived from higher vascular land plants on the Arctic hinterlands and transported via rivers onto the broad Arctic shelves (Fig. 1.23; Volkman, 1986). Partly settled on the coastal shelf and/or incorporated into the newly formed sea ice, they are then transported through the entire Arctic Ocean and released during sea-ice melt (Fahl and Stein, 1997, 1999, 2007; Xiao et al., 2013).

Chapter 2

2.1 Motivation

Ongoing global climate change strongly affects one of the most important components of the Earth's climate system, the Arctic sea ice. Recent observations and model simulations clearly indicate that the burning of fossil fuels and the resulting increase in CO₂ and other greenhouse gas emissions (GHGs) have profoundly led to enhanced warming of the Arctic (north of 67°N) (Serreze et al., 2006, 2009; Notz and Stroeve, 2016; Walsh et al., 2017; Dai et al., 2019). Here, the climate dilemma is, that the Arctic experiences a two to three times greater warming than any other region on Earths (Fig. 1.14). Unnatural warming of the Arctic Ocean and rising atmospheric temperatures trigger extensive sea-ice/ice-sheet loss and additionally accelerates and contributes to climate change around the world with disastrous consequences (Serreze and Barry, 2011; Stocker et al., 2013). The latitudinal homogenisation of ocean and atmospheric temperatures due to the drastic sea-ice loss may trigger complex feedback loops for example the Arctic Amplification, a phenomenon that relates to lowered meridional temperature gradients and largely affects European climate (Fig. 1.14, 1.15; Miller et al., 2010; Serreze and Barry, 2011; Cohen et al., 2014).

Model simulations predict nearly ice-free Arctic summers in approximately 30–50 years (Screen and Simmonds, 2010). A substantial decrease of Arctic sea-ice extent in September of nearly ~30%, which was recorded by satellite observations since the late 1970s, has been attributed to a combination of internal forcing and anthropogenic global warming (Overland et al., 2010; Bintanja et al., 2011; Niederdrenk et al., 2018; Ding et al., 2019).

The southernmost continent Antarctica is a highly protected area under one of the world's most successful international agreements, the Antarctic Treaty (1959), and is only accessible for scientific purposes. Besides, the Arctic Ocean and surrounding regions strongly contrast Antarctica and have become one of the main focusses of conflicting political, military and economic interests, with irreversible consequences for the polar environment. The improved accessibility to the Arctic due to the reduced sea ice will increase economic activities such as marine traffic, including sea freight, resource extraction by exploration vessels (oil, gas, fishery) and cruise liners (tourism) (Stroeve et al., 2007, 2012; Post et al., 2013; Serreze et al., 2015; Kozmenko et al., 2018).

Why study past sea-ice reconstruction in higher latitudes and adjacent seas?

In A.D. 870 Vikings recorded the number of weeks per year where sea ice occurred along north Iceland's coast; the first known tracing of sea-ice conditions. Curious and brave sailors depicted the harrows of traversing Arctic Ocean in the mid-1700s and in the early 1900s by keeping first notes on Northern Hemisphere shipping lanes and sea-ice conditions. Nowadays, fairly reliable sea-ice trends are tracked back until 1953, including satellite records, shipping routes and ice charts from research institutes all

over the world (<http://nasa.gov>). Since 1979, satellites have monitored changes of sea-ice conditions in the high north, i.e., sea-ice thickness, extent and melt, but this short time period allows limited assessment of the natural variability (Meier et al., 2014; Fetterer et al., 2017). Why is there need of modern, short and long term past sea-ice records? It is clear that sea ice regulates many complex physical and thermodynamic processes at the ocean-atmosphere-interface in the climate system. Its sensitivity and fast reaction to changes in the environmental conditions shows that sea ice is a prime indicator for global, anthropogenic climate change (Ricker et al., 2018). Palaeoceanography and the sea-ice history reveal not only important information on ocean/atmospheric temperatures, salinities, sea-ice conditions and primary productivity, they also contextualize the critical role and pace of small and large scale and/or abrupt climate changes in an environment not affected by human activity and solely based on natural forcings. Therefore, paleoclimate parameters form the basis to understand cause and implications of internal climate variations and their magnitude in the climate system. This helps to distinguish between internal and external climate drivers and improves sea-ice forecasts (Stroeve et al., 2018). A direct comparison of proxy records and climate models show that the latter has underestimated significant acceleration of Arctic sea-ice loss during the last decades (Comiso et al., 2008; Rampal et al., 2011; Ogi and Rigor, 2013) and therefore attributes 50–60% of Arctic sea-ice sensitivity to external radiative forcings (Kay et al., 2011; Stroeve et al., 2012; Ding et al., 2019).

Why are the Fram Strait and especially the NEG continental shelf important research areas in the context of the past sea-ice history? Enormous amounts of drift ice and freshwater are yearly exported (10%) from the Arctic through the highly dynamic Fram Strait along the NEG shelf to the lower latitudes, and therefore impact global freshwater budget, ocean circulation, and energy redistribution (Tilling et al., 2015; Zamani et al., 2019). Increased export of drift ice and freshwater off NEG could promote a strengthened Polar Water advection carried by the EGC through the Fram Strait (Dmitrenko et al., 2017; Sejr et al., 2017). Furthermore, local landfast ice dynamics and hydrology of fjords on the NEG continental stabilizes marine tidewater outlet glaciers of NEGIS and prevents ice shelf retreat and disintegration (Kirillov et al., 2017). These glaciers have a capacity to increase sea-level rise by 1.1 m alone, providing freshwater supply to the world's ocean that could potentially cause disruptions in AMOC (Morlighem et al., 2014).

Past variability in Arctic sea-ice coverage, ice sheet growth/decay and water mass distribution have previously been reconstructed in the Fram Strait off Northeast Greenland. However, open questions still exist about the natural centennial to decadal scale climate variability in the Arctic region, particularly during warm periods, which could work as useful analogue models to ongoing anthropogenic warming. Within the last 15 years a stronger incursion of warm recirculating Atlantic Water was recognized on the outer and inner NEG continental shelf, causing intensive bottom melting of the marine-terminating outlet glaciers of NEGIS. Additionally, rising air temperatures and extreme sea-ice loss play a crucial role in the NEGIS grounding line retreat and instability of the outlet glaciers (Straneo et al., 2012; Mouginit et al., 2015; Wilson et al., 2017; Dai et al., 2019).

Early 1980s expeditions to the Fram Strait only obtained interglacial (e.g. Holocene) sedimentary sequences with sedimentation rates of 1–5 cm/ky, too low for sufficient high-resolution past climate reconstructions. Since then, much progress has been made on the Holocene past sea-ice history of the eastern Fram Strait, including the Yermak Plateau, western Svalbard margin and Barents Sea (see review by Belt, 2018). Contrastingly, there are no high-resolution Holocene sedimentary sequences obtained from the western Fram Strait (i.e., the NEG margin and shelf).

In paleoceanography and paleoclimatology, biomarkers are key proxies to reconstruct past sea-ice conditions, primary productivity and the input of organic matter (marine and terrestrial). Sedimentary sections with high sedimentation rates recovered from the inner and outer NEG continental margin allow for the first time a high-resolution biomarker-based sea-ice reconstruction to address the following research objectives and hypothesis:

Hypothesis 1: *The sea-ice variability along the NEG continental margin is controlled by changes in drift ice from the central Arctic Ocean and local processes.*

One of the major goals of this thesis targeted the reconstruction of sea-ice variability during the Holocene based on two downcore sediment records on the outer (PS93/025) and inner NEG continental shelf (PS100/270). The outer shelf is influenced by both processes, drift and local sea-ice formation whilst the inner shelf predominately by local sea ice.

Hypothesis 2: *The sea-ice history in the eastern and western Fram Strait is controlled by different processes.*

The western Fram Strait is dominated by a cold, fresh surface water while the eastern Fram Strait underlies a warm, saline regime. A comparison between these Fram Strait regions was made to understand plausible driving mechanisms of the Holocene climate variability on both Fram Strait sides, such as solar insolation and other internal, local forcings.

Hypothesis 3: *The Atlantic Water inflow has influenced sea-ice changes on the NEG Shelf.*

Multiproxy analysis of Core PS100/270 evidenced the influence of warm recirculating Atlantic Water on the inner NEG continental shelf during the Holocene. Bottom melt of marine terminating outlet 79NG facilitated a freshwater source at the ocean surface. Hence, the resulting ocean stratification largely favored increased sea-ice formation during the mid to late Holocene. The following chapters outline the palaeoceanography and sea-ice history of the NEG continental shelf since the late Weichselian to present in more detail, and further contextualize the critical role of warm Atlantic Water advection on the shelf in light of recent warming and sea-ice retreat.

Hypothesis 4: *The seasonal formation and history of the NEW Polynya are reflected in the biomarker records.*

The NEW Polynya forms a unique habitat with high primary productivity during the spring and summer months. Highly correlating peak biomarker concentrations and accumulation rates of Core PS93/025 indicate a stable ice margin during the last 1 ka, reflecting a regular seasonal formation of the NEW Polynya at the outer NEG continental shelf.

Hypothesis 5: *Past changes in the extent of NEGIS in relationship to sea-ice variability are reflected in the sedimentary record.*

Data from the inner NEG continental shelf clearly indicate how closely the local landfast ice barrier is connected to the marine terminating outlet glaciers of NEGIS and vice versa. Additionally, the intrusion of warm AW changed the behavior of both key climate components.

2.2 Thesis Outline and declaration of author's contribution

This dissertation is divided into 7 main chapters, containing introductory and background information (chapters 1 and 2), details about the methodology (ch. 3), three scientific manuscripts (ch. 4 to 6), and a summary and outlook section (ch. 7).

Chapter 1 addresses an overview and background information, (i) the Fram Strait and NEG continental shelf, (ii) the role of Arctic sea ice in the both the natural climate system and an ongoing anthropogenic future perspective, (iii) from an ancient to a modern Arctic Ocean and (iv) common past climate proxies in the Arctic environment.

Chapter 2 gives introduction into the motivation, main hypothesis and aims, scientific background and wider context of this study.

Chapter 3 describes the main methodology used for generation of the biomarker-based proxy records and organic bulk parameters from the sedimentary sections PS93/025, PS100/270, multi-corer and surface samples. The justification for choosing these specific biomarkers and bulk parameters are explained within each science chapter.

Chapters 4, 5 and 6 contain three manuscripts that have been written for individual publication in international peer-reviewed scientific journals. Due to the stand-alone character of these manuscripts, repetition of some key components is unavoidable.

Chapter 7 summarises the main findings in each of the science chapters and discusses the remaining gaps in the state of knowledge of this work, as well as suggestions for future research.

This cumulative PhD thesis comprises a collection of three joint-authorship manuscripts which have been or will be published a peer-reviewed articles in recognized scientific journals. Patterns of authors contribution in the individual manuscripts are explained in the following.

Chapter 4: Holocene changes in sea-ice cover and polynya formation along the eastern North Greenland shelf: New insights from biomarker records

Authors: Nicole Syring, Ruediger Stein, Kirsten Fahl, Maximilian Vahlenkamp, Marc Zehnich, Robert F. Spielhagen, Frank Niessen

Publication state: This manuscript is published in the Journal Quaternary Science Reviews 231 (2020) 106173.

N. Syring, R. Stein and K. Fahl devised this project, main conceptual ideas and study outline. N. Syring performed all of the laboratory work, including the sampling of the box and kastenlot core PS93/025, the preparation of the sample material (freeze-drying, grinding), the processing of organic bulk parameters (TOC, CNS) and lipid biomarkers (HBIs, sterols), while K. Fahl checked for quality control of the data. Beforehand, physical properties were measured aboard during RV Polarstern expedition PS93 by F. Niessen. AMS ^{14}C datings were provided by R. Spielhagen and M. Zehnich. The age model for Core PS93/025 was developed in cooperation between M. Vahlenkamp and N. Syring. A preliminary version of the manuscript based on interpretation of prepared individual plots of the data was performed by N. Syring with strong support of R. Stein and K. Fahl. Afterwards, the input of all co-authors was incorporated to the final version of the first paper.

Chapter 5: Holocene interactions between glacier retreat, sea-ice formation and Atlantic Water advection at the inner Northeast Greenland continental shelf near 79°N

Authors: Nicole Syring, Jeremy M. Lloyd, Ruediger Stein, Kirsten Fahl, Dave H. Roberts, Louise S.L. Callard

Publication state: this paper was submitted to the Journal Paleooceanography and Paleoclimatology in June 2020, under review.

N. Syring, J. Lloyd, R. Stein and K. Fahl designed this manuscript. N. Syring performed the sampling of the Core PS100/270, the preparation of the sample material (freeze-drying, grinding), the processing of organic bulk parameters (TOC, CNS) and lipid biomarkers (HBIs, sterols) while K. Fahl did the quality control of the data. J. Lloyd performed the foraminiferal analysis and interpretation. Physical properties were measured at Durham University by L. Callard. AMS ^{14}C datings were provided by J. Lloyd and N. Syring, while J. Lloyd created the age model for this study. N. Syring took the lead in writing the first version of the manuscript, with focus on the sea-ice history, with strong support and ideas for improvement by R. Stein and K. Fahl. The co-authors J. Lloyd and D. Roberts provided critical feedback and input related to reconstructions of the NEGIS history. All authors discussed and commented on the manuscript.

Chapter 6: Sea-ice biomarker proxies in surface and subsurface sediments from the Northeast Greenland Shelf - Signals for (paleo) environmental conditions and diagenetic degradation

Authors: Nicole Syring, Ruediger Stein, Kirsten Fahl, Xiaotong Xiao

Publication state: Preliminary report to be included in a more comprehensive study on climate and degradation-controlled biomarker records, i.e., being part of a manuscript to be submitted to, for example, Organic Geochemistry or Marine Geochemistry.

N. Syring, R. Stein and K. Fahl contributed to the design and implementation of the research this study. N. Syring performed the sampling of multicorer and surface samples (partly H. Kolling), the preparation of the sample material (freeze-drying, grinding), the processing of organic bulk parameters (TOC, TC) and lipid biomarkers (HBIs, sterols) while K. Fahl did the quality control of the data. Pb-210 dating was provided by W. Geibert. N. Syring wrote the first version of the manuscript with strong support R. Stein and K. Fahl to the final version. All authors contributed to the final version of the manuscript.

Chapter 3

3.1 Data set & material and methods

This chapter introduces investigations carried out in this PhD thesis on long (PS93/025, PS100/270) and short cores (PS109/45-3, PS109/76-1, PS109/105-1) and surface samples collected from the NEG continental shelf (Table 3.1). Additional proxy records supplementing the own records from Cores PS93/025 and PS100/270 are used to develop a more local and regional understanding of sea-ice history as well as glacier retreat on the inner and outer NEG shelf during the Holocene. Surface samples from this particular area were used to reflect the modern environmental setting. The second part of this chapter describes the main methodology which have been used to generate proxy records from the studied sedimentary sections. The strategy and the decision behind the acquisition of the investigated material and the basic interpretation of the sedimentary sequences at both sites are discussed in the following.

Table 3.1: Locations and coring information of the investigated sites.

| Cores | Gear | Latitude (°N) | Longitude (°E) | Depth (mbsl) | Cruise | Year | Recovery (m) |
|-------------|-----------------|---------------|----------------|--------------|--------|------|--------------|
| PS93/025-1 | Giant Box Corer | 80° 28.84′ | 8° 29.24′ | 291.3 | PS93.1 | 2015 | 0.41 |
| PS93/025-2 | Kastenlot Corer | 80° 28.90′ | 8° 29.40′ | 290.2 | PS93.1 | 2015 | 2.58 |
| PS100/270 | Gravity Corer | 79° 29.824′ | 18° 8.399′ | 424 | PS100 | 2016 | 9.44 |
| PS109/45-3 | Multicorer | 80° 08.854′ | 17° 42.136′ | 206 | PS109 | 2017 | 0.33 |
| PS109/76-1 | Multicorer | 79° 37.213′ | 19° 17.323′ | 366 | PS109 | 2017 | 0.36 |
| PS109/105-1 | Multicorer | 78° 28.880′ | 18° 33.371′ | 440 | PS109 | 2017 | 0.36 |

3.2 Data acquisition

Target sites for this study were selected based on detailed bathymetry surveys during three RV *Polarstern* expeditions on the barely surveyed NEG continental shelf (PS93/Stein, 2016; PS100/Kanzow, 2017; PS109/Kanzow, 2018). High-resolution seabed maps along the cruise track were detected with the hull-mounted ATLAS Hydrosweep DS3 multibeam echosounding systems with an instrument frequency between 13.6–16.4 kHz and a calibration using sound velocity measurements of the water column collected from CTD stations. Data processing was achieved and cleaned in CARIS Hips and Sips. Sub-bottom profiler data was carried out with a hull-mounted Parasound DS III-P70 system (pulse mode between 4–20 kHz, pulse length of 0.5 ms. Seismic profiles were visualised using PS3 file formats on SeNT v 2.02. These basic parameters allow a detailed view on the ocean sea floor, the specification of the general geological imprints e.g. ice sheet extent across the Northeast Greenland and provide information on sediment transport, erosion and deposition. Results show a seafloor morphology, that is highly influenced by recent and past glacial activity, eroding icebergs exported from the central Arctic Ocean via the EGC and strong bottom current activity. For example, end moraines

characterise on the mid-shelf in the northern Westwind Trough suggest an advanced ice-sheet during the Last Glacial Maximum (Evans et al, 2009; Winkelmann et al., 2010). Strong bottom current activity relocates Holocene fine-grained sediment material ($<2\%$ $<63\mu\text{m}$) and cause a non-uniform deposition with low average sedimentation rates of 3–5 cm/ky. Thus, parasound profiles helped to select coring stations in morphological depressions filled up with deposited Holocene fine-grained material and sedimentations rates up to 30 cm/ky on the continental margin, allowing a suitable high-resolution past sea-ice reconstruction on a centennial to decadal timescale (cf., Köhler and Spielhagen, 1990; Spielhagen et al., 2011; Müller 2012).

Core PS93/025 – Outer NEG continental shelf

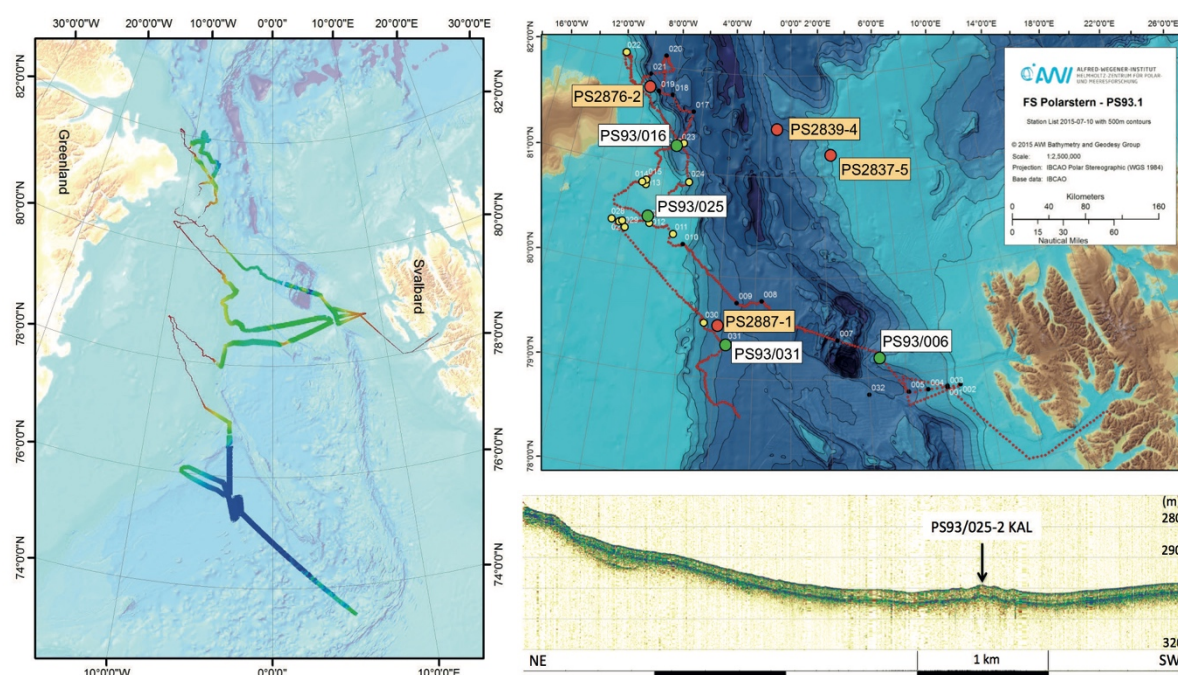


Figure 3.1: Map to the left shows swath bathymetry coverage of PS93.1 and the parasound profile of Kastenlot Core PS93/025-2 in the bottom right corner. The scale in black and white below shows the distance in km, the depth has been determined by the Shipboard Parasound system (UTC, 00:45 (NE) – 04:00 (SW), in 08 July 2015). Upper right map shows the locations of sediment cores achieved during expedition PS93.1 where Kastenlot Core PS93/025-2 is highlighted as green circle (Source: Stein, 2016).

Giant Box Core PS93/025-1 and a Kastenlot Core PS93/025-2 were recovered from the Belgica Bank during RV *Polarstern* Expedition to the Greenland Sea and Fram Strait in 2015 (Fig. 3.1; Stein, 2016). These cores were collected from an undisturbed Holocene sediment package of up to 4 m near $80^{\circ}30'N$ in the deepest part of a depression below 280 m water depth, probably a remnant of a former glacial trough during the LGM (Fig. 3.1; Stein et al., 2016). Based on the geophysical properties, these cores were spliced together at 27 cm to obtain a continuous and complete sedimentary record, named as PS93/025 (Fig. 3.2). Core PS93/025 (258 cm) consists of a homogenous dark greyish brown (2.5Y 4/2) silty clay that shows a magnetic susceptibility (MS, 500–1000 10^6 SI) and wet bulk density (WDB, 1.5–1.7 g cm^{-3}) decreasing from bottom to top (Fig. 3.2; Stein et al., 2016).

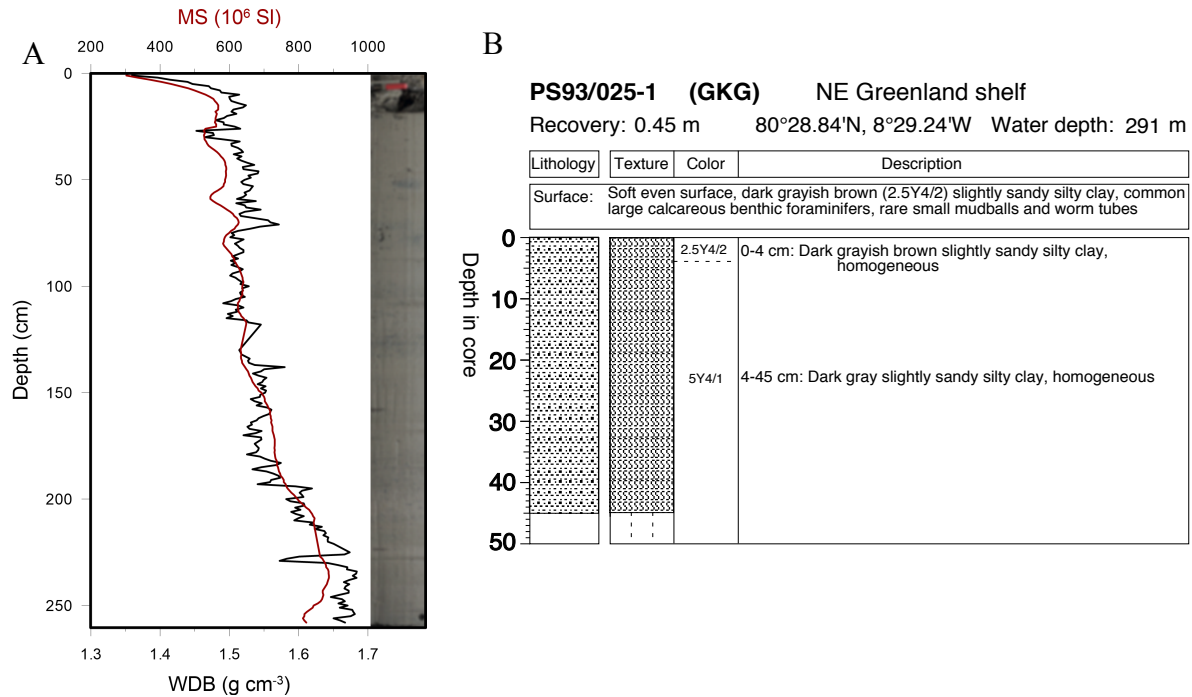


Figure 3.2: A) Wet bulk density, magnetic susceptibility and photograph of Core PS93/025. B) Sediment composition, including the main lithology, texture and color, of Box Core PS93/025-1, which is more or less as of PS93/025-2 (Source: Stein, 2016).

Core PS100/270 – Inner NEG continental shelf

The second manuscript of this thesis addresses the 10 m laminated Holocene Gravity Core PS100/270, was taken during RV *Polarstern* expedition to the Fram Strait in 2016 (Fig. 3.3; Kanzow, 2017). This core was collected in front of embayment of present-day 79NG (Fig. 3.3) and consists of stratified sediments of a glaciomarine origin, which probably relate to variations in the source from marine terminating outlet glaciers of NEGIS catchments. A number of cores from NEG contain laminated silty clays which often display alternating (partly rhythmic) red and grey to brown colour bands with no obvious change in grain size. Surface samples investigated aboard are characterized by a rich and diverse benthic assemblage with the dominance of calcareous species e.g. *C. reniforme*, *C. neoteretis*, *E. excavatum*, *I. hellenae* and *Quinqueloculina* spp., indicative for the intrusion of Atlantic Water towards the shelf (Kanzow, 2017). The core was split, logged and described sedimentologically at the Durham University, afterwards shipped to AWI where it has been archived and used for post-cruise analysis, including lipid biomarker extraction and organic bulk parameter measurements. In total, 162 sediment samples were collected to reconstruct the history of NEGIS from the late Weichselian through the Holocene.

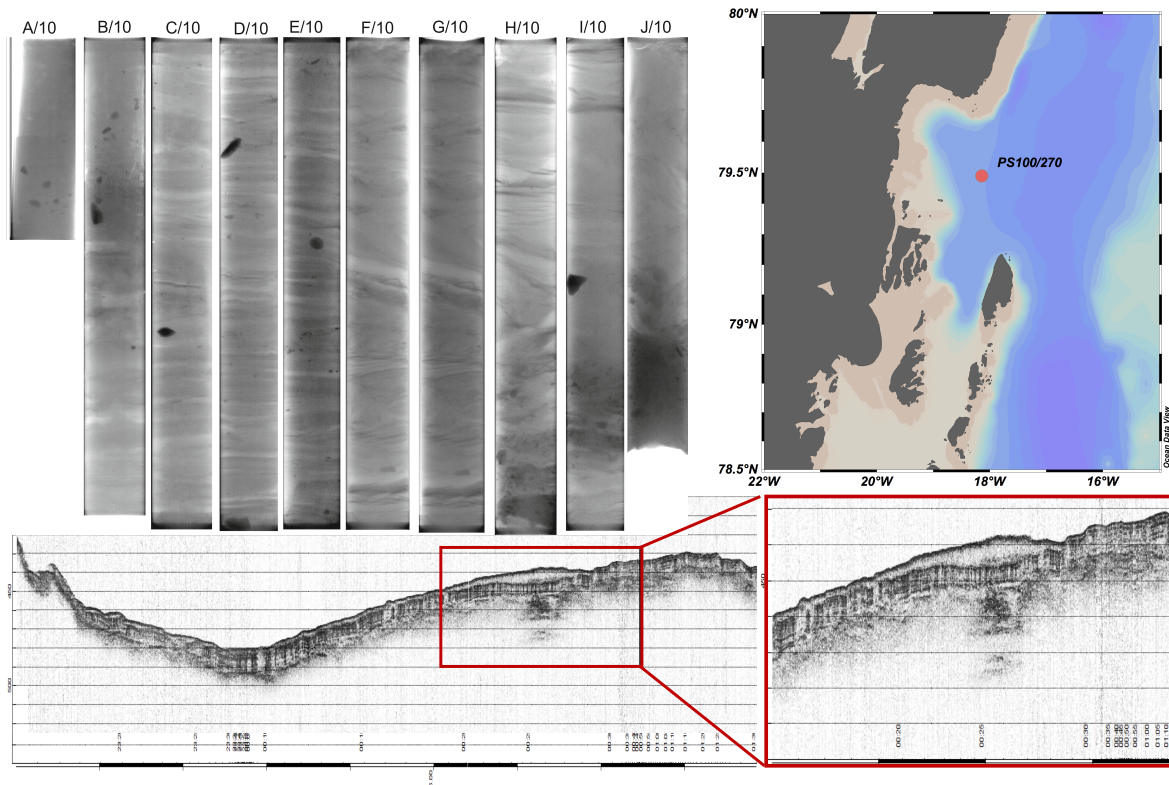
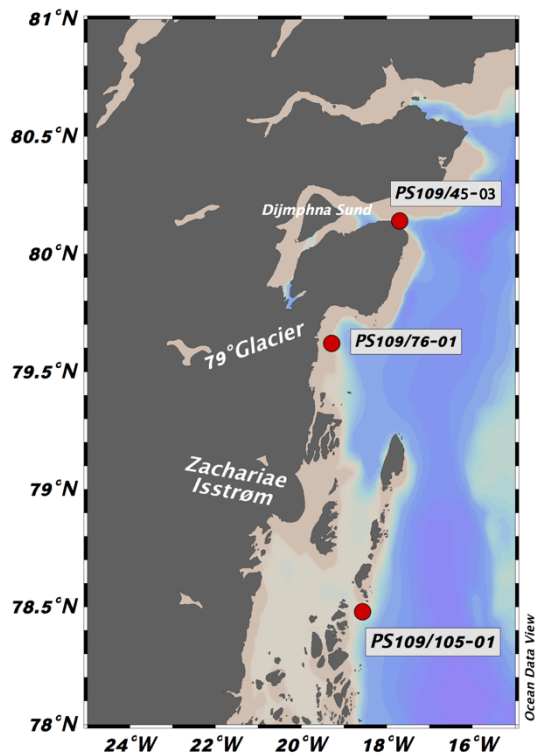


Figure 3.3: X-ray image with a distinct lamination to the left, research area and parasound profile of Core PS100/270 (Source: Kanzow, 2017).

Multi-Corer PS109/45-3, PS109/76-1 and PS109/105-1 – Inner NEG continental shelf



Sediment material from three multicorer (MUC) located in the Djimphna Sund (PS109/45-3), in front of the 79NG (PS109/76-1) and in the Jøkelbugten region near ZI (PS109/105-1) were taken during RV *Polarstern* expedition PS109 (Fig. 3.4; Kanzow, 2018). These short sediment cores up to 40 cm long were collected to recover undisturbed near-surface sediments, allowing the reconstruction of (sub-) recent climate conditions covering the last few decades to centuries on the NEG continental shelf. All cores were processed for organic bulk parameters and lipid biomarker measurements.

Figure 3.4: Core locations of MUCs recovered during Expedition PS109 on the inner NEG continental shelf in relatively shallow water depths (206 m, 366 m and 440 m) (Kanzow, 2018).

Surface samples - NEG continental shelf

The 27 surface sediment samples used in this thesis, were collected from the NEG continental shelf (20°W–5°W and 74°N–81°N) between 2015 and 2018 during *RV Polarstern* research expeditions to western Fram Strait to study modern environmental and climatic conditions, based on proxy data (see chapter 6). These data are useful for the interpretations of paleo-records.

3.3 Organic-geochemical methods – Proxies used for past climate reconstructions

General laboratory investigations and storage of sample material

This chapter describes our organic geochemical methods used in this PhD work, including analytical procedures for the extraction, purification, analysis and common statistical evaluation of lipid biomarkers, i.e., HBIs (IP₂₅, HBI II and HBI III (E- and Z-isomers)) and sterols (brassicasterol, dinosterol, β -sitosterol and campesterol), along with organic bulk parameters in marine sediment samples from the NEG continental shelf. A general inter-laboratory analytical procedure of marine Arctic biomarkers focusing on biomarker extraction, quantification and interpretation have been outlined in Belt et al. (2014).

For this PhD study surface and downcore sediments were sub-sampled during the expeditions at ca. 10–20 g per surface location or core horizon, transferred to glass vials and stored in a freezer under a dark environment at -20°C until extraction. Sample material was freeze-dried at the Alfred-Wegener-Institute in Bremerhaven using a STERIS Lyovac GT 2-E for five days and later finely ground and homogenized.

Determination of organic bulk parameters

Total organic carbon (TOC) extracts were measured using a Carbon-Sulfur Determinator PC controlled (CS-125, Leco and ELTRA CS 800). These marine sediments often contain carbonate (CaCO₃), which were removed for TOC measurements by adding hydrochloric acid to dry 100 μ g sediment sample. This approach includes a standard sediment of known TOC content as reference for the linear calibration. In order to calculate the inorganic carbon (CaCO₃) and C/N ratio, amounts of total carbon (TC) and total nitrogen (TN) were determined by using a Carbon-Nitrogen-Sulfur Analyser (Elementar III, Vario). CaCO₃ = (TC – TOC) * 8.333 (8.333 stoichiometric factor) calculations were implemented under the assumption that the contained carbonate refers to calcite. The C/N ratio was calculated based on the TOC and TN values (cf., Stein and Macdonald, 2004).

For the foraminiferal analysis done by co-authors in one of the joint papers, it is referred to chapter 5.

Sediment extraction and evaluation of lipid biomarkers

1) Internal standards

Two internal standards were added to each 5 g dry and homogenized sediment samples prior to the DCM/methanol-based extraction procedure for lipid biomarker quantification. Internal standard for the

quantification of the HBIs is 7-hexylnonadecane (7-HND, 0.076 $\mu\text{g}/\text{sample}$) and for sterols 5 α -androstan-3 β -ol (androstanol, 10.7 mg/sample). In addition, 9-octyl-8-heptadecene (9-OHD, 0.1 μg) and squalane (3.2 mg/sample) serve as internal standards for routine methodical checks (Fig. 3.5).

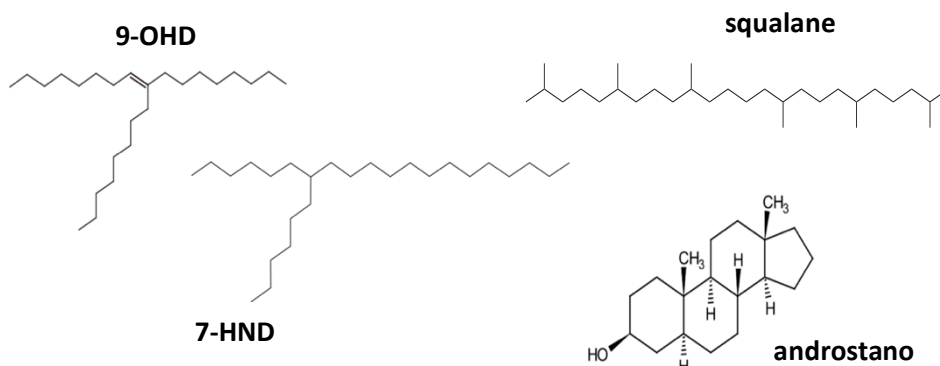


Figure 3.5: Chemical structure of internal standards.

2) DCM/methanol method

Upon addition of the internal standards, 30 ml of dichloromethane/methanol (DCM/MeOH, 2:1 v/v) was added to each sample followed by ultrasonification (15 min) and centrifugation (2000rpm, 3 min) three times.

3) Purification via column chromatography

Pasteur pipettes were plugged with cotton wool, filled with chromatography-grade silica gel (ca. 0.7 g; 60–200 μm particle size) and conditioned with 2 x 1 ml of ethylacetate/*n*-hexane and 5 x 1 ml of *n*-hexane. Subsequently, open column chromatography with SiO_2 as a stationary phase was carried out on lipid extracts to separate the hydrocarbon fraction (5 ml *n*-hexane) from the sterol fraction (9 ml ethylacetate/*n*-hexane) (Fig. 3.6).

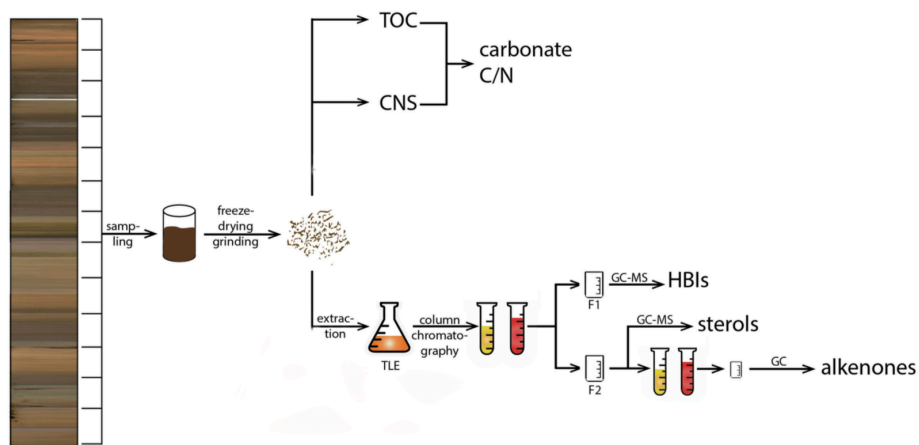


Figure 3.6: Schematic representation of the laboratory procedures including all processes from sampling to the GC-MS measurement. TLE = Total Lipid Extract, GC-MS = Gas Chromatograph-Mass Spectrometry (modified after Kremer, 2018).

4) Silylation of sterols

Finally, the sterol fraction was derivatized by adding 200 μl of bis-trimethylsilyl-trifluoroacet-amide (BSTFA) at 60°C on a heating station for 2 hours.

5) Gas chromatography measurements

Two different gas chromatography-mass spectrometers (GC-MS) with similar basic configuration were used to measure the extracted samples (Fig. 3.7). The hydrocarbon fraction was carried out using an gas chromatograph Agilent Technologies 7890B GC system (30m DB-1MS column, 0.25 mm i.d., 0.25 μm film thickness) coupled to a mass spectrometer Agilent 5977A MSD (70 eV constant ionization potential, Scan 50–550 m/z , 1 scan/s, ion source temperature 230°C, Performance Turbo Pump) with the temperature program: 60°C (3 min), 150°C (heating rate: 15°C/min), 320°C (heating rate: 10°C/min) and 320°C (15 min, isothermal). The sterols were measured with a GC Agilent 6850 GC coupled to an Agilent 5975C VL MSD (conditions see above) with the temperature sequence: 60°C (2 min), then 150°C (heating rate: 15°C/min), 320°C (heating rate: 3°C/min) and 320°C (20 min isothermal).

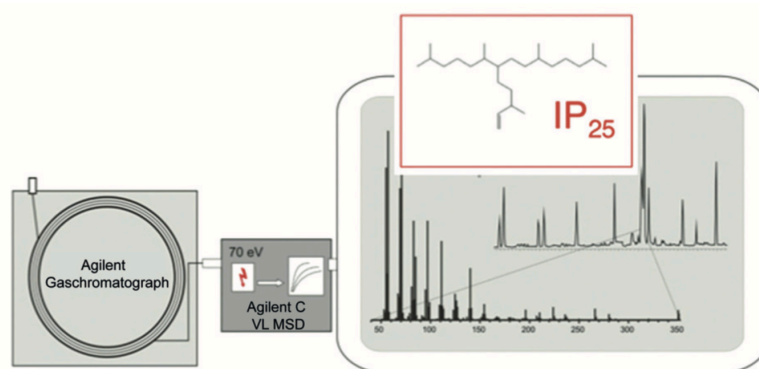


Figure 3.7: Investigated biomarker fractions were measured with GC-MS (Source: Stein et al., 2012).

6) Qualification and quantification of lipid biomarkers

Component assignment was based on comparison of GC retention time (RTs), Kovats Retention Indices (RIs), and electron ionization mass spectra with those of reference compounds. HBIs were measured in the Selected Ion Monitoring (SIM) mode due to its higher sensitivity with a detection window between 17–19 minutes (sterols: Boon et al., 1979; Volkman, 1986; HBIs: Belt et al., 2007; Brown and Belt, 2016).

The concentration of each biomarker was calculated by setting its individual GC-MS ion responses in relation to those of respective internal standards. For the quantification of IP₂₅, HBI II and HBI III, their molecular ions (m/z 350 for IP₂₅, m/z 348 for HBI II, and m/z 346 for HBI III) (Fig. 3.8) were compared to the fragment ion m/z 266 of the internal standard 7-HND. The calculated Kovats Index for IP₂₅ is 2085, for HBI II 2084 and 2046 for HBI III.

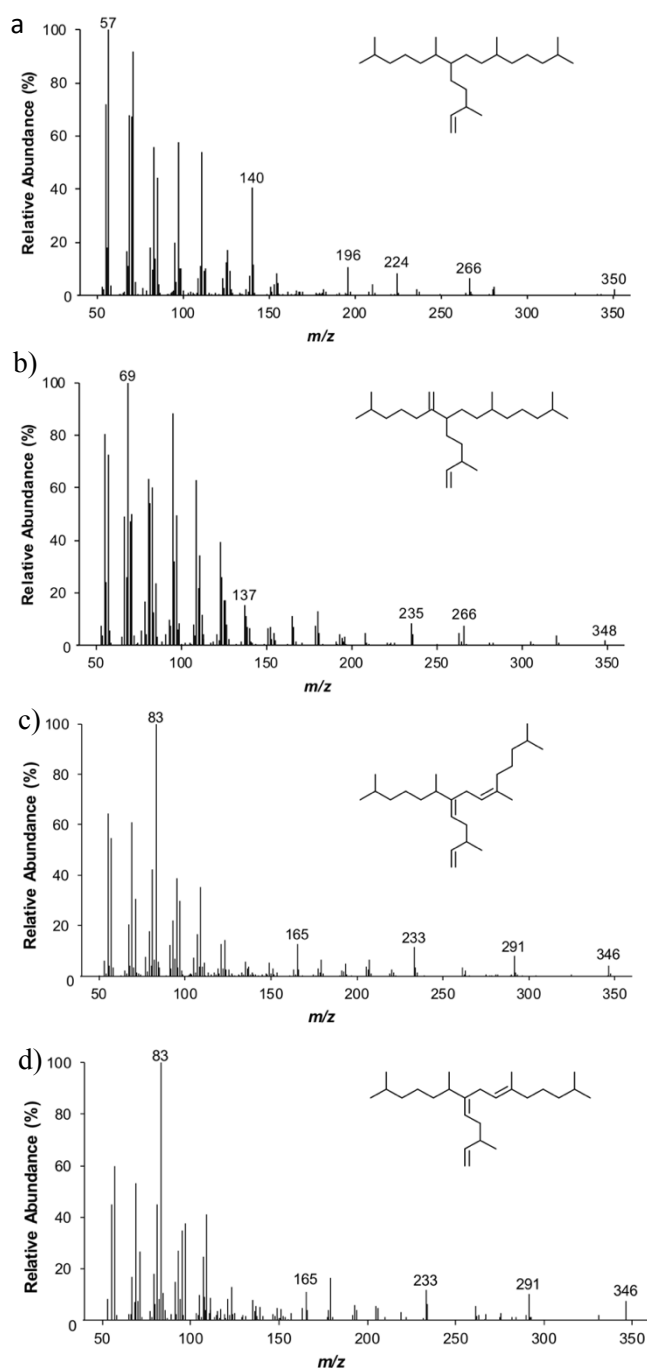


Figure 3.8: Background-corrected TIC chromatograms of a) IP₂₅, b) HBI II diene, c) HBI III (E-isomere) and d) HBI III (Z-isomere) (modified after Köseoğlu, 2018).

For the quantification of the sterols trimethylsilyl (TMS) ethers, the molecular ions m/z 470 for brassicasterol, m/z 472 for campesterol, m/z 486 for β -sitosterol, and m/z 500 for dinosterol (Fig. 3.9) were used in relation to the molecular ion m/z 348 of the internal standard androstanol. The different responses of these ions were balanced by an external calibration.

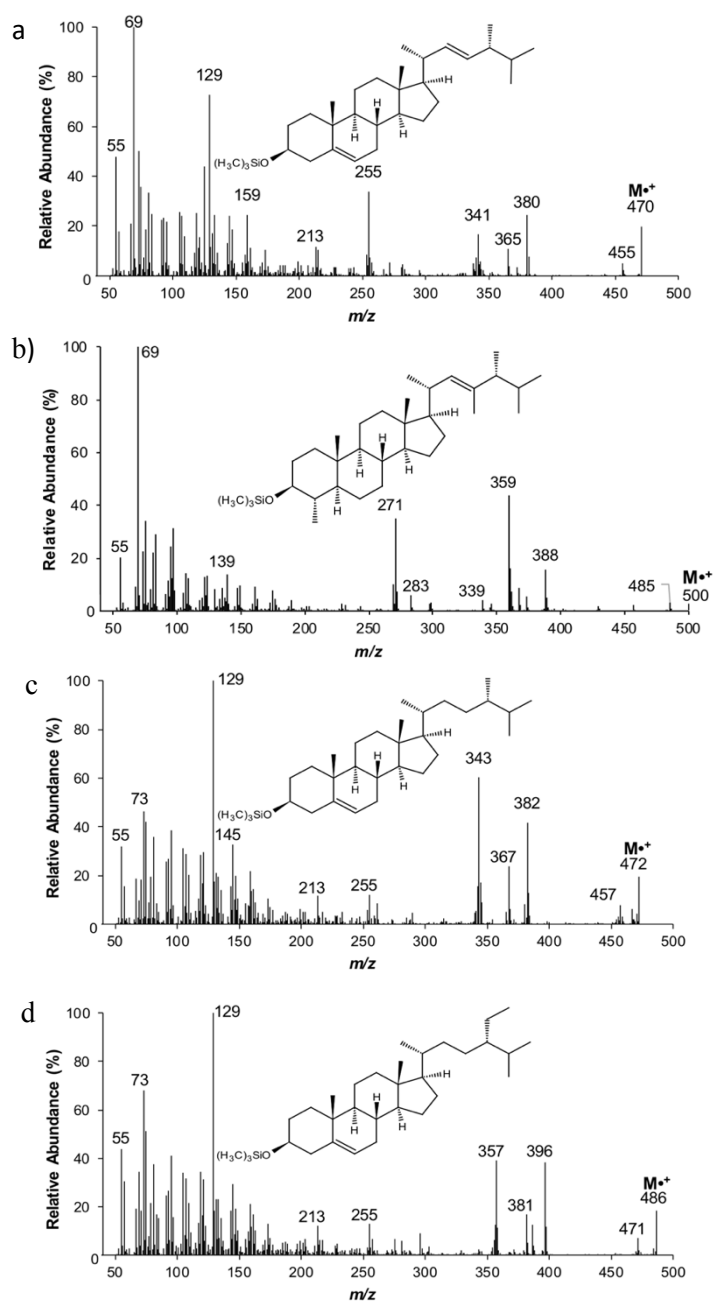


Figure 3.9: Background-corrected TIC chromatograms of a) brassicasterol, b) campesterol, c) β -sitosterol and d) dinosterol (modified after Köseoğlu, 2018).

The retention indices for brassicasterol (as 24-methylcholesta-5, 22E-dien-3 β -O-Si(CH₃)₃), 24-methylenecholesterol (as (3*S*,8*S*,9*S*,10*R*,13*R*,14*S*,17*R*)-10,13-dimethyl-17-[(2*R*)-6-methyl-5-methylideneheptan-2-yl]-2,3,4,7,8,9,11,12,14,15,16,17-dodecahydro-1*H*-cyclopenta[*a*]phenanthren-3-O-Si(CH₃)₃), campesterol (as 24-methylcholest-5-en-3 β -O-Si(CH₃)₃), β -sitosterol (as 24-ethylcholest-5-en-3 β -O-Si(CH₃)₃), and dinosterol (4 α ,23,24-Trimethyl-5 α -cholest-22E-en-3 β -O-Si(CH₃)₃) were calculated to be 1.6108, 1.61418, 1.6503, 1.7053, and 1.7289 (normalized to androstanol set to be 1.000), respectively. For further details we refer to Fahl and Stein (2012).

Chapter 4

Holocene changes in sea-ice cover and polynya formation along the eastern North Greenland shelf: New insights from biomarker records

Nicole Syring ^{a,*}, Ruediger Stein ^{a,b}, Kirsten Fahl ^a, Maximilian Vahlenkamp ^b, Marc Zehnich ^{c,d}, Robert F. Spielhagen ^d, Frank Niessen ^a

^a Alfred Wegener Institute Helmholtz Centre for Polar and Marine Research (AWI), Am Alten Hafen 26, Bremerhaven, 27568, Germany

^b Faculty of Geosciences (FB5), University of Bremen, Klagenfurter Str. 4, Bremen, 28359, Germany

^c Academy of Sciences, Humanities and Literature, Geschwister-Scholl-Str. 2, 55131 Mainz, Germany

^d GEOMAR Helmholtz Centre for Ocean Research, Wischhofstr. 1-3, Geb. 4, 24148 Kiel, Germany

State: This manuscript is published in the Journal Quaternary Science Reviews 231 (2020) 106173.

Abstract

Understanding the processes controlling the natural variability of sea ice in the Arctic, one of the most dynamic components of the climate system, can help to constrain the effects of future climate change in this highly sensitive area. For the first time, a high-resolution biomarker study was carried out to reconstruct past sea-ice variability off eastern North Greenland. This area is strongly influenced by cold surface waters and drift ice transported via the East Greenland Current, meltwater pulses from the outlet glaciers of the Northeast Greenland Ice Stream and the build-up of landfast ice. The well-dated Holocene sedimentary section of Core PS93/025 provides insights into variations of the sea-ice conditions (regional and local sea-ice signal), oceanic and atmospheric circulation and the biotic response to these changes. These biomarker records show a reduced to variable sea-ice cover during the early Holocene between 10.2 and 9.3 ka, followed by a steady increase in sea-ice conditions during the mid Holocene. During the last 5–6 ka, sea-ice conditions remained more stable representing a seasonal to marginal sea-ice situation. Based on our biomarker records, stable sea-ice edge conditions, with a fully developed polynya situation occurred since the last 1 ka

4.1 Introduction

4.1.1 Background

Arctic sea ice is a key component in our climate system, regulating the global heat budget, influencing the atmospheric circulation (Serreze et al., 2016) and the global ocean circulation via the Atlantic Meridional Overturning Circulation (AMOC; Sévellec et al., 2017). Alternations in Arctic sea-ice extent can result in major changes to deep-water formation in the Nordic Seas (Rudels and Quadfasel, 1991) and lower latitudinal climate of the North Atlantic region (Overland and Wang, 2005). Thus, the recent dramatic loss of Arctic sea ice (Fig. 4.1) can affect global climate beyond the polar regions, changing the planetary albedo, surface heat and freshwater flux (Thomas and Dieckmann, 2008; Sévellec et al., 2017). Sea ice is not only an important factor for biodiversity and -productivity in the Arctic, providing a habitat to ice-associated species including organisms such as sea ice-algae, fish, birds, and marine mammals (Rudels et al., 1996; Dieckmann and Hellmer, 2003), it also acts as insulating layer between the ocean and the atmosphere (Stroeve et al., 2012).

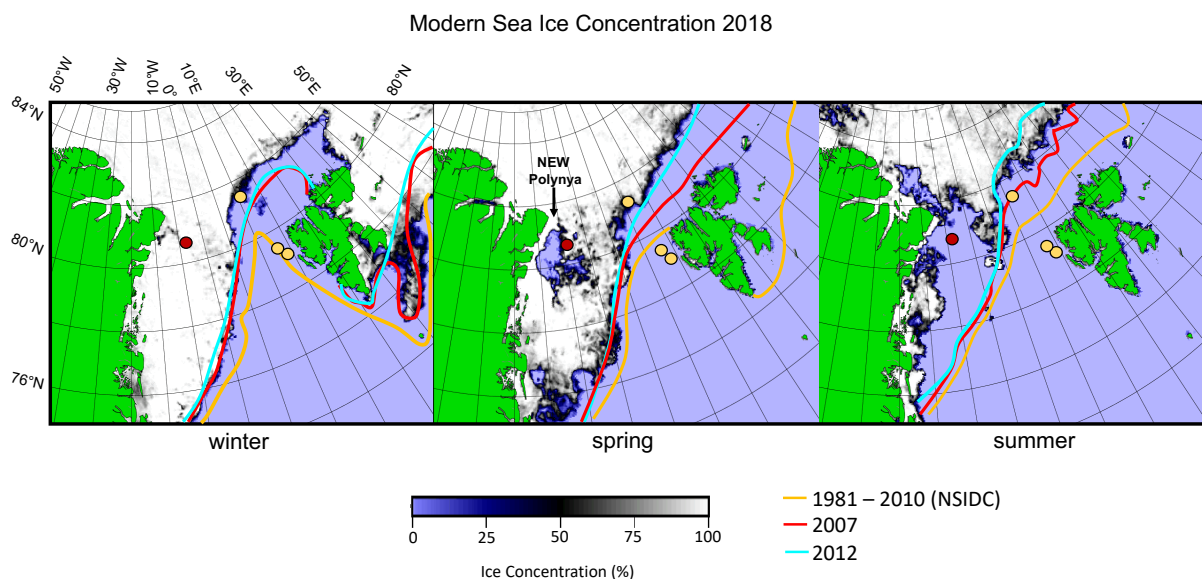


Fig. 4.1: Modern sea ice-concentration in the Fram Strait (Spren et al., 2008; <https://seaice.uni-bremen.de>, 2018). Closed sea ice cover during winter, seasonal opening of the Northeast-Water Polynya (NEW Polynya) during spring and strongly reduced sea ice during summer. Orange, red and blue lines showing the sea-ice extent from 1981-2010 and the extremely sea-ice reduced years 2007 and 2012 (<https://nsidc.org>). Red dot shows the location of Core PS93/025, yellow dots the locations of other cores used in this study.

The particular importance of Arctic sea ice with respect to recent anthropogenic climate change is that it is one of the most dynamic components of the climate system. Due to a reduction in the ice-ocean albedo effect, declining Arctic sea ice is expected to amplify anthropogenic climate change in the polar regions (Manabe et al., 1992; Randall et al., 1998; Screen and Simmonds, 2010). Over the past three decades, summer sea-ice extent and thickness have declined by 50%, much faster than predicted by

climate models (see review by Stroeve et al., 2012; Serreze et al., 2016; Walsh et al., 2017; Notz and Stroeve, 2018).

The oceanographic and sea-ice conditions on the eastern North Greenland shelf are influenced by the outflow of freshwater and sea ice (drift ice) from the central Arctic Ocean, as well as by rivers, fjords, islands and marine-terminating outlet glaciers from the Greenland coastline in the west (Arndt et al., 2017, Fig. 4.2b,c). The knowledge about regional and local drivers of the sea-ice history and oceanic and atmospheric interactions on the eastern North Greenland continental shelf during the Holocene, however, remains fragmentary due to its low accessibility. Over the last years reduced sea-ice conditions have enabled a number of research expeditions into this area, allowing the recovery of sediment cores for detailed studies of paleoclimate and paleoceanographic conditions. Furthermore, proxy-based methods for past sea-ice reconstructions have been further developed and applied within the Fram Strait and Arctic Ocean regions (e.g., de Vernal et al., 2013; Pieńkowski et al., 2016; Belt, 2018; Belt et al., 2019; Limoges et al., 2018).

The Holocene (0–11.7 ka), generally more climatically stable than the previous glacial transition (Grootes et al., 1993), was punctuated by rapid changes in climate and ocean dynamics (Mayewski et al., 2004; Sundqvist et al., 2014). In the Northern Hemisphere, the Holocene is roughly divided into three main intervals: (1) the early Holocene (~11.7–9 ka); (2) the mid Holocene (~9 to 5 ka) and (3) the late Holocene (~5–0 ka) (Briner et al., 2016; Renssen et al., 2009; Wanner et al., 2011). Especially, the late Holocene near-boundary conditions witnessed short-term alternations (<500 yrs.), e.g. the Medieval Warm Period, Roman Warm Period and Little Ice Age (Ljungqvist, 2010). A declining solar insolation, freshwater influence, volcanic activity, and changes in the AMOC have been suggested as drivers for these short-term climate events (Andersen et al., 2004a,b; Laskar et al., 2004; Rohling and Pälike, 2005; Renssen et al., 2006; Wanner et al., 2011). The Arctic Oscillation (AO) and North Atlantic Oscillation (NAO) regulate sea level pressure and the outflow of drift ice through the Fram Strait (Rigor et al., 2002), and significantly influence the weather and climate in the Northern Hemisphere on interannual-decadal timescales (Darby et al., 2012). Positive or negative AO/NAO modulations control the extensity of the Transpolar Drift system moving sea ice from Siberian shelves and the central Arctic Ocean in the direction of Greenland (Rigor et al., 2002; Bennike et al., 2004). So far, short-term variability of sea-ice extent is not sufficiently resolved in climate models, even though they have great relevance for predictions of the short-term variability in future climate (Loeb et al., 1997; Dieckmann and Hellmer, 2003; Funder et al., 2011).

This study utilizes biomarkers preserved in marine sediments from Core PS93/025-2, recovered from the outer eastern North Greenland shelf in the Northeast-Water Polynya (NEW Polynya, Fig. 4.1). This site is ideally suited to identify and disentangle the driving mechanisms of sea-ice distribution in the western Fram Strait. As proxies for the reconstruction of sea-ice cover we have used the sea-ice proxy IP₂₅, a highly branched isoprenoid (HBI) monoene with 25 carbon atoms (Belt et al., 2007), in combination with specific open-water phytoplankton and terrestrial higher land plant biomarkers

(Müller et al., 2009; Stein et al., 2012; Belt and Müller, 2013; Belt et al., 2015, 2019; for further details see chapter 4.1.1). Based on these high-resolution biomarker data we are able to reconstruct sea-ice variability, primary productivity, terrigenous input and seasonal formation of the NEW Polynya that evolved during the Holocene at the eastern North Greenland shelf. Our results are compared with the eastern Fram Strait sea-ice trends.

4.1.2 Regional Setting

The Fram Strait is the only deep-water connection between the Arctic and global oceans. Arctic Deep Water, filling the Fram Strait at depths greater than 800 m is overlain by Atlantic Intermediate Water (AIW) (Aagaard and Coachman, 1968a; Rudels and Quadfasel, 1991). The upper water layer is zonally divided by local surface ocean currents. On the eastern side of the Fram Strait relatively warm, saline Atlantic surface waters enter the Arctic Ocean via the West Spitsbergen Current (WSC, Fig. 4.2a). In contrast, the western Fram Strait is dominated by the outflow of cold Arctic surface waters of the East Greenland Current (EGC) (Aagaard and Coachman, 1968; Rudels et al., 1999). The low-saline EGC flows south along the eastern North Greenland shelf (Fig. 4.2a).

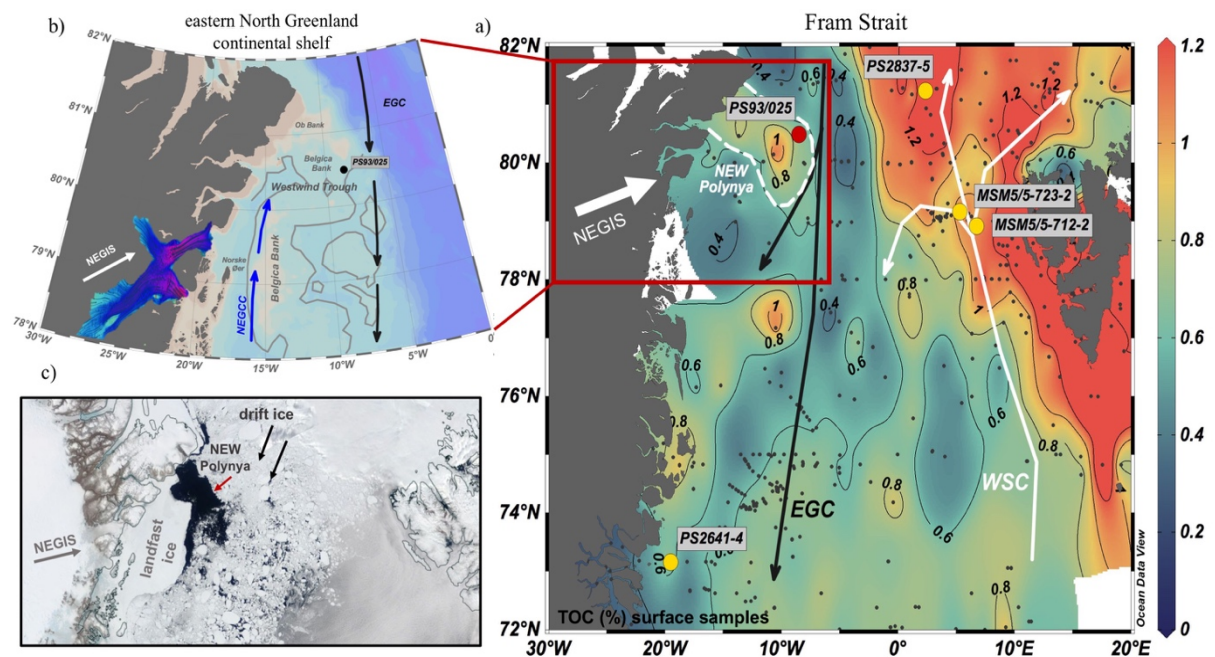


Fig. 4.2: a) Distribution of total organic carbon (TOC) in surface sediments from the Norwegian-Greenland Sea and Fram Strait (Birgel and Stein, 2004; supplemented). Kastenlot Core PS93/025 (red circle) location at 80°N at the outer rim of the NEW Polynya (white dashed line, assumed area based on the TOC concentrations). Major surface ocean currents in the study area are the East Greenland Current (black arrows) and the West Spitsbergen Current (white arrows). Locations of further cores discussed in the text are marked as yellow circles. Northeast Greenland Ice Stream (NEGIS). b) Detailed map of the eastern North Greenland continental margin, including Core PS93/025 (black dot) taken from the upper edge of the Belgica Bank above the Westwind Trough, the southward flowing EGC (black arrow) and the northward flowing coastal Northeast Greenland Coastal Current (NEGCC, blue arrow). Norske Øer Ice Barrier is located in front of NEGIS. c) Satellite image (June 2019, credit: NASA Worldview: <https://worldview.earthdata.nasa.gov>) displaying outlet glaciers of NEGIS, landfast ice build-up along the coast, drift ice transported from the central Arctic Ocean and in between the seasonal formation of the NEW Polynya.

These regional ocean currents result in a strong zonal surface temperature gradient. This zonal difference in sea-surface temperature causes a large disparity in sea-ice cover between the western and eastern Fram Strait. Consequently, west Spitsbergen is characterized by the northernmost ice-free water conditions during winter, while the sea-ice cover along the continental shelf off eastern North Greenland stretches much further south, due to regional sea-ice build-up and transport from the Arctic Ocean (Aagaard, 1982; Vinje et al., 1977). Sediments, drift ice and low-saline water masses formed on the Eurasian shelves are transported via the Transpolar Drift across the central Arctic Ocean and eventually through the Fram Strait (Aagaard and Coachman, 1968; Eicken et al., 1995; Reimnitz et al., 1995; Schlichtholz and Houssais, 1999; Smedsrud et al., 2017).

Sea-ice conditions over the wide continental eastern North Greenland shelf in the western Fram Strait between 79–80°N are additionally influenced by the waxing and waning of the ~700 km long Northeast Greenland Ice Stream (NEGIS), the largest ice stream in eastern North Greenland (Aagaard and Coachman, 1968b, Fig. 4.2b). This fast-flowing ice stream (20 m/year) drains 20% of the Greenland Ice Sheet and seasonally supplies large amounts of ice and freshwater to the eastern North Greenland shelf (Rignot and Kanagaratnam, 2006; Joughin et al., 2010; Rignot et al., 2011).

The coastal area north of NEGIS at ~80°N is characterized by the highly variable NEW Polynya (Fig. 4.1). Coastal polynyas are mostly ice-free areas surrounded by a denser sea-ice cover (Smith et al., 1990; WMO, 1985; Stirling, 1980). Northerly winds in combination with local ocean currents remove ice from the coastal region while grounding of icebergs and ice islands can prevent ice advection from the Arctic into the polynya region (Barber and Massom, 2007).

When the NEW Polynya opens up in April/May, reaching its final extension in summer, an anticyclonic circulation pattern appears over almost the entire ~300 km wide and shallow Belgica Bank with water depths ranging from 40 to 300 m (Bourke and Garrett, 1987; Kuklinski and Bader, 2007, Fig. 4.1, 4.2c). A combined effect of a fast-ice barrier (the Norske Øer Ice Barrier), katabatic winds and a northward flowing North East Greenland Coastal Current (NEGCC) form the NEW Polynya (Fig. 4.2b, Schneider and Budéus, 1997). The water column in the NEW Polynya is characterized by AIW at the bottom overlain by Polar Water (PW) that circulates anticyclonic at the surface (Bourke and Garrett, 1987). Additionally, the surface waters in the polynya region are affected by melting of sea ice along the marginal ice zone and freshwater input from ice melting on land. The freshwater input from these processes stratifies the upper water column and fosters intense biological production until nutrients become depleted (Hirche et al., 1991; Schneider and Budéus, 1994; Budéus and Schneider, 1995). A significant ecosystem for primary producers (e.g., diatom blooms), marine mammals and seabirds is supported by the seasonally reduced ice cover of the recurring seasonal NEW Polynya (Stirling, 1980; Wadhams, 1981; Barber and Massom, 2007). Today, sea-ice cover varies from a dense sea-ice cover in winter to stable-ice-edge conditions during late spring/summer. This is also supported by elevated Total Organic Carbon (TOC) concentrations in sediments here, relative to surrounding areas (Fig. 4.2a; Birgel

and Stein, 2004). However, understanding of the evolution and processes leading to polynya formation remain inconclusive.

4.2 Material and methods

4.2.1 Sediment material

Kastenlot Core PS93/025-2 was taken during RV Polarstern Cruise PS93.1 (2015) on the continental shelf off eastern North Greenland (80°28.90'N, 8°29.40'W) in 290.2 m water depth (Fig. 4.2a,b, Stein, 2016). The coring location was selected based on detailed Hydrosweep and Parasound surveys. These surveys were used to identify small depressions with thick fillings of deglacial to Holocene sediments on the eastern North Greenland shelf, an area that is generally characterized by lag deposits due to strong bottom current activity. The recovered sediments consist of dark grayish brown, homogenous silty clay with relatively low magnetic susceptibility and wet bulk density values (Stein, 2016). Because of coring loss in the upper 25 cm of giant Kastenlot Core PS93/025-2, we correlate the uppermost part of the kastenlot core with a Box Core (GKG) PS93/025-1 covering the upper 43 cm of near surface sediments, based on the TOC content and spliced the records together at 27 cm to obtain a continuous and complete sedimentary record (named as Core PS93/025). From the Kastenlot and GKG cores, subcores were taken for multidisciplinary studies. One set of subcores devoted to biomarker analysis, was stored at -20°C to prevent biomarker degradation.

4.2.2 Methods

4.2.2.1 Chronology

The age model is based on 19 accelerator mass spectrometry (AMS) ^{14}C ages measured on macro- and microfossil species, including benthic foraminifera (mixed species), planktic foraminifera (*Neogloboquadrina pachyderma*), bivalves, and scaphopods (not further identified) from GKG Core PS93/025-1 and Kastenlot Core PS93/025-2 (Table 4.1). AMS ^{14}C dating was carried out at the Alfred Wegener Institute Bremerhaven using the “Mini Carbon Dating System (MICADAS) and at the Leibniz-Laboratory in Kiel (Graphite Target). Radiocarbon ages were converted to calibrated calendar years before present (cal. years BP) using the calibration software CALIB 7.1 and the Marine13 calibration curve (Stuiver et al., 2019; Table 4.1). Five AMS ^{14}C ages at depths of 93.5 cm, 110.5 cm, 130.5 cm, 238 cm and 264 cm (Table 4.1, grey shaded areas) turned out to be reworked material within the sedimentary section and were therefore excluded. At a depth of 93.5 cm two ^{14}C datings were performed on two different organism groups (bivalve and benthic foraminifera), but only one was used for the age model (Table 4.1).

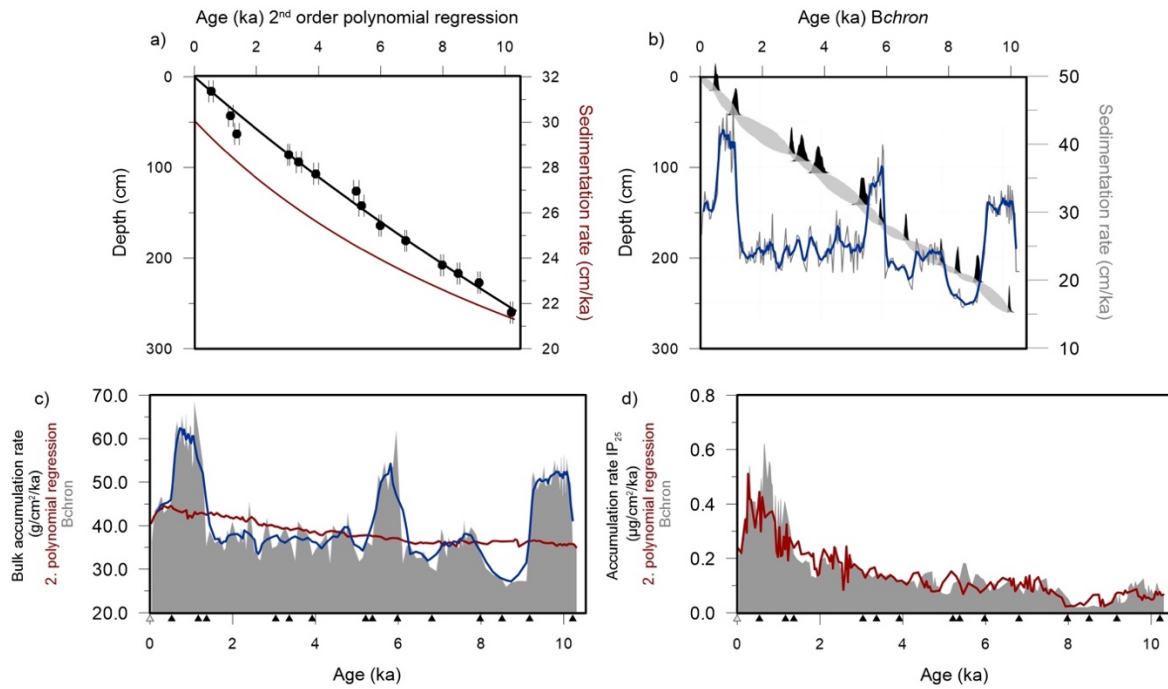


Fig. 4.3: a) Age model based on the 2. order polynomial regression with a relatively constant sedimentation rate (Zehnich et al., 2020). Black dots with error bars demonstrate measured corrected AMS ^{14}C ages for Core PS93/025 (Table 4.1). b) *Bchron* age model (blue, bold line represents 5-point average, excluding two outliers at 62.5 and 125.5 cm, Table 4.1, Haslett and Parnell, 2008) used in this study, showing a variable sedimentation rate over the Holocene. c) Bulk accumulation rates based on 2. polynomial regression by Zehnich et al., 2020 (red line) and our *Bchron* age model (blue line, grey shaded area with blue, bold line marking the 5-point average). d) Accumulation rates of IP_{25} emphasize similar trends of age models shown in a) and b).

Based on the radiocarbon ages we present two age models (Fig. 4.3). The first approach uses a 2nd order polynomial regression through the radiocarbon ages (see Zehnich et al., 2020). The second chronology is based on modeling by using the Bayesian R package *Bchron* (Parnell et al., 2008) and the marine 13 calibration curve (Reimer et al., 2013). With the *Bchron* model, two outliers at 62.5 and 125.5 cm would lead to extreme values up to 100 cm/kyr in the calculated sedimentation rate for which no evidence is found in the core data. We therefore excluded these two results from the Bayesian model. In the present study we have used the *Bchron* age model for three reasons: Firstly, the Bayesian chronology remains within the error margin for the individual radiocarbon measurements; secondly, the 2nd order polynomial can only curve once, which may not fully reflect the variable nature of sediment input or flux under changing climatic conditions; thirdly, the Bayesian approach provides uncertainties and increases robustness of the age model. 10,000 age-depth realizations were obtained to estimate the median age and 95% confidence intervals at 1 cm resolution (Fig. 4.3). We acknowledge that application of the *Bchron* age model results in a higher variability of calculated sedimentation rates and that a possible vertical displacement (from reworking or bioturbation) of some of the dated materials cannot be ruled out. Nevertheless, the overall trends are very similar for both age models as shown, for example, in the IP_{25} accumulation rate records (Fig. 4.3). The sedimentation rates from the *Bchron* age model range between 25–30 cm/kyr over the past 10.2 ka, except for three intervals of high sedimentation rates (up to ~40–45 cm/kyr) between 0.8–1.1 ka, 5.7–6 ka and 9–10 ka (Fig. 4.3).

| Lab-ID | Depth (cm) | Material | AMS ¹⁴ C | CALIB median | CALIB 2 sigma min |
|--------------|------------|----------------------|---------------------|--------------|-------------------|
| AWI 2053.1.1 | 15,5 | Benthic foraminifer | 926 ± 73 | 536 | 426 |
| AWI 2054.1.1 | 42,5 | Benthic foraminifer | 1614 ± 75 | 1171 | 990 |
| AWI 2055.1.1 | 62,5 | Benthic foraminifer | 1816 ± 77 | 1369 | 1228 |
| KIA 52138 | 85,5 | Bivalve | 3225 ± 30 | 3036 | 2932 |
| KIA 51161* | 93,5 | Bivalve | 3805 ± 25 | 3752 | 3655 |
| AWI 2056.1.1 | 93,5 | Benthic foraminifer | 3485 ± 84 | 3365 | 3150 |
| AWI 2057.1.1 | 106,5 | Benthic foraminifer | 3930 ± 81 | 3918 | 3686 |
| AWI 2058.1.1 | 125,5 | Benthic foraminifer | 4909 ± 89 | 5217 | 4956 |
| AWI 2059.1.1 | 141,5 | Benthic foraminifer | 5026 ± 83 | 5381 | 5185 |
| KIA 52139 | 110,5 | Scaphopod | 2521 ± 29 | 2198 | 2106 |
| BETA 445522* | 130,5 | Bivalve | 3610 ± 30 | 3506 | 3412 |
| KIA 52140 | 163,5 | Bivalve | 5595 ± 35 | 5980 | 5897 |
| BETA 445523* | 180,5 | Bivalve | 6340 ± 30 | 6805 | 6709 |
| KIA 52762 | 208 | Planktic foraminifer | 7515 ± 45 | 7973 | 7868 |
| KIA 52763 | 217 | Planktic foraminifer | 8055 ± 40 | 8507 | 8404 |
| KIA 52764 | 227 | Planktic foraminifer | 8535 ± 40 | 9167 | 9023 |
| KIA 51162* | 238 | Scaphopod | 8005 ± 35 | 8459 | 8379 |
| KIA 51162* | 260 | Bivalve | 9380 ± 40 | 10213 | 10138 |
| KIA 52141 | 264 | Bivalve | 9250 ± 40 | 10080 | 9918 |

Table 4.1: AMS ¹⁴C radio carbon ages for kastenlot core PS93/025-2, using a marine reservoir correction of 400 years. Bold CALIB median numbers were used for both age models (red ones were excluded in the *Bchron* age model)

4.2.2.2 Organic bulk sediment parameters

Total organic carbon (TOC), total carbon (TC) and total nitrogen (TN) were measured using freeze-dried and homogenized bulk sediment samples in intervals of 1 cm. TOC measurements were performed with a Carbon-Sulfur Analyser (CS-125, Leco) after removing any carbonate by adding hydrochloric acid to a 0.1 g subsample. TC and TN contents were measured on sediment samples of 20 mg sediment with a Carbon-Nitrogen-Sulfur Analyser (Elementar III, Vario). Subsequently, the carbonate content (CaCO₃) was calculated from TOC and TC (CaCO₃=(TC–TOC) x 8.333), assuming that carbonate predominantly occurs in the form of calcite, where 8.333 is the stoichiometric calculation factor. The TOC vs. total nitrogen (C/N) ratio may give some first-order information about the organic-carbon source, with higher/lower values more indicative for a terrigenous/marine origin (for details and limitations of this approach see Stein and Macdonald, 2004).

4.2.2.3 Extraction and analysis of lipid biomarkers

Specific highly branched isoprenoids, so called HBIs, (IP₂₅, HBI diene (HBI II) and HBI z-triene (HBI III)) and the sterols brassicasterol (24-methylcholesta-5,22-dien-3β-ol), dinosterol (4α,23,24-Trimethyl-5α-cholest-22E-en-3β-ol), β-sitosterol (24-ethylcholest-5-en-3β-ol) and campesterol (24-methylcholest-5-en-3β-ol) were extracted and analyzed. 5 g of freeze-dried and homogenized sediment

were extracted in intervals between 1 and 3 cm. For the extraction, dichloromethane/methanol (DCM/MeOH, 2:1 v/v) was added to the sediment samples additionally with the internal standards 7-hexylnonadecane (7-HND, 0.076 µg/sample), 9-octylheptadec-8-ene (9-OHD, 0.1 µg/sample), 5 α -androstan-3 β -ol (androstanol, 10.7 µg/sample) and squalane (3.2 µg/sample) for the quantification of lipid biomarkers in each sample, followed by ultrasonification (15 min) and centrifugation (3 min) three times. Subsequently, we separated the hydrocarbon fraction (5 ml *n*-hexane) from the sterol fraction (9 ml ethylacetate/*n*-hexane) by open silica gel column chromatography. Finally, the sterol fraction was silylated by adding 200 µl of BSTFA (bis-trimethylsilyl-trifluoroacet-amide) at 60°C for 2 hours. Two different gas chromatography-mass spectrometers (GC-MS) with similar basic configuration were used to measure the extracted samples. The hydrocarbon fraction was measured with a gas chromatograph Agilent Technologies 7890B GC system (30m DB-1MS column, 0.25 mm i.d., 0.25 µm film thickness) coupled to a mass spectrometer Agilent 5977A MSD (70 eV constant ionization potential, Scan 50–550 *m/z*, 1 scan/s, ion source temperature 230°C, Performance Turbo Pump) with the temperature program: 60°C (3 min), 150°C (heating rate: 15°C/min), 320°C (heating rate: 10°C/min) and 320°C (15 min, isothermal). The sterols were measured with a GC Agilent 6850 GC coupled to an Agilent 5975C VL MSD (conditions see above) with the temperature sequence: 60°C (2 min), then 150°C (heating rate: 15°C/min), 320°C (heating rate: 3°C/min) and 320°C (20 min isothermal).

Component assignment was based on comparison of GC retention times with those of reference compounds and published mass spectra (sterols: Boon et al., 1979; Volkman, 1986; HBIs: Belt et al., 2007; Brown and Belt, 2016). The concentration of each biomarker was calculated by setting its individual GC–MS ion responses in relation to those of respective internal standards. For the quantification of the sterols (quantified as trimethylsilyl ethers), the molecular ions *m/z* 470 for brassicasterol, *m/z* 472 for campesterol, *m/z* 486 for β -sitosterol, and *m/z* 500 for dinosterol were used in relation to the molecular ion *m/z* 348 of the internal standard androstanol. For the quantification of IP₂₅, HBI II and HBI III, their molecular ions (*m/z* 350 for IP₂₅, *m/z* 348 for HBI II, and *m/z* 346 for HBI III) were compared to the fragment ion *m/z* 266 of the internal standard 7-HND. The different responses of these ions were balanced by an external calibration. For further details we refer to Fahl and Stein (2012), Brown et al. (2014) and Belt (2018).

The calculated Kovats Index for IP₂₅ is 2085, for HBI II 2084 and 2046 for HBI III. All biomarkers of this study were normalized against the amount of sediment and TOC content.

We calculated the PIP₂₅ indices according to the equation by Müller et al. (2011), where *c* is a concentration balance factor (to account for concentration differences between IP₂₅ and phytoplankton biomarkers (P), i.e., brassicasterol, dinosterol or HBI III):

$$(1) \quad \text{PIP}_{25} = \frac{[\text{IP}_{25}]}{([\text{IP}_{25}] + c[\text{P}])} \quad \text{with} \quad c = \frac{\text{mean} [\text{IP}_{25}]}{\text{mean} [\text{P}]}$$

On average, concentrations of brassicasterol are about five times higher, dinosterol about ten times higher and HBI III about two times lower than the IP₂₅ concentrations in Core PS93/025, resulting in balance factors of 0.23, 0.11 and 2.44, respectively. Biomarker concentrations were converted into accumulation rates by using the following equations (e.g. Stein and Macdonald, 2004):

$$(1) \text{ Porosity} = \frac{(\text{GD} - \text{WBD})}{(\text{GD} - 1.026)} * 100$$

$$(2) \text{ TSAR} = \text{LSR} * (\text{WBD} - 1.026 \text{ PO}/100)$$

$$(3) \text{ TOCAR} = \text{TSAR} * \text{TOC}/100$$

$$\text{CaCO}_3\text{AR} = \text{TSAR} * \text{CaCO}_3/100$$

$$\text{BMAR} = \text{TSAR} * \text{BM}$$

LSR = sedimentation rate (cm ky⁻¹)

TSAR = total sediment accumulation rate (g cm⁻² ky⁻¹)

WBD = wet bulk density (g cm⁻³)

TOCAR = total organic carbon accumulation rate (g cm⁻² ky⁻¹)

TOC = total organic carbon (%)

CaCO₃AR = carbonate accumulation rate (g cm⁻² ky⁻¹)

BM = biomarker concentration (μg g⁻¹ Sed)

BMAR = biomarker accumulation rate (μ g cm⁻² ky⁻¹)

PO = porosity (%)

WBD = wet bulk density (g cm⁻³)

4.2.2.4 Statistical analyses

Significant shifts in biomarker records of Core PS93/025 (Fig. 4.4) were identified using the changepoint analysis from the R package ECP with a significance level of 99% (James Matteson; R Core Team, 2018). The variability of average HBI and sterol concentrations of the five intervals defined in the Holocene record of Core PS93/025 is shown in Fig. 4.5. For spectral analysis, IP₂₅, brassicasterol and HBI III time series were resampled at 0.03 kyr resolution prior to spectral analysis. Then spectral analysis was carried out using the multitaper method (MTM) with three 2π tapers (Thomson, 1982) and LOWSPEC noise estimation as implemented in the R package „astrochron“ (Meyers, 2012). Confidence levels were calculated by applying the LOWESS-based (Cleveland, 1979) procedure of Ruckstuhl et al. (2001).

4.3 Results

4.3.1 Organic/inorganic bulk parameters

In the following, data are presented versus age. Single records of the bulk parameters versus depth are available in the supplementary material A.1. The TOC record of Core PS93/025 can be divided into three intervals with low values of 0.5–0.6% between 10.2–7.9 ka, constant values of ~0.6% from 7.9–5.1 ka and increasing values from 5.1 ka towards the top, reaching 0.8–0.9% in the last 1 ka (Fig. 4.4).

High C/N ratios of 7.5–9 occur in the lower part of the core between 10.2–8.8 ka whereas lower values between about 6 and 7.5 are typical for the interval from 8.8 ka onwards (Fig. 4.4). Maximum inorganic carbon (IC) values of 0.8–1.0% (i.e., 7–8.5% CaCO₃) were determined in the lower part between 10.2–7.9 ka. After 7.9 ka, IC values sharply decrease, and values of 0.55–0.65% (i.e., 4.5–5.5% CaCO₃) are typical for the interval between 7.9–5.5 ka. In the upper part of the core between 5.5 ka and the top, IC values vary between 0.35 and 0.65% (i.e., 3–5.5% CaCO₃), with higher values of 0.6–0.65% (i.e., 5–5.5% CaCO₃) most dominant in the interval between 1.3–0.6 ka (Fig. 4.4).

4.3.2 Biomarker

Results of all biomarker records are plotted in $\mu\text{g g}^{-1}$ TOC and as accumulation rates in $\mu\text{g cm}^{-2} \text{ky}^{-1}$ versus age (Fig. 4.4). In addition, each biomarker is plotted in $\mu\text{g g}^{-1}$ Sed and $\mu\text{g g}^{-1}$ TOC versus depth, presented in the supplementary material A.2. Due to the good correlation of campesterol and β -sitosterol, both records were combined into one record of terrigenous biomarkers that is used in the discussion. The sterols (brassicasterol, dinosterol, campesterol and β -sitosterol) of Core PS93/025 vary more or less synchronously over the entire Holocene record, which can be subdivided into three main intervals (Fig. 4.4). High concentrations of the phytoplankton biomarkers brassicasterol (4–6 $\mu\text{g g}^{-1}$ TOC) and dinosterol (~8–10 $\mu\text{g g}^{-1}$ TOC) and the terrigenous biomarkers campesterol and β -sitosterol (both ~13 $\mu\text{g g}^{-1}$ TOC) occur between 10.2–9.3 ka. Relatively stable, but low values of brassicasterol (~2 $\mu\text{g g}^{-1}$ TOC), dinosterol (~4 $\mu\text{g g}^{-1}$ TOC), campesterol and β -sitosterol (~5 $\mu\text{g g}^{-1}$ TOC), are obvious between 9.3–1 ka. During the last 1 ka, all sterols reach maximum values with brassicasterol (up to 8 $\mu\text{g g}^{-1}$ TOC), dinosterol (up to 15.5 $\mu\text{g g}^{-1}$ TOC), campesterol and β -sitosterol (both up to 22.5 $\mu\text{g g}^{-1}$ TOC) (Fig. 4.4).

The IP₂₅ record can also be subdivided into three intervals. Low IP₂₅ values of 0.4 $\mu\text{g g}^{-1}$ TOC characterize the interval between 10.2–7.9 ka, while slightly higher values of ~0.6 $\mu\text{g g}^{-1}$ TOC were found between 7.9–4.8 ka (Fig. 4.4). From 4.8 ka onwards, the IP₂₅ concentrations increase continuously, reaching maximum values of 1.4 $\mu\text{g g}^{-1}$ TOC during the last 1 ka (Fig. 4.4). The HBI III record was divided into five intervals. High HBI III concentrations occur from 10.2 to 9.3 ka (values up to ~0.6 $\mu\text{g g}^{-1}$ TOC), between 7.9 and 5.5 ka (up to 0.4 $\mu\text{g g}^{-1}$ TOC) and during the last 1 ka (up to 0.8 $\mu\text{g g}^{-1}$ TOC), intercalated by intervals of lower concentrations between 9.3 and 7.9 and 5.5 and 1 ka with values below 0.1 $\mu\text{g g}^{-1}$ TOC (Fig. 4.4). Overall, accumulation rates of all biomarkers reflect similar trends during the Holocene.

4.4. Discussion

4.4.1 Proxies used for past sea-ice reconstructions on the eastern North Greenland shelf: some general aspects

In this study past sea-ice reconstructions on the eastern North Greenland shelf were carried out by using the sea-ice proxy IP₂₅ (Belt et al., 2007) in combination with the tri-unsaturated HBI (HBI III, phytoplankton biomarker) and specific sterols (phytoplankton and terrigenous biomarkers). IP₂₅ is produced by diatoms that inhabit the sea ice with highest concentrations during spring algae blooms (Belt et al., 2007; Brown et al., 2014, 2016). Thus, IP₂₅ is a reliable and direct indicator for past seasonal sea-ice presence. Sediment traps studies evidence the release of ice algal organic carbon (OC) containing the IP₂₅ signal, that sinks to the ocean surface during the ice melt (Belt et al., 2008; Fahl and Stein, 2012). Over the past years, IP₂₅ has been successfully used to reconstruct sea-ice variability across the Arctic (for reviews see Stein et al., 2012; Belt and Müller, 2013; Belt, 2018) even in regions with a near-permanent sea-ice cover (Xiao et al., 2015a).

However, this proxy has a few limitations (Belt, 2018). Sea-ice algae are absent in ice-free areas but also absent or only occur in very minor amount in areas characterised by a more closed and thick sea-ice cover that prevents significant algae productivity. Thus, IP₂₅ is not found or only found in very minor amount in the underlying sediments. Additionally, several other factors may hamper the IP₂₅ production and accumulation, for example lower salinities in fjords or near-coastal surface waters due to large river input or meltwater discharge (Xiao et al., 2013; Hörner et al., 2016; Ribeiro et al., 2017), or brine channels within the sea ice, or reduced light availability through an overlying snow cover (Belt and Müller, 2013). Lately, the discussion about degradation of IP₂₅ in terms of ice-algal carbon as foodstock (grazing) within the water column, and oxidation of IP₂₅ within the sea ice, has received greater awareness (for details see Belt, 2018). Another substitutional sea-ice proxy (biosynthesized by Arctic diatoms) and often very well correlated with IP₂₅, might be the HBI II diene (Brown et al., 2014c), with concentrations often somewhat higher than those of the IP₂₅ (for details see Belt, 2018).

IP₂₅ in combination with open-water phytoplankton biomarkers allows a more detailed classification of sea-ice conditions. As open-water phytoplankton biomarkers Müller et al. (2009, 2011) originally used specific sterols (brassicasterol, dinosterol), and proposed a combined phytoplankton-IP₂₅ proxy (PIP₂₅) that allows a more semi-quantitative description of spring sea-ice conditions (for PIP₂₅ calculations see subchapter 4.2.2.3; for general information about methods and interpretation of the approach see Müller et al., 2011; Belt et al., 2015; Smik et al., 2016). According to Müller et al. (2011), sea-ice conditions were classified into ice-free conditions (PIP₂₅ = 0), a low to variable sea-ice cover (PIP₂₅ > 0.1) with low IP₂₅ and high phytoplankton biomarker values, the marginal ice zone (PIP₂₅ > 0.5) with intermediate values and extended sea-ice conditions (PIP₂₅ > 0.75) with high IP₂₅ and low phytoplankton biomarker values. A perennial closed sea-ice cover would result in IP₂₅ and phytoplankton biomarker

concentrations near zero, i.e. PIP_{25} would become indeterminable and thus often artificially set to 1. These extreme values, however, have to be interpreted with caution and the single biomarker concentrations should be considered as well (cf., Stein et al., 2017; Belt, 2018). Furthermore, the degree of accuracy of PIP_{25} may depend on the combination of specific phytoplankton biomarkers (and their pelagic origin), the c balance factor (cf., subchapter 4.2.2.3), the algorithmic relationship between the PIP_{25} and the different sea-ice conditions, as well as the temporal shifts within the downcore records (Belt, 2018).

More recently, the HBI III triene (e and z triene) has been used as a complimentary proxy to IP_{25} . HBI III is probably an indicator for pelagic diatom productivity of the species *Rhizosolenia setigera* in the photic zone of the water column, and is strongly associated in (sub-) polar regions with the Marginal Ice Zone (MIZ) (Collins et al., 2013; Smik et al., 2016; Belt et al., 2017, Belt, 2018). The consideration of ice-associated IP_{25} and HBI II alongside with the pelagic HBI III triene (e and z triene) might help to distinguish between different sea-ice scenarios (see Belt, 2018). Positively correlated IP_{25} and HBI III profiles were assumed to reflect rapidly changing (advancing/retreating) sea-ice margins or offshore polynyas (cf., Belt, 2018) and negatively correlated profiles are attributed to temporal shifts in the winter/summer sea-ice margin (Belt et al., 2015; Berben et al., 2017). Furthermore, different interpretations of the proxy data might be possible when using this approach in different regions. For example, based on data of surface sediments from the Barents Sea and around Svalbard, Smik et al. (2016) concluded that the HBI III triene in combination with IP_{25} ($P_{III}IP_{25}$) is a promising indicator for winter sea-ice extent and/or the MIZ. Findings from eastern North Greenland fjord surface sediment samples seem to support this statement since HBI III concentrations were also found to be most abundant in locations proximal to the ice edge (Ribeiro et al., 2017). In contrast to the Barents Sea area, however, the HBI maximum concentrations correlate with the mid-July MIZ in the Greenland fjord area that is characterized by much heavier sea-ice conditions in general.

To identify terrigenous organic carbon, we have used specific sterols (β -sitosterol and campesterol), C/N ratios and TOC values. For further details of the identification of organic carbon sources see Stein and McDonald (2004); Fahl and Stein (1999, 2012) and Belt (2018).

In summary, multivariate analysis of individual open-water phytoplankton and terrigenous biomarkers in combination with IP_{25} and PIP_{25} records may help to identify different sea-ice scenarios and organic carbon source areas (marine vs. freshwater) (see Fig. 4.6 and suppl. mat. A.1).

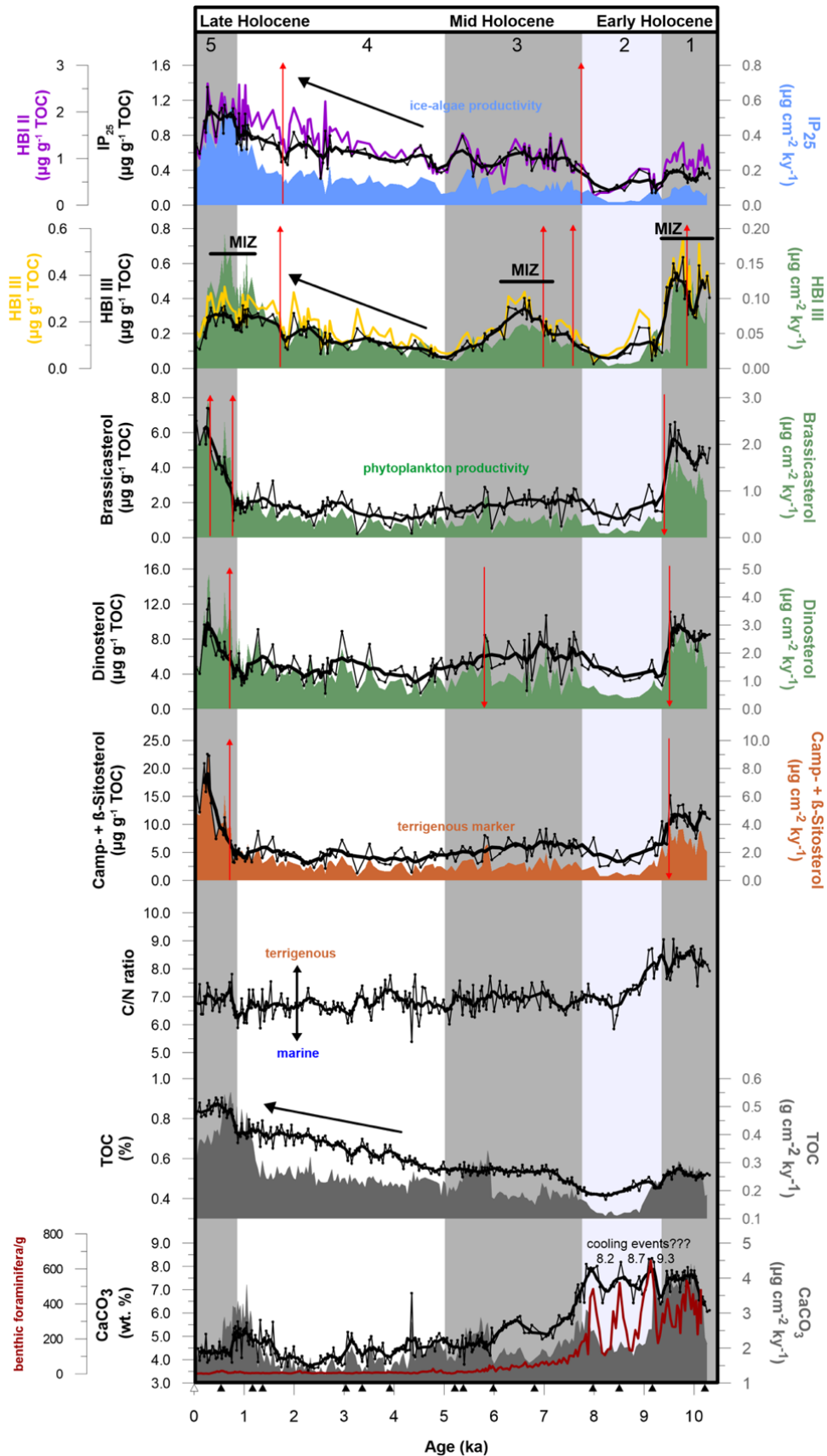


Fig. 4.4: Organic bulk parameters (TOC, CaCO₃ and C/N ratio), planktic foraminiferal counts (red curve, Zehnich et al., 2020), biomarker concentrations (left) and accumulation rates (right, colored shaded curves) of Core PS93/025. Thick black line shows 5-point average trend. Significant shifts within the biomarker records are indicated by red arrows and based on the change-point analyses with a confidence level of 99.5% (HBI III e-triene = yellow, HBI III z-triene = green). Gray bars separate five intervals of climate changes during the Holocene discussed in the text. Black triangles mark corrected ¹⁴C-dated core depths.

4.4.2 Sea-ice variability off eastern North Greenland during the Holocene

Early Holocene (10.2–7.9 ka)

During the late Holocene between 10.2–9.3 ka, low IP_{25} and HBI II fluxes reflect reduced to moderate sea-ice algae productivity, while considerably high phytoplankton biomarker concentrations and fluxes of brassicasterol, dinosterol and HBI III (Fig. 4.4) indicate prolonged open-water conditions with enhanced biological productivity at the outer eastern North Greenland continental shelf. Such a reduced sea-ice situation is also clearly reflected in the related minimum $P_{BIP_{25}}$, $P_{DIP_{25}}$ and $P_{IIIIP_{25}}$ indices of <0.3 (Fig. 4.7) and the scatter plot of IP_{25} indices against the phytoplankton biomarker brassicasterol and HBI III (Fig. 4.6). Considering the generally reduced sea-ice conditions and the distinct HBI III maximum, this may represent a winter MIZ situation (Fig. 4.4, interval 1) as proposed by Belt et al. (2015) for the modern Barents Sea. Strongly reduced sea-ice conditions were also reconstructed for the inner East Greenland shelf (Core PS2641-4) and the eastern Fram Strait (MSM5/5-712-2 and MSM5/5-723-2) during the early Holocene based on relatively high phytoplankton biomarker values, high $CaCO_3$ and lowered IP_{25} and IRD contents (Müller et al., 2012). The eastern Fram Strait sea-ice conditions during the early Holocene most likely correspond to the present-day summer situation (cf., Fig. 4.1c). The low sea-ice coverage and relatively warm surface water conditions due to the intensified inflow of warmer recirculating Atlantic Water from the eastern towards the western Fram Strait (Koç et al., 1993; cf., Carstens et al., 1997; Volkmann, 2000; Pados and Spielhagen, 2014), favored planktic blooms at our core site, as reflected by elevated numbers of planktic and benthic foraminifers and highest (biogenic) $CaCO_3$ content and flux (Fig. 4.4). Warmer sea-surface conditions were also reconstructed for the Nordic Seas and the East Greenland shelf based on foraminifers and diatoms (Bauch et al., 2001; Andersen et al., 2004a, 2004b). The appearance of *Armeria scabra* and the sub-arctic mussel *Mytilus edulis*, both species are well-known for their occurrence in eastern North Greenland, further support warmer summer temperatures than today during the early Holocene between 10–8.5 ka (Hjort and Funder, 1974; Bennike and Weidick, 2001).

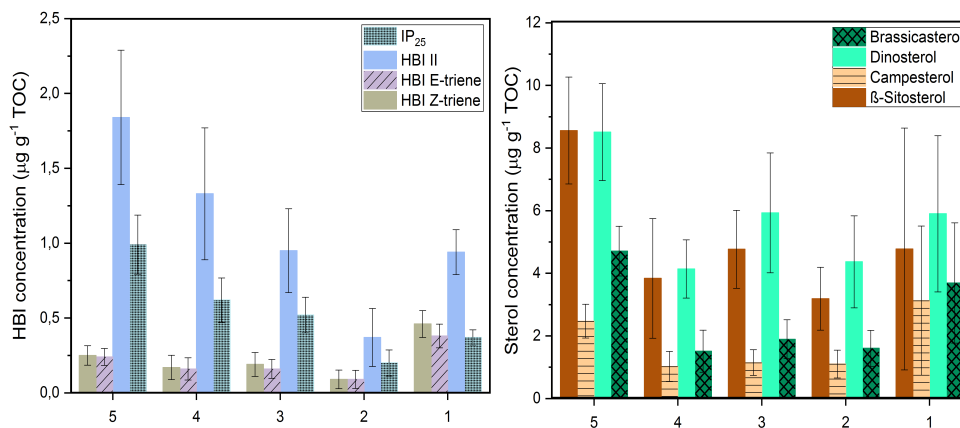


Fig. 4.5: Average of the HBI and sterol concentrations with error bars (± 1 sample SD in each case) for the defined five time intervals of our Holocene record (cf., Fig. 4.4).

During this warmer early Holocene period, elevated fluxes of terrigenous organic matter indicated by high β -sitosterol and campesterol values and high C/N ratios (Fig. 4.4), and the decrease of IRD deposition (Telesiński et al., 2014; Zehnich et al., 2020) may have resulted from melting by local glaciers from eastern North Greenland and related meltwater discharge (cf., Blaschek and Rensen, 2013). This may have provided nutrient-rich freshwater to the eastern North Greenland shelf causing stratification of the surface layer and intensified phytoplankton growth (Waniek et al., 2005). This explanation would also explain the high positive correlation between the phytoplankton (i.e., brassicasterol and dinosterol) and the terrigenous biomarkers (β -sitosterol and campesterol) (suppl. material A.3).

In summary, our data of Core PS93/025 and multiproxy records (e.g., IRD, $\delta^{18}\text{O}$, $\delta^{13}\text{C}$, benthic and planktic foraminifera abundances) from other nearby cores (Telesiński et al., 2014) relate the phase between 10.2 and 9.3 ka to be linked to the Holocene Thermal Maximum (HTM), where increased mean local summer insolation led to summer temperatures 4–5°C warmer than today in northern Greenland (Kaufman et al., 2004; Laskar et al., 2004; Reeh, 2004; Lecavalier et al., 2017).

Around 9.3 ka a prominent change in environmental conditions occurred, as reflected in a significant shift from high to low concentrations and accumulation rates of all biomarkers (Figs. 4.4) suggesting reduced sea-ice and open-water algal productivity. This change may be related to an extended sea-ice over as shown in the elevated PIP₂₅ indices (Fig. 4.7). Superimposed to this change towards an increased sea-ice cover, three distinct maxima and minima in the higher-resolution carbonate concentration and planktic foraminifer are obvious, implying short-term disturbances in sea-surface conditions (Fig. 4.4).

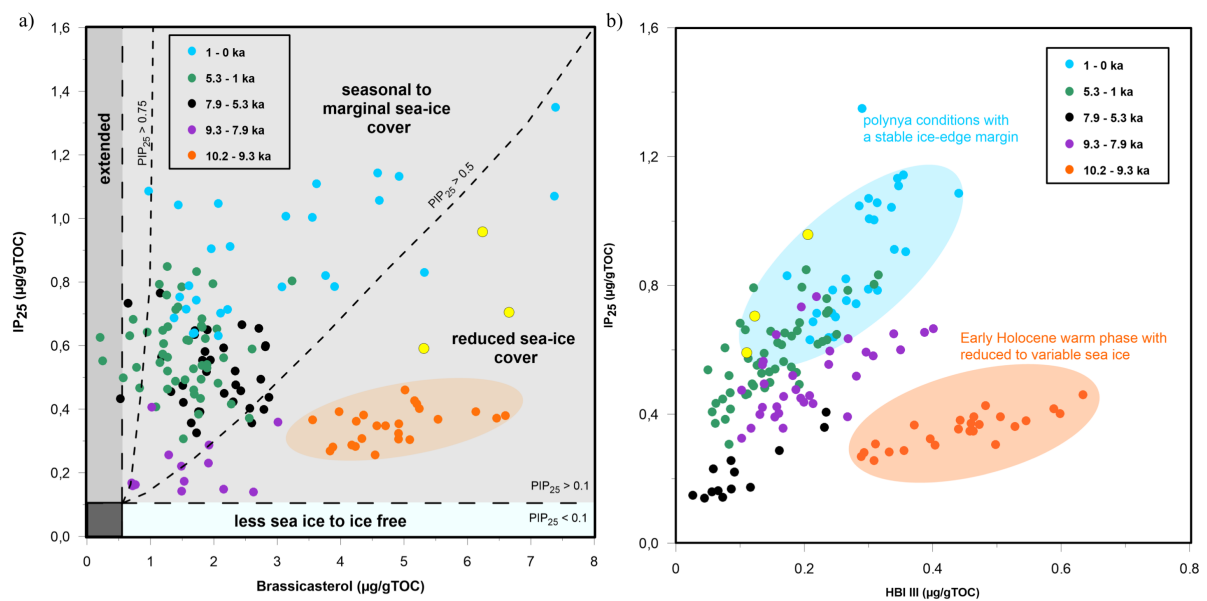


Fig. 4.6: a) Scatter plot ($\mu\text{g g}^{-1}$ TOC) of IP₂₅ versus brassicasterol with different sea-ice scenarios after Müller et al. (2011). b) scatter plot ($\mu\text{g g}^{-1}$ TOC) IP₂₅ versus HBI III of Core PS93/025-2 highlighting the early Holocene warm phase (orange shaded area) and the assumed seasonal formation of the NEW polynya during the last 1 ka (blue shaded area). Data from the five Holocene intervals are indicated by different colors. Yellow dots reflect surface samples.

A reasonable explanation for these disturbances might be short-lived small cooling events, similar to the 8.2 Event (Kobashi et al., 2007; Rasmussen et al., 2007; Thomas et al., 2007), which was probably triggered by freshwater outbursts from the Laurentide Ice Sheet-dammed lakes into the North Atlantic Ocean and had a considerable impact on the thermohaline circulation (Barber et al., 1999; Yu et al., 2010). Thus, the minima in our records (Fig. 4.4) between 7.9–9.3 ka may reflect increased sea-ice conditions and strongly reduced phytoplankton productivity due to abrupt freshwater outbursts.

Mid Holocene (7.9–4.9 ka)

Elevated IP₂₅ and HBI II values, but overall low and stable (with minor fluctuations) phytoplankton biomarker (brassicasterol and dinosterol) and terrigenous biomarker concentrations and accumulation rates revealed during the mid Holocene (Fig. 4.4). Rising PIP₂₅ indices indicate a gradual transition from reduced to seasonal sea-ice conditions along the outer eastern North Greenland continental shelf (Fig. 4.8b). Contemporaneously, decreasing CaCO₃ concentrations and relatively low abundances of foraminifers (Zehnich et al., 2020) occur during the same interval.

In fact, a decreasing warm Atlantic Water advection may have caused a gradual cooling evidenced by lowered SSTs in the Fram Strait (Bauch et al., 2001; Jennings et al., 2002; Müller et al., 2012) and constantly reduced phytoplankton productivity at Core PS93/025. Meanwhile, increased abundances of Arctic diatom taxa point to a strengthened EGC between 6.8 and 5.5 ka (Ran et al., 2006) that would have transported more sea ice (drift ice) from the Arctic along the eastern North and East Greenland shelf southward towards Iceland (Andrews et al., 2009; Cabedo-Sanz et al., 2016). Maximum concentration and flux of HBI III (Fig. 4.4) might indicate the build-up of a stable MIZ in the interval between about 7 and 6 ka. Following Ribeiro et al. (2017) and their study of surface sediments from the eastern North Greenland shelf, this probably represents a (spring) summer MIZ situation (Fig. 4.4, interval 3).

The late Holocene (5–1 ka)

During the late Holocene, the three PIP₂₅ indices do not show any trend, but fluctuate around 0.6 (Fig. 4.7). These values represent typical seasonal to marginal sea-ice conditions. The ice-associated IP₂₅ and HBI II records only display a minor increase between 5 and 1 ka (Fig. 4.4 and 4.5). This is in contrast to several IP₂₅ records from other Arctic regions, including the Yermak Plateau (Müller et al., 2009), north of Iceland (Cabedo-Sanz and Belt, 2016) and Spitsbergen (Müller et al., 2012). Continuously rising P_BIP₂₅ and P_DIP₂₅ in the eastern Fram Strait (Müller et al., 2012) point to extended sea-ice conditions following the Neoglacial Cooling trend (Fig. 4.8). This difference in sea-ice conditions between the eastern and western Fram Strait is also supported by model simulations indicating an increase of sea ice by 30% at 6 ka at the eastern Fram Strait and around Spitsbergen and only a minor increase in sea-ice concentrations at the western Fram Strait (Müller et al., 2011).

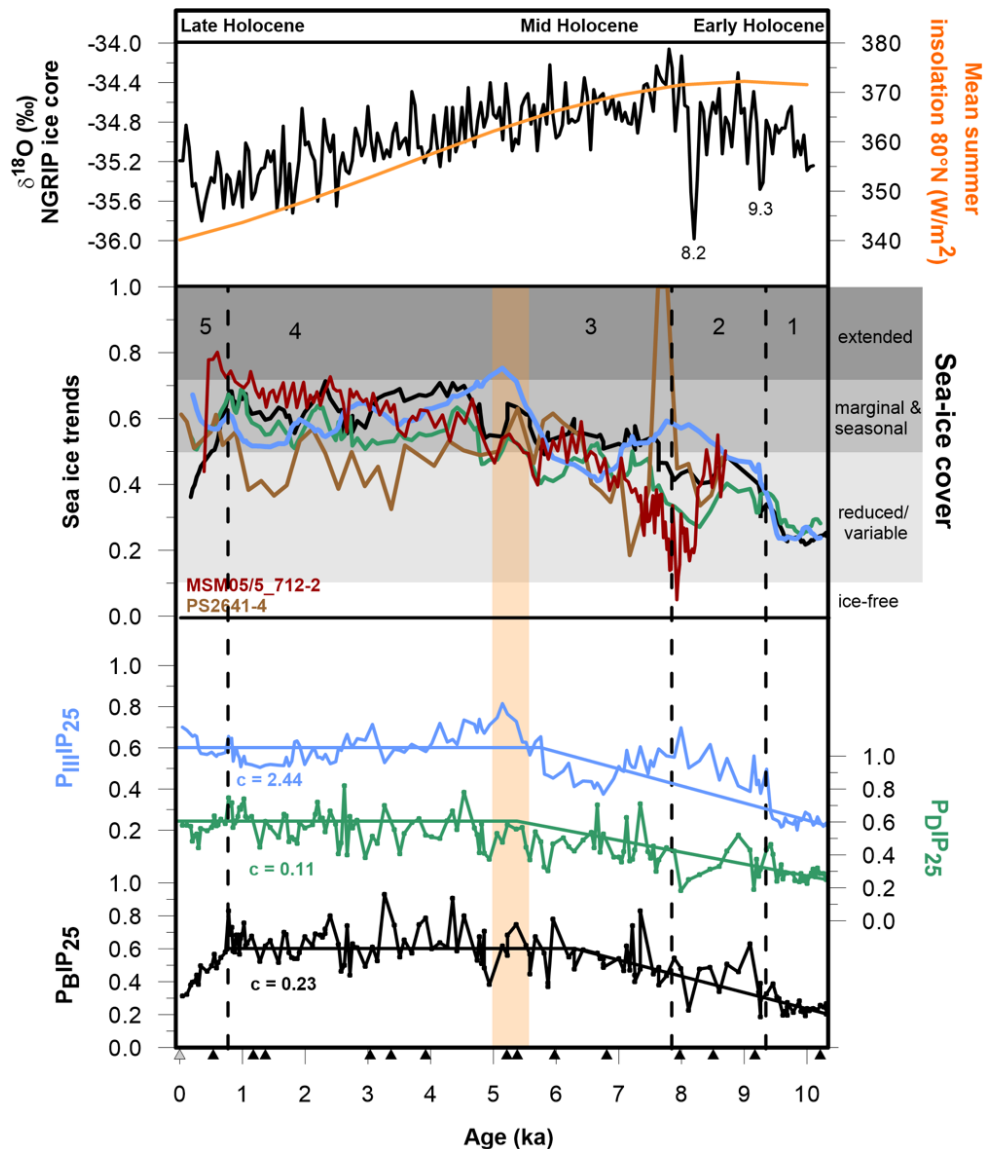


Fig. 4.7: P_BIP₂₅ (black line), P_DIP₂₅ (green line) and P_{III}IP₂₅ (blue line) records of Core PS93/025. Upper part displays Holocene sea-ice trends with additional data (calculated with brassicasterol as phytoplankton) from the eastern Fram Strait (MSM05/5-712-2; Müller et al., 2012), East Greenland continental shelf (PS2641-4; Müller et al., 2012) and this study (PS93/025-2). Black triangles mark corrected ¹⁴C-dated core depths. $\delta^{18}\text{O}$ values of the NGRIP ice core (NGRIP Members, 2004) and summer insolation (orange curve; Laskar et al., 2004) show the Holocene cooling trend.

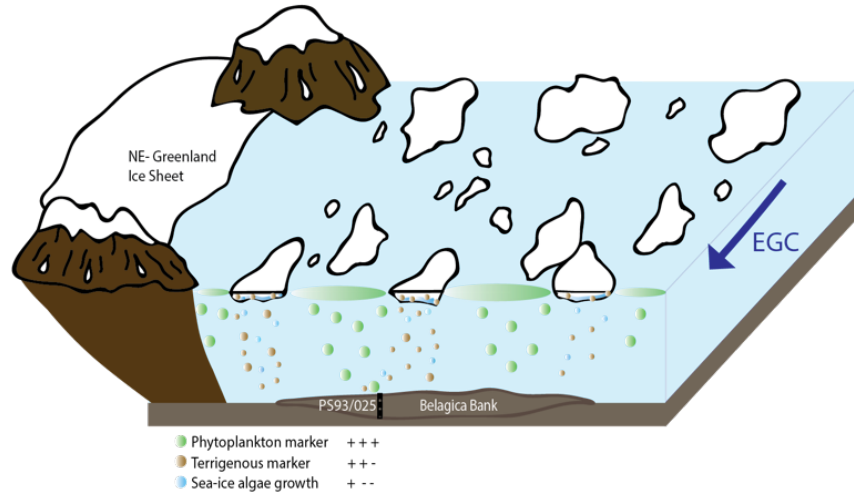
The increase in sea-ice cover in the eastern Fram Strait may be explained by a declining inflow of warm Atlantic Water via the WSC (cf., Werner et al., 2013). The western Fram Strait, on the other hand, is continuously influenced by the cold EGC and drift-ice export from the Arctic Ocean.

Sea-ice distribution and NEW Polynya formation during the last 1 ka

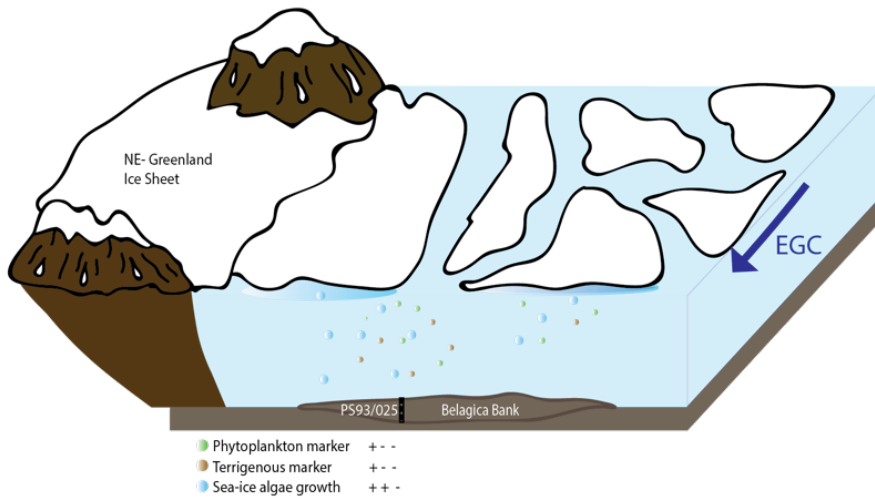
During the last 1 ka, maximum concentrations and accumulation rates of IP₂₅ and open-water phytoplankton and terrigenous biomarkers, as well as TOC were recorded at Core PS93/025 (Figs. 4.4). These significant changes are related to the seasonal formation of the NEW Polynya with suitable environmental conditions for the generation of these biomarkers. Sea ice was pushed towards the open

ocean by strong katabatic winds coming from the Greenland Ice Sheet and causing the NEW Polynya to open up (Fig. 4.8c). Such open-water conditions in its center and sea-ice melting at the margins caused increased fluxes of terrigenous suspension and nutrients to the surface waters within the polynya and favored primary productivity, indicated by highest brassicasterol, dinosterol and HBI III values (Fig. 4.4) in the NEW Polynya. The build-up of a stationary (summer) MIZ is especially reflected in the elevated HBI III concentrations (light blue field in Fig. 4.6b; cf., Belt et al., 2015; Ribeiro et al., 2017). Low carbonate fossil deposition (Zehnich et al., 2020) and low CaCO₃ accumulation during this interval of high productivity (Fig. 4.6) may result from carbonate dissolution, a process that is commonly observed in areas of high productivity and seasonal sea-ice formation (Steinsund and Hald, 1994; Knies et al., 2003). Similar findings were recorded for the recent NEW Polynya situation, where nutrients are constantly supplied by the NEGCC and favor primary productivity (Schneider and Budéus, 1997). Dissolved organic carbon occurs in a larger amount within the NEW Polynya compared to the surrounding surface waters and is most likely released by melting sea ice and ice algae (Skoog et al., 2001). Unfortunately, foraminifer assemblages from Core PS93/025 do not give a hint on carbonate dissolution during the late Holocene (Zehnich et al., 2020). Core top biomarker concentrations in our record match very well with modern observations of sea-ice cover and TOC values in the NEW Polynya (Fig. 4.2a; Birgel and Stein, 2004). Knies et al. (2017) described Arctic polynyas as sea-ice factories and connected the increase in seasonal sea-ice cover with a strengthened outflow of drift ice from the Arctic Ocean along the Greenland shelves during the last 0.5 ka. Ice algae benefit from the light and nutrients availability and are able to grow within the melting sea ice (Belt et al., 2007), which would explain the elevated number of sympagic algae produced IP₂₅ and HBI III (Fig. 4.4 and 4.5, interval 5). Several other studies based on foraminifer and diamicton records from East Greenland and Southeast Greenland and other marine and terrestrial proxies support a strengthening of the EGC during the last 0.6–0.7 ka (Jennings and Weiner, 1996; Nesje et al., 2000; Seppä et al., 2002; Andersson et al., 2003; Moros et al., 2006; Bendle and Rosell-Melé, 2007; Sejrup et al., 2010; Mernild et al., 2011; Cabedo-Sanz and Belt, 2016).

a) Early Holocene - variable to reduced sea ice cover



b) Mid to late Holocene - seasonal and marginal sea-ice cover



c) Last 1 ka - open NEW Polynya

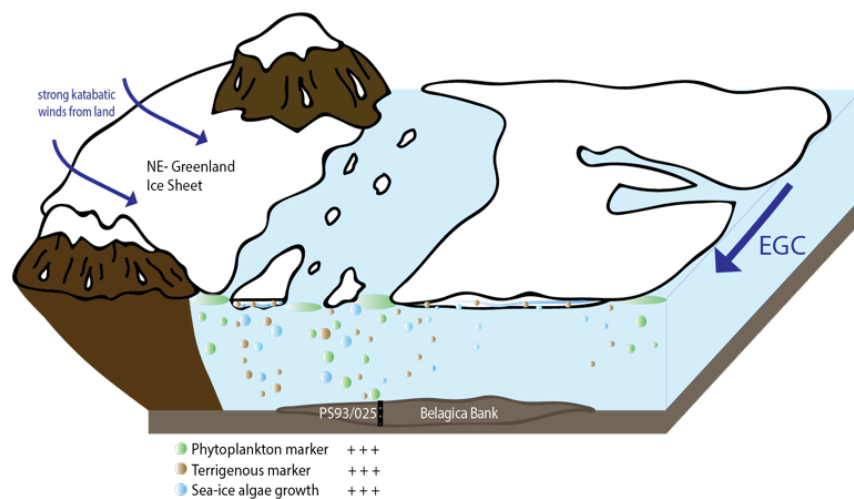


Fig. 4.8: Schematic illustration of sea-ice variability on the eastern North Greenland shelf during the a) early Holocene b) mid to late Holocene and c) the last 1 ka. Variations of each biomarker production is characterized by coloured dots and patches (blue: sea-ice algae, green: phytoplankton and brown: terrigenous marker). Core location PS93/025 is highly influenced by the NEGIS, the EGC, and the NEW Polynya.

4.4.3 Short-term cyclic variability in Holocene environmental conditions

Spectral analysis reveals significant power at frequencies exceeding the 90% confidence level and corresponding to periodicities of 110–130, 170, 220 and 500 years in the proxy records of IP₂₅, HBI III and brassicasterol throughout the Holocene (Fig. 4.9). Such short-term cycles of 110–130 year periods have been observed in the oxygen isotope record of the NGRIP (NGRIP Members 2004) and are likely linked to variations in solar activity (Vonmoos et al., 2006). A spectral power centered around a period of 200 years (brassicasterol) may correspond to the De Vries/Suess cycle of solar activity. North Atlantic variability at this timescale has been previously found in the 512 year $\Delta^{14}\text{C}$ cycle and is connected to variabilities in the North Atlantic Deep Water Formation (NADW) (Stuiver and Braziunas, 1993). While the exact period of spectral peaks may be biased by uncertainties in the age model, the correspondence between our and other oceanic and terrestrial variations in paleoclimate proxies with cyclic signals in solar activity (Stuiver et al., 1995; Ito and Yu, 1999; Chapman and Shackleton, 2000; Hu et al., 2003; Zhao et al., 2010) suggests a possible key role of the amount of total solar irradiance as a driver of oceanic and atmospheric change in the Arctic region. Thus, the atmospheric response to reduced solar irradiance could lead to increasing Arctic sea-ice drift and cooling of both the ocean surface and high northern latitude continents and trigger the negative state of AO/NAO (Xu et al., 2014).

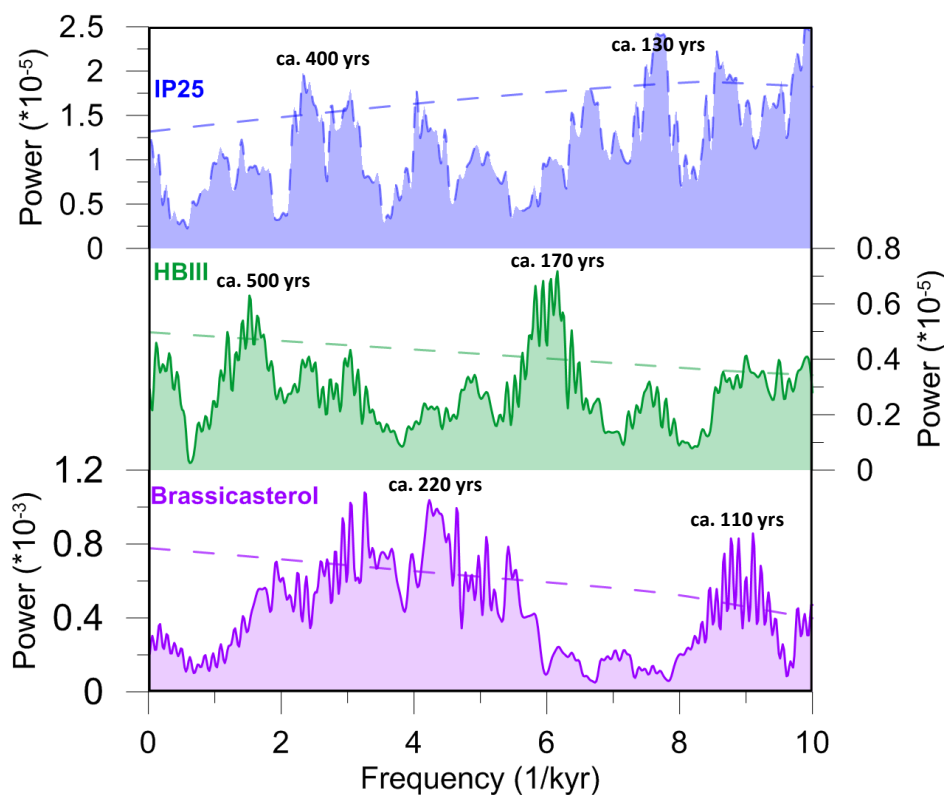


Fig. 4.9: LOWSPEC MTM power spectra of the Holocene (a) IP₂₅ concentration, (b) HBI III concentration and (c) brassicasterol concentration at Site PS93/025. Dashed lines represent the 90% confidence level.

4.5 Conclusions

A new high-resolution biomarker record from Core PS93/025 provides new insights into the Arctic sea-ice evolution and for the first time documents the formation of the NEW Polynya on the eastern North Greenland continental shelf during the late Holocene. The presence of IP₂₅ throughout the Core PS93/025 confirms that there has been seasonal sea ice in the area during the entire record. Our biomarker proxies indicate relatively rapid changes in sea-ice conditions at ~9 ka and ~1 ka, i.e., sea-ice conditions progressed through three major stages over the course of the Holocene. During the early Holocene, we recorded a reduced but variable sea-ice cover. Between about 9.3 and 5.5 ka, sea-ice coverage increased towards seasonal conditions. Based on terrigenous biomarkers and IRD we assume a stronger regional than local sea-ice signal at core site PS93/025, due to the high influence of drift ice transported from the central Arctic Ocean along the eastern North Greenland shelf. During the late Holocene, especially during the last 1 ka, our records reflect the seasonal formation of the NEW Polynya leading to stable sea-ice edge conditions and a fully developed polynya situation. Probably, cyclic changes in the solar activity acted as trigger for the short-term variability in sea-ice cover during Holocene times.

Data availability

Data related to this article are available at doi: <https://doi.org/10.1594/PANGAEA.905516>

Acknowledgements

We gratefully thank Captain Wunderlich and his crew of RV *Polarstern* for the excellent support and cooperation during the entire cruise. Thanks to Walter Luttmner/AWI for technical support during the laboratory work, and Gesine Mollenhauer/AWI for high-precision express analyses of small-scale ¹⁴C samples with the AWI MICADAS system. Thanks to Simon Belt (Biogeochemistry Research Centre, University of Plymouth/UK) for providing the 7-HND standard for IP₂₅ quantification. Many thanks to the three anonymous reviewers for numerous constructive suggestions for improving the manuscript. ASI-AMSR2 sea ice concentration data were provided by <https://seaice.uni-bremen.de/>. This publication is a contribution to the Research Programme PACES II, Topic 3 (The earth system from a polar perspective: Data, modeling and synthesis) of the Alfred Wegener Institute Helmholtz Centre for Polar und Marine Research (AWI). The studied samples and data were provided by AWI (Grant No. AWI-PS93.1_01).

Supplementary Material

- A.1. Results bulk parameters
- A.2. Results biomarker against $\mu\text{g g}^{-1}$ Sed and $\mu\text{g g}^{-1}$ TOC
- A.3. Scatter plots of individual biomarkers

Chapter 5

Holocene interactions between glacier retreat, sea-ice formation and Atlantic Water advection at the inner Northeast Greenland continental shelf

Nicole Syring ^{a,*}, Jeremy M. Lloyd ^b, Ruediger Stein ^{a,c}, Kirsten Fahl ^a, Dave H. Roberts ^b, Louise Callard ^d, Colm O'Cofaigh ^b

^a Alfred Wegener Institute (AWI) Helmholtz Centre for Polar and Marine Research, Bremerhaven, Germany

^b Department of Geography, Durham University, Durham, UK

^c MARUM – Center for Marine Environmental Sciences and Faculty of Geosciences, University of Bremen, Bremen, Germany

^d School of Geography, Politics and Sociology, Newcastle University, Newcastle upon Tyne, UK

State: This paper was submitted to the Journal Paleoclimatology and Paleoclimatology in June 2020, under review.

Abstract

During the past four decades significant decrease in Arctic sea ice and a dramatic ice mass loss of the Greenland Ice Sheet (GIS) has been coincident with global warming and an increase atmospheric CO₂. In Northeast Greenland significant mass loss from the outlet glaciers Nioghalvfjærdsbræ (79NG) and Zachariæ Isstrøm (ZI) and intensive seasonal breakup of the local Norske Øer Ice Barrier (NØIB) have also been observed since 2000. In order to better understand the processes driving these modern changes, studies of paleoclimate records are important and of major societal relevance. A multiproxy study including organic-geochemical and micropaleontological proxies was carried out on a marine sediment core recovered directly in front of 79NG. Data from Core PS100/270 evidenced a strong inflow of warm recirculating Atlantic Water across the Northeast Greenland shelf from the early Holocene between ~10 and 7.9 ka. An overall high in phytoplankton productivity occurred within a stable sea-ice margin regime, accompanied by 79NG retreat most probably triggered by peak solar insolation and changes in the local ocean circulation. Enhanced basal melt of the underside of 79NG at ~ 7.9 ka then led to the total disintegration of the ice shelf. The released freshwater drove surface water stratification and strengthened the formation of the local landfast ice barrier, which is shown by lowered biomarker values and foraminifera abundances towards the end of the early Holocene. Near perennial sea-ice conditions with short summers and 79NG retreat to the inner fjord then prevailed from ~7.9 ka to present.

5.1 Introduction and regional setting

In the past three decades, anthropogenic climate change has had a rapid and dramatic effect on Arctic sea ice and the GIS (Dai et al., 2019; Shepherd et al., 2019). The drastic increase of atmospheric CO₂ concentrations has led to rising ocean and atmosphere temperatures, which (in the Arctic) are compounded by polar amplification and complex positive feedback loops e.g. albedo feedback (Kay et al., 2011; Notz and Marotzke, 2012; Day et al., 2012; Thackeray et al., 2019; Dai et al., 2019). GIS surface-melt and its related accelerated mass loss coincided with a period of rapidly shrinking seasonal sea-ice extent in the Arctic Ocean and surrounding marginal seas during the late 20th/early 21st century (Abdalati and Steffen, 2001; Mote, 2007; Tedesco, 2007; Stroeve et al., 2007; Comiso et al., 2008; Parkinson and Cavalieri, 2008). The main drivers of GIS mass change and observed Arctic summer sea-ice loss are increased atmospheric temperatures and oceanic heat flux (van den Broeke, 2009; Sasgen et al., 2012; Enderlin et al., 2014; Notz and Stroeve, 2016). Changes in the dynamics of atmospheric temperatures and oceanic heat flux might lead to surface and bottom melt of ice sheets, the disintegration and speed up of marine-terminating outlet glaciers and ice streams, as well as thinning of multiyear sea ice and decreasing formation of first-year ice on the Siberian shelves (Maslanik et al., 2007; Holland et al., 2008; Thomas et al., 2009; Nick et al., 2009; Rignot et al., 2012; Krumpfen et al., 2019). Both are key components of the climate system, while the strong negative shift in mass balance of GIS may cause global a sea-level rise of up to 0.09 to 0.88 m by the year 2100, causing irreversible damage to the environment and enormous economic impacts on our society (Meredith et al., 2019; Stern, 2007; Nordhaus, 2019).

Recent satellite observations show that GIS mass loss and the Arctic sea-ice loss have doubled since the beginning of this century (Kjeldsen et al., 2015). The Northeast Greenland Ice Stream (NEGIS) is one of the largest (700 km long) ice streams of GIS (Fig. 5.1A, B) and interactions between the marine terminating outlet glaciers of NEGIS, local sea-ice formation, drift ice and regional ocean dynamics influence and control environmental conditions on the Northeast Greenland (NEG) continental shelf (Fig. 5.1C).

These parameters strongly depend on the incoming radiation and atmospheric and ocean circulation and their dynamics affect climate on a regional and global scale by regulating heat and mass exchange between the ocean and atmosphere, surface albedo, primary production, deep-water formation and sea-level rise (Fahnenstock et al., 1993; Arndt et al., 2015). NEGIS currently drains approximately 12% (320 000 km²) of the GIS via three main outlet glaciers: Nioghalvfjærdsbræ (79NG), Zachariæ Isstrøm (ZI) and Storstrømmen with flow speeds up to >1 km per year (Fig. 5.1C; Rignot and Mouginot, 2012; Khan et al., 2014; Larsen et al., 2018). The drainage basins of 79NG and ZI hold approximately 1.1 m of sea-level equivalent (Mouginot et al., 2015).

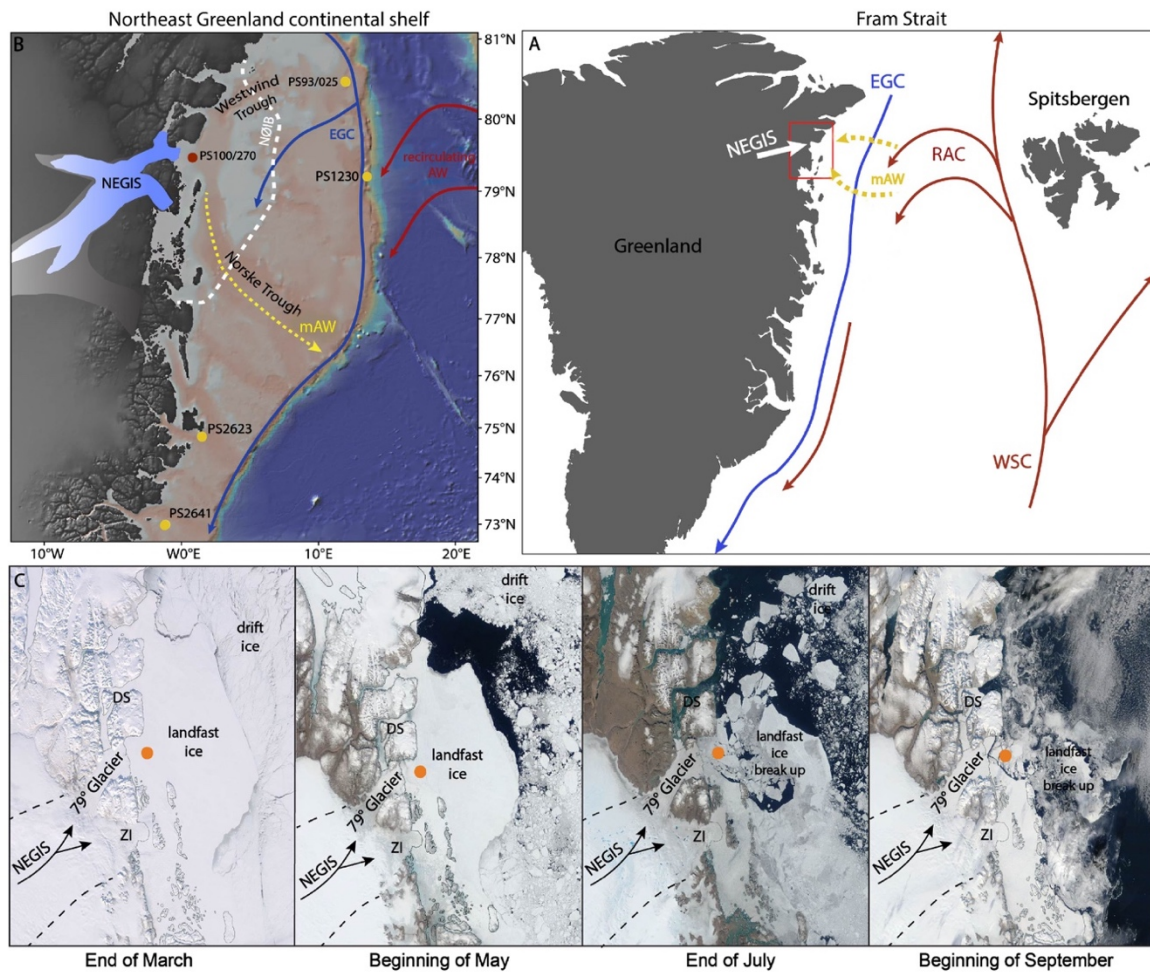


Figure 5.1: A) Overview map of the Fram Strait, showing the main ocean currents: warm West Spitsbergen Current = WSC (red arrows), Return Atlantic Current (RAC), and the cold East Greenland Current = EGC, modified recirculating Atlantic Water = mAW (yellow, dashed arrows) (map created with ODV, Schlitzer et al., 2018). Red rectangle marks the study area, including the North East Greenland Ice Stream = NEGIS (white arrow) and its marine terminating outlet glaciers 79°N Glacier (79NG), Zachariæ Isstrøm (ZI). B) Schematic map with characteristic features of the NEG continental shelf: EGC, NEGIS, Norske and Westwind troughs, Norske Øer Ice Barrier = NØIB, location of Core PS100/270 (this study, orange circle) and locations of other cores mentioned in the text (yellow dots) (map created with GeoMapApp, Ryan et al., 2009). C) Modern seasonal sea-ice conditions with a closed sea-ice cover in March, the seasonal formation of the Northeast Water Polynya = NEW Polynya in May and lowest sea-ice extent in September (satellite images, <https://worldview.earthdata.nasa.gov>, 2019).

The study area is located to the east of the floating ice shelves of 79NG and ZI, which front NEGIS (Fig. 5.1B). The total length of the floating ice tongue of 79NG is ~80 km and 21 km in width, with contemporary basal melt rates of $10.4 \pm 3.1 \text{ m yr}^{-1}$ (Joughin et al., 2001; Reeh et al., 2001; Schaffer et al., 2020). Similar basal conditions occur at the ZI, although this glacier has experienced collapse and rapid retreat since 2002 (Rignot and Kanagaratnam, 2006; Khan et al., 2014; Mouginit et al., 2015). Until recently the northeast sector of the GIS was considered to be relatively stable compared to other regions of Greenland, however, this region is now seen to be more and more threatened by anthropogenic climate changes (Helm et al., 2014; Khan et al., 2014). In particular ZI has undergone significant thinning and glacier retreat along with acceleration (velocity has tripled since 2002) with the consequence of losing approximately 95% of its residual ice shelf (Mouginit et al., 2015).

Concurrently, 79NG lost ~30% of its floating ice tongue and suffers from grounding-line retreat (2 km inland) between 1998 and 2014 (Mouginot et al., 2015; Mayer et al., 2018). Ice-flow models for example by Choi et al. (2017) indicate that 79NG is less vulnerable than ZI due to its upward-sloping bed close to the present ground line and a series of pinning points close to the calving front (Choi et al., 2017). Satellite-derived data suggest that ZI is actually at its tipping point and 79NG very close to it (Mouginot et al., 2015, 2019; Krieger et al., 2020).

Large supplies of freshwater originate from bottom melting of 79NG, compromising a freshwater volume ranging between $11 \text{ km}^3 \text{ a}^{-1}$ (0.4mSv) and $30 \text{ km}^3 \text{ a}^{-1}$ (1.0 mSv), accounting for 4% and 13% of the recent freshwater loss from the GIS (Anhaus et al., 2019). Recent observations show a rapid, active melting at 79NG grounding zone, resulting in a mass loss accompanied by a thinning of the ice margin, reduced ice-shelf strength and, hence, a reduced buttressing effect (Rignot et al., 1997; Seroussi et al., 2011).

The East Greenland Current (EGC) carries Polar Water (PW, salinities less than 34.5‰, temperatures below 0°C) and drift ice from the interior of the Arctic Ocean southward along the NEG continental shelf, where it circulates anticlockwise through the Norske and Westwind Trough around the Belgica Bank (Fig. 5.1A, B; Bourke and Garrett, 1987; Budéus and Schneider, 1995; Johnson and Niebauer, 1995; Topp and Johnson, 1997). Warmer Atlantic Water (AW) crosses the inner shelf from the east via the narrow and deep channels in the Norske and Westwind Troughs, which converge at a relatively shallow sill at their western end near the margin of the NEGIS ice shelf (Fig. 5.1B; Reeh et al., 2001; Mayer et al., 2000; Straneo et al., 2012, Schaffer et al., 2020).

The Norske Øer Ice Barrier (NØIB), an area of a semi-permanent fast-ice between $78\text{--}80^\circ\text{N}$, varies annually in size and thickness. This ice barrier stretches 75–150 km from the coast towards the middle of the shelf and is bordered by drift ice floating southward via the EGC (Fig. 5.1C). The Northeast Water (NEW) Polynya, another important feature of the NEG continental shelf is located at the northern tip of NØIB (Fig. 5.1C; Budéus and Schneider, 1995). Two ice barriers support the seasonal formation of the NEW Polynya, the Ob Ice Barrier by pushing drift ice eastwards while NØIB blocks the northward flowing sea ice which is entrained in the NEG Coastal Current (Schneider and Budéus, 1995). This reduces outlet glaciers calving into the EGC due to its buttressing effect (Fig. 5.1C; Schneider and Budéus, 1994, 1995, 1997; Reeh et al., 2001; Dupont and Alley, 2005). Recent observations show that calving does not occur when the NØIB forms in front of the glaciers. When this occurs, the glacier itself advances slowly against the sea ice or pushes it ahead, but ice-margin conditions basically do not change. Past studies indicate that since August 1997 the NØIB fast ice now regularly breaks up during late summer (every summer between 2002 and 2005), resulting in a significant and increased iceberg release from the floating ice tongues of 79NG and ZI, a rare event that previously probably took place only every ~50 years (Higgins, 1989, 1991; Reeh et al., 2001; Hughes et al., 2011). Perennial sea-ice conditions of NØIB with 1 to 2 occasional break ups between 1982 to 2000 have changed from being a rare event to an annually occurring episodes and a predominately first

year fast sea-ice matrix after 2000 (Sneed et al., 2016). Reduced fast ice thickness, the presence of meltwater on the ice barrier and additionally melting due to warm AW pulses from below weakens the NØIB. Consequently, recent changes in NØIB stability might affect the dynamic of local currents, the NEW Polynya and lead to increased flux of AW into the glacier cavity below 79NG (Hughes et al., 2011; Wilson and Straneo, 2015).

5.1.1 Aim of this study

Recent studies have suggested that in Northeast Greenland the GIS advanced to the edge of the continental shelf during the Last Glacial Maximum (LGM) and retreated to the present coast by the beginning of the Holocene (11.5–9.0 ka; Evans et al., 2009; Winkelmann et al., 2010; Arndt et al., 2015, 2017; Larsen et al., 2018). Furthermore, there is evidence that 79NG and the ice shelf retreated up to 80 km inland during the early Holocene Thermal Maximum 10 to 8.0 ka (Bennike and Weidick, 2001) when high summer insolation increased atmospheric temperatures up to 4–5°C warmer than today and reduced sea-ice concentration on the outer NEG continental shelf (Kaufmann et al., 2004; Laskar et al., 2004; Reeh, 2004; Syring et al., 2020). However, the interaction between the ice-sheet and its shelf dynamics and sea-ice formation on the NEG shallow marine shelf system during the Holocene remains very poorly understood.

This study investigated past Holocene marine climate and sea-ice records from a gravity core collected from the sea floor adjacent to the present 79NG shelf (Core PS100/270, Fig. 5.1A). This core records a history of proximal/distal glaciomarine and sub-ice shelf conditions as 79NG grounding line and ice shelf retreated passed this site during the LGM to Holocene recession. Critically, it also contains a record of sea-ice conditions throughout the Holocene. In order to understand regional ice/ocean/climate feedbacks this record is compared with similar sedimentary records from the East Greenland continental shelf between 70° and 75°N (Stein et al., 1993; Nam et al., 1995; Evans et al., 2002; Stein, 2008). This detailed study presents a multiproxy analysis based on specific biomarkers, organic bulk parameters and benthic foraminifera data as summarized in Table 5.1. Based on these different proxies we aim to provide key insights into past sea-ice formation, primary production of open-water phytoplankton, terrigenous input by vascular land plants, but also the influence of AW entering the inner NEG shelf, the timing of 79NG marine terminating outlet glacier retreat and ice-shelf disintegration during the Holocene. Furthermore, these data will be related to sea-ice settings from a nearby core PS93/025 from the outer NEG and East Greenland records e.g. PS2623 and PS2641 from the inner continental shelf (Stein, 2008; Kolling et al., 2017; Syring et al., 2020).

5.2 Material and Methods

5.2.1 Material

Core PS100/270 was recovered aboard the RV Polarstern cruise PS100 in 2016 close to the floating ice tongue of 79NG on the inner NEG continental shelf (79°29.83'N, 18°8.40'W; 424 m water depth, Fig. 5.1B, Kanzow, 2016). This core was selected and studied in detail to reconstruct past sea-ice formation, terrigenous input, primary productivity and the influence of warm AW on the shelf, using biomarker, bulk parameter and microfossil proxy data. The total core length of Core PS100/270 is 9.51 m. Once retrieved the core was split, photographed and described on board, then wrapped in film and stored in plastic tubes in a cold store at 4°C. A total of 162 sub-samples were subsequently collected and stored at -20°C to prevent biomarker degradation prior to lipid extraction. The first 80 cm of the Core PS100/270 were sampled every 2 cm and afterwards every ~8 cm. These samples were freeze dried and ground.

5.2.2 Methods

Physical properties and lithostratigraphy

Once split the cores were immediately described and information on grain size, sedimentary structures, sediment colour, sorting, bed contacts, clast abundance and microfossil content was recorded. Additional information on sedimentary structures was provided post-cruise from x-radiographs of the split core sections produced from a GEOTEK XCT scanner. Based on these datasets a lithostratigraphic log (including main lithofacies units) was produced (Fig. 5.3). Magnetic susceptibility and wet bulk density were measured on split 1 m sections of the core using a GEOTEK Multi-Sensor Core Logger (MSCL).

Total organic carbon and carbonate

Concentrations for total organic carbon (TOC) were determined with a Carbon-Sulfur Analyser (CS-125, Leco) after removing any carbonate by adding hydrochloric acid to a 0.1 g subsample. 20 mg of the sediment was used for total carbon (TC) and total nitrogen (TN) measurements, which were performed with a Carbon-Nitrogen-Sulfur Analyser (Elementar III, Vario). Based on these bulk parameters TOC and TC, the carbonate (CaCO₃) content was calculated by $\text{CaCO}_3 = (\text{TC} - \text{TOC}) \times 8.333$ (8.333 as stoichiometric factor), assuming that calcite is the predominant carbonate phase.

Lipid biomarker extraction and analysis

Specific highly branched isoprenoids (HBIs), including IP₂₅, HBI II and HBI III (E- and Z-isomers) and certain type sterols brassicasterol (24-methylcholesta-5,22-dien-3 β -ol) and dinosterol (4 α ,23,24-Trimethyl-5 α -cholest-22E-en-3 β -ol), as well as β -sitosterol (24-ethylcholest-5-en-3 β -ol) and campesterol (24-methylcholest-5-en-3 β -ol) were extracted to facilitate climate reconstructions. Internal standards 7-hexylnonadecane (7-HND, 0.076 μ g/sample), 9-octylheptadec-8-ene (9-OHD, 0.1 μ g/sample), 5 α -androstan-3 β -ol (androstanol, 10.7 μ g/sample) and squalane (3.2 μ g/sample) for the quantification of lipid biomarkers in each sample were added to 5 g of freeze-dried and homogenized sediment material. For the extraction, dichloromethane/methanol (DCM/MeOH, 2:1 v/v) was added to the sediment samples, followed by ultrasonification (15 min) and centrifugation (3 min) three times. Subsequently, we separated the hydrocarbon fraction (5 ml *n*-hexane) from the sterol fraction (9 ml ethylacetate/*n*-hexane) by open silica gel column chromatography. Finally, the sterol fraction was silylated by adding 200 μ l of BSTFA (bis-trimethylsilyl-trifluoroacet-amide) at 60°C for 2 hours. Two different gas chromatography-mass spectrometers (GC-MS) with similar basic configuration were used to measure the extracted samples. The hydrocarbon fraction was measured with a gas chromatograph Agilent Technologies 7890B GC system (30m DB-1MS column, 0.25 mm i.d., 0.25 μ m film thickness) coupled to a mass spectrometer Agilent 5977A MSD (70 eV constant ionization potential, Scan 50–550 *m/z*, 1 scan/s, ion source temperature 230°C, Performance Turbo Pump) with the temperature program: 60°C (3 min), 150°C (heating rate: 15°C/min), 320°C (heating rate: 10°C/min) and 320°C (15 min, isothermal). The sterols were measured with a GC Agilent 6850 GC coupled to an Agilent 5975C VL MSD (conditions see above) with the temperature sequence: 60°C (2 min), then 150°C (heating rate: 15°C/min), 320°C (heating rate: 3°C/min) and 320°C (20 min isothermal).

Component assignment was based on comparison of GC retention times with those of reference compounds and published mass spectra (sterols: Boon et al., 1979; Volkman, 1986; HBIs: Belt et al., 2007; Brown and Belt, 2016). The concentration of each biomarker was calculated by setting its individual GC-MS ion responses in relation to those of respective internal standards. For the quantification of the sterols (quantified as trimethylsilyl ethers), the molecular ions *m/z* 470 for brassicasterol, *m/z* 472 for campesterol, *m/z* 486 for β -sitosterol, and *m/z* 500 for dinosterol were used in relation to the molecular ion *m/z* 348 of the internal standard androstanol. For the quantification of IP₂₅, HBI II and HBI III, their molecular ions (*m/z* 350 for IP₂₅, *m/z* 348 for HBI II, and *m/z* 346 for HBI III) were compared to the fragment ion *m/z* 266 of the internal standard 7-HND. The different responses of these ions were balanced by an external calibration. For further details we refer to Fahl and Stein (2012), Brown et al. (2014) and Belt (2018).

The calculated Kovats Index for IP₂₅ is 2085, for HBI II 2084 and 2046 for HBI III. All biomarkers of this study were normalized against the amount of sediment and TOC content. In order to distinguish between different sea-ice settings IP₂₅ was combined with open-water phytoplankton biomarkers (see

Table 5.1), resulting in the so-called “PIP₂₅ index” (Müller et al., 2011; Smik et al., 2016). We calculated the PIP₂₅ indices according to the equation by Müller et al. (2011), where c is a concentration balance factor (to account for concentration differences between IP₂₅ and phytoplankton biomarkers (P), i.e., brassicasterol, dinosterol or HBI III (Z-isomere):

$$(1) \text{ PIP}_{25} = \frac{[\text{IP}_{25}]}{([\text{IP}_{25}] + c [\text{P}])} \quad \text{with } c = \frac{\text{mean} [\text{IP}_{25}]}{\text{mean} [\text{P}]}$$

The HBI II and HBI III (E-isomere), also proposed as proxies for sea-ice and productivity reconstructions (see Belt 2018; Belt et al., 2019), were determined but not presented and discussed in this paper. However, these data are available online under doi:

Biomarker concentrations were converted into accumulation rates by using the following equations (e.g. Stein and Macdonald, 2004):

$$(1) \text{ TSAR} = \text{LSR} * (\text{WBD} - 1.026 \text{ PO}/100)$$

$$(2) \text{ TOCAR} = \text{TSAR} * \text{TOC}/100$$

$$\text{CaCO}_3\text{AR} = \text{TSAR} * \text{CaCO}_3/100$$

$$\text{BMAR} = \text{TSAR} * \text{BM}$$

LSR = sedimentation rate (cm ky⁻¹)

WBD = wet bulk density (g cm⁻³)

TOC = total organic carbon (%)

BM = biomarker concentration (μg g⁻¹ Sed)

PO = porosity (%)

TSAR = total sediment accumulation rate (g cm⁻² ky⁻¹)

TOCAR = total organic carbon accumulation rate (g cm⁻² ky⁻¹)

CaCO₃AR = carbonate accumulation rate (g cm⁻² ky⁻¹)

BMAR = biomarker accumulation rate (μg cm⁻² ky⁻¹)

Foraminiferal analysis

A total of 31 sub-samples were collected for foraminiferal analysis, sampled at approximately 10 cm intervals for the first 100 cm, then every 32 cm down to a core depth of 450 cm, then every 64 cm to the base of the core. Sample volume varied between 0.5 and 5 ml (cm³) depending on average foraminiferal concentration (estimated based on initial scanning of samples). The variation in sample size was designed to allow approximately 300 to 500 specimens to be counted from all samples. Once extracted samples were soaked in deionized water for several hours to help disaggregate the sediment. Samples were then washed through a 500 μm and 63 μm mesh sieve to concentrate the foraminifera. The material collected on the 63 μm mesh sieve was retained for foraminiferal analysis. Foraminifera were identified and counted from the wet residue under a binocular microscope straight away. Counting the foraminifera before drying reduced damage to agglutinated specimens and also smaller fragile calcareous species.

| Proxy | Source | Interpretation/Comments | References |
|--|--|--|--|
| IP₂₅ & HBI II | IP ₂₅ : sea-ice associated pennate diatom (<i>Pleurosigma</i> and <i>Haslea spp.</i>) HBI II: certain sympagic diatoms (e.g. <i>Berkeleya rutilans</i>) | source-specific, sensitive & stable proxy seasonal Arctic spring sea-ice cover (late Miocene to Holocene) combination with open-water phytoplankton marker allows to distinguish between sea-ice conditions (e.g. seasonal vs. perennial) → PIP ₂₅ index | Belt et al. (2007, 2015, 2016) Brown et al., 2014 Müller et al. (2009, 2011, 2012) Fahl and Stein (2012) Stein et al. (2016) Köseoğlu et al. (2018a,b) Reviews by: Stein et al. (2012) Belt and Müller (2013) Belt (2018) |
| HBI III | pelagic diatoms (<i>Rhizosolenia setigera</i>) often abundant in spring MIZ phytoplankton bloom | pelagic productivity may reflect Marginal Ice Zone (MIZ) conditions | Smik et al. (2016) Belt et al. (2017) Stein et al. (2017) Xiao et al. (2017) |
| brassicasterol | biosynthesized by a broad marine/fluvial algae group | open-water phytoplankton productivity proxy is limited in regions influenced by strong riverine input for example the Siberian shelves (Kara and Laptev Sea) | Yunker et al. (1995) Volkman et al. (2008) Jaffe et al. (1995) Fahl et al. (2003) Belt et al. (2013) |
| dinosterol | predominantly by Dinoflagellates detected in minor amounts in sea-ice & diatom cultures (<i>Navicula spp.</i>) | open-water phytoplankton productivity | Review by: Volkman, 1986 Volkman et al. (1993) |
| campesterol & β-sitosterol | main producer are vascular land plants minor constituted by diatoms | terrigenous input | Rontani et al. (2014) Fahl and Stein (2007) |
| accumulation rate | | accumulation rate provides information about absolute changes in sediment fluxes/input | e.g. Stein and MacDonald (2004) |
| foraminifera | biological productivity | planktic foraminifera: surface water productivity, temperature benthic foraminifera: water-mass characteristics (e.g. Atlantic Water inflow) | e.g. Hald and Korsun (1997); Jennings et al. (2011); Perner et al. (2015) |

Table 5.1: Overview of investigated biomarker and micropaleontological proxies origin and interpretations.

Samples were counted immediately to prevent dissolution of smaller fragile calcareous specimens.

Once counted samples were air dried to preserve the material for further analysis.

Accumulation rates of foraminifera (FAR as individuals cm⁻² ky⁻¹) were calculated following Ehrmann and Thiede (1985):

$$\text{FAR} = \text{TSAR} * \text{FN},$$

where TSAR is the total sediment accumulation rate (g cm⁻² ky⁻¹) and FN the foraminifera number (individuals per gram sediment).

5.3 Results

5.3.1 Age model of Core PS100/270 and sedimentation rates

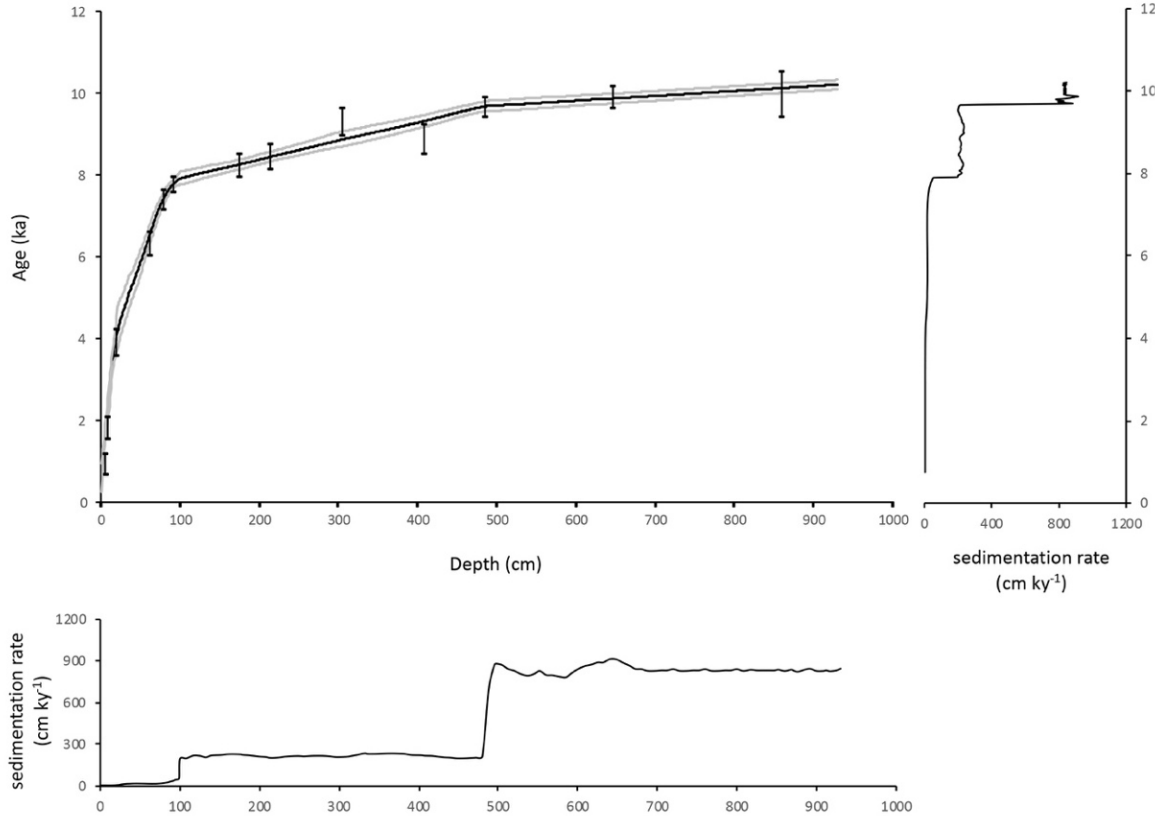


Figure 5.2: Age versus depth profile for Core PS100/270 including calibrated radiocarbon dates (Table 5.2) used for age model reconstructions (left) and sedimentations rates against age (right) and depth (below).

The core chronology is based on 13 accelerator mass spectrometry (AMS) ^{14}C ages (Fig. 5.2, Table 5.2) measured on mixed benthic foraminifera and a prominent articulated bivalve found at 480–484 cm. In addition, 5 ^{14}C AMS ages were also measured from planktic foraminifera (Table 5.2). Although the planktic foraminifera AMS dates were not used in generating the age model, there is a high degree of correlation between the planktic and mixed benthic foraminiferal ages (Table 5.2). This indicates very little difference in age of surface and deep waters on the continental shelf of NEG. AMS ^{14}C dating was carried out at the Alfred Wegener Institute Bremerhaven using the Mini Carbon Dating System (MICADAS) and through the UK NERC AMS radiocarbon facility. Radiocarbon ages were converted to calibrated calendar years before present (cal. Years BP) using the calibration software CALIB 7.1 (Stuiver et al., 2019) and the Marine13 curve (Reimer et al., 2013), and no additional local reservoir age correction was applied ($\Delta R=0$). The Bayesian accumulation age-depth modelling programme, *Bacon 2.2* (Blaauw and Christen, 2011) was used to create a suitable age model for Core PS100/270

(Fig. 5.2). Calculated sedimentation rates vary significantly through the core. The bottom section between 930 to 470 cm shows high sedimentation rates of up to 900 cm ky^{-1} , followed by an abrupt decrease to relatively stable values of $\sim 200 \text{ cm ky}^{-1}$ until 80 cm. There is then a further decrease to relatively low sedimentation rates from 80 cm to the surface of $<50 \text{ cm ky}^{-1}$ (Fig. 5.2).

| Lab-ID | Depth (cm) | Material | AMS ^{14}C | Error \pm | CALIB median | CALIB min. | CALIB max. |
|---------------|------------|----------------------|---------------------|-------------|--------------|------------|------------|
| AWI 4345.1.1 | 3–4 | mixed benth. foram. | 1.483 | 59 | 1129 | 883 | 1297 |
| AWI 4346.1.1 | 6–7 | mixed benth. foram. | 2.339 | 62 | 1700 | 1558 | 1890 |
| AWI 4347.1.1 | 17–18 | mixed benth. foram. | 4.051 | 67 | 3744 | 3420 | 3989 |
| AWI 4348.1.1 | 59–60 | mixed benth. foram. | 6.028 | 75 | 6360 | 6149 | 6614 |
| AWI 4349.1.1 | 77–78 | mixed benth. foram. | 7.020 | 79 | 7332 | 7190 | 7488 |
| UCIAMS-211080 | 88–92 | mixed benth. foram. | 7.440 | 40 | 7691 | 7583 | 7808 |
| AWI 4350.1.1 | 170–175 | mixed benth. foram. | 7.928 | 83 | 8234 | 8117 | 8352 |
| AWI 4351.1.1 | 210–215 | mixed benth. foram. | 8.118 | 85 | 8424 | 8310 | 8547 |
| AWI 4352.1.1 | 300–304 | mixed benth. foram. | 8.849 | 88 | 8845 | 8680 | 9042 |
| AWI 4353.1.1 | 404–408 | mixed benth. foram. | 8.500 | 85 | 9298 | 9158 | 9447 |
| UCIAMS-211061 | 480–484 | bivalve | 9145 | 50 | 9663 | 9542 | 9786 |
| UCIAMS-211081 | 644.5–645 | mixed benth. foram. | 9345 | 45 | 9869 | 9744 | 9988 |
| AWI 2795.1.1 | 856 | mixed benth. foram. | 9.437 | 104 | 10123 | 10005 | 10241 |
| AWI 4354.1.1 | 3–4 | mixed plankt. foram. | 1.434 | 58 | | | |
| AWI 4355.1.1 | 6–7 | mixed plankt. foram. | 2.198 | 63 | | | |
| AWI 4356.1.1 | 17–18 | mixed plankt. foram. | 3.702 | 68 | | | |
| AWI 4357.1.1 | 59–60 | mixed plankt. foram. | 6.024 | 79 | | | |
| AWI 4358.1.1 | 210–215 | mixed plankt. foram. | 7.799 | 86 | | | |

Table 5.2: AMS ^{14}C radio carbon ages for GC PS100/270 were determined on articulated bivalve and mixed benthic/planktic foraminifers. Bold CALIB median numbers were used for our *Bacon* age model. AMS ^{14}C ages in grey are from planktic foraminifera, which were excluded from further age calibrations due to the high correlation with benthic foraminifera.

5.3.2 Lithofacies and bulk organic parameters

Based on sediment description and x-ray images, the sedimentary sequence in Core PS100/270 can be divided into four lithofacies units (LF1–4), which are explained in detail below (Fig. 5.3). Sedimentology, organic bulk parameters i.e., TOC (%) and CaCO_3 (wt.%) and the physical properties such as magnetic susceptibility (MS, 10^6 SI) and wet bulk density (WBD, g cm^{-3}), are plotted against depth (Fig. 5.3).

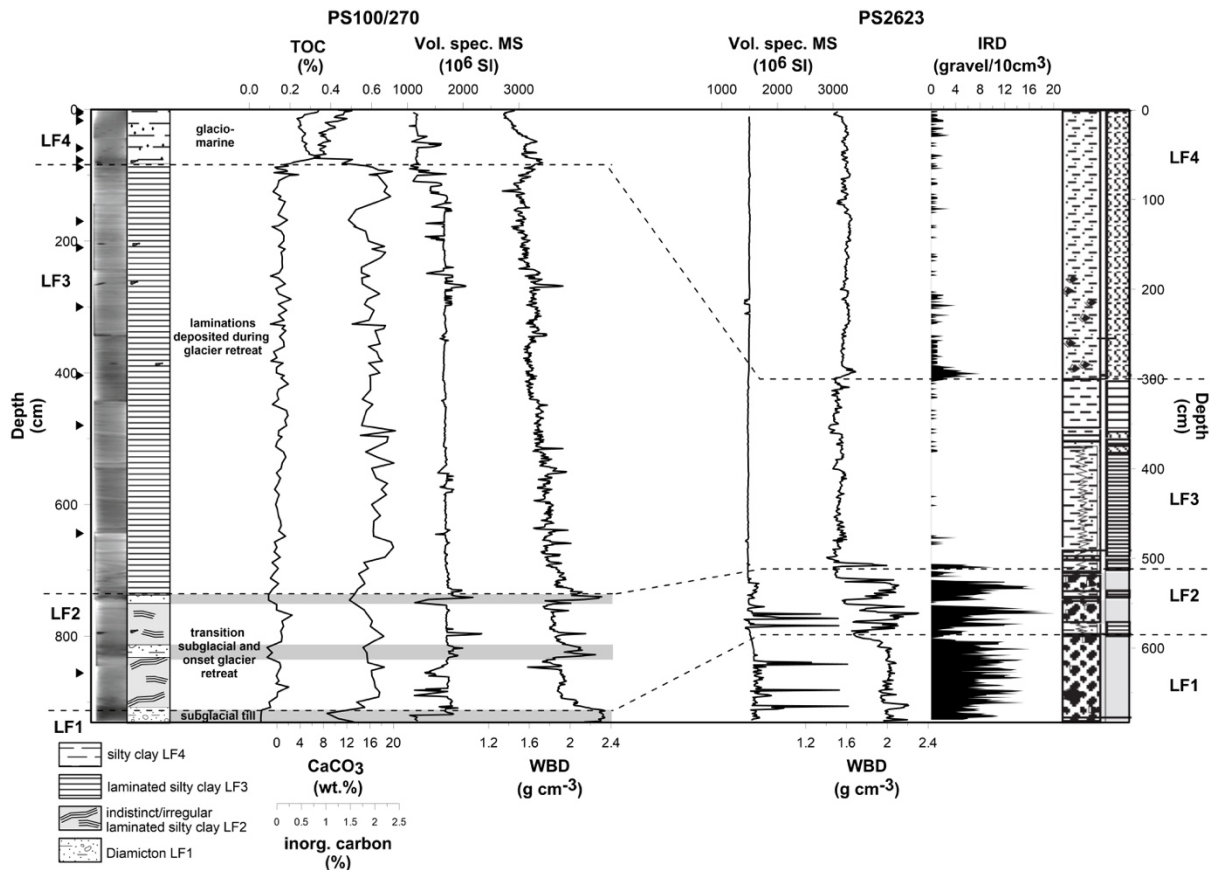


Figure 5.3: X-ray image and main lithology with lithofacies units LF1 to LF4 and interpreted depositional environment, and records of total organic carbon (TOC (%), CaCO₃ (wt. %) and physical properties (MS (10⁶ SI), WBD (g cm⁻³)), from GC PS100/270 (black lines) (this study). Grey shading indicates the basal diamicton and two intercalated diamicton horizons at 820 cm and 740 cm. Black triangles mark position of corrected ¹⁴C AMS dates. To the right is the record from Core PS2623 (East Greenland, south of Shannon island) illustrating lithofacies, together with records of physical properties (MS (10⁶ SI), WBD (g cm⁻³)) and ice-rafted debris (IRD (gravel/10cm³)) (Stein, 2008 and further references therein). Dashed lines show potential correlations between the cores.

LF1 represents a stiff, over-consolidated diamicton at the bottom of the core between 930 to 910 cm that consists of a massive dark reddish to grey sandy silt matrix with abundant large black sub-angular, sub-rounded clasts (<5 cm) and a fining upward trend. It is intercalated with colour banded silty clay, containing granule to gravel size clasts (Fig. 5.3). This diamicton is characterized by low values of TOC (<0.1%), CaCO₃ (8 wt.%) and MS (~800 10⁶ SI), but high WBD values (~2.4 g cm⁻³). Accumulation rates of TOC and CaCO₃ cannot be calculated for this unit (Supplementary Fig. B.1).

LF2 between (910 to 730 cm) represents a transition from a stiffer diamicton to an indistinct, irregular, partly laminated silty clay (Fig. 5.3). This unit shows relatively moderate, but slightly increased TOC (~0.2 to 0.15%) and CaCO₃ (16 to 20 wt.%) content and higher MS values (~1800 10⁶ SI). This unit is also characterized by a significant reduction in WBD (down to 1.6 g cm⁻³) (Fig. 5.3). This interval occasionally contains fine silty layers and/or lenses and is intercalated with diamicton horizons at 820 cm and 740 cm, where most of the bulk parameters and physical properties, except for the WBD that shows distinct maxima, drop back to very low values (Fig. 5.3). However, accumulation rates of TOC

(up to $2.5 \text{ g cm}^2 \text{ ky}^{-1}$) and CaCO_3 (up to $300 \text{ g cm}^2 \text{ ky}^{-1}$) are highest in LF2 (Supplementary Fig. B.1b, c).

LF3 (730 to 80 cm) predominately consists of strongly laminated reddish to grey/brown silty clays ranging between $<1 \text{ cm}$ and a few cm with rare black granule clasts. The upper part of this unit (130 to 80 cm), is characterized by a gradual transition from strongly laminated to homogenous silty clay (Fig. 5.3). TOC (0.1%), CaCO_3 (18 to 20 wt.%) and MS ($1600 \cdot 10^6 \text{ Sl}$) are all relatively constant and show only minor fluctuations while the WBD (down to 1.6 g cm^{-3}) is further decreasing (Fig. 5.3). Accumulation rates of TOC ($\sim 0.25 \text{ g cm}^2 \text{ ky}^{-1}$) and CaCO_3 ($\sim 30 \text{ g cm}^2 \text{ ky}^{-1}$) are significantly decreased during this interval.

The final unit, LF4, comprising the upper part of the core between 80 to 0 cm, consists of very soft, but massive brownish silty clay to clay with occasional granule to gravel sized clasts visible from 32 cm onwards (Fig. 5.3). TOC (0.5 %) values increase and all other parameters, including CaCO_3 (4 wt.%), MS ($\sim 1000 \cdot 10^6 \text{ Sl}$) and WBD (1.4 g cm^{-3}) decrease through this unit (Fig. 5.3). The unit LF4 is characterized by minimum TOC and CaCO_3 accumulation rates (Supplementary Fig. B.1b, c).

5.3.3 Biomarkers

The biomarker data of LF1 (diamicton) are limited to 2 samples. The diamicton is characterized by low values of all HBIs; IP_{25} ($0.4 \mu\text{g g}^{-1} \text{ TOC}$), HBI III ($\sim 0.25 \mu\text{g g}^{-1} \text{ TOC}$) (Fig. 5.4). Phytoplankton biomarkers brassicasterol ($25 \mu\text{g g}^{-1} \text{ TOC}$) and dinosterol ($10 \mu\text{g g}^{-1} \text{ TOC}$), but also terrigenous biomarkers β -sitosterol ($120 \mu\text{g g}^{-1} \text{ TOC}$) and campesterol ($20 \mu\text{g g}^{-1} \text{ TOC}$) are somewhat higher during this interval (Fig. 5.4). LF2 is characterized by strongly fluctuating, but overall high concentrations of all HBIs i.e., IP_{25} (0.4 to $0.9 \mu\text{g g}^{-1} \text{ TOC}$), HBI III (0.5 to $2 \mu\text{g g}^{-1} \text{ TOC}$), and the sterols brassicasterol (10 to $60 \mu\text{g g}^{-1} \text{ TOC}$) and dinosterol (2 to $15 \mu\text{g g}^{-1} \text{ TOC}$), β -sitosterol (40 to $160 \mu\text{g g}^{-1} \text{ TOC}$), campesterol (5 to $30 \mu\text{g g}^{-1} \text{ TOC}$), (Fig. 5.4). Highest biomarker accumulation rates (Supplementary Fig. B.1 a to i) with strong fluctuations occur during LF2: sea-ice associated biomarker IP_{25} (ranging between 1 to $1.6 \mu\text{g cm}^2 \text{ ky}^{-1}$), pelagic producers HBI III (up to $3 \mu\text{g cm}^2 \text{ ky}^{-1}$), dinosterol (up to $160 \mu\text{g cm}^2 \text{ ky}^{-1}$) and brassicasterol (up to $100 \mu\text{g cm}^2 \text{ ky}^{-1}$), and terrigenous biomarker (up to $300 \mu\text{g cm}^2 \text{ ky}^{-1}$, Supplementary Fig. B.1 d to i). In LF3 lipid biomarkers indicate similar strongly fluctuating trends with distinct peaks as in LF2, except for HBI III, which strongly decrease $\sim 500 \text{ cm}$ (down to $0.3 \mu\text{g g}^{-1} \text{ TOC}$) (Fig. 5.4). Strongly fluctuating trends, but overall much lowered accumulation rates of all biomarkers are displayed in LF3, i.e., IP_{25} ($\sim 0.2 \mu\text{g cm}^2 \text{ ky}^{-1}$), HBI III ($0.2 \mu\text{g cm}^2 \text{ ky}^{-1}$), dinosterol ($\sim 25 \mu\text{g cm}^2 \text{ ky}^{-1}$), brassicasterol ($\sim 15 \mu\text{g cm}^2 \text{ ky}^{-1}$) and terrigenous biomarker ($\sim 25 \mu\text{g cm}^2 \text{ ky}^{-1}$) (Supplementary Fig. B.1 d to i). The upper 80 cm show minimum lipid biomarkers concentrations and accumulation rates (Supplementary Fig. B.1 d to i).

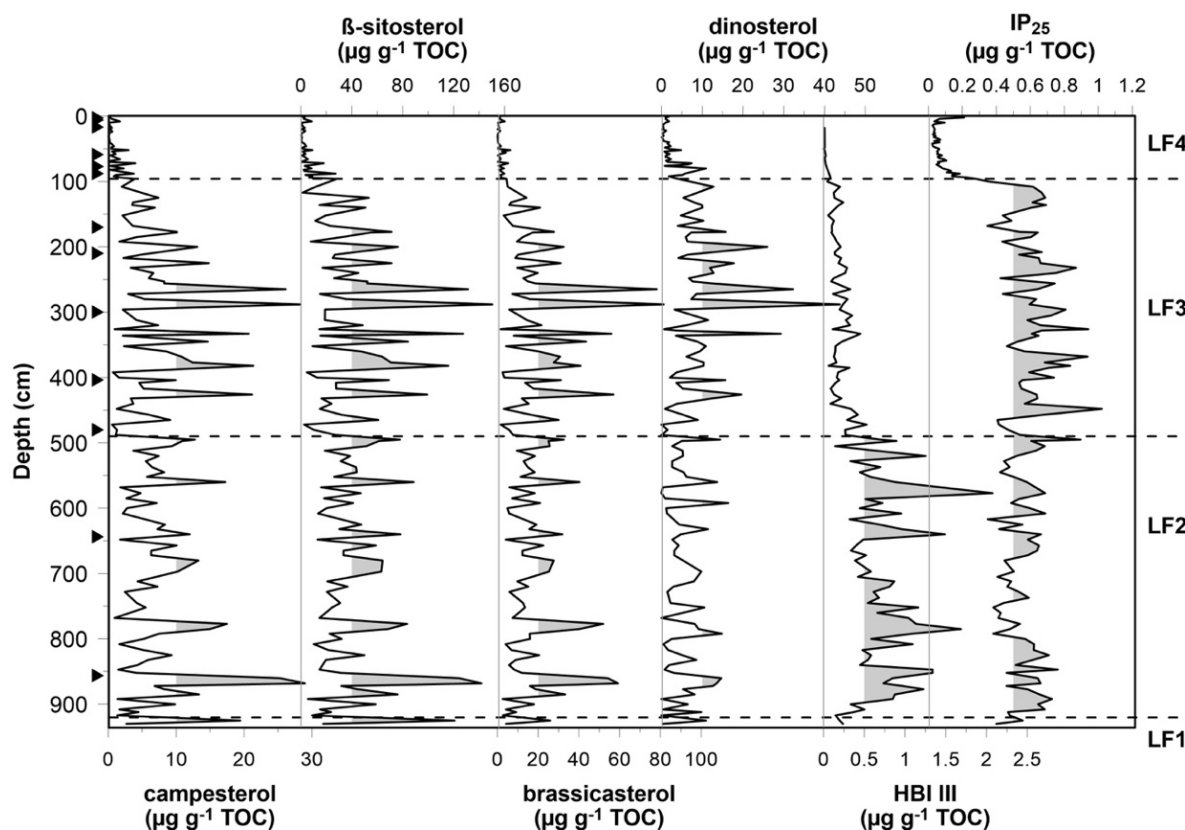


Figure 5.4: Lipid biomarker concentrations ($\mu\text{g g}^{-1}$ TOC), including terrigenous biomarkers β -sitosterol and campesterol, phytoplankton biomarkers brassicasterol, dinosterol and HBI III and sea-ice associated biomarker IP_{25} against depth (cm). Grey shaded areas highlight maxima of these records. Black triangles mark position of corrected AMS ^{14}C dates.

5.3.4 Foraminifera

A total of 35 calcareous and 12 agglutinated benthic foraminiferal species were identified from the samples counted (Fig. 5.5). The abundance of agglutinated specimens was generally very low (no single species having a relative abundance greater than 1% in any sample). Selected benthic foraminiferal species and planktic foraminiferal abundance are plotted for Core PS100-270 against depth in Fig. 5.5. Absolute abundance of foraminifera varies from a minimum of 0 (sample at 928 cm) up to a maximum of 860 specimens per ml. Abundance of planktic specimens tracks that of benthic specimens, but is approximately an order of magnitude lower.

The diamicton (LF1) at the base of the core (930–910 cm) is barren of foraminifera (Fig. 5.5) and therefore accumulation rates cannot not be calculated for this unit. The overlying weakly laminated silty clay LF2 unit (910–730 cm) is characterized by a low diversity and sparse fauna with absolute abundance below 30 specimens per ml of sediment (Fig. 5.5).

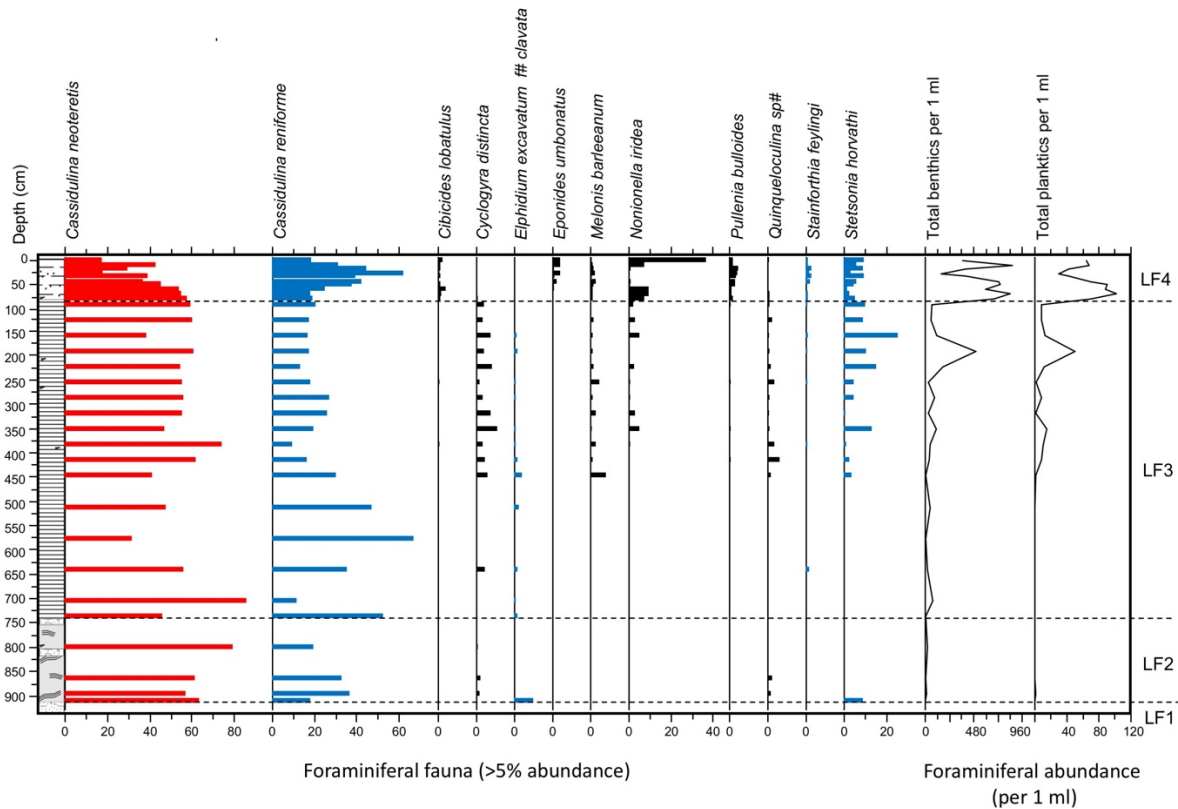


Figure 5.5: Foraminiferal assemblage of Core PS100/270 plotted against depth (cm), including only planktic and benthic species with an abundance $\geq 5\%$. *Cassidulina neoteretis* characterizes warm Atlantic Water and *Cassidulina reniforme* cold Polar Water advection on the inner shelf. The major lithofacies types LF1 to LF4 are indicated (cf. Fig. 5.3).

The impoverished fauna is dominated by *Cassidulina neoteretis* (50–80%) with *Cassidulina reniforme* also abundant (20–40%). The transition to LF3 (the strongly laminated silty clays, 730–80 cm) is accompanied by a gradual increase in foraminiferal abundance (Fig. 5.5). Accumulation rates of benthic foraminifera are highest through LF2 with 10000–30000 indiv. $\text{cm}^{-2} \text{ky}^{-1}$ and two extreme maxima of 45000 and 60000 indiv. $\text{cm}^{-2} \text{ky}^{-1}$ in LF2 and LF3, respectively, while the range of planktic foraminifera remains much lower (between 6000 to 2000 indiv. $\text{cm}^{-2} \text{ky}^{-1}$), but also show highest contents during these intervals (Supplementary Fig. B.1 j and k). Abundance is initially relatively low, varying between 10 and 100 specimens per ml, then starts to increase from approximately 200 cm. LF3 is co-dominated by *C. neoteretis* and *C. reniforme* with dominance fluctuating between these two species (Fig. 5.5). The accumulation rates of both species *C. neoteretis* (5000 to 50000 indiv. $\text{cm}^{-2} \text{ky}^{-1}$) and *C. reniforme* (about 3000 to 10000 indiv. $\text{cm}^{-2} \text{ky}^{-1}$) also reach highest levels during LF2 and LF3 (see discussion below). From approximately 450 cm abundance of *C. reniforme* decreases to stabilize at approximately 20% with *C. neoteretis* returning to dominance (approximately 60%). This interval is also characterized by the increase in abundance of other subsidiary species (Fig. 5.5).

The transition to the upper massive silty clay LF4 unit at 80 cm is accompanied by an abrupt increase in foraminiferal abundance (up to 850 specimens per ml). Initially *C. neoteretis* continues to dominate,

but the abundance of *C. reniforme* gradually increases reaching a peak abundance of 60% at 30 cm before reducing towards the top of the core as *C. neoteretis* increases slightly along with a range of other species, particularly *Nonionella iridea* (Fig. 5.5). Accumulation rates of benthic (down to 1000 indiv. cm⁻² ky⁻¹) and planktic (near zero values) foraminifera are lowest in LF4, a similar pattern as recorded by the organic bulk parameters and lipid biomarkers (Supplementary Fig. B.1 j and k).

5.4 Discussion

This multiproxy-based study provides the first detailed examination of the interaction between local past sea-ice variability (NØIB) and marine terminating outlet glaciers and ice-shelf evolution on the NEG continental shelf.

5.4.1 Late Weichselian initial deglaciation (>10 ka)

The retreat of ice across the continental shelf of NEG is recorded by mega-scale glacial lineations, grounding zone wedges and moraines in both Norske Trough and Westwind Trough (Evans et al., 2009; Winkelmann et al., 2010; Arndt et al., 2017). Both 79NG and ZI had retreated to the present coast by 11.5–10.0 ka (Larsen et al., 2018.).

The lowest unit, LF1, in Core PS100/270 is characterized by a stiff, over consolidated diamicton that we interpret as a subglacial till, which implies, that the location of Core PS100/270 on the inner continental shelf was covered by grounded ice as 79NG marine terminating outlet glacier retreated from the continental shelf (Fig. 5.3). Core PS2623 obtained from the south of Shannon Island on the East Greenland shelf also shows a lithostratigraphy that is similar to the one of Core PS100/270 (Fig. 5.3), with over-consolidated diamict layers characterized by maximum values of IRD, magnetic susceptibility and WDB during the initial deglaciation (Fig. 5.3; Stein, 2008). A terrestrial source is supported by the dark reddish to grey sandy, silt matrix that constitutes the diamicton which points to a mid-Devonian sand/siltstones source originating from the NEG hinterland (Stein et al., 1993, Stein, 2008; Stein et al., 2016). In addition, this is supported by the lack of foraminifera within this unit (Fig. 5.5, 5.8). The presence of biomarkers with relatively low HBIs and higher terrigenous and phytoplankton biomarkers values may indicate high amounts of reworked terrestrial material within the subglacial till (Fig. 5.6, 5.7).

Given our present understanding of the deglacial history of the inner shelf and present coast of NEG this diamict was probably deposited between 13–10 ka as ice moved back onshore (Larsen et al., 2018). The age model derived for PS100/270 suggests the transition from the subglacial till to overlying laminated unit (hence an estimate of the timing of deglaciation at this core site) took place near 10.1 ka (Fig. 5.2, Table 5.2). With the grounded ice present, sea-ice formation, open-water productivity and terrigenous input via sea-ice melt was absent during this interval.

5.4.2 Early Holocene (~10 to 9.6 ka)

The over consolidated subglacial till is overlain by a silty clay consisting of rhythmical irregular and indistinct laminations (Fig. 5.3). This switch from LF1 to LF2 reflects a transition from subglacial conditions to proximal glaciomarine conditions as 79NG grounding-line retreated westward. Sedimentation rates in unit LF2 of Core PS100/270 are very high at this point reaching approximately 800–900 cm ky^{-1} (Fig. 5.2) and reflects an excess of sediment being pumped into suspension from the proximal glacial margin. Further, the laminated nature of LF2 and high sedimentation rates indicate ice proximal conditions until at least 9.6 ka, suggesting that the grounded 79NG was relatively stable for at least a few hundred years.

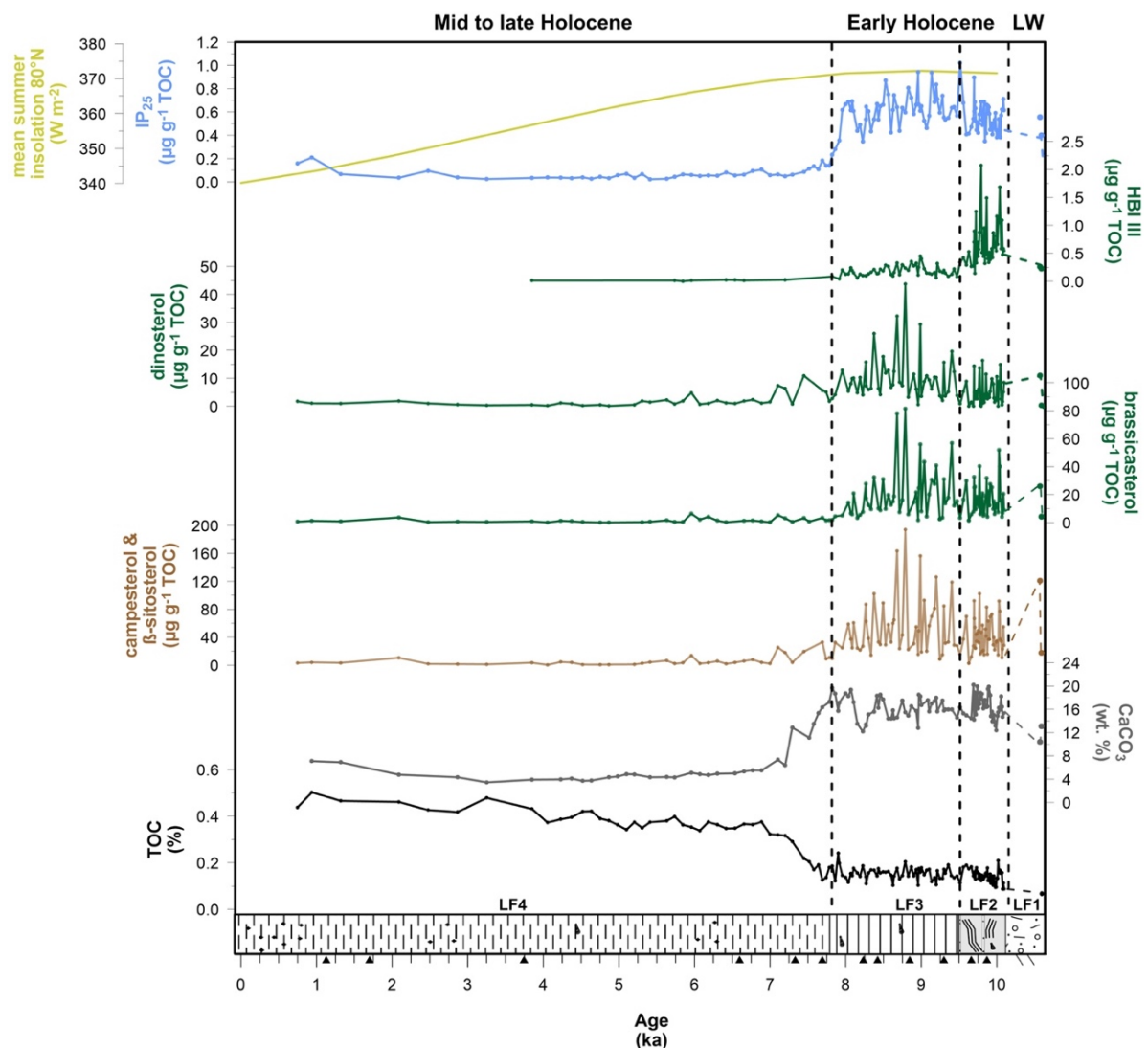


Figure 5.6: Lithology (divided into four lithofacies, LF1–4), total organic (TOC) and inorganic (CaCO_3) carbon (%), lipid biomarker concentrations ($\mu\text{g g}^{-1}$ TOC) and mean summer solar insolation (W m^{-2} , Laskar et al., 2004), plotted against age (ka).

The intercalated diamicton horizons with increased clasts at 820 and 740 cm might be related to debris flows in a glaciomarine environment, phases of increased IRD supply possibly linked to iceberg calving from the proximal ice margin, or a re-advance of the ice tongue of 79NG. Hence, the lower part of Core PS100/270 are dominated by sediments derived in a proximal proglacial environment. A similar situation is also recorded in the lithofacies of Core PS2623 where the alternations of diamictons and laminated sediments are interpreted as advance and retreat of the ice margin (Fig. 5.3; Stein, 2008).

Highest sympagic, pelagic and terrigenous biomarker and bulk parameter concentrations and accumulation rates of Core PS100/270 mark the transition from subglacial to an open-ocean environment with warmer conditions during the early Holocene Thermal Maximum (HTM) with peak solar insolation values (Fig. 5.6, 5.7; Laskar et al., 2004).

Rising air temperatures ($\sim 8^{\circ}\text{C}$ NEEM ice core record) and sea-surface temperatures ($2\text{--}5^{\circ}\text{C}$), may have forced an earlier nearly complete seasonal breakup of the local NØIB probably starting already in April/May (which is comparable to the present-day situation at the end of July) (Fig. 5.1C; Bauch et al., 2001; Rimbu et al., 2003; Andersen et al., 2004; Bendle and Rosell-Melé, 2007; Buizert et al., 2018; Zehnich et al., 2020). This is evidenced by high IP_{25} concentrations and accumulation rates, suggesting increased sea-ice breakup, thinning and local drifting of NØIB ice floes. This enabled light and nutrients to penetrate through seasonal sea-ice formation in spring/summer and favor sea-ice algae growths (Fig. 5.6, 5.7). Sympagic producers of IP_{25} correlate positively with pelagic producers of HBI III, most likely indicating the predominance of well-developed MIZ conditions (Fig. 5.6, 5.7). Seasonal to marginal sea-ice conditions are shown in the IP_{25} vs. phytoplankton biomarkers brassicasterol and dinosterol relationship (Fig. 5.9), consistent with PIP_{25} indices fluctuating around 0.6 (Fig. 5.10). This environmental setting offers ideal conditions for production of all lipid biomarkers between 9.6 to ~ 10 ka on the inner NEG continental shelf (Fig. 5.7 and 5.11). Additionally, high terrigenous biomarker concentration and accumulation rates show that sea-ice melt released terrigenous particles and bound nutrients into the water column, triggering open-water primary productivity as reflected in the increased phytoplankton biomarker fluxes (Fig. 5.7). Highest CaCO_3 contents and accumulation rates are interpreted as increased supply of detrital carbonate (Fig. 5.6, 5.7), based on the negative correlation between carbonate and foraminifers (Supplementary Fig. B.2). Furthermore, PIP_{25} values show a very prominent short-term variability that might reflect short-term cyclic changes in sea-ice extent with periods of about 100 to 70 years (Fig. 5.10). Such cyclicity was also found in Core PS93/025 at the outer NEG continental shelf (Syring et al., 2020) and linked to cyclic changes in solar activity as a potential driving force (e.g., Vonmoos et al., 2006).

Meanwhile, rising air temperatures resulted in intensified surface melt of the GIS (MacGregor et al., 2018), while regional records show a strengthened Westspitsbergen Current at this time (Jennings et al., 2011), potentially increasing the flux of recirculating AW onto the NEG continental shelf within the Return Atlantic Current (RAC) (Bauch et al., 2001; Evans et al., 2009; Schaffer et al., 2020; Zehnich et al., 2020).

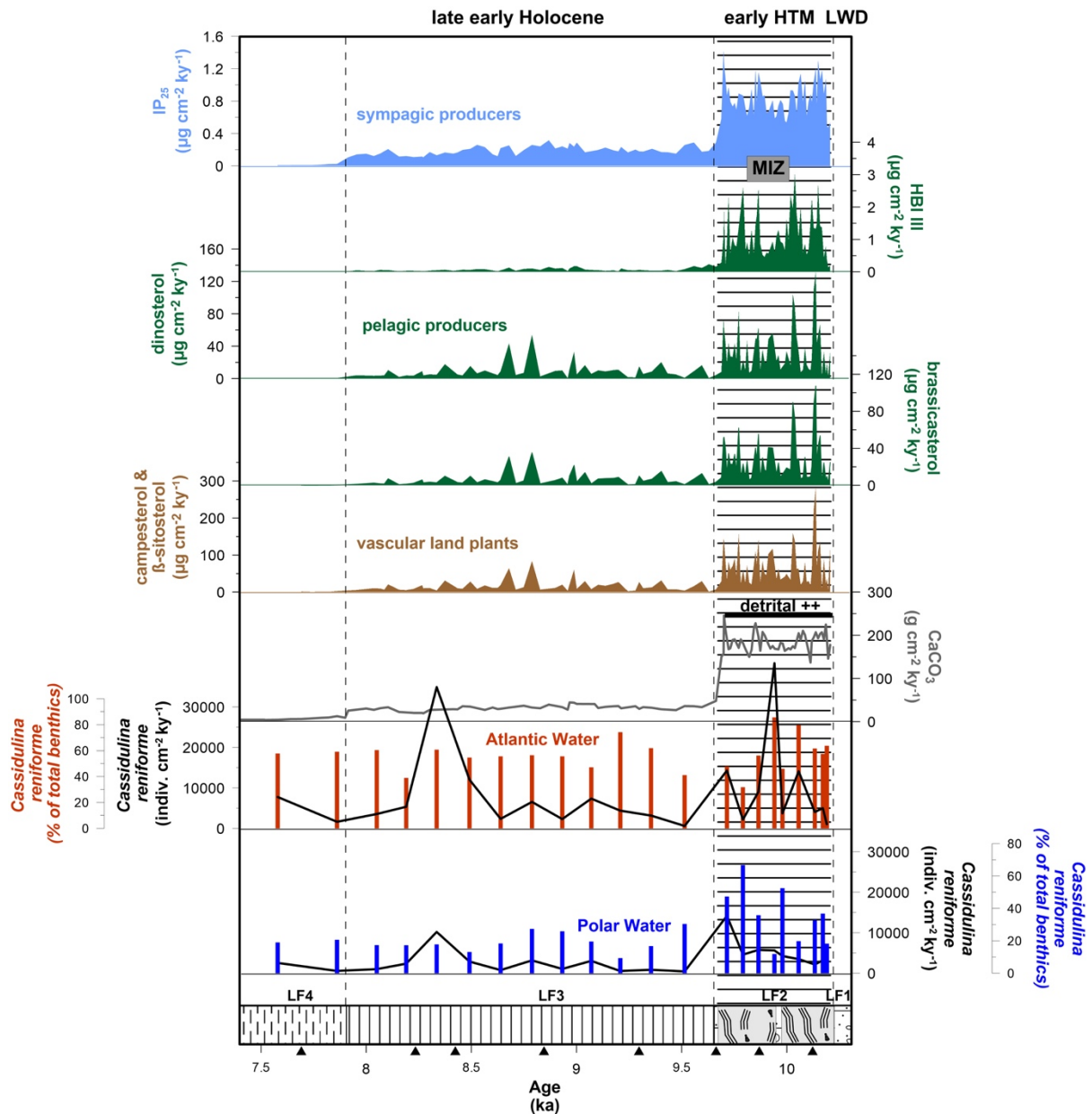


Figure 5.7: Accumulation rates ($\mu\text{g cm}^{-2} \text{ky}^{-1}$, $\text{indiv. cm}^{-2} \text{ky}^{-1}$) of total organic (TOC) and inorganic carbon (CaCO_3), terrigenous biomarkers (β -sitosterol, campesterol), phytoplankton biomarkers (brassicasterol, dinosterol, HBI III), sea-ice associated biomarker (IP_{25}), cold and warm water benthic foraminifera, plotted against age (ka). Foraminiferal relative abundance is shown by the bars and accumulation rates are shown by the solid lines. Hatched area marks highest concentrations of all markers in the marginal ice zone = MIZ.

Indeed, this is supported by the dominance of the benthic foraminifera, *Cassidulina neoteretis* (Fig. 5.7, 5.8), typically indicating presence of AW (e.g., Hald and Korsun, 1997), within the lower section of the laminated unit immediately after the transition from the subglacial till. This indicates a strong presence of recirculating AW on the inner continental shelf of NEG immediately on deglaciation of the PS100/270 core site (Fig. 5.11).

A strong westward advection of AW onto the NEG continental shelf at that time is also reflected in the assemblages and isotope data of planktic and benthic foraminifers determined at the nearby Core

PS93/025 (Zehnich et al., 2020). The increased AW influence probably caused relatively high levels of basal melting at the grounding line or of any ice shelf present within Norske or Westwind Troughs.

The relatively high abundance of *Cassidulina reniforme* (a typical glaciomarine indicator) and presence (although only present in one sample) of *Stetsonia horvathi* support the interpretation of this transition indicating proximal glaciomarine conditions (Fig. 5.5 and 5.8). It is likely that the mix of relatively cold and fresh meltwater from the grounded margin along with the presence of relatively warm and saline recirculating AW produces the mixed and variable assemblage within the lower laminated unit (Fig. 5.8; Evans et al., 2009; Schaffer et al., 2020). Highest accumulation rates of *Cassidulina neoteretis* and *Cassidulina reniforme* support these findings (Fig. 5.8). A planktic foraminifera-based study by Hald et al. (2007) on six high-resolution sediment cores identifies variations in temperature and extent of AW in the northern North Atlantic during the Holocene, suggesting that there was a time-transgressive intensified warm AW inflow from south towards the Arctic Ocean during the late early Holocene. Werner et al. (2016) stated that the higher influx of warm AW was the result of large-scale reorganization of the ocean circulation following the Holocene.

In combination the sedimentological parameters, the presence of relatively warm water benthic foraminifers, sea-ice associated biomarker IP₂₅ consistent with high sterol concentrations and accumulation rates and the IP₂₅-phytoplankton biomarker relationship determined in Core PS100/270, all strongly support the existence of an extensive, but seasonal sea-ice cover, and high overall productivity with pelagic spring/summer blooms and high terrigenous input (Fig. 5.7, 5.8, 5.9). Certainly, warmer atmospheric conditions and also the flux of relatively warm recirculating AW strongly controlled the onset of intensive thinning, mass ice loss and grounding-line retreat inland during the HTM. Together with the disintegration of NØIB, it is assumed that the reduced buttressing effect on the ice shelf would have encouraged increased ice discharge due to the speed up of 79NG and ZI, facilitating rapid ice margin disintegration and glacier retreat. Results of Core PS100/270 correspond well to model simulations by Dyck et al. (2010) and other paleo-climate reconstructions from the outer NEG continental shelf (PS93/025) which infer a general decrease of sea-ice concentrations during the early HTM, driven by the combination of an atmospheric and ocean forcing (Fig. 5.11; Syring et al., 2020; Zehnich et al., 2020).

5.4.3 Late early Holocene (9.6 to 7.9 ka)

Late early Holocene sediments are characterized by the deposition of finely laminated silty clays, and reflect a more distal proglacial environment as the grounded ice-stream margin and ice shelf retreated inland (Fig. 5.3). After 9.6 ka sedimentation rates on the inner shelf abruptly reduce from >800 cm ky⁻¹, but still remain relatively high during this time (>200 cm ky⁻¹, Fig. 5.2). Only minor abundances of granule to gravel sized clasts (possibly IRD) were observed from core x-raydiographs and during

sample investigations within our sedimentary facies, supporting suspension settling from 79NG meltwater plumes, i.e., a predominance of meltwater-derived sedimentation (Fig. 5.3).

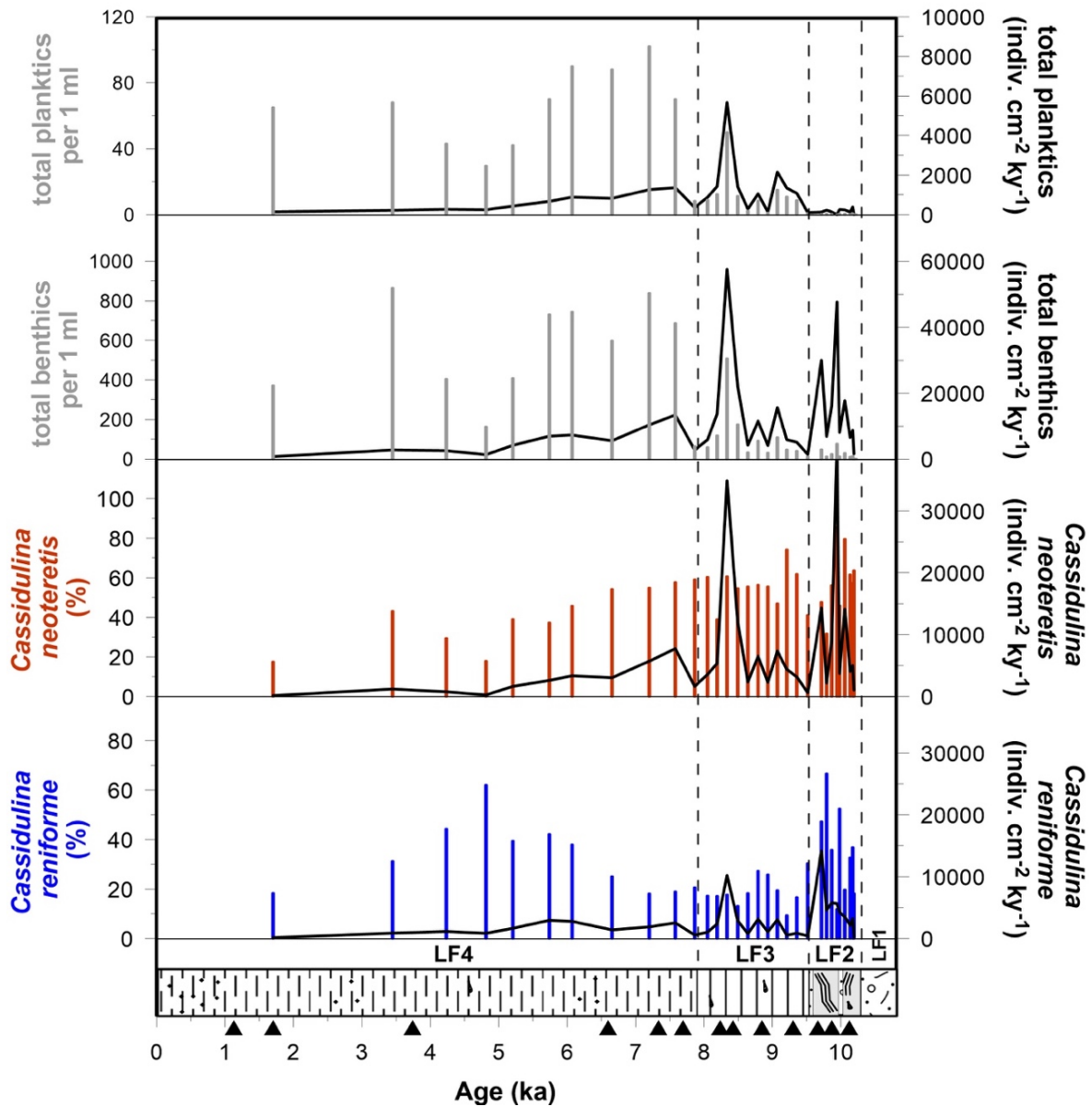


Figure 5.8: Relative abundance (bars) and accumulation rate (solid black lines) of *Cassidulina reniforme* (cold water indicator) and *Cassidulina neoteretis* (warm water indicator) plotted against age (ka). Absolute abundance (grey bars) and accumulation rates (solid black lines) of planktic and benthic foraminifera plotted against age (ka). The major lithofacies units LF1 to LF4 are shown to the left. Black triangles mark position of corrected ^{14}C AMS dates.

Furthermore, generally low concentration of IRD over the entire record, might indicate the influence of cold, fresh polar waters transported via the EGC, preventing iceberg melt and release of ice rafted debris to the core site. The environmental conditions seem to be similar to those recorded at Core PS2623 where also minimum IRD was found in this interval (Fig. 5.3; Stein, 2008).

Lipid biomarker concentrations are similar to early HTM values, while absolute accumulations rates are two to three times lower during this interval. Also notable, however, is the abrupt decrease of the pelagic biomarker HBI III (Fig. 5.6, 5.7). Based on our records, we therefore assume a change in environmental conditions from a stable sea-ice margin towards the formation of a more extensive seasonal (spring) landfast sea-ice cover (NØIB), comparable to satellite images from modern times (Fig. 5.1C, beginning of May).

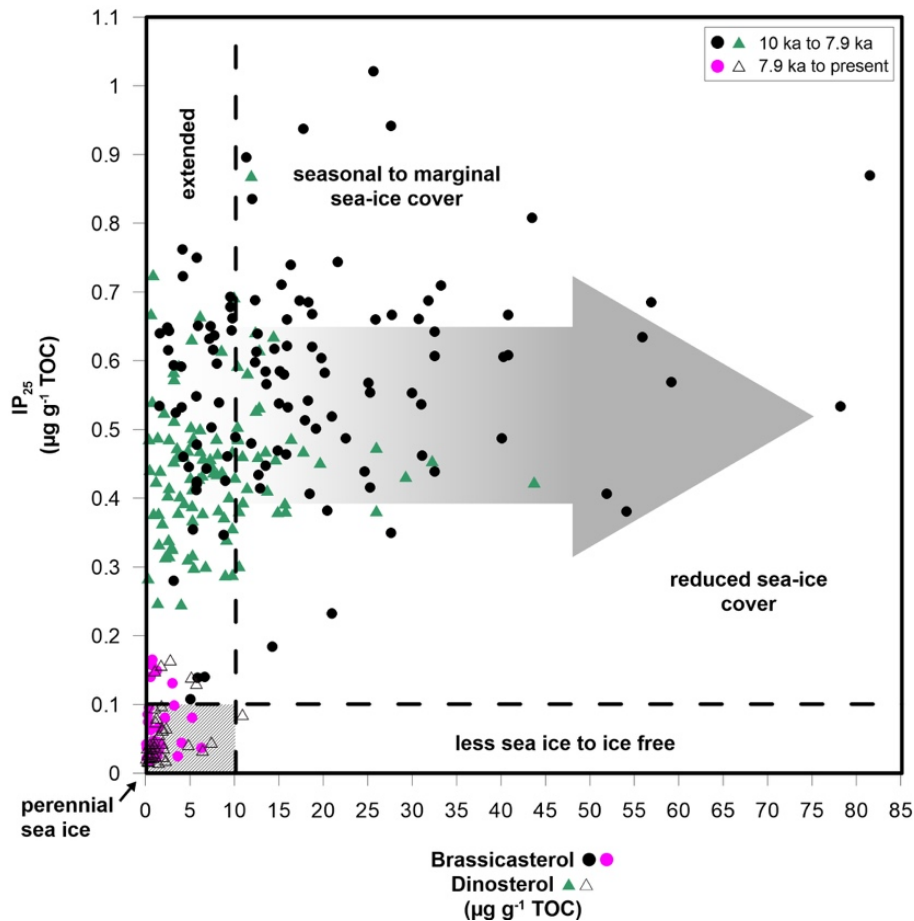


Figure 5.9: Sea-ice associated biomarker IP₂₅ ($\mu\text{g g}^{-1}$ TOC) versus phytoplankton biomarkers brassicasterol and dinosterol ($\mu\text{g g}^{-1}$ TOC). Black dot and green triangle show phytoplankton marker concentrations from the interval between 10 ka to 7.9 ka and pink dot and white triangle from the interval between 7.9 to present. Classification of different sea-ice settings are according to Müller et al. (2011). Large grey arrow indicates transition from most extended sea-ice conditions to reduced sea-ice cover. Most of the data points between 7.9 ka to present occur in the lower left corner, representing extended to perennial sea-ice conditions.

At the same time, HBI III concentrations are extremely low throughout the interval of elevated IP₂₅ concentrations during the late early Holocene, suggesting an extensive sea-ice cover associated with harsh winters and only short (nearly ice-free) summers on the inner NEG continental shelf (Fig. 5.6, 5.7). Summers with shorter periods of open-water areas, increased algae productivity and sea-ice melt would explain the lower accumulation rates of the phytoplankton markers brassicasterol and dinosterol, as well as lower accumulation rates of terrigenous biomarkers campesterol and β -sitosterol (Fig. 5.6,

5.7). Our interpretation of extended sea-ice conditions at this time is illustrated in the IP₂₅/phytoplankton biomarker plot (Fig. 5.9).

During this interval the benthic foraminiferal assemblage (Fig. 5.5) as well as their high accumulation rates (Fig. 5.7, 5.8) indicate a strong influence of recirculating AW within the RAC recorded at Core PS100/270. This is supported by the dominance of *C. neoteretis* (60%), with low relative abundance of *C. reniforme* through the record and also other relatively warm water indicators also increasing (e.g. *Nonionella iridea* and *Melonis barleeanum*) (Fig. 5.8). Continuing high but variable AW advection towards the NEG continental shelf until about 8 ka is also recorded in the assemblages and isotope data of foraminifers at Core PS93/25 (Zehnich et al., 2020) as well as Core PS1230 (Bauch et al., 2001). This would potentially encourage relatively high rates of basal melting of the floating ice tongue of 79NG glacier and at the grounding line. This basal meltwater rises up, leading to a stratification of the water column with the cold, fresh and relatively low-density meltwater layer spreading underneath the fast ice separating it from the warmer, more salty and denser sea water below. Thus, the colder water layer acts as a barrier and additionally stabilizes the fast ice (Mayer et al., 2000). In addition, the supply of freshwater to the NEG continental shelf may trigger changes in the local fjord, marine productivity, ocean and atmospheric temperatures (Bamber et al. 2012; Straneo and Cenedese, 2015; Cape et al., 2019).

The extensive seasonal sea-ice conditions (development of NØIB) and the further retreat of 79NG due to basal melting and grounding-line retreat recorded at core site PS100/270 are highlighted in Figure 11. This fits with previous investigations from 79NG fjord that suggest ice-shelf disintegration between 9.0–7.7 ka (Bennike and Weidick, 2001). These interpretations are consistent with modern observations and support the suggestion that the recent enhanced intrusion of warm recirculating AW (e.g. warmer waters between 0.5–0.8°C in 2006–2007) and rising atmospheric temperatures make both 79NG and ZI particularly vulnerable to surface and submarine melting (Ingleby and Huddleston, 2007; Holland et al., 2008; Seale et al., 2011; Beszczynska-Möller et al., 2012; Schaffer et al., 2020).

5.4.4 Mid to late Holocene (7.9 ka to present)

After the total ice-shelf break up and grounding-line retreat of 79NG towards the inner fjord at ~7.9 ka (Fig. 5.11), the sedimentary regime at core site PS100/270 was dominated by a hemipelagic massive brownish silty clay to clay with extremely low sedimentation rates (Fig. 5.2; 5.3) indicating a change to a distal glaciomarine environment. The decrease of all biomarker concentrations and accumulation rates to minimum values confirm the presence of a lasting to nearly permanent sea-ice cover (NØIB) with extremely low primary productivity during the mid to late Holocene (Fig. 5.6, 5.7). During the summer months, biomarker records indicate only sufficient thinning of the sea-ice cover to allow very minor productivity of brassicasterol, dinosterol and HBI III (Fig. 5.7).

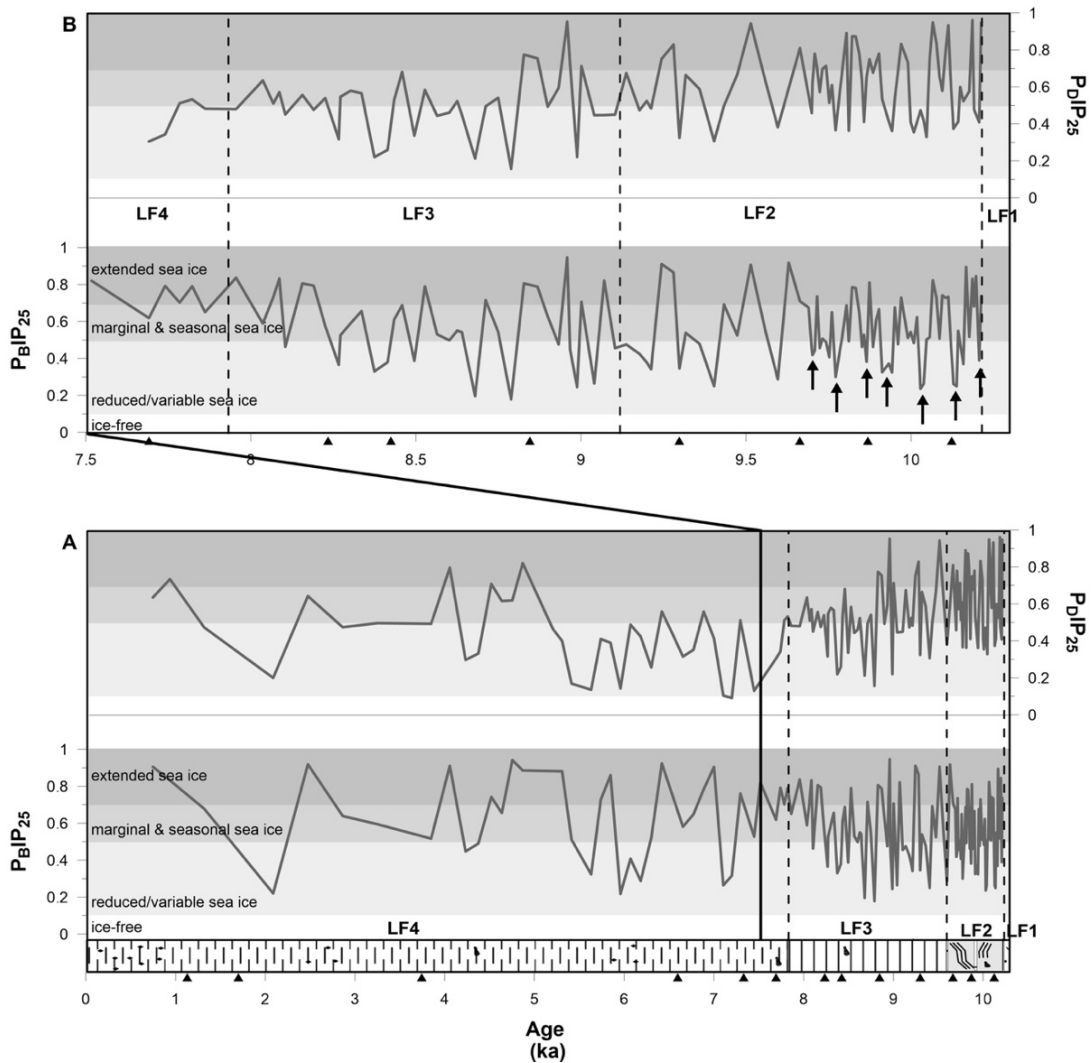


Figure 5.10: $P_{BIP_{25}}$ and $P_{DIP_{25}}$ indices of GC PS100/270, plotted against age (ka). (A) complete Holocene record, (B) the early Holocene. PIP_{25} values <0.1 indicate ice-free conditions, between 0.1 to 0.5 a reduced/variable sea-ice cover, between 0.5 to 0.8 seasonal to marginal sea-ice conditions and above 0.8 extended to perennial sea-ice cover (classification according to Müller et al., 2011). Black triangles mark the corrected ^{14}C -dated AMS core depths.

The IP_{25} vs. phytoplankton biomarkers brassicasterol and dinosterol relationship (Fig. 5.9) points to a predominantly perennial sea-ice cover during the mid to late Holocene, PIP_{25} indices demonstrate stable seasonal sea-ice conditions, with occasional intervals of extended to perennial sea-ice conditions (Fig. 5.11). Sneed et al. (2016) described the modern NØIB as a region of perennial landfast ice, varying annually in thickness and extent, but also more frequent seasonal breakup since 2007.

The relative abundance of *C. neoteretis* remains relatively high until approx. 6.5 ka, but then starts to fall as the relatively cold-water indicator, *C. reniforme*, increases to over 40% of the assemblage from 6 to 2.5 ka (Fig. 5.8). Although relative abundances of foraminifera are high during this interval (Fig. 5.5), accumulation rates of both benthic species (cold and warm) clearly indicate a decreasing trend (Fig. 5.8).

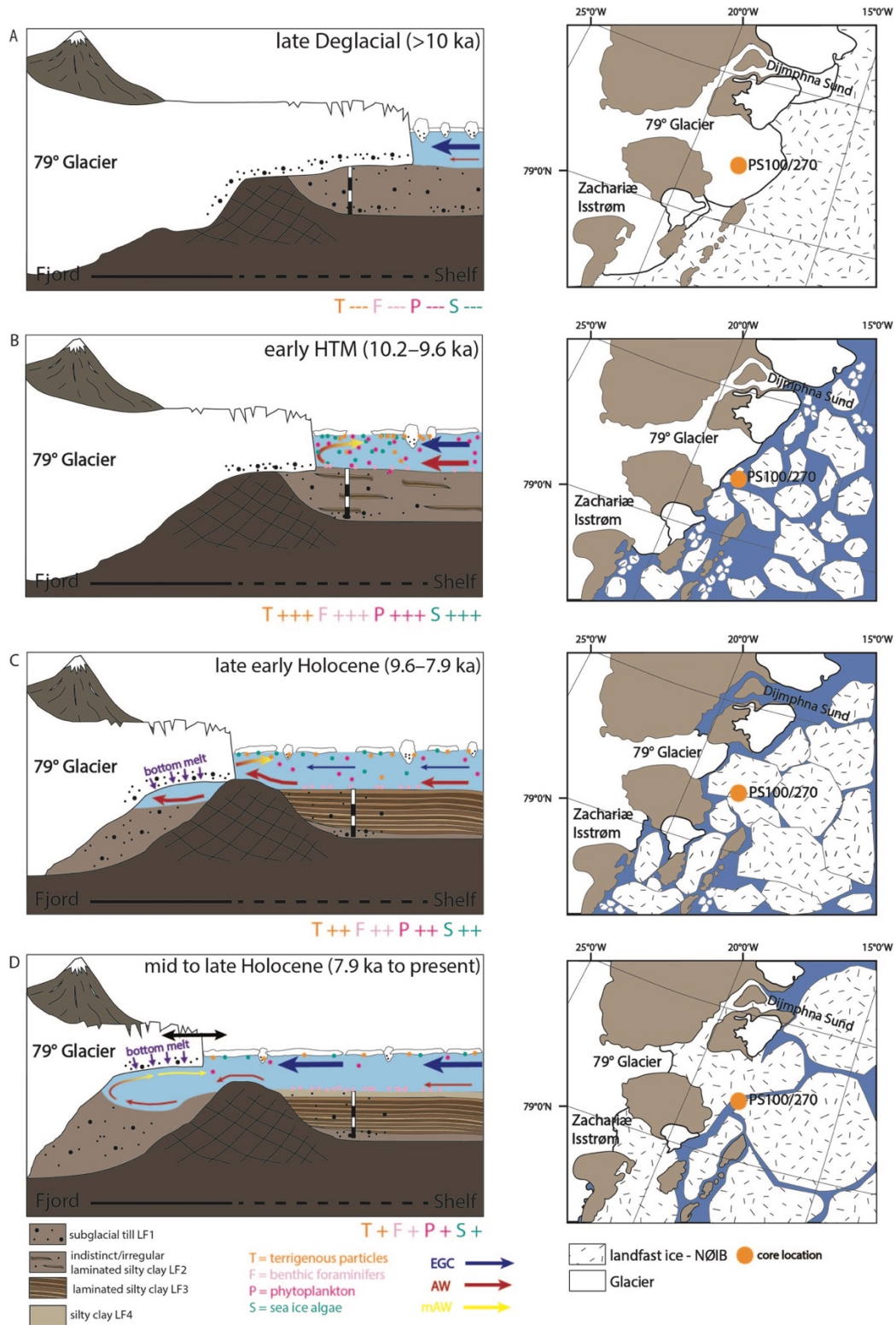


Figure 5.11: Conceptual model representing the interaction between local sea-ice formation, 79NG retreat and ocean circulation on the NEG continental shelf. The four stages (A) to (D) represent the time intervals of lithofacies units LF1–4: A) the initial late Weichselian deglacial (>10 ka), B) early Holocene Thermal Maximum (10.2–9.6 ka), C) late early Holocene (9.6–7.9 ka) and D) mid to late Holocene (7.9 to present) (according to Schaffer et al. 2020). The black and white bar represents the core location. The thicknesses of colored arrows indicate stronger/weaker influence of East Greenland Current = EGC (blue), warm recirculating Atlantic Water = AW (red) and modified recirculating Atlantic Water = mAW (yellow). Top views of the research area to the right show 79NG retreat and extension of the Norske Øer Ice Barrier (NØIB) during these four stages.

This may suggest a continued presence of relatively warm recirculating AW through the mid to late Holocene, but potentially a reduction in flux of this warmer water to the inner continental shelf. The dominance of *C. reniforme* supports this along with a slight increase in abundance of *S. horvathi*, an indicator of harsh conditions, often found below perennial sea ice or an ice shelf. This would most likely reduce the basal melting driven by ocean circulation along the inner continental shelf and within the 79NG fjord and may have contributed to the re-advance of the ice shelf through the 79NG fjord from around ~4.5 ka onwards (Bennike and Weidick, 2001) (Fig. 5.11). A cooler subsurface recirculating AW on the NEG shelf also correlates well with a cooling in Atlantic sourced waters recorded in the Fram Strait since 6 ka (Werner et al., 2016). This relative cooling in subsurface water conditions corresponds well with the Neoglacial Cooling identified in many regions of Greenland (e.g. Koç et al., 1993; Jennings et al., 2002; McGregor et al., 2015; McKay et al., 2018).

In fact, minimum solar insolation and a strengthened EGC, evidenced by lowered SST, support the influence of colder polar waters towards the inner shelf during the mid to late Holocene (Bauch et al., 2001; Jennings et al., 2002; Laskar et al., 2004; Ran et al., 2006; Müller et al., 2012). The overall onset of harsh conditions with relatively low biomarker concentrations and cooler SST were also observed at the outer NEG core site PS93/025 and at the inner East Greenland margin (PS2641) (Kolling et al., 2016; Syring et al., 2020, Zehnich et al., 2020).

Sedimentation rate reduces significantly in the upper section of the core leading to lower temporal resolution in our record, hence, identification of shorter term variability is not possible from this record.

5.5 Conclusion

Detailed sedimentological, organic geochemical and foraminiferal investigations of Core PS100/270 from the inner NEG shelf reflect distinct changes in 79NG and sea-ice conditions during the end of the last glacial period and through the Holocene. 79NG retreated from the core site at approximately 10.2 ka and stayed close until 9.6 ka indicated by highest sedimentation rates in a proximal glaciomarine environment. The grounding line of 79NG may have been pinned at the islands at the mouth of the fjord at this time, but between 9.6 and 7.9 ka, both the grounding line and ice shelf had retreated through the fjord, and this is reflected by a dramatic reduction in sedimentation rate.

The records presented here, show a rapid 79NG retreat and ice shelf disintegration during the early Holocene between 9.6 to 7.9 ka, while sea-ice formation increased during the Holocene. Terrigenous matter supply and/or surface productivity are mainly influenced by fluctuations in the Greenland ice-sheet dynamics, meltwater input, ice-berg drift, seasonal build-up of NØIB and ocean circulation. Rising air temperatures and the influence of warm AW advection are assumed to be the main drivers. Overall four different stages of 79NG retreat and increased sea-ice formation have been identified during the end of the late Weichselian deglaciation into the Holocene:

- A. Late Weichselian deglacial conditions with a grounded 79NG covering the core location PS100/270, indicated by deposition of a subglacial till.
- B. Onset of rapid 79NG retreat during the early HTM due to increased inflow of warm recirculating AW towards the inner NEG shelf, proximal glaciomarine sedimentation off a grounded ice margin pinned on the inner NEG shelf, predominance of seasonal to marginal sea-ice conditions characterized by short-term cyclic variability probably linked to cyclic changes in solar activity, and overall high marine productivity and input of terrigenous matter during the early HTM.
- C. Retreat of 79NG from 9.6 to 7.9 ka towards the inner fjord and continuing high AW advection, increased prolonged seasonal sea-ice conditions, lowered primary productivity and periods of sea-ice melting during shorter summers occurring in the late early Holocene.
- D. Harsher conditions during the mid to late Holocene with a weaker warm recirculating AW advection and a more extensive seasonal sea-ice cover (development of NIØB) with a nearly absent primary production.

Data availability

All data, including downcore biomarker and bulk parameter concentrations ($\mu\text{g g}^{-1}$ TOC, $\mu\text{g g}^{-1}$ Sed), as well as accumulation rates ($\mu\text{g cm}^{-2} \text{ky}^{-1}$, $\text{g cm}^{-2} \text{ky}^{-1}$), foraminifers' assemblages (total benthics and planktics per 1 ml) and calibrated ages (ka) are available from Pangaea.

Supplementary figures

B.1 Accumulation rates

B.2 Carbonate vs. foraminifera plot

Acknowledgements

We gratefully thank Captains Schwarze and Wunderlich and the of RV *Polarstern* as well Chief Scientist Torsten Kanzow (PS100 + PS109) for excellent support and cooperation during both cruises. Thanks to Walter Luttmer/AWI for technical support during the laboratory work, and Gesine Mollenhauer/AWI for high-precision express analyses of small-scale ^{14}C samples with the AWI MICADAS system. Thanks to Simon Belt (Biogeochemistry Research Centre, University of Plymouth/UK) for providing the 7-HND standard for IP_{25} quantification. ASI-AMSR2 sea-ice concentration data were provided by <https://seaice.uni-bremen.de/>. This publication is a contribution to the Research Program PACES II, Topic 3 (The earth system from a polar perspective: Data, modeling and synthesis) of the Alfred Wegener Institute Helmholtz Centre for Polar und Marine Research (AWI). The studied samples and data were provided by AWI (Grant No. AWI-PS100). This research was also supported by the UK NERC (Grant No. NE/N011228/1) and NERC Radiocarbon Laboratory grant 2113.0418.

Chapter 6

Sea-ice biomarker proxies in surface and subsurface sediments from the Northeast Greenland Shelf - Signals for (paleo) environmental conditions and diagenetic degradation

Nicole Syring ^{a,*}, Ruediger Stein ^{a,b}, Kirsten Fahl ^a, Xiaotong Xiao ^c

^a Alfred Wegener Institute (AWI) Helmholtz Centre for Polar and Marine Research, Bremerhaven, Germany

^b MARUM – Center for Marine Environmental Sciences and Faculty of Geosciences, University of Bremen, Bremen, Germany

^c Institute of Marine Organic Geochemistry, Ocean University of China, Qingdao, PR China

State: Preliminary manuscript to be extended by more comprehensive data on climate and degradation-controlled biomarker records as well as further AMS ¹⁴C datings, i.e., extended version of the manuscript to be submitted to, for example, Organic Geochemistry or Marine Chemistry.

Abstract

The Northeast Greenland continental shelf reflects strong dynamics in the sea-ice – ice-sheet – ocean interactions. Modern sea-ice distribution on the shelf became highly variable since 2000. This is most evident by seasonally earlier break ups and ice melt of the landfast sea-ice cover and intensive thinning of outlets (79° Glacier and Zachariæ Isstrøm) from the Northeast Greenland Ice Stream due to increased pCO₂ induced anthropogenic warming and the enhanced inflow of warm recirculating Atlantic Water towards Northeast Greenland continental shelf. In general, satellite-derived sea-ice data are in good agreement with results of investigated surface samples of this study and demonstrate three distinct areas: the near-perennial ice conditions north of 82°N, the Northeast Water Polynya and drift ice supply on the outer shelf, and the local Norske Øer Ice Barrier and glaciers on the inner shelf. Furthermore, organic bulk parameters and biomarkers records determined in a number of multicorer sections from different Arctic regions are interpreted in terms of sea-ice conditions, primary productivity, terrigenous supply and diagenetic alteration. The preliminary data of this study indicate that i) the prominent decrease from maximum biomarker concentrations in surface sediments to minimum numbers within the upper ~5cm is probably related to early diagenetic degradation and ii) the primary signal of organic matter and biomarker input and its change through time are preserved in the subsurface sedimentary records and can be used for paleoenvironmental reconstructions. In order to quantify the degradation of organic matter, however, further more detailed biomarker studies are needed.

6.1 Introduction and regional setting

Current climate model predictions for the Arctic forecast a steady increase in atmospheric temperatures of 6–8°C, warming sea-surface temperatures between 0.05 to 0.5°C per decade and precipitation of 20–30% by the end of 2100 (Meredith et al., 2019). This will result in accelerating and extreme sea-ice loss and retreat of local glaciers (Fig. 6.1C; Rysgaard and Glud, 2007; Alexander et al., 2018). Sea-ice regulates the local and regional surface climate, including temperature, precipitation patterns and cyclone frequencies (Honda et al., 1999; Alexander et al., 2004; Rinke et al., 2006; Ogi and Wallace, 2007; Lawrence et al., 2008; Francis et al., 2015; Bintanja et al., 2017; Pedersen et al., 2019). The strong decline of Arctic sea-ice cover and Greenland’s ice-sheet triggers extreme changes in the behavior of the surface albedo, water-mass formation, structure and circulation, ocean-ice-atmosphere heat flux and surface-water productivity, etc. (Fig. 6.1; Nghiem et al., 2012; Stroeve et al., 2014; Francis et al., 2015; Sévellec et al., 2017). These are all processes and factors of major relevance in the (global) climate system. Thus, understanding of processes controlling modern and past sea-ice conditions is of overall interest in (paleo) climate research. The study of sediment cores representing past climatic conditions may allow to reconstruct processes driving past climate change, results that may be used to test and approve climate models for future climate predictions (Alexander et al., 2018; Niederdrenk et al., 2018; Ding et al., 2019).

In this context, the Northeast Greenland (NEG) continental shelf is a key area of special interest. This area is characterized by four distinct and unique high Arctic marine environments: the highly productive Northeast-Water Polynya (NEW Polynya), the near perennial Norske Øer Ice Barrier (NØIB), the local marine-terminating outlet glaciers of the Northeast Greenland Ice Stream (NEGIS) and drift ice transported from the central Arctic Ocean via the cold, fresh East Greenland Current (EGC) along the shelf (Fig. 6.1, <https://nsidc.org>). The West Spitsbergen Current builds the warm, saline counterpart to the EGC (Fig. 6.1).

Along Northeast Greenland’s coast, the abutting NØIB is the main control on the behavior of the outlet glaciers Nioghalvfjærdsbrae (79NG) and Zachariae Isstrøm (ZI) by buttressing the glaciers and prevents them from calving (Fig. 6.1B; Hughes et al., 2011; Sneed et al., 2016). This landfast sea-ice barrier was assumed to be perennial before 2000, however, it has completely disintegrated almost every summer since 2000. The likely cause of this are regional changes in the ocean heat supply and atmosphere, including extended thinning, meltwater on the ice barrier and warming of the water beneath NØIB (Sneed et al., 2016). The intrusion of warm recirculating Atlantic Waters increased during the past two decades and have entered the inner NEG continental shelf via the Westwind and Norske, reached the undersides of the floating glaciers tongues of 79NG and ZI and caused intensified sub-bottom melting (Münchow et al., 2020; Schaffer et al., 2020).

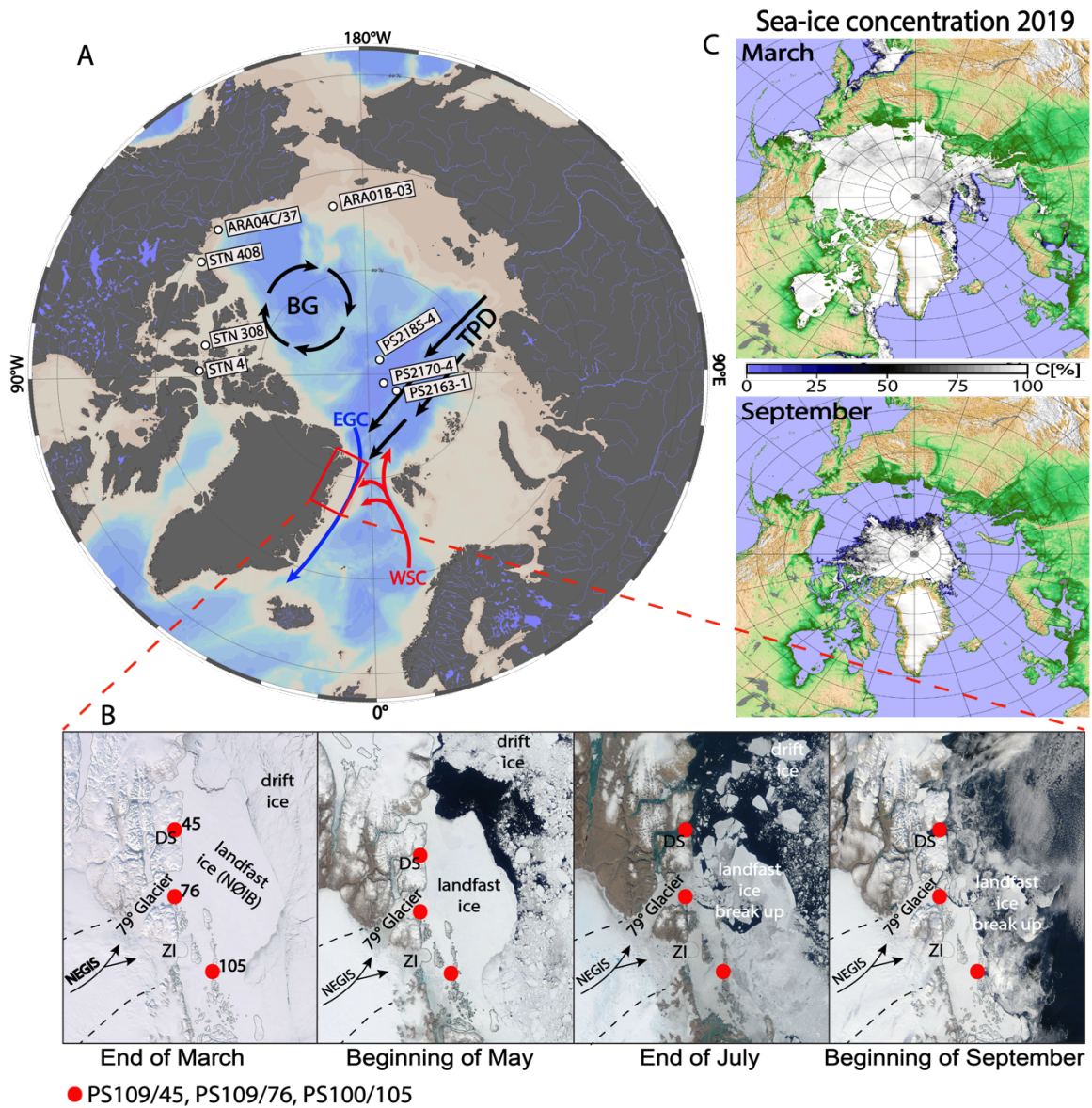


Figure 6.1: A. Map of the Arctic Ocean showing the broad shelf areas (beige), wind-driven ocean currents named Beaufort Gyre (BG) and Transpolar Drift (TD) and rivers (violet) of the surrounding continental land masses. Simplified representation of warm Atlantic Water (red) entering the high North via the West Spitsbergen Current (WSC) and cold, fresh waters (blue) flow south via the East Greenland Current (EGC). Other multicorer stations in the central Arctic Ocean (Xiao et al., 2015), Beaufort Sea (Rontani et al., 2018; Wu et al., 2020) and Chukchi Sea (Kim et al., 2019) were selected for a comparison of degradational processes with this study (red box). B. Satellite-derived images of the NEG continental shelf (Nasa Worldview, 2019) showing investigated multicorer stations (red dots) and prominent features: marine terminating outlet glaciers (79° Glacier and Zacharæa Isström) of the Northeast Greenland Ice Stream (NEGIS), the Norske Øer landfast ice barrier (NØIB), which is bounded by drift ice from the central Arctic Ocean to the east during winter (March), spring (May), summer (July) and autumn (September). C. Sea-ice concentration (2019) of the winter (March) and autumn (September) season.

This is now becoming one of the main drivers, next to atmospheric warming for extensive mass loss of NEGIS marine-terminating outlet glaciers, which are continually retreating further inland (Anhaus et al., 2019; Schaffer et al., 2020). Accordingly, satellite-derived observations show significantly greater amounts of freshwater outbursts from Northeast Greenland's glaciers entering the continental shelf. This plays a crucial role in altering local and global ocean dynamic, changing primary productivity in the

coastal NEW Polynya (for further explanation see chapter 4), altering local sea-ice formation and has the potential to raise sea-level by up to 0.5 m by the end of this century (Rahmstorf et al., 2015; Böning et al., 2016; Sejr et al., 2017; Bamber et al., 2018; Knies et al., 2018; Aschwanden et al., 2019).

Ongoing anthropogenic warming also highly influences and increases the land-to-ocean organic carbon flux and further, by the exposure of more open-water spots due to thinning sea-ice, which enhances primary productivity by about 50% (Rysgaard et al., 2007; Paulsen et al., 2017). Phytoplankton blooms and their production benefit from the major nutrient supply by organic and inorganic carbon transported via rivers towards the Arctic shelves (e.g. Kara and Laptev Sea), and later be incorporated into the newly formed sea ice (Rachold et al., 2004 and references therein).

Preservation of organic matter is often susceptible to diagenetic alteration (chemical, physical or biological processes) in the water column or sediment and therefore concentrations can be underestimated (Leventer, 2013). However, to distinguish quantitatively between varying diagenetic processes that may vary from region to region, represents a big challenge (Belt and Müller, 2013). Suspended terrigenous sterols (indicative for higher vascular land plants) often suffer intensive degradation en route, mostly by photooxidation and autoxidation (Rontani et al., 2014). Under the assumption that drift ice was transported via the Transpolar Drift (TPD) from the Siberian shelves towards the Fram Strait and finally arrived at the NEG continental shelf, incorporated terrigenous sterols, released during sea-ice melt, may have underlain by a strong degradation during their transport resulting in an enrichment of more refractive and stable compounds at sites of final deposition (for further explanation see discussion).

In this study, we report preliminary results of biomarker analyses in surface sediments and three short sediment cores (Fig. 6.1; PS109/76, PS109/45 and PS109/105) from the NEG continental shelf between 76°N to 85°N. The main objectives of this study are to (i) determine the biomarker distribution in surface sediments representing modern environmental conditions, (ii) to determine the changes in biomarker composition with depth in the uppermost near-surface sediments, (iii) to discuss the changes of the biomarker distributions vs. depth (time) in relationship to climate-controlled changes in biomarker input/flux and influences of diagenesis-controlled degradation processes, and (iv) to compare the new biomarker records from the NEG continental shelf with similar records from other Arctic regions (Fig. 6.1).

6.2 Background information of lipid biomarkers and organic bulk parameters

The molecular sea-ice proxy “IP₂₅”, a monounsaturated highly branched isoprenoid (HBI) alkene with 25 C atoms is an established proxy for past sea-ice reconstruction in many subarctic and Arctic regions (Belt et al., 2007; Belt, 2018). The IP₂₅ molecule is biosynthesized by four sea-ice dwelling diatom species (sea-ice algae; Brown et al., 2014).

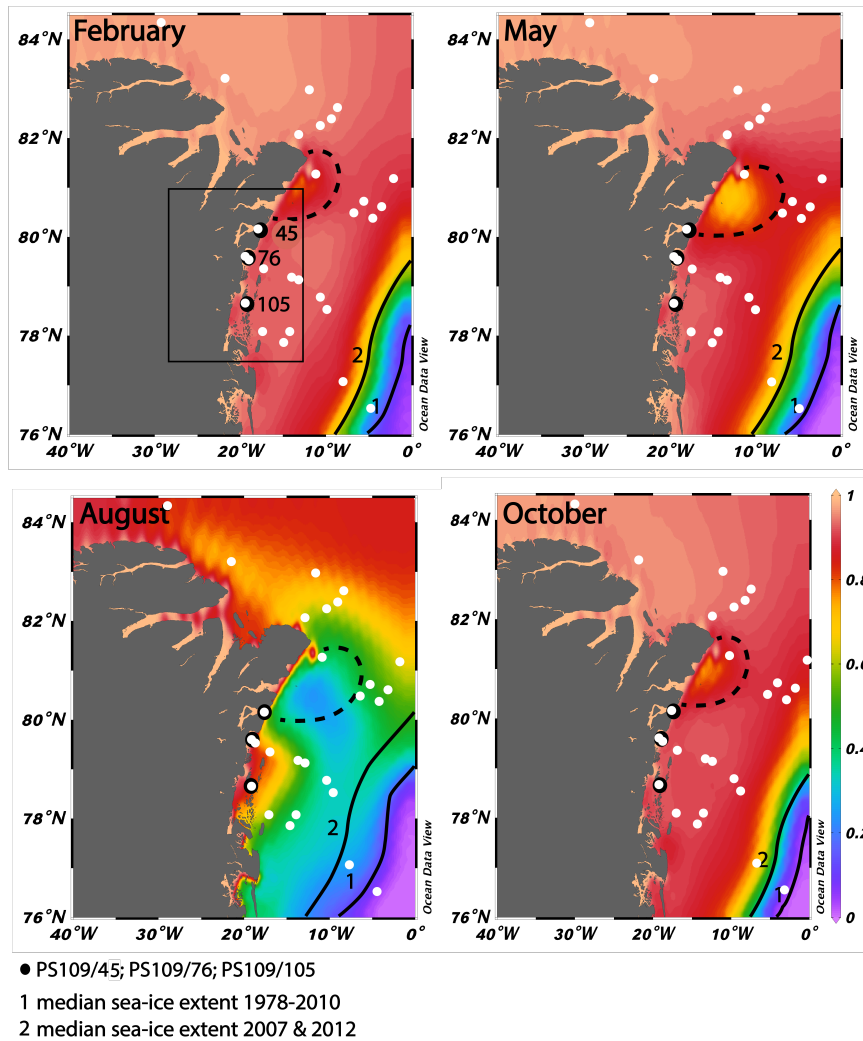


Figure 6.2: Modern satellite-derived average sea-ice concentrations (1978 to 2017) show the seasonal formation of the NEW Polynya (dashed line) during winter (February), spring (May), summer (August) and autumn (October) (<http://nsidc.org/>). White dots represent collected surface samples and black dots multicorer stations PS109/45, PS109/76 and PS109/105 off the NEG continental shelf. Black rectangle marks the satellite-derived cutout of Fig. 6.1.

The diatoms inhabit the first few cm at the base of the sea ice, and for algal colonization the ice must be thin enough to allow enough light to penetrate (Brown et al., 2011; Belt et al., 2013). These species therefore live predominantly in areas which are seasonally ice-covered, but have also occasionally been detected in central Arctic Ocean sediments (Belt et al., 2007; Brown et al., 2014c; Xiao et al., 2015a,b). IP_{25} has therefore been used as direct proxy for the presence of past sea ice on different time scales back into the Miocene (e.g. Knies et al., 2014; Stein et al., 2016; Belt, 2018). By combining IP_{25} and a phytoplankton biomarker (brassicasterol, dinosterol), the so-called PIP_{25} -index allows more semi-quantitative estimates of the sea-ice extent and its change through time (Müller et al., 2011):

$$PIP_{25} = [IP_{25}] / ([IP_{25}] + [\text{phytoplankton biomarker}] \times c)$$

$$c = \text{mean conc. } [IP_{25}] / \text{mean conc. } [\text{phytoplankton biomarker}]$$

Detailed information about the c-factor is provided in chapter 4.

This approach gives more detailed information on different sea-ice settings such as perennial sea-ice cover (high PIP₂₅), stable ice-margin (intermediate PIP₂₅) or ice-free conditions (low PIP₂₅). Recently, Smik et al. (2016) proposed to use an alternative alkene (the HBI III Z-isomer) as phytoplankton biomarker for the PIP₂₅ calculation. Both phytoplankton biomarker methods were used for calculating PIP₂₅ in this study. Further detailed information of sea-ice proxy IP₂₅, other HBIs, PIP₂₅ indices and limitations of these proxies are well explained in the reviews by Stein et al. (2012), Belt and Müller, (2013) and Belt (2018).

The terrigenous biomarkers β -sitosterol and campesterol are predominately derived from higher vascular land plants and phytoplankton biomarkers brassicasterol and dinosterol reflect changes in the open-water primary productivity (Volkman, 1986; Volkman et al., 1993). Brassicasterol may be produced by both marine and freshwater diatoms, thus is less source-specific in shelf areas of the Arctic Ocean strongly influenced by river discharge e.g. Laptev Sea, Kara Sea and Mackenzie Delta (Yunker et al., 1995; Hörner et al., 2016; Wu et al., 2020 in review). Organic bulk parameters, such as C/N ratios and $\delta^{13}\text{C}_{\text{org}}$ values, may provide estimates of higher/lower marine and/or terrigenous input (for further details see Stein and McDonald, 2004).

6.3 Material and Methods

6.3.1 Material

Surface and multicorer samples

Surface sediment samples (Table 6.1) and three multicorer (MUC) PS109/76-1, PS109/45-3 and PS109/105-2 from the NEG continental shelf were taken for biomarker and bulk parameter investigations during several RV *Polarstern* expeditions in recent years (2016 to 2018) (Stein, 2016; Kanzow, 2017, 2018; Damm, 2019). In total 27 surface sediment samples (Table 6.1) were collected by means of multicorer and giant box corer. These surface samples are assumed to represent variable conditions in modern sea-ice cover and seasonal primary productivity controlling modern organic carbon and biomarker deposition. MUC cores were sampled every cm aboard. Further each sample slice was divided into two parts, one half for biomarker, total organic carbon (TOC) and inorganic carbon (CaCO_3) measurements and the other for age determinations. To guarantee a low biomarker degradation, these samples were freeze-dried, homogenized and stored in glass vials at -20°C . Sediments of Cores PS109/76, PS109/45 and PS109/105 mostly consist of dark greyish brown, partly reddish silty clay with coarser particles of a few mm. Surprisingly, Pb datings yield no significant results, suggesting that these samples are not corresponding to modern times (<500 a), but could rather be correlated to older ages. Three ^{14}C accelerator mass spectrometry (AMS) ages were measured on a second multicore tube station PS109/105-2 that reveals ages around 6 ka, i.e. presenting a mid to late Holocene time interval with very low sedimentation rate (pers. communication Jeremy Llyod, Durham).

| Station | Latitude | Longitude | TOC (%) | IP ₂₅ ($\mu\text{g g}^{-1}$ TOC) | HBI II ($\mu\text{g g}^{-1}$ TOC) | HBI III ($\mu\text{g g}^{-1}$ TOC) | brassicasterol ($\mu\text{g g}^{-1}$ TOC) | dinosterol ($\mu\text{g g}^{-1}$ TOC) | terr. sterols ($\mu\text{g g}^{-1}$ TOC) |
|--------------|----------|-----------|---------|--|------------------------------------|-------------------------------------|--|--|---|
| PS109/19-2 | 80,15 | -7,95 | 0,47 | 13,59 | 23,08 | 4,55 | 34,86 | 38,72 | 117,45 |
| PS109/105-1 | 78,47 | -18,56 | 0,51 | 11,38 | 15,25 | 3,47 | 34,93 | 12,81 | 108,54 |
| PS109/115-2 | 78,03 | -16,54 | 0,33 | 6,57 | 8,38 | 1,72 | 17,15 | 7,54 | 111,91 |
| PS109/125-1 | 77,80 | -13,63 | 0,66 | 5,54 | 9,37 | 1,25 | 26,62 | 11,01 | 266,63 |
| PS109/129-1 | 77,91 | -13,18 | 0,24 | 9,90 | 15,91 | 1,95 | 39,01 | 25,98 | 345,30 |
| PS109/139-1 | 76,80 | -8,63 | 0,56 | 3,31 | 5,70 | 1,12 | 66,09 | 45,80 | 203,57 |
| PS109/36-2 | 76,80 | -8,63 | 0,47 | 19,24 | 32,27 | 5,71 | 50,95 | 28,63 | 83,47 |
| PS109/45-3 | 80,15 | -17,70 | 0,46 | 22,17 | 10,30 | 1,65 | 46,22 | 13,30 | 76,32 |
| PS109/76-1 | 79,62 | -19,29 | 0,56 | 5,50 | 4,98 | 1,23 | 17,83 | 6,92 | 39,68 |
| PS109/85-2 | 79,56 | -19,23 | 0,13 | 23,44 | 23,93 | 4,10 | 68,88 | 25,17 | 166,45 |
| PS109/93-2 | 79,19 | -17,12 | 0,55 | 6,25 | 8,46 | 1,54 | 10,81 | 6,02 | 42,70 |
| PS115.1/4-2 | 76,39 | -4,80 | 0,57 | 0,14 | 0,15 | 0,12 | 54,68 | 12,31 | 120,24 |
| PS115.1/6-1 | 78,44 | -8,96 | 0,78 | 0,30 | 0,45 | 0,05 | 33,22 | 20,75 | 75,33 |
| PS115.1/7-1 | 78,46 | -10,53 | 0,73 | 0,35 | 0,50 | 0,06 | 21,11 | 15,74 | 126,96 |
| PS115.1/9-4 | 78,93 | -11,76 | 0,91 | 0,45 | 0,62 | 0,10 | 26,83 | 22,88 | 73,59 |
| PS115.1/11-1 | 78,93 | -11,74 | 0,26 | 0,77 | 0,90 | 0,29 | 69,58 | 41,66 | 135,23 |
| PS115.1/17-2 | 82,18 | -10,51 | 0,40 | 0,22 | 0,17 | 0,02 | 12,05 | 7,43 | 47,52 |
| PS115.1/18-1 | 82,11 | -11,24 | 0,25 | 0,24 | 0,20 | 0,01 | 17,23 | 9,06 | 48,56 |
| PS115.1/19-2 | 81,96 | -12,65 | 0,46 | 0,38 | 0,35 | 0,02 | 18,95 | 10,28 | 44,88 |
| PS115.1/21-2 | 82,00 | -13,23 | 0,49 | 0,40 | 0,43 | 0,03 | 52,29 | 23,91 | 74,82 |
| PS115.1/22-2 | 82,28 | -9,47 | 0,56 | 0,13 | 0,13 | 0,01 | 5,11 | 3,30 | 25,64 |
| PS115.1/26-1 | 82,50 | -11,49 | 0,46 | 0,16 | 0,12 | 0,02 | 11,02 | 5,03 | 52,03 |
| PS115.1/47-2 | 84,24 | -29,60 | 0,32 | 0,06 | 0,06 | | 8,96 | 4,89 | 42,61 |
| PS115.1/48-2 | 83,12 | -20,54 | 0,32 | 0,32 | 0,29 | 0,03 | 33,05 | 17,13 | 79,78 |
| PS115.1/50-2 | 80,89 | -3,49 | 0,55 | 0,50 | 0,80 | 0,07 | 28,20 | 18,33 | 73,47 |
| PS115.1/51-2 | 80,48 | -8,49 | 0,89 | 0,71 | 1,21 | 0,11 | 35,72 | 23,33 | 70,10 |
| PS115.1/52-2 | 80,35 | -6,84 | 0,47 | 0,35 | 0,39 | 0,09 | 12,80 | 8,05 | 71,94 |
| mean values | | | | 4,90 | 6,09 | 1,13 | 31,64 | 17,26 | 100,92 |

Table 6.1: List of collected surface samples from the NEG continental shelf with coordinates and biomarker data. Mean values are used to calculate the c factor (cf., chapter 6.2).

6.3.2 Methods

Total organic carbon, carbonate and C/N ratio

Freeze dried and homogenized samples of all multicores (PS109/76-2, PS109/45-3 and PS109/105-2) were measured each cm for total organic carbon (TOC), total carbon (TC) and total nitrogen (TN). Concentrations of TOC were determined with an ELTRA CS 800 Carbon-Sulfur Determinator (PC controlled) after removing any carbonate by adding hydrochloric acid to a 0,1 g subsample. For TC and TN measurements, 20 mg of sediment were used and performed with a Carbon-Nitrogen-Sulfur Analyser (Elementar III, Vario). Based on the bulk parameters TOC and TC, CaCO_3 content was calculated by $\text{CaCO}_3 = (\text{TC} - \text{TOC}) \times 8.333$ (8.333 as stoichiometric factor), assuming that calcite is the predominant carbonate phase. To distinguish between a more terrestrial higher plant and a more marine origin of the organic matter, C/N ratios (TOC/TN) provide a first rough estimate of the primary source.

C/N ratios >15 reflect more or less a terrigenous and ratios <10 a marine origin (Bordovskiy, 1965; Meyers, 1994). However, C/N ratios should be taken with caution and general limitations of this proxy are described in Stein and Macdonald, 2004.

Lipid biomarker analysis

Lipid biomarkers, including sea-ice proxy IP₂₅, phytoplankton marker HBI III, brassicasterol (24-methylcholesta-5,22-dien-3 β -ol) and dinosterol (4 α ,23,24-Trimethyl-5 α -cholest-22E-en-3 β -ol), as well as terrigenous marker β -sitosterol (24-ethylcholest-5-en-3 β -ol) and campesterol (24-methylcholest-5-en-3 β -ol) were extracted and carried out for past climate reconstructions. Thus, 5 g of freeze-dried and ground sediment was extracted each cm and, followed by dissolution in dichloromethane/methanol (DCM/MeOH, 2:1 vol/vol) and by ultrasonification (15 min.) and centrifugation (3 min) three times. At first, internal standards 7-hexylnonadecane (7-HND, 0.076 μ g/sample), 9-octylheptadec-8-ene (9-OHD, 0,01 μ g/sample), 5 α -androstan-3 β -ol (Androstanol, 1,07 μ g/sample) and Squalan (0,32 μ g/sample) were added per sample for quantification. Separation of the hydrocarbon and sterol fraction were implemented by open column chromatography using SiO₂ gel and 5 ml n-hexane and 10 ml ethylacetat/n-hexane as solvents. As a final step before measuring, sterols were silylated with 200 μ l of BSTFA (bis-trimethylsilyl-trifluoroacet-amide) at 60°C for 2 hours. Hydrocarbon and sterol extracts were measured and integrated by using two different gas chromatography – mass spectrometers (GC-MS) with similar settings. GC-MS Agilent Technologies 7890B GC system coupled to a mass spectrometer Agilent 5977A MSD was used for the hydrocarbon fraction and run the temperature program as following: 60°C (3 min), afterwards 15°C/min until 150°C, 10 °C/min until 320°C is reached and in the final step 320°C (15 min, isothermal). The sterols were measured with a GC Agilent 6850 GC coupled to an Agilent 5975C VL mass selective detector with the temperature sequence: 60°C for 2 min, then 15°C/min until 150°C, 3°C/min until 320°C is reached and 320°C for 4 min (isothermal). The comparison of different retention times allow the identification of individual compounds, including IP₂₅ (m/z350), the HBI II (m/z 348) and the HBI III (m/z 346) with 7-hexylnonadecane as an internal standard (Belt et al., 2007; Brown et al., 2014) and brassicasterol (m/z 470), campesterol (m/z 472), β -sitosterol (m/z 486) and dinosterol (m/z 500) (Boon et al., 1979; Volkman, 1986) with Androstanol (m/z 348) as internal standard for the quantification. A detailed introduction of the calibration methodology for hydrocarbon and sterol quantification is described by Fahl and Stein (2012) and Belt et al., 2013, 2014.

6.4 Results

Organic bulk parameters and lipid biomarker concentrations were determined in 27 surface samples and three short cores to get information about modern and past sea-ice conditions and diagenetic alteration of organic matter on the NEG continental shelf.

6.4.1 Surface samples

Lowest biomarker concentrations occur north of 82°N and along the outer NEG continental shelf (Fig. 6.3): IP_{25} ($0\text{--}3\ \mu\text{g g}^{-1}\ \text{TOC}$) and HBI II ($0\text{--}3\ \mu\text{g g}^{-1}\ \text{TOC}$), terrigenous biomarkers ($\sim 50\ \mu\text{g g}^{-1}\ \text{TOC}$), phytoplankton-derived biomarkers brassicasterol ($0\text{--}20\ \mu\text{g g}^{-1}\ \text{TOC}$), dinosterol ($0\text{--}10\ \mu\text{g g}^{-1}\ \text{TOC}$) and HBI III ($0\text{--}1\ \mu\text{g g}^{-1}\ \text{TOC}$). These samples reflect near perennial sea-ice conditions (Fig. 6.4).

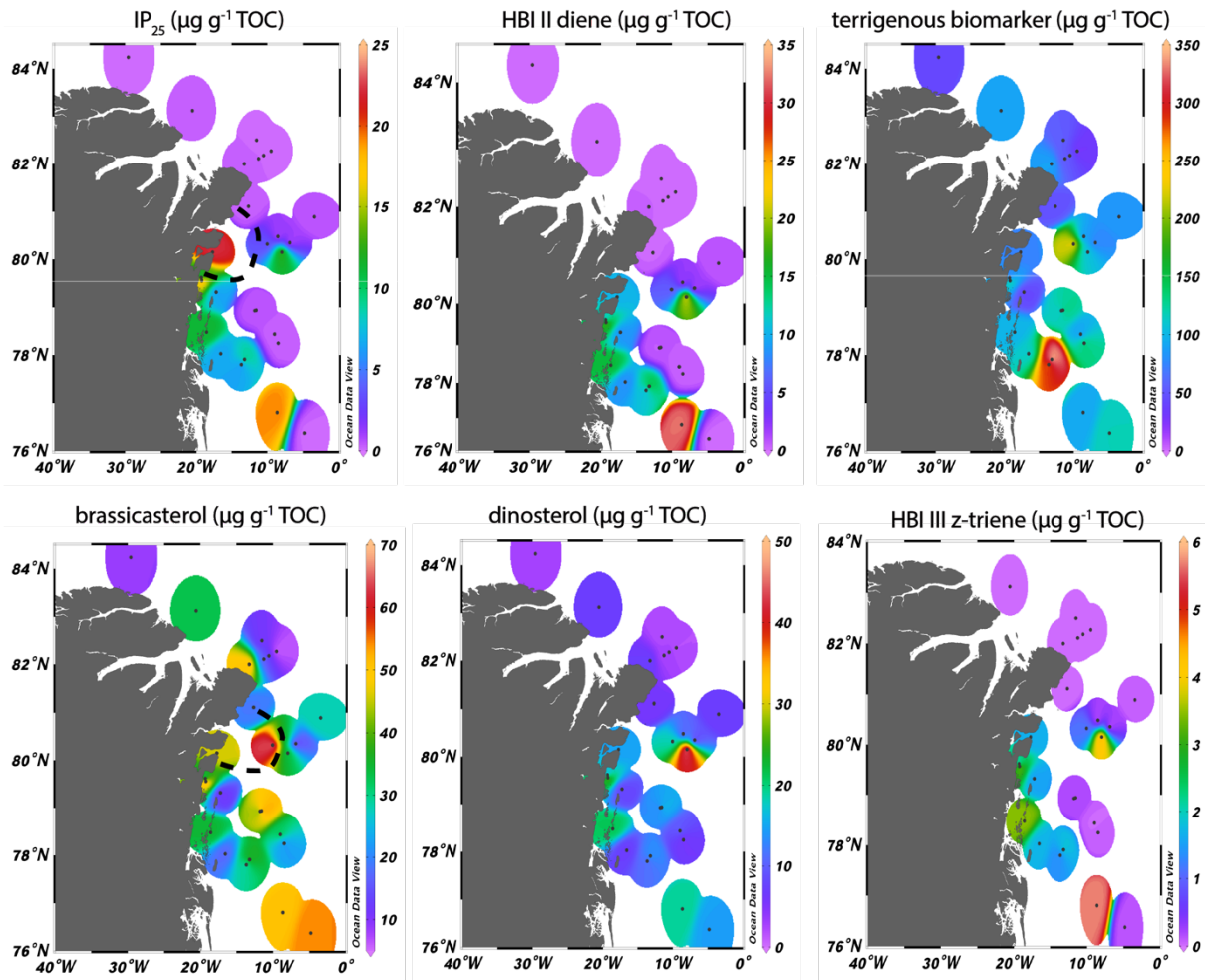


Figure 6.3: Overview maps showing collected surface sediment samples (black dots) and biomarker concentrations from the NEG continental shelf. Concentrations ($\mu\text{g g}^{-1}\ \text{TOC}$) of sea-ice associated biomarkers IP_{25} and HBI II, terrigenous biomarkers, phytoplankton biomarkers brassicasterol, dinosterol and HBI III are indicated by the color shaded areas. Dashed line indicates the NEW Polynya.

The inner NEG continental shelf is dominated by overall intermediate biomarker concentrations to relatively high biomarker concentrations of sympagic produced IP_{25} with values up to $25\ \mu\text{g g}^{-1}\ \text{TOC}$ and phytoplankton marker brassicasterol (up to $70\ \mu\text{g g}^{-1}\ \text{TOC}$) were observed within or near the NEW Polynya (Fig. 6.3). Samples from the inner shelf mainly range in the MIZ (Fig. 6.4).

In contrast, dinosterol (up to $20\ \mu\text{g g}^{-1}\ \text{TOC}$), HBI III (up to $2\ \mu\text{g g}^{-1}\ \text{TOC}$) and terrigenous biomarkers ($100\text{--}250\ \mu\text{g g}^{-1}\ \text{TOC}$) within the NEW Polynya are relatively low (Fig. 6.3). Intermediate

concentrations of sea-ice biomarkers IP₂₅ (~13 $\mu\text{g g}^{-1}$ TOC) and HBI II (~15 $\mu\text{g g}^{-1}$ TOC), phytoplankton biomarker brassicasterol (~40 $\mu\text{g g}^{-1}$ TOC), dinosterol (~25 $\mu\text{g g}^{-1}$ TOC) and HBI III (~3 $\mu\text{g g}^{-1}$ TOC) occur close to the outlets 79NG and ZI of NEGIS. Outer shelf surface samples are partly distributed in the MIZ or reflect reduced to variable sea-ice conditions (Fig. 6.4).

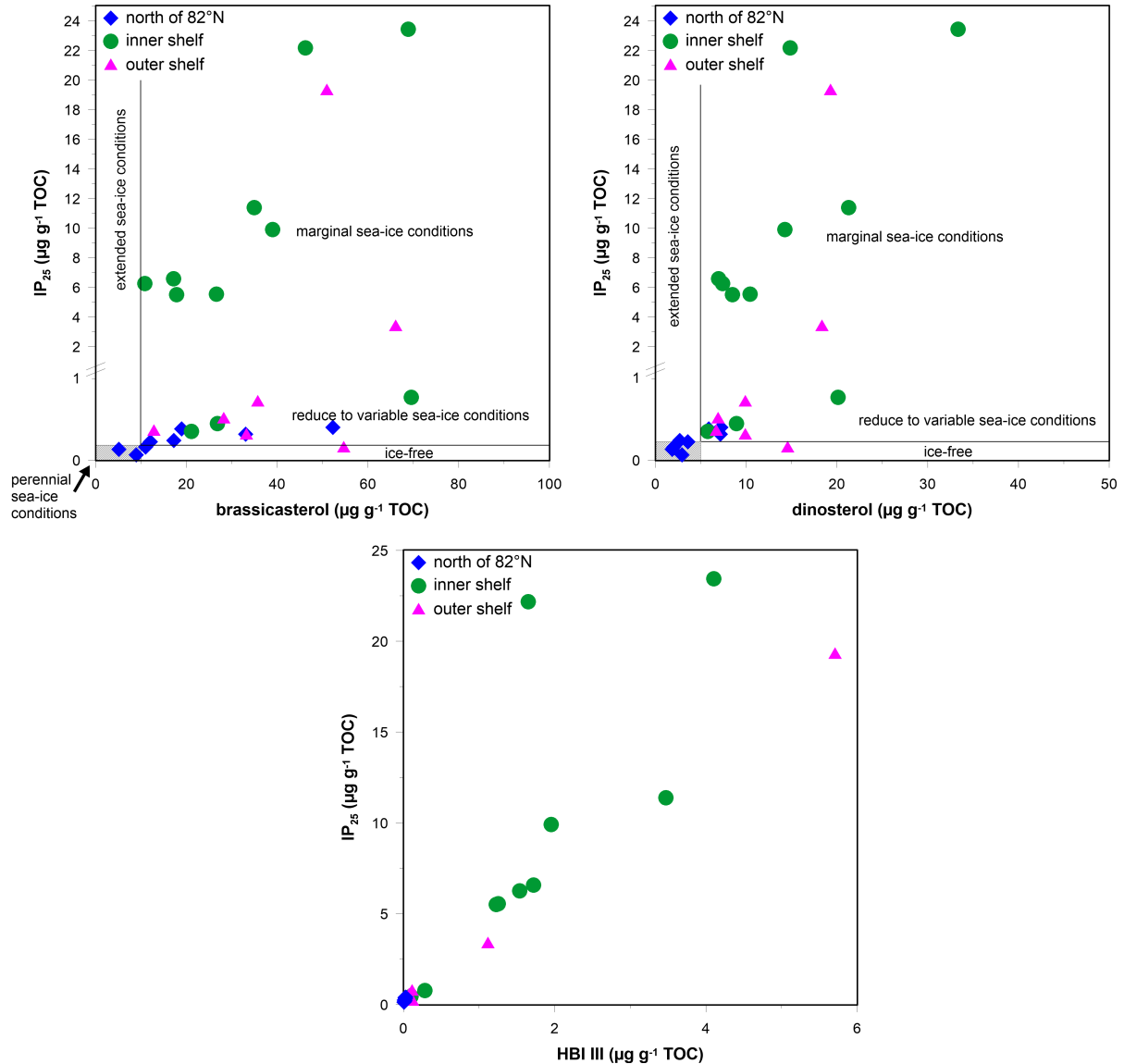


Figure 6.4: IP₂₅ ($\mu\text{g g}^{-1}$ TOC) versus phytoplankton brassicasterol, dinosterol and HBI ($\mu\text{g g}^{-1}$ TOC) showing surface samples in the three distinct environmental areas: north of 82°N, inner and outer shelf. Classification of different sea-ice settings are according to Müller et al. (2011).

6.4.2 Subsurface samples

The studied MUCs were taken from the Dijnphna Sound (PS109/45-3, 0–33 cm), within the embayment of the 79NG (PS109/76-1, 0–36 cm) and near Jøkelbugten region close to Zachariae Isstrøm (PS109/105-1, 0–36 cm) (Fig. 6.1).

Organic bulk parameters

TOC contents of MUCs PS109/105 while PS109/45 range between 0.1 to 0.5% while MUC PS109/76 shows much lower TOC values between ~0.08 to 0.2%. Inorganic carbon (CaCO_3) is highest in PS109/76 with maximum values of 20 wt.% and lowest of 8 wt.%, but overall strongly fluctuates throughout the 36 cm (Fig. 6.5). CaCO_3 content of PS109/45 seems more stable, displaying elevated values up to 16 wt.% in the top 10 cm and lowered values below 10 cm (Fig. 6.5). CaCO_3 content of PS109/105 shows an opposite trend with lowered values between 4 to 6 wt.% in the top 10 cm and slightly increased values up to 10 wt.% and one distinct peak (16 wt.%) below 10 cm (Fig. 6.5). C/N ratios of all short cores fall rarely below 8 and point towards a predominantly terrigenous source of organic matter (Fig. 6.5).

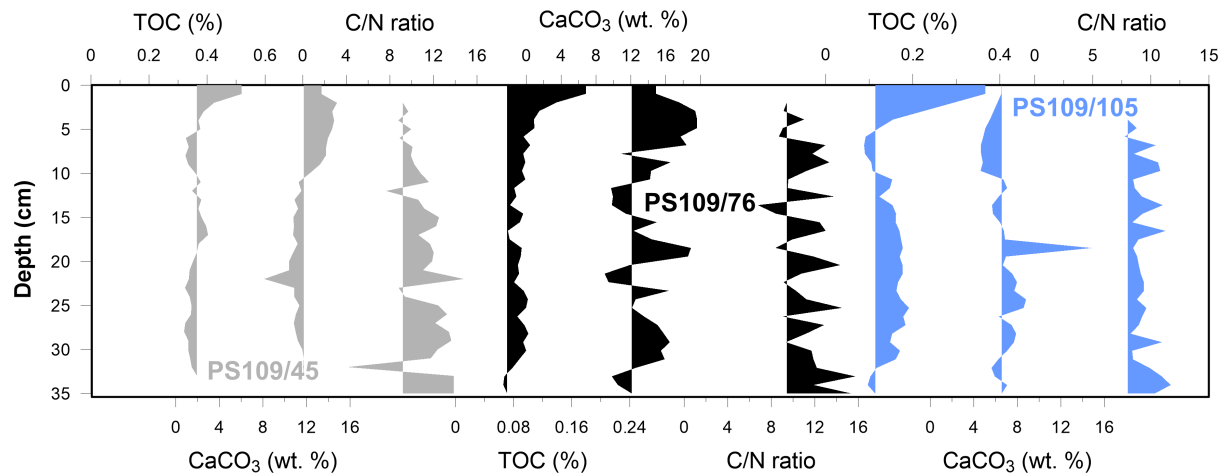


Figure 6.5: Organic bulk parameter records of PS109/45 (grey), PS109/76 (black) and PS109/105 (blue) against depth (cm). Shaded areas mark the maxima and minima of each record.

Lipid biomarker

In contrast, MUCs PS109/76 and PS109/105 sharply drop off after the first 3 cm, but fluctuate and show recurrent intervals/cycles of high values similar to the ones at the beginning (Fig. 6.6). Terrigenous biomarker concentrations (β -sitosterol plus campesterol) are on average $20 \mu\text{g g}^{-1}$ TOC in PS109/76 and $\sim 5 \mu\text{g g}^{-1}$ TOC in PS109/105 (PS109/76 is almost four times higher in terrigenous biomarker concentrations). Phytoplankton biomarker brassicasterol ranges between 2.5 and $\sim 10 \mu\text{g g}^{-1}$ TOC in PS109/76 and between 1 and $5 \mu\text{g g}^{-1}$ TOC in PS109/105, dinosterol between ~ 4 and $10 \mu\text{g g}^{-1}$ TOC in PS109/76 and 1 and $6 \mu\text{g g}^{-1}$ TOC in PS109/105 and HBI III mostly between 0.08 and $0.16 \mu\text{g g}^{-1}$ TOC in PS109/76 and between 0.05 and $0.5 \mu\text{g g}^{-1}$ TOC in PS109/105 (Fig. 6.6).

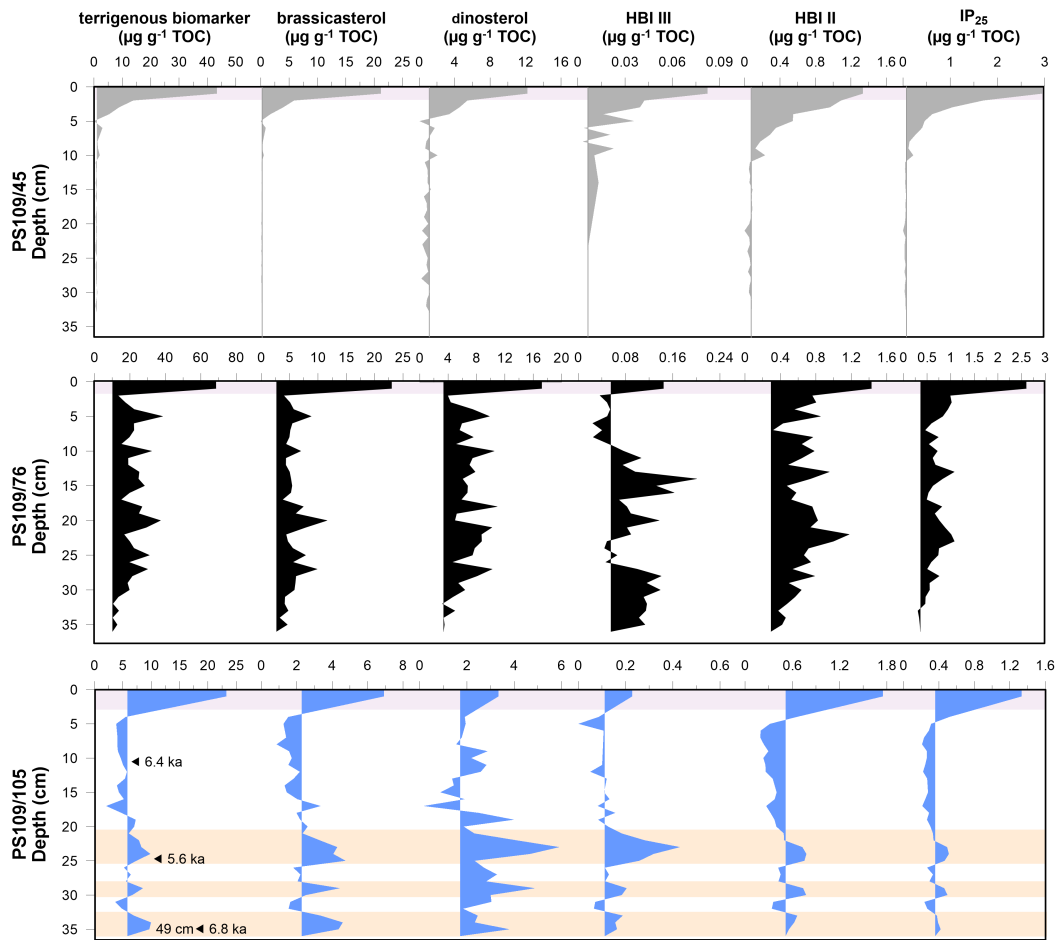


Figure 6.6: Lipid biomarker downcore profiles of PS109/45 (grey), PS109/76 (black) and PS109/105 (blue) against depth (cm). Each biomarker column runs downward e.g. first column represent terrigenous biomarkers, second column brassicasterol and so on. Shaded areas mark the maxima and minima of each record. Grey bar at the top of each record series represent degradational processes in the upper cm. Orange bars in PS109/105 indicate contemporaneous maxima of all parameters.

Additionally, all phytoplankton biomarkers of PS109/105 exhibit a high distinct peak between 20 to 25 cm and two smaller peaks at 28–30 cm and 33–36 cm which correlate positively with elevated TOC and sea-ice associated biomarker concentrations of HBI II and IP₂₅ (Fig. 6.6). The latter show that HBI II values range between 0.2 and 1.6 $\mu\text{g g}^{-1}$ TOC in both MUCs and IP₂₅ concentrations vary between 0.25 and 1.25 $\mu\text{g g}^{-1}$ TOC in PS109/76 and on average around 0.4 $\mu\text{g g}^{-1}$ TOC in PS109/105 (Fig. 6.6).

6.5 Discussion

In order to study modern sea-ice distribution, past climate reconstruction and diagenetic alteration of sediments of in a highly versatile environmental system (Fig. 6.1, 6.2), organic bulk parameters (TOC, C/N and CaCO₃) and lipid biomarkers (HBIs, specific sterols) were determined in a number of sediment surface samples (Table 6.1) and sub-surface sediments of three MUCs (PS109/45, PS109/76 and PS109/105) located on the inner and outer NEG continental shelf (Fig. 6.1B).

Overall, results of measured lipid biomarker surface concentrations generally match with the satellite-derived data (Fig. 6.2, 6.3, <http://nsidc.org/>). Nonetheless, these results should be considered with caution, because i) the study of surface sediment is limited to a relative small number of samples, ii) there is no exact age control of the MUC cores and iii) the study area is characterized by diverse environmental conditions such as the NØIB landfast ice barrier on the inner shelf, the NEW Polynya in the North and extensive amounts of drift ice (low IP₂₅ values) to the east.

6.5.1 Modern sea-ice conditions

According to surface samples of this study, the area between 82°N and 84°N document lowest concentrations of all biomarkers. Cold harsh environmental conditions all year round and minor seasonal sea-ice break up during summer months are probably the reason for minimum concentration in this area (Fig. 6.2, 6.3, 6.4). Short sea-ice break ups allow only little phytoplankton growth and productivity in the open-water milieu after long phases of extended to permanent sea-ice conditions. This area is usually characterized by thickest sea ice off NEG. Sea ice formed on the Siberian shelves drifts across the central Arctic via the TPD and gets pushed against NEG rugged coast, where it becomes more compact and piles up.

South of 82°N most of the fjord systems off NEG are bound by a semi-permanent sea-ice cover to the east. Recent years, especially 2018 and 2019, demonstrate increased seasonal sea-ice break-up along the NEG coast and show that the thick sea-ice cover is highly susceptible to rising air temperatures (<http://nsidc.org/>). Therefore, it was possible to maneuver for the first time on the NEG shelf north of 84°N with *RV Polarstern* up to the southern edge of the Morris Jesup Rise during Expedition PS115.1 in 2018 (Damm et al., 2019).

Highest IP₂₅ and phytoplankton marker brassicasterol concentrations were observed within or near the NEW Polynya (Fig. 6.3, 6.4). The seasonal formation of the NEW Polynya starts in spring (April/May) and freezes-up again in late autumn/early winter (October/November) (Fig. 6.1B, 6.2). Surface samples located near this MIZ are subject to a pronounced seasonality, which is well documented in modern sea-ice concentrations (Fig. 6.2). Surprisingly, not all biomarkers like dinosterol and HBI III indicate a high productivity and/or enhanced terrigenous supply within the NEW Polynya, which is usually quite common due to ideal environmental conditions comprising sea-ice melt and open-water spots.

The predominance of intermediate biomarker concentrations is indicated by modern satellite-derived sea-ice observations (Fig. 6.2) and results from direct proxy measurements (Fig. 6.3, 6.4) near the two marine outlets 79NG and ZI of NEGIS, bounded by the NØIB to the east. Since 2000 sea-ice conditions have drastically changed from perennial conditions towards a seasonal sea-ice cover and/or stable ice margin with frequent seasonal breakups and/or the complete disintegration of NØIB during summer (Fig. 6.1B; Sneed et al., 2016). Simultaneously, sea-ice biomarkers IP₂₅ and HBI II, next to moderate phytoplankton biomarker concentrations of brassicasterol, dinosterol and HBI III and terrigenous

material of this study express seasonal sea-ice condition rather than a perennial ice-cover. Large parts of the middle and outer NEG shelf become relatively ice-free during the summer months, but are still influenced by drifting ice floes (regional and local). Drift ice from the interior of the Arctic Ocean exhibits relatively low IP_{25} concentrations and is a characteristic feature along the NEG and East Greenland continental shelf. Based on our low sea-ice biomarker concentrations of IP_{25} and HBI II (Fig. 6.3, 6.4), reduced sea-ice to seasonal sea-ice conditions appear predominant. Beside wide areas of open water and sea-ice melt may accommodate enhanced phytoplankton productivity to some extent. On the other hand, nutrient supply by the cold, fresh EGC is limited in this area (e.g. Hirche et al., 1991).

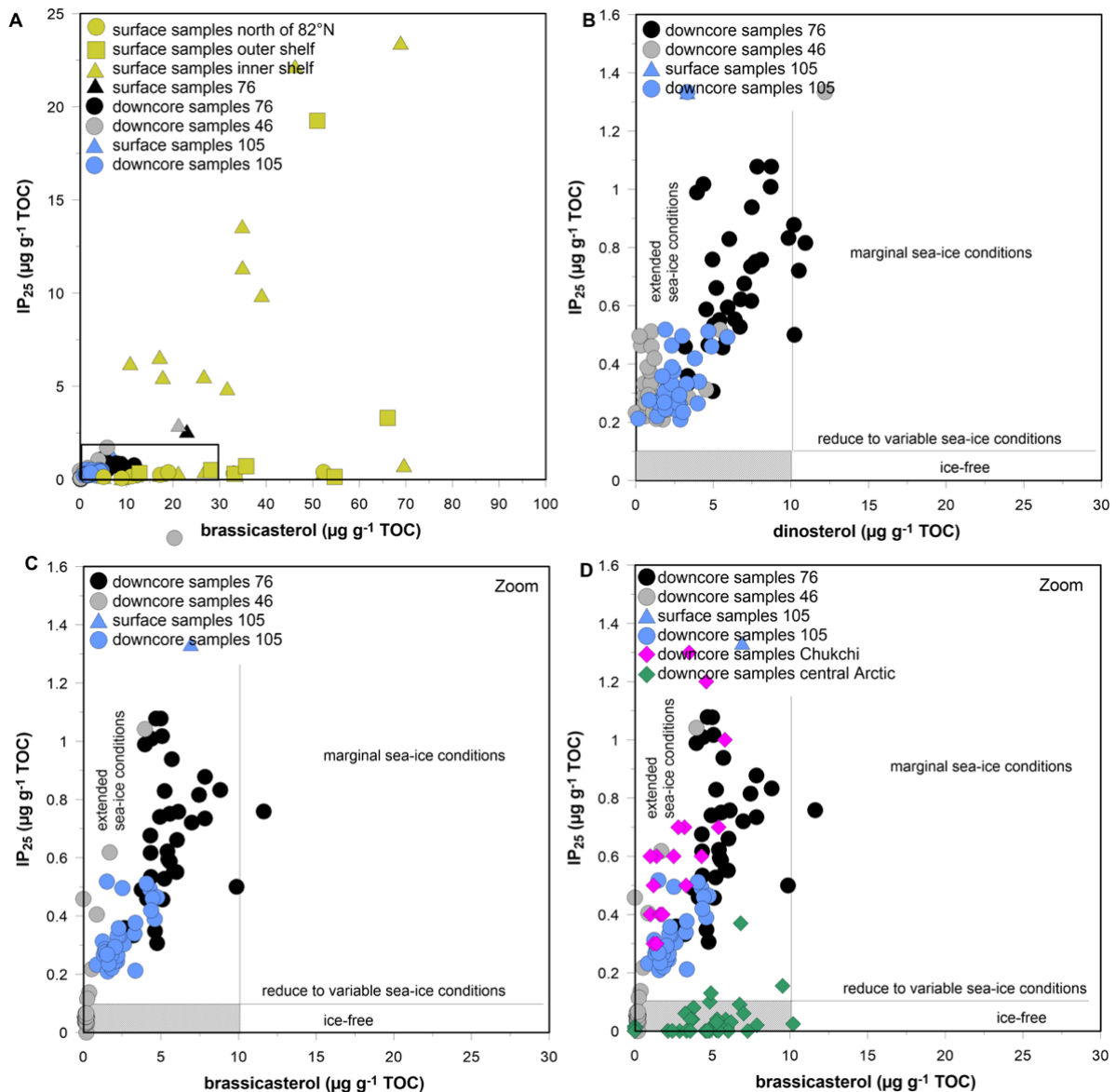


Figure 6.7: A. IP_{25} ($\mu\text{g g}^{-1}$ TOC) versus phytoplankton brassicasterol ($\mu\text{g g}^{-1}$ TOC) showing surface samples together with PS109/45, PS109/76 and PS109/105 downcore records. B/C/D Concentrations of all MUCs (zoomed in from black rectangle in A) displaying IP_{25} against each phytoplankton biomarker B) dinosterol, C) brassicasterol and D) brassicasterol in comparison with records from the central Arctic Ocean (Xiao et al., 2015) and Chukchi Sea (Kim et al., 2019). Lower left rectangle marks the perennial ice zone.

6.5.2 Past climate reconstructions

Core top samples of all MUC cores with a fresh surface (0–2 cm) often contain considerably higher concentrations of TOC and lipid biomarkers than the downcore material (Fig. 6.5 and 6.6) as also observed in other Arctic records (Fig. 6.7 and 6.8; Müller et al., 2009, 2011; Müller and Stein, 2014; Xiao et al., 2015; Kolling et al., 2020; Wu et al., 2020). A circum-Arctic study by Kolling et al. (2020) on surface samples shows similar biomarker concentrations in the Baffin Bay, Beaufort Sea, Chukchi Sea and Northeast Greenland regions. Surface samples of PS109/45, PS109/76 and PS109/105 reflect stable-ice edge to ice free conditions (Fig. 6.7A). Besides, preliminary results of this study can be compared with the uppermost 80 cm of Gravity Core PS100/270, located in front of the marine terminating 79NG, representing the last ~7.9 ka and characterised by low sedimentation rates. Based on the AMS ^{14}C ages of PS109/105 (for explanation see chapter 6.3.1), the investigated MUC cores of this study suggest a mid to late Holocene age, and also relatively low sedimentation rates. Nonetheless, an exact age control for these records are not ensured.

Dijmphna Sound (PS109/45)

Very low organic bulk parameter and near zero biomarker concentrations occur between 33 cm to 10 cm of PS109/45, which afterwards gradually increase and prevail highest values within the uppermost 10 cm (Fig. 6.8). C/N ratios mostly above 10 demonstrate a higher terrigenous influence rather than a marine signal at the PS109/45 station. Perhaps, these low concentrations below 10 cm (Fig. 6.8) are related to extended to perennial sea-ice conditions as suggested from the IP_{25} vs. phytoplankton plot (Fig. 6.7). The extensive sea-ice cover hampers the colonization of sea-ice algae and primary productivity due to the lack of light, nutrients and open water spots. On the other hand, minor phytoplankton productivity could be possible also beneath an extensive sea-ice layer through leads and polynyas, allowing at least some light penetration (Willems and Heinemann, 2016) and would explain lowered dinosterol concentrations throughout the record (Fig. 6.8). Neoglacial Cooling during the mid to late Holocene may have blocked the Dijmphna Sound with extensive sea-ice masses all year round (see data record PS100/270; see chapter 5). These extremely low biomarker concentrations in the Dijmphna Sound are comparable to perennial sea-ice conditions in the central Arctic Ocean (Fig. 6.7; Xiao et al., 2015). Nowadays, sea ice in the Dijmphna Sound starts to break up in late July/early August and the Sound itself becomes ice-free in late August/September and underlies generally cool conditions (Fig. 6.1B). Anyhow, in recent years the ice margin in the Dijmphna Sound frequently disappeared completely and caused major calving events there (Reeh et al., 2017; <https://worldview.earthdata.nasa.gov>). Results of PS109/45 are similar to those from central Arctic Ocean records (Fig. 6.8; Xiao et al., 2015).

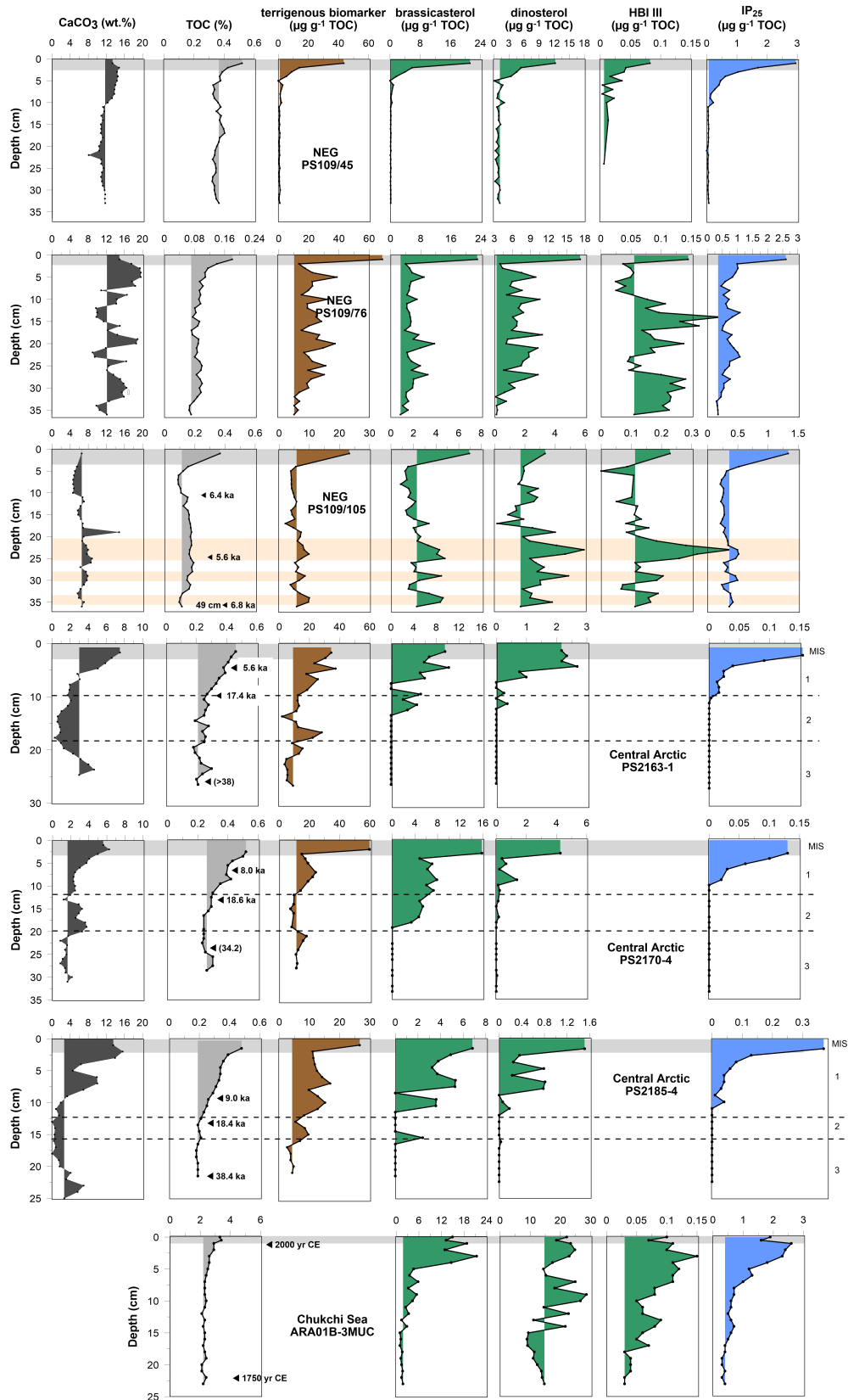


Figure 6.8: Multicorer records of this study (NEG MUCs PS109/45, PS109/76 and PS109/105) in comparison with records from the central Arctic Ocean (Xiao et al., 2015) and Chukchi Sea (Kim et al., 2019). Organic bulk parameter TOC (%), represent terrigenous biomarkers, phytoplankton biomarkers brassicasterol, dinosterol and HBI III and sea-ice biomarker IP₂₅ against depth (cm). Grey bars at the top of each record series highlight prominent maxima decreasing downwards that may represent degradational processes in the upper first cm. Orange bars in PS109/105 indicate contemporaneous maxima of all parameters.

Embayment of 79NG (PS109/76)

PS109/76 biomarker records sharply drop off after the first 3 cm, but fluctuate and show recurrent intervals/cycles of high values, similar to the peak at the top (Fig. 6.8). In the embayment of the 79NG, sea-ice conditions at PS109/76 seem highly variable and might indicate a small-scale cyclicality pattern (up to 4 cycles) (Fig. 6.8). TOC (~0.08%) values are relatively low compared to those of PS109/45 and PS109/105. Phases of increased/lowered CaCO₃ anticorrelate with minimum/maximum intervals of C/N ratios, possibly triggered by strong variations between marine vs. terrigenous input. Sympagic biomarker IP₂₅ along with the presence of pelagic produced HBI III and high sterol concentrations of brassicasterol, dinosterol and terrigenous biomarkers support the existence of a stable, seasonally sea-ice margin, high overall productivity, and vertical stabilization, which is necessary for the pelagic spring and summer blooms on the inner NEG shelf (Fig. 6.8). The IP₂₅ vs. phytoplankton plot supports the assumption of marginal sea-ice conditions (Fig. 6.7). These biomarker records are partially disrupted by changing conditions with lowered primary productivity (minimum values) e.g. at ~5, ~15 and ~25 cm (Fig. 6.8).

Jøkelbugten area (PS109/105)

Southward of PS109/76, PS109/105 located near Jøkelbugten close to ZI, is also characterized by a cyclicality pattern (two larger cycles), different though from PS109/76, showing overall much lowered TOC and biomarker concentrations (PS109/76 values are two times higher, Fig. 6.8). A precipitous decrease of nearly all biomarkers are found between 3 and ~20 cm right after the maximum values within upper cm (Fig. 6.8), which shows the presence of an extensively sea-ice covered region with seasonally open waters.

Still relatively low TOC, high terrigenous and phytoplankton biomarker concentrations of brassicasterol, dinosterol and HBI III and intermediate sea-ice associated HBI II and IP₂₅ values in the second part of the record after ~20 cm pointing towards marginal to partly reduced sea-ice conditions with prolonged summers and open waters (Fig. 6.7, 6.8). Pronounced peaks of phytoplankton biomarkers at 23 cm, 28 cm and 35 cm show intervals of enhanced primary productivity, which correlate positively with TOC and sea-ice algae productivity. The scatter plot of IP₂₅ vs. the phytoplankton biomarkers brassicasterol and dinosterol are consistent with these outcomes of extended towards marginal sea-ice conditions (Fig. 6.7).

6.5.3 Diagenetic degradation vs. primary signal

Diagenetic effects, i.e., degradation processes, may have altered organic bulk parameters and lipid biomarker concentrations in sedimentary records and should be considered when interpreting organic-geochemical proxies for reconstructions of the paleoenvironment (Rontani et al., 2011, 2014, 2018).

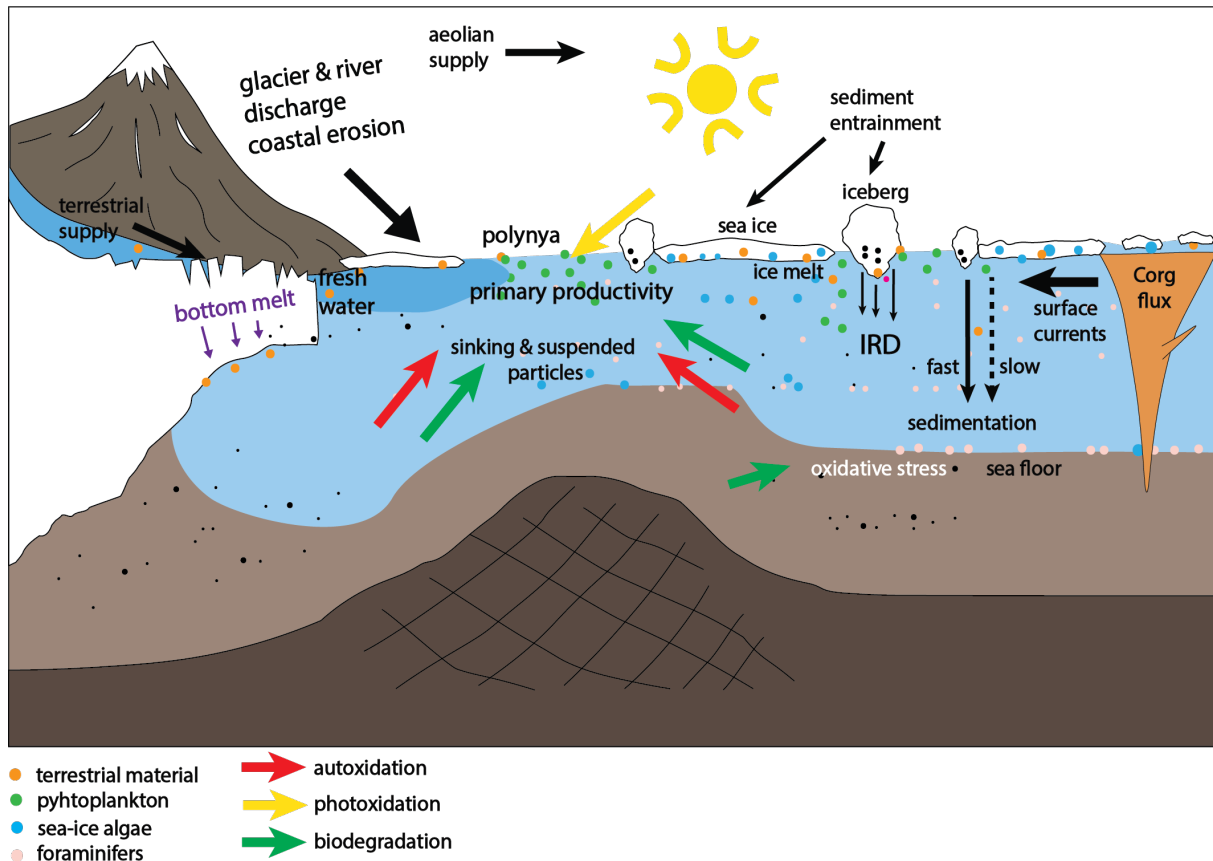


Figure 6.9: Simplified schematic showing general processes on an Arctic shelf, including sediment supply and accumulation, primary productivity and degradation processes (modified after Stein, 2008 and Rontani et al., 2014).

However, most of the related studies of Arctic sediments only incidentally mention diagenetic degradation under the assumption that a predominately primary signal prevails. In this context, primary signal means the value of a specific proxy (e.g. biomarker concentrations, TOC content etc.) that is related to the primary input and accumulation of specific (biogenic and non-biogenic) particles in the sediment. These signals may already obtain, of course, information about diagenetic processes that have occurred before the particles have reached the seafloor, e.g., degradation of organic matter through the transport by rivers, ice and glaciers and its pathway in the open ocean (Fig. 6.9; Belt and Müller, 2013; Rontani et al., 2014, 2018). Concerning degradation of organic matter, three main processes can be distinguished (Fig. 6.9; cf., Rontani et al., 2014): i) photoxidation: through sunlight, depending on the light absorption, ii) autoxidation: through oxygen for example in the euphotic zone or in the sediment, while pace of this degradation process is relatively slow and iii) biodegradation: comprises the breakdown of organic matter through microbial activity, such as bacteria and fungi (Rontani et al., 2014, 2018). Degradation of HBIs, for example, depends on the number of double bonds, the higher the unsaturation, the higher susceptible to degradation, which confirms that IP₂₅ is less prone to photo-degradation (Rontani et al., 2011).

Sediment traps deployed at the southern Lomonosov Ridge, for example, show that marine organic matter (bulk parameters and lipid biomarkers) decrease systematically from 150 to 1550 m depth,

indicating biochemical degradation during its path from the surface water towards the deep ocean (Fahl and Stein, 2012). In these biomarker records, IP₂₅ is decreasing by a factor of 5 and brassicasterol by a factor of 3, the change of calculated PIP₂₅ indices become smaller with increasing water depth (Fahl and Stein, 2012). Sympagic produced biomarkers seem often to be more susceptible towards biotic and abiotic degradation in the water column than their counterpart, the pelagic communities (Leventer, 2013; Rontani et al., 2018a,b). Hence, decreasing biomarker concentration during the transfer through the water column need to be considered when interpreting absolute biomarker concentrations and calculated PIP₂₅ indices in sedimentary records (Fahl and Stein, 2012).

Surprisingly, degradation of IP₂₅ usually does not occur in the sea-ice habitat itself, while HBIs with more double bonds react more sensitive to oxidation in Arctic sea ice (Rontani et al., 2014a). In the photic zone of the ocean, pelagic grazing and nutrient recycling may modify the biomarker signal, but would also mean, that the impact on all biomarkers might take place equally. Roughly one third of biomarker material have been degraded in the water column, which significantly alters the amount of sediment accumulation. Of course, the primary signal could underlie diagenetic processes after sediment accumulation such as biodegradation through oxidative stress (Rontani et al., 2014). Pathways of diagenetic processes in the Arctic Ocean are shown in Fig. 6.9.

To receive more detailed insights into diagenetic alteration affecting downcore biomarker records, this study was compared to records (Fig. 6.7, 6.8) from the Chukchi Sea (Kim et al., 2019), central Arctic Ocean (Fig. 6.7, 6.8; Xiao et al., 2015) and Beaufort Sea, Canada (Rontani et al., 2018). Surface and downcore samples from the NEG continental shelf and other Arctic regions show that absolute numbers in surface samples (first few cms) are often much higher than downcore concentrations (Fig. 6.8; Müller et al., 2009, 2011; Müller and Stein, 2014; Xiao et al., 2015; Kim et al., 2019; Kolling et al., 2020; Wu et al., 2020).

When concentrations of organic bulk parameters and lipid biomarkers are low or near zero within the records or in specific intervals, it is important to notice, if they were altered by diagenesis and/or because it is a climate-induced signal driven by changes in the primary fluxes, for example during glacial/interglacial stages. Records from the central Arctic Ocean represent the transition in a two-step change from the last glacial period to Holocene interglacial period and probably obtain a climate-induced signal rather than diagenetic alteration (Fig. 6.8; Stein et al., 1994a, b; Xiao et al., 2015). Organic bulk parameters and biomarkers show distinct maxima typical for the Holocene sections (Stein et al., 1994b). Time frames are generally much wider in the central Arctic Ocean due to the extremely low sedimentation rates. In contrast, Holocene sedimentation rates of our records from the NEG continental shelf are higher and show a distinct decrease within the first ~5 cm, respectively, except for CaCO₃ (Fig. 6.8). Up to a five-time higher concentration occurs in surface samples than those of the downcore records off NEG continental shelf, depending on the area on the shelf (Fig. 6.7A).

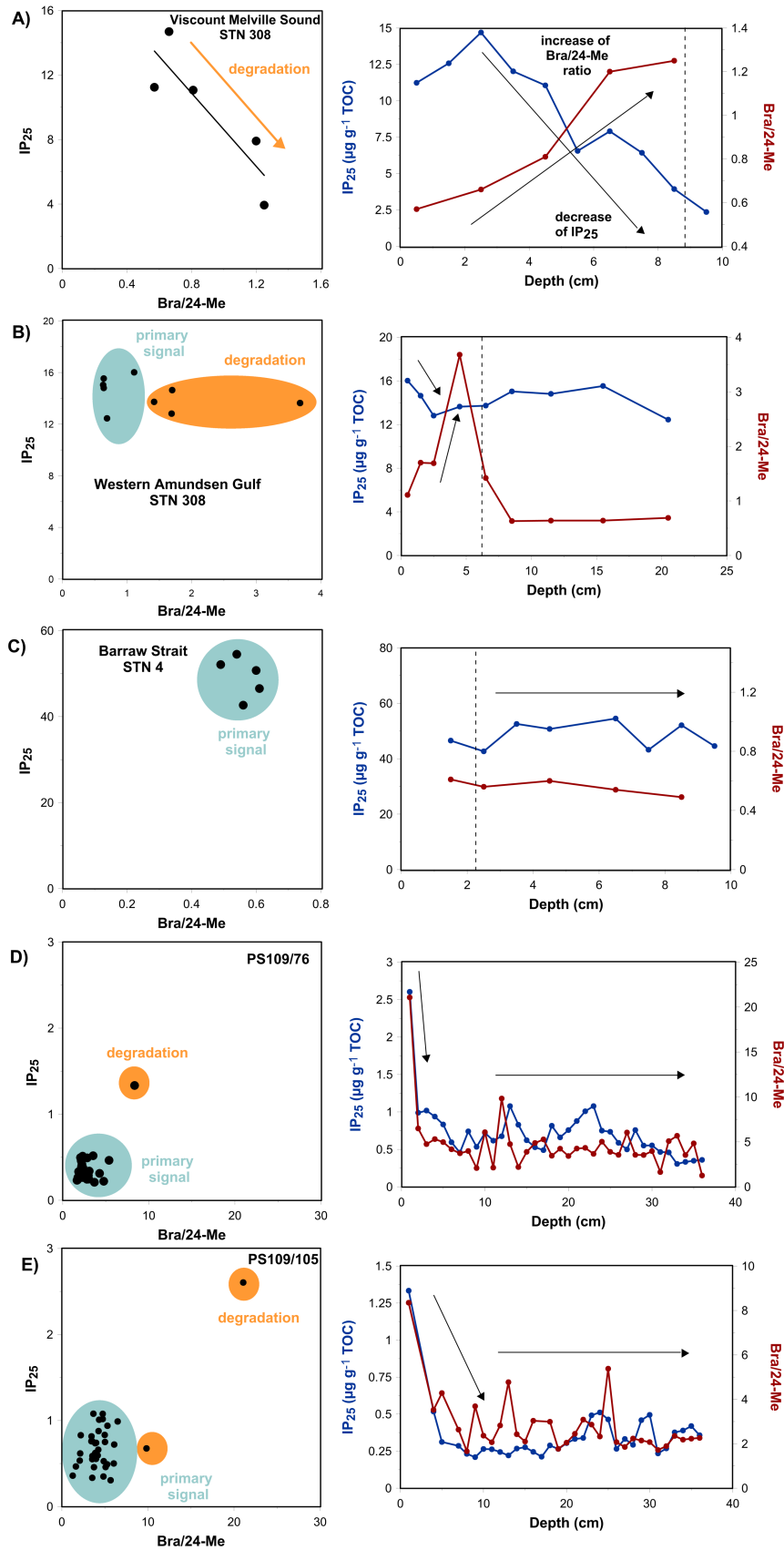


Figure 6.10: Comparison of MUC records from the Beaufort Sea (A–C; Rontani et al., 2018) and this study (D and E). X-y plot IP₂₅ vs. Bra/24-Me are shown to the left and syngagic biomarker IP₂₅ and Bra/24-Me vs. depth (cm) to the right for different regions A) Viscount Melville Sound STN 308, B) Western Amundsen Gulf STN 408, C) Barrow Strait STN 4, D) PS109/76 and E) PS109/105. Dashed lines in A–C represent their redox boundaries.

To describe diagenetic alteration, Rontani et al. (2018) compared IP₂₅ concentrations and epi-brassicasterol/24-methylenecholesterol (Bra/24-Me) ratios in records from the Beaufort Sea, which were partly accumulated under anoxic and oxic sediment conditions. 24-Me reacts stronger than brassicasterol towards autoxidative processes in phytoplanktonic cells, suggesting an increase in the Bra/24-Me ratio might be potentially attributed to diagenetic alteration in marine sediments (Fig. 6.10A). Decreasing IP₂₅ concentrations along with increasing Bra/24-Me at site STN 308, i.e., a negative correlation between both proxies were related to enhanced aerobic biodegradation or autoxidation (Fig. 6.10A; Rontani et al., 2018). This is shown in the negative trend in the IP₂₅ vs. Bra/24-Me plot (Fig. 6.10A). The distribution of cluster of points in the IP₂₅ vs. Bra/24-Me plot and the negative correlation in the uppermost ~5 cm in the Western Amundsen Gulf MUC records (Fig. 6.10B) probably also reflects biomarker degradation (Fig. 6.10B). The quite well-correlating records of IP₂₅ and Bra/24-Me of MUCs from the Barrow Strait, PS109/76 and PS109/105, on the other hand, suggest that the sedimentary signal is predominately primary (Fig. 6.10C–E). The latter is characterized by distinct point clouds in the IP₂₅ vs. Bra/24-Me plot while surface samples significantly stand out due to their high biomarker concentration (Fig. 6.10 C–E). 24-Me was below detection limit in PS109/45, aligning with near zero biomarker concentration and were therefore neglected (Fig. 6.8).

One possible explanation for the strong decline in the upper few cm of our records might be related to autoxidation and/or aerobic biodegradation of biomarkers in sediments possessing an oxic layer at the top (Robson and Rowland, 1988; Rontani et al., 2018). The contact between accumulated sea-ice algae or phytoplankton material and oxygen could facilitate a pathway for biomarker degradation within near-surface sediments. Consistent with this assumption, is the strong decrease in biomarker concentration of all NEG continental shelf collected MUCs (Fig. 6.8).

6.6 Conclusion

Preliminary results of this study of modern and past sea-ice distribution on the NEG continental shelf can be summarized as follows:

- In general, results from measured surface biomarker concentration and satellite-derived sea-ice concentrations (2019) are consistent. Nearly all surface samples reflect extended (permanent) to marginal seasonal sea-ice conditions.
- Our MUC records show the presence of sea ice varying from near perennial conditions (PS109/45) and a mix of extensive seasonal sea-ice cover (PS109/105) and a stable sea-ice margin (PS109/76 and PS109/105).
- Although diagenetic processes probably controlled the strong decrease of organic carbon and biomarker proxies in the uppermost ~5 cm, the primary signal is preserved in the downcore records and gives information about paleoenvironmental conditions.

- However, further detailed organic-geochemical data are still needed to quantify degradation processes and its contribution to the biomarker signal in the sediments.

Acknowledgements

We thank the captain and the crew of RV *Polarstern* for excellent cooperation during the cruises PS109 in 2017 and PS115.1 in 2018. Thanks to W. Luttmer for technical support during the laboratory work and Santi (voller Name) for her assistance in the sample preparation. Thanks to Simon Belt and colleagues (Biogeochemistry Research Centre, University of Plymouth) for providing the internal standard for the IP₂₅ analyses. Furthermore, we thank Walter Geibert for the possibility to measure Pb-dates at the AWI and Dr. Henriette Kolling for data processing of modern sea-ice concentrations. ASI-AMSR2 sea ice concentration data were provided by <https://seaice.uni-bremen.de/>. This publication is a contribution to the Research Programme PACES II, Topic 3 (The earth system from a polar perspective: Data, modeling and synthesis) of the Alfred Wegener Institute Helmholtz Centre for Polar und Marine Research (AWI). The studied samples and data were provided by AWI (Grant No. AWI-PS109 and PS115.1).

Chapter 7

7.1 Conclusion

This dissertation addresses the fundamental challenge of providing for the first-time high-resolution late Weichselian deglacial to Holocene paleoclimate reconstructions off the western Fram Strait on the Northeast Greenland (NEG) continental shelf obtained from multi-proxy biomarker investigations. The data presented encompasses significant relationships between sea-ice, ocean and ice-sheet interactions, as well as primary productivity, terrigenous supply and warm Atlantic Water advection on the NEG continental shelf. So-called highly branched isoprenoids (HBIs), specific sterols, organic bulk parameters and microfossil assemblages were used to form the methodological approach for these reconstructions. Sympagic produced biomarkers IP₂₅ and HBI II, typically positively correlated, were partly combined with specific phytoplankton-derived biomarkers and/or considered individually next to terrigenous biomarkers and planktic/benthic foraminiferal records and successfully represent reliable past climate proxies in this unique region. P_{III}IP₂₅ index based on the combination of IP₂₅ and phytoplankton HBI III, which are supposed to be more closely related to a sea-ice and open-water marginal ice zone system, did not obtain similar promising results like in the Barents Sea and should be considered with caution as it may strongly vary from region to region. On the other hand, good and promising results were achieved by P_BIP₂₅ and P_DIP₂₅ indices (based on the combination of IP₂₅ and open-water phytoplankton biomarker brassicasterol and dinosterol, respectively) and/or direct IP₂₅ vs. phytoplankton biomarkers plots in this region. The Northeast Greenland continental shelf is characterized by a perpetual seasonal sea-ice presence during the last ~10.2 ka; however, past climate conditions strongly vary from the outer (PS93/025) and inner (PS100/270) shelf systems due to the stronger/weaker influence of drift ice and/or local sea-ice formation.

Chapter 4 describes the Holocene sea-ice evolution on the outer Northeast Greenland shelf by indicating very clearly how drift ice from the interior of the central Arctic Ocean and the seasonal formation of the Northeast Water Polynya are the main components in this this particular region. In a combinatory approach with other paleo related proxies such as stable isotopic ($\delta^{18}\text{O}$ and $\delta^{13}\text{C}$) and IRD records from another study on the same sediment core along with our organic bulk parameters and biomarkers it was possible to reconstruct, that drift ice dominates this area while local sea-ice formation plays a secondary role (Fig. 7.1).

Chapter 5 displays findings of past climate reconstructions on the inner shelf regime of Northeast Greenland covering the late Weichselian to Holocene history, determined by four distinct lithofacies types. Based on planktic and benthic foraminiferal assemblages and flux rates, we described for these four stages how fast the 79NG retreated back into the inner fjord and the final disintegration of the floating ice shelf. Intensified bottom melting at the underside of 79NG was encouraged by the intrusion of recirculating warm Atlantic Water towards the inner shelf.

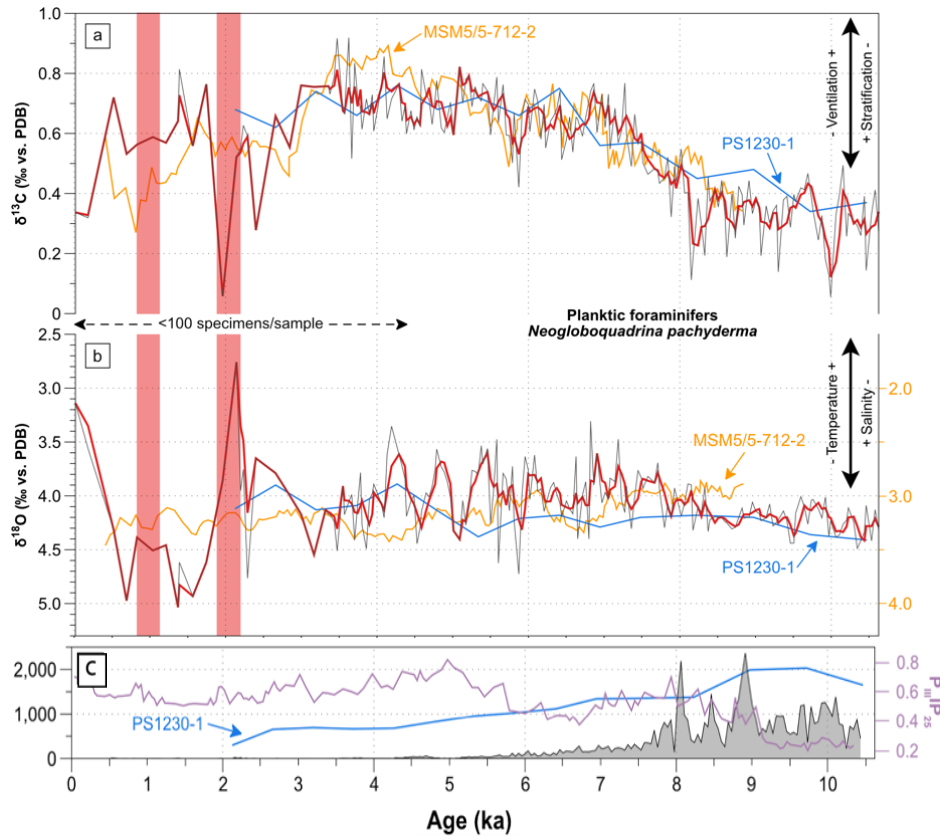


Figure 7.1: Planktic (*N. pachyderma*) isotope records of a) $\delta^{13}\text{C}$ b) $\delta^{18}\text{O}$ and benthic (*C. neoteretis*) isotope records c) $\delta^{13}\text{C}$, d) $\delta^{18}\text{O}$ and $\Delta\delta^{18}\text{O}$ of Core PS93/025 against age (ka) during the Holocene (Zehnic et al., 2020). A 5-point moving average is shown in red. Blue records represent data from Core PS1230-1 (Bauch et al., 2001) and orange records data from Core MSM5/5-712-2 (Müller et al., 2012). Red bars indicate warm small-scale intervals. c) Planktic foraminifera flux ($\text{ind./cm}^2 \text{ka}$) and the $P_{III}IP_{25}$ index (Syring et al., 2020).

Additional freshwater probably generated a relatively well-stratified surface layer, which triggered near perennial sea-ice conditions of the local landfast ice barrier. These findings were further corroborated by evidence of minimum organic bulk parameters and biomarkers concentration and accumulation rates, and in direct x-y IP_{25} vs. phytoplankton biomarker plots. During the early Holocene both locations were affected by an intensified intrusion of warm recirculating Atlantic Water. However, due to the constant supply of cold, fresh waters by the East Greenland Current, the western Fram Strait underlies generally cooler conditions compared to the eastern Fram Strait, which is fed by the inflow of the warm, saline West Spitsbergen Current. This validates the assumption that the Neoglacial cooling trend is not reflected in our sea-ice biomarker records.

Chapter 6 highlights findings of modern and sub-recent sea-ice conditions on the Northeast Greenland continental shelf, contextualised in terms of the sedimentary signal related to primary input and/or diagenetic processes).

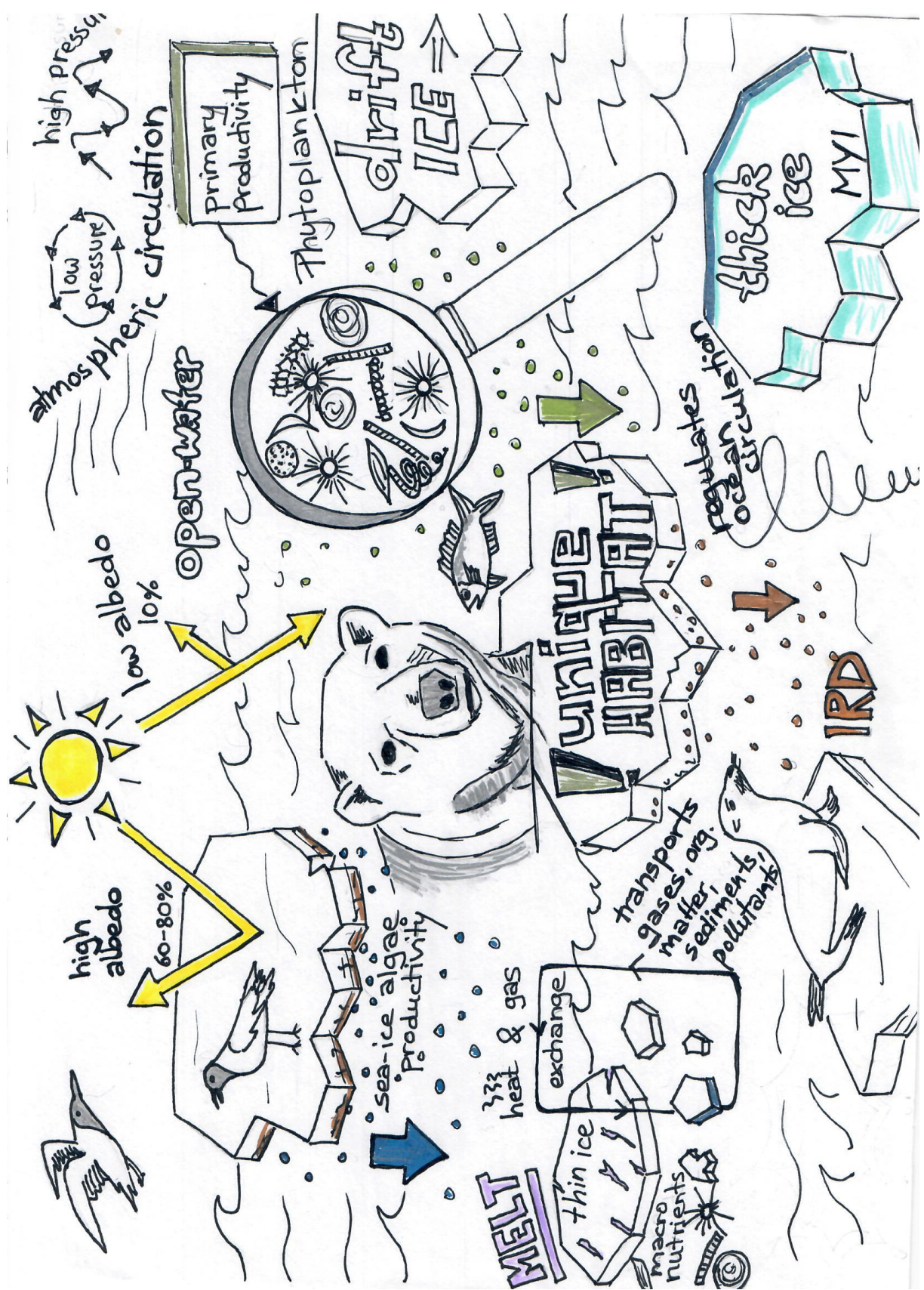
All of the findings emphasise the rapid Holocene sea-ice and ice-sheet fluctuations in the eastern Fram Strait, a highly versatile and sensitive environmental system, which were interpreted together with changes in the solar insolation pattern.

7.2 Outlook

The approach of combining reliable paleo proxies on the Northeast Greenland continental shelf is an essential tool to successfully reconstruct past climate conditions as a whole and could serve recent and future climate model for a more precise estimation of natural and anthropogenic climate mechanisms and drivers. In terms of methodology it could be useful to verify which paleo proxies are most useful in this specific area. For example, the HBI III data were more valid considered as single record instead that as a factor in the $P_{III}IP_{25}$ index. Single records of dinosterol and HBI III often indicated a stronger correlation during stages of MIZ, posing the interesting question of how closely are they connected in terms (i) seasonality, (ii) production and (iii) accumulation. Diagenetic alteration may affect organic bulk parameters and biomarkers during transport via rivers, sea ice and in the open ocean as well as in the sedimentary sections. Thus, it is necessary to evaluate whether the sedimentary records still obtain a primary climate-induced signal and/or a diagenetic overprint.

Long-term trends in sea-ice behaviour are specular in the eastern and western Fram Strait, though with discrepancies in the track of the Neoglacial Cooling near 5 ka. Further palaeoceanographic investigations on Holocene sedimentary records could achieve valuable insights into the dynamics of the EGC history and may confirm if the environmental conditions stayed generally cooler, because of these cold and fresh waters and/or other driving mechanisms. A comparison between both sides of the Fram still remains crucial to identify how fast and to what extent these contrasting systems react to (abruptly) changing climate conditions, but also in what sense local conditions are implicated.

As part of a substantial project of reconstructing small-scale variations of the Holocene circum-Greenland sea-ice history (i.e., off North Greenland, Northeast Greenland, East Greenland, Southwest Greenland and Northwest Greenland), this dissertation with its first detailed Holocene sedimentary sea-ice records from the NEG continental shelf is a fundamental contribution that may help to answer overarching research questions related to sea-ice dynamics, primary productivity, terrigenous supply, oceanography. The present study, combined with additional high-resolution sea-ice and ice-sheet records from Northeast Greenland and adjacent shelf areas, offers an excellent basis for further research investigations concerning, such as (i) how closely the ice shelves of the Northeast Greenland Ice Stream and landfast sea-ice barrier act with each other, and (ii) which additional proxies could potentially better resolve the identification of drift ice and local sea-ice signal.



References

- Aagaard, K., Coachman, L.K., **1968**. The East Greenland Current north of Denmark Strait: part I. *Arctic* 21, 181–200.
- Aagaard, K., Coachman, L.K., **1968**. The East Greenland Current North of Denmark Strait: Part II. *Arctic* 21, 267–290.
- Aagaard, K., **1982**. Inflow from the Atlantic Ocean to the Polar Basin. The Arctic Ocean: The Hydrographic Environment and the Fate of Pollutants, in: Rey, L. (Ed.). Palgrave Macmillan UK, London, 69–81.
- Aagaard, K., Swift, J.H., Carmack, E.C., **1985**. Thermohaline circulation in the Arctic Mediterranean Seas. *J. Geophys. Res. Ocean.* 90, 4833–4846.
- Aagaard, K., Foldvik, A., Hillman, S.R., **1987**. The West Spitsbergen Current: Disposition and water mass transformation. *J. Geophys. Res. Ocean.* 92, 3778–3784.
- Aagaard, K., Carmack, E.C., **1989**. The role of sea ice and other fresh water in the Arctic circulation. *J. Geophys. Res. Ocean.* 94, 14485–14498.
- Abdalati, W., Steffen, K., **2001**. Greenland Ice Sheet melt extent: 1979–1999. *J. Geophys. Res. Atmos.* 106, 33983–33988.
- Alexander, M.A., Bhatt, U.S., Walsh, J.E., Timlin, M.S., Miller, J.S., Scott, J.D., **2004**. The Atmospheric Response to Realistic Arctic Sea Ice Anomalies in an AGCM during Winter. *J. Clim.* 17, 890–905.
- Alexander, M.A., Scott, J.D., Friedland, K.D., Mills, K.E., Nye, J.A., Pershing, A.J., Thomas, A.C., **2018**. Projected sea surface temperatures over the 21st century: Changes in the mean, variability and extremes for large marine ecosystem regions of Northern Oceans. *Elementa* 6.
- Alley, R.B., Mayewski, P.A., Sowers, T., Stuiver, M., Taylor, K.C., Clark, P.U., **1997**. Holocene climatic instability: A prominent, widespread event 8200 yr ago. *Geology* 25, 483–486.
- Alley, R.B., **2004**. Abrupt Climate Change. *Sci. Am.* 291, 62–69.
- Alley, R.B., Spencer, M.K., Anandkrishnan, S., **2007**. Ice-sheet mass balance: assessment, attribution and prognosis. *Ann. Glaciol.* 46, 1–7.
- Alley, R.B., Andrews, J.T., Brigham-Grette, J., Clarke, G.K.C., Cuffey, K.M., Fitzpatrick, J.J., Funder, S., Marshall, S.J., Miller, G.H., Mitrovica, J.X., Muhs, D.R., et al., **2010**. History of the Greenland Ice Sheet: paleoclimatic insights. *Quat. Sci. Rev.* 29, 1728–1756.
- AMAP, 2017. Snow, water, ice and permafrost in the Arctic (SWIPA) **2017**. Oslo, Norway: Arctic Monitoring and Assessment Programme (AMAP). 269.
- Ambaum, M.H.P., Hoskins, B.J., Stephenson, D.B., **2001**. Arctic Oscillation or North Atlantic Oscillation? *J. Clim.* 14, 3495–3507.
- Andersen, C., Koç, N., Jennings, A., Andrews, J.T., **2004a**. Nonuniform response of the major surface currents in the Nordic Seas to insolation forcing: Implications for the Holocene climate variability. *Paleoceanography* 19, 1–16.
- Andersen, C., Koç, N., Moros, M., **2004**. A highly unstable Holocene climate in the subpolar North Atlantic: evidence from diatoms. *Quat. Sci. Rev.* 23, 2155–2166.
- Andersson, C., Risebrobakken, B., Jansen, E., Dahl, S.O., **2003**. Late Holocene surface ocean conditions of the Norwegian Sea (Vøring Plateau). *Paleoceanography* 18 (2), 1044.
- Andrews, J.T., **2000**. Icebergs and iceberg rafted detritus (IRD) in the North Atlantic: facts and assumptions. *Oceanography* 13, 100–108.
- Andrews, J.T., Darby, D., Eberle, D., Jennings, A.E., Moros, M., Ogilvie, A., **2009**. A robust, multisite Holocene history of drift ice off northern Iceland: implications for North Atlantic climate. *The Holocene* 19, 71–77.
- Andrews, J.T., Jennings, A.E., Coleman, G.C., Eberl, D.D., **2010**. Holocene variations in mineral and grain-size composition along the East Greenland glaciated margin (ca 67°–70°N): Local versus long-distance sediment transport. *Quat. Sci. Rev.* 29, 2619–2632.

- Anhaus, P., Smedsrud, L.H., Årthun, M., Straneo, F., **2019**. Sensitivity of submarine melting on North East Greenland towards ocean forcing 1, 1–29.
- Arndt, J. E., W. Jokat, B.D., R. Myklebust, J. A. Dowdeswell, A., Evans, J., **2015**. A new bathymetry of the Northeast Greenland continental shelf: Constraints on glacial and other processes. *Geochem. Geophys. Geosyst.* 16, 3733–3753.
- Arndt, J.E., Jokat, W., Dorschel, B., **2017**. The last glaciation and deglaciation of the Northeast Greenland continental shelf revealed by hydro-acoustic data. *Quat. Sci. Rev.* 160, 45–56.
- Arrigo, K.R., van Dijken, G.L., **2011**. Secular trends in Arctic Ocean net primary production. *J. Geophys. Res. Ocean.* 116.
- Arrigo, K.R., Perovich, D.K., Pickart, R.S., Brown, Z.W., van Dijken, G.L., Lowry, K.E., Mills, M.M., Palmer, M.A., Balch, W.M., Bahr, F., Bates, N.R., Benitez-Nelson, C., et al. **2012**. Massive Phytoplankton Blooms Under Arctic Sea Ice. *Science.* 336, 1408–1408.
- Aschwanden, A., Fahnestock, M.A., Truffer, M., Brinkerhoff, D.J., Hock, R., Khroulev, C., Mottram, R., Khan, S.A., **2019**. Contribution of the Greenland Ice Sheet to sea level over the next millennium. *Sci. Adv.* 5, 9396.
- Backman, J., Jakobsson, M., Frank, M., Sangiorgi, F., Brinkhuis, H., Stickley, C., et al., **2008**. Age model and core-seismic integration for the Cenozoic Arctic coring expedition sediments from the Lomonosov Ridge. *Paleoceanography* 23, PA1S03.
- Bakke, J., Lie, Ø., Heegaard, E., Dokken, T., Haug, G.H., Birks, H.H., Dulski, P., Nilsen, T., **2009**. Rapid oceanic and atmospheric changes during the Younger Dryas cold period. *Nat. Geosci.* 2, 202–205.
- Bamber, J., van den Broeke, M., Ettema, J., Lenaerts, J., Rignot, E., **2012**. Recent large increases in freshwater fluxes from Greenland into the North Atlantic. *Geophys. Res. Lett.* 39.
- Bamber, J.L., Tedstone, A.J., King, M.D., Howat, I.M., Enderlin, E.M., van den Broeke, M.R., Noel, B., **2018**. Land Ice Freshwater Budget of the Arctic and North Atlantic Oceans: 1. Data, Methods, and Results. *J. Geophys. Res. Ocean.* 123, 1827–1837.
- Barber, D.C., Dyke, A., Hillaire-Marcel, C., Jennings, A.E., Andrews, J.T., Kerwin, M.W., Bilodeau, G., McNeely, R., Southon, J., Morehead, M.D., Gagnon, J.-M., **1999**. Forcing of the cold event of 8,200 years ago by catastrophic drainage of Laurentide lakes. *Nature* 400, 344–348.
- Barber, D.G., Massom, R.A., **2007**. Chapter 1 The Role of Sea Ice in Arctic and Antarctic Polynyas. *Elsevier Oceanogr. Ser.* 74, 1–54.
- Barber, D.G., Lukovich, J. V, Keogak, J., Baryluk, S., Fortier, L., Henry, G.H.R., **2008**. The Changing Climate of the Arctic. *Arctic* 61, 7–26.
- Barry, R.G., **1996**. The parameterization of surface albedo for sea ice and its snow cover. *Prog. Phys. Geogr. Earth Environ.* 20, 63–79.
- Bauch, H.A., Erlenkeuser, H., Spielhagen, R.F., Struck, U., Matthiessen, J., Thiede, J., Heinemeier, J., **2001**. A multiproxy reconstruction of the evolution of deep and surface waters in the subarctic Nordic seas over the last 30,000yr. *Quat. Sci. Rev.* 20, 659–678.
- Belt, S.T., Cooke, D.A., Robert, J.-M., Rowland, S., **1996**. Structural characterisation of widespread polyunsaturated isoprenoid biomarkers: A C₂₅ triene, tetraene and pentaene from the diatom *Haslea ostrearia simonsen*. *Tetrahedron Lett.* 37, 4755–4758.
- Belt, S.T., Allard, W.G., Massé, G., Robert, J.-M., Rowland, S.J., **2000**. Highly branched isoprenoids (HBIs): identification of the most common and abundant sedimentary isomers. *Geochim. Cosmochim. Acta* 64, 3839–3851.
- Belt, S.T., Massé, G., Allard, W.G., Robert, J.-M., Rowland, S.J., **2001**. Identification of a C₂₅ highly branched isoprenoid triene in the freshwater diatom *Navicula sclesvicensis*. *Org. Geochem.* 32, 1169–1172.
- Belt, S.T., Massé, G., Rowland, S.J., Poulin, M., Michel, C., LeBlanc, B., **2007**. A novel chemical fossil of palaeo sea ice: IP₂₅. *Org. Geochem.* 38, 16–27.
- Belt, S.T., Brown, T.A., Rodriguez, A.N., Sanz, P.C., Tonkin, A., Ingle, R., **2012**. A reproducible method for the extraction, identification and quantification of the Arctic sea ice proxy IP₂₅ from marine sediments. *Anal. Methods* 4, 705–713.

- Belt, S.T., Brown, T.A., Ringrose, A.E., Cabedo-Sanz, P., Mundy, C.J., Gosselin, M., Poulin, M., **2013**. Quantitative measurement of the sea ice diatom biomarker IP₂₅ and sterols in Arctic sea ice and underlying sediments: Further considerations for palaeo sea ice reconstruction. *Org. Geochem.* 62, 33–45
- Belt, S.T., Müller, J., **2013**. The Arctic sea ice biomarker IP₂₅: a review of current understanding, recommendations for future research and applications in palaeo sea ice reconstructions. *Quat. Sci. Rev.* 79, 9–25.
- Belt, S. T., Brown, T. A., Ampel, L., Cabedo-Sanz, P., Fahl, K., Kocis, J. J., Masse, G., Navarro-Rodriguez, A., Ruan, R., Xu, Y., **2014**. An inter-laboratory investigation of the Arctic sea ice biomarker proxy IP₂₅ in marine sediments: key outcomes and recommendations. *Clim. Past* 10, 155–166.
- Belt, S.T., Cabedo-Sanz, P., Smik, L., Navarro-Rodriguez, A., Berben, S.M.P., Knies, J., Husum, K., **2015**. Identification of paleo Arctic winter sea ice limits and the marginal ice zone: Optimised biomarker-based reconstructions of late Quaternary Arctic sea ice. *Earth Planet. Sci. Lett.* 431, 127–139.
- Belt, S.T., Smik, L., Brown, T.A., Kim, J.-H., Rowland, S.J., Allen, C.S., Gal, J.-K., Shin, K.-H., Lee, J.I., Taylor, K.W.R., **2016**. Source identification and distribution reveals the potential of the geochemical Antarctic sea ice proxy IPSO₂₅. *Nat. Commun.* 7, 12655.
- Belt, S.T., Brown, T.A., Smik, L., Tatarek, A., Wiktor, J., Stowasser, G., Assmy, P., Allen, C.S., Husum, K., **2017**. Identification of C₂₅ highly branched isoprenoid (HBI) alkenes in diatoms of the genus *Rhizosolenia* in polar and sub-polar marine phytoplankton. *Org. Geochem.* 110, 65–72.
- Belt, S.T., **2018**. Source-specific biomarkers as proxies for Arctic and Antarctic sea ice. *Org. Geochem.* 125, 277–298.
- Belt, S.T., **2019**. What do IP₂₅ and related biomarkers really reveal about sea ice change? *Quat. Sci. Rev.* 204, 216–219.
- Belt, S.T., Smik, L., Köseo, D., Knies, J., Husum, K., **2019**. A novel biomarker-based proxy for the spring phytoplankton bloom in Arctic and sub-arctic settings – HBI T₂₅. *Earth Plan. Sci. Lett.* 523, 115703
- Bendle, J.A.P., Rosell-Melé, A., **2007**. High-resolution alkenone sea surface temperature variability on the North Icelandic Shelf: implications for Nordic Seas palaeoclimatic development during the Holocene. *The Holocene* 17, 9–24.
- Benn, D. I., and D.J.A.E., **2010**. *Glaciers & Glaciation*, 2nd ed., Hodder Educ., London, U. K.
- Bennike, O., **2004**. Holocene sea-ice variations in Greenland: onshore evidence. *The Holocene* 14, 607–613.
- Bennike, O., Weidick, A., **2001**. Late Quaternary history around Nioghalvfjærdsfjorden and Jøkelbugten, North-East Greenland. *Boreas* 30, 205–227.
- Berben, S.M.P., Husum, K., Navarro-Rodriguez, A., Belt, S.T., Aagaard-Sørensen, S., **2017**. Semi-quantitative reconstruction of early to late Holocene spring and summer sea ice conditions in the northern Barents Sea. *J. Quat. Sci.* 32, 587–603.
- Berger, A., **1978**. Long-Term Variations of Daily Insolation and Quaternary Climatic Changes. *J. Atmos. Sci.* 35, 2362–2367.
- Beszczynska-Möller, A., Fahrbach, E., Schauer, U., Hansen, E., **2012**. Variability in Atlantic water temperature and transport at the entrance to the Arctic Ocean, 1997–2010. *ICES J. Mar. Sci.* 69, 852–863.
- Bintanja, R., Graverson, R.G., Hazeleger, W., **2011**. Arctic winter warming amplified by the thermal inversion and consequent low infrared cooling to space. *Nat. Geosci.* 4, 758–761.
- Bintanja, R., Andry, O., **2017**. Towards a rain-dominated Arctic. *Nat. Clim. Chang.* 7, 263–267.
- Birgel, D. and Stein, R. **2004**. Northern Fram Strait und Yermak Plateau: Distribution, Variability and Burial of Organic Carbon and Paleoenvironmental Implications, In: Stein, R. and Macdonald, R.W. (Eds.), *The Organic Carbon Cycle in the Arctic Ocean*. Springer-Verlag, Berlin, 279–294
- Blaauw, M., Christen, J.A., **2011**. Flexible paleoclimate age-depth models using an autoregressive gamma process. *Bayesian Anal.* 6, 457–474.
- Blaschek, M., Renssen, H., **2013**. The impact of early Holocene Arctic shelf flooding on climate in an atmosphere–ocean–sea–ice model. *Clim. Past* 9, 2651–2667.

- Bogus, K., Harding, I.C., King, A., Charles, A.J., Zonneveld, K.A.F., Versteegh, G.J.M., **2012**. The composition and diversity of dinosporin in species of the Apectodinium complex (Dinoflagellata). *Rev. Palaeobot. Palynol.* 183, 21–31.
- Böning, C.W., Behrens, E., Biastoch, A., Getzlaff, K., Bamber, J.L., **2016**. Emerging impact of Greenland meltwater on deepwater formation in the North Atlantic Ocean. *Nat. Geosci.* 9, 523–527.
- Boon, J.J., Rijpstra, W.C., De Lange, F., De Leeuw, J.W., Yoshioka, M., Shimizu, Y., **1979**. Black Sea sterol – a molecular fossil for dinoflagellate blooms. *Nature* 277, 125–127.
- Bordovskiy, O.K., **1965**. Accumulation of organic matter in bottom sediments. *Mar. Geol.* 3, 33–82.
- Bourke, R.H., Garrett, R.P., **1987**. Sea ice thickness distribution in the Arctic Ocean. *Cold Reg. Sci. Technol.* 13, 259–280.
- Briner, J. P., McKay, N. P., Axford, A., Bennike, O., Bradley, R. S., de Vernal, A., Fisher, D., Francus, P., Fréchette, B., Gajewski, K., Jennings, A., Kaufman, D. S., Miller, G., Rouston, C., and Wagner, B. **2016**. Holocene climate change in Arctic Canada and Greenland, *Quat. Sci. Rev.*, 147, 340–364.
- Brinkhuis, H., Schouten, S., Collinson, M. E., Sluijs, A., Damsté, J. S. S., Dickens, G. R., et al., & the E. 302 S., **2016**. Episodic fresh surface waters in the Eocene Arctic Ocean. *Nature* 441, 606–609.
- Brown, T.A., Belt, S.T., Philippe, B., Mundy, C.J., Massé, G., Poulin, M., Gosselin, M., **2011**. Temporal and vertical variations of lipid biomarkers during a bottom ice diatom bloom in the Canadian Beaufort Sea: further evidence for the use of the IP₂₅ biomarker as a proxy for spring Arctic sea ice. *Polar Biol.* 34, 1857–1868.
- Brown, T.A., Belt, S.T., Tatarek, A., Mundy, C.J., **2014**. Source identification of the Arctic sea ice proxy IP₂₅. *Nat. Commun.* 5, 1–7.
- Brown, T.A., Yurkowski, D.J., Ferguson, S.H., Alexander, C., Belt, S.T., **2014**. H-Print: a new chemical fingerprinting approach for distinguishing primary production sources in Arctic ecosystems. *Environ. Chem. Lett.* 12, 387–392.
- Brown, T.A., Belt, S.T., **2016**. Novel tri- and tetra-unsaturated highly branched isoprenoid (HBI) alkenes from the marine diatom *Pleurosigma* intermedium. *Org. Geochem.* 91, 120–122.
- Budéus, G., Schneider, W., **1995**. On the hydrography of the Northeast Water Polynya. *J. Geophys. Res. Ocean.* 100, 4287–4299.
- Budéus, G., Schneider, W., Kattner, G., **1997**. Distribution and exchange of water masses in the Northeast Water polynya (Greenland Sea). *J. Mar. Syst.* 10, 123–138.
- Buizert, C., Keisling, B.A., Box, J.E., He, F., Carlson, A.E., Sinclair, G., DeConto, R.M., **2018**. Greenland-Wide Seasonal Temperatures During the Last Deglaciation. *Geophys. Res. Lett.* 45, 1905–1914.
- Cabedo-Sanz, P., Belt, S.T., Knies, J., Husum, K., **2013**. Identification of contrasting seasonal sea ice conditions during the Younger Dryas. *Quat. Sci. Rev.* 79, 74–86.
- Cabedo-Sanz, P., Belt, S.T., **2016**. Seasonal sea ice variability in eastern Fram Strait over the last 2000 years. *Arktos* 2, 22.
- Cabedo-Sanz, P., Belt, S.T., Jennings, A.E., Andrews, J.T., Geirsdóttir, Á., **2016**. Variability in drift ice export from the Arctic Ocean to the North Icelandic Shelf over the last 8000 years: A multi-proxy evaluation. *Quat. Sci. Rev.* 146, 99–115
- Campbell, W.J., **1965**. The wind-driven circulation of ice and water in a polar ocean. *J. Geophys. Res.* 70, 3279–3301.
- Cape, M.R., Straneo, F., Beaird, N., Bundy, R.M., Charette, M.A., **2019**. Nutrient release to oceans from buoyancy-driven upwelling at Greenland tidewater glaciers. *Nat. Geosci.* 12, 34–39.
- Carstens, J.; Hebbeln, D.; Wefer, G. **1997**. Distribution of planktic foraminifera at the ice margin in the Arctic (Fram Strait), *Marine Micropaleontology*, 29, 257–269
- Cavalieri, D.J., Parkinson, C.L., **2012**. Arctic sea ice variability and trends, 1979-2010. *Cryosphere* 6, 881–889.
- Chapman, M.R., Shackleton, N.J., **2000**. Evidence of 550-year and 1000-year cyclicities in North Atlantic circulation patterns during the Holocene. *The Holocene* 10, 287–291.
- Cheng, W., Chiang, J.C.H., Zhang, D., **2013**. Atlantic Meridional Overturning Circulation (AMOC) in CMIP5 Models: RCP and Historical Simulations. *J. Clim.* 26, 7187–7197.

- Choi, Y., Morlighem, M., Rignot, E., Mouginot, J., & Wood, M. **2017**. Modeling the response of Nioghalvfjærdsfjorden and Zachariae Isstrøm glaciers, Greenland, to ocean forcing over the next century. *Geophys. Res. Lett.*, 44, 11,071–11,079.
- Cleveland, W.S., **1979**. Robust Locally Weighted Regression and Smoothing Scatterplots. *J. Am. Stat. Assoc.* 74, 829–836.
- Coachman, L.K., **1963**. The Movement of Atlantic Water in the Arctic Ocean.
- Coachman, L.K., **1969**. Physical Oceanography in the Arctic Ocean: 1968. *Arctic* 22, 214–224.
- Coachman, L.K., Aagaard, K., **1974**. Physical Oceanography of Arctic and Subarctic Seas BT - Marine Geology and Oceanography of the Arctic Seas, in: Herman, Y. (Ed.). Springer Berlin Heidelberg, Berlin, Heidelberg, 1–72.
- Cohen, J., Screen, J.A., Furtado, J.C., Barlow, M., Whittleston, D., Coumou, D., Francis, J., Dethloff, K., Entekhabi, D., Overland, J., Jones, J., **2014**. mid-latitude weather. *Nat. Publ. Gr.* 7.
- Collins, L.G., Allen, C.S., Pike, J., Hodgson, D.A., Weckström, K., Massé, G., **2013**. Evaluating highly branched isoprenoid (HBI) biomarkers as a novel Antarctic sea-ice proxy in deep ocean glacial age sediments. *Quat. Sci. Rev.* 79, 87–98.
- Comiso, J.C., Parkinson, C.L., Gersten, R., Stock, L., **2008**. Accelerated decline in the Arctic sea ice cover 35, 1–6.
- Cronin, T.M., Gemery, L., Briggs, W.M., Jakobsson, M., Polyak, L., Brouwers, E.M., **2010**. Quaternary Sea-ice history in the Arctic Ocean based on a new Ostracode sea-ice proxy. *Quat. Sci. Rev.* 29, 3415–3429.
- Cronin, T.M., Polyak, L., Reed, D., Kandiano, E.S., Marzen, R.E., Council, E.A., **2013**. A 600-ka Arctic sea-ice record from Mendeleev Ridge based on ostracodes. *Quat. Sci. Rev.* 79, 157–167.
- Curry, J.A., Schramm, J.L., Ebert, E.E., **1995**. Sea Ice-Albedo Climate Feedback Mechanism. *J. Clim.* 8, 240–247.
- Dai, A., Luo, D., Song, M., Liu, J., **2019**. Arctic amplification is caused by sea-ice loss under increasing CO₂. *Nat. Commun.* 1–13.
- Damm, E., Bauch, D., Krumpen, T., Rabe, B., Korhonen, M., Vinogradova, E., Uhlig, C., **2018**. The Transpolar Drift conveys methane from the Siberian Shelf to the central Arctic Ocean. *Sci. Rep.* 8, 4515.
- Damm, V., **2019**. The Expedition PS115/1 of the Research Vessel POLARSTERN to the Greenland Sea and Wandel Sea in 2018. *Berichte zur Polar- und Meeresforschung = Reports on Polar and Marine Research*, 727.
- Darby, D.A., **2008**. Arctic perennial ice cover over the last 14 million years. *Paleoceanography* 23.
- Darby, D., Ortiz, J., Grosch, C. et al. **2012**. 1,500-year cycle in the Arctic Oscillation identified in Holocene Arctic sea-ice drift. *Nature Geoscience*, 5, 897–900
- Day, J.J., Hargreaves, J.C., Annan, J.D., Abe-Ouchi, A., **2012**. Sources of multi-decadal variability in Arctic sea ice extent. *Environ. Res. Lett.* 7, 34011.
- de Vernal, A., Rochon, A., **2011**. Dinocysts as tracers of sea-surface conditions and sea-ice cover in polar and subpolar environments. *IOP Conf. Ser. Earth Environ. Sci.* 14, 12007.
- de Vernal, A., Gersonde, R., Goosse, H., Seidenkrantz, M.-S., Wolff, E.W., **2013**. Sea ice in the paleoclimate system: the challenge of reconstructing sea ice from proxies – an introduction. *Quat. Sci. Rev.* 79, 1–8.
- de Vernal, A., Rochon, A., Fréchette, B., Henry, M., Radi, T., Solignac, S., **2013**. Reconstructing past sea ice cover of the Northern Hemisphere from dinocyst assemblages: status of the approach. *Quat. Sci. Rev.* 79, 122–134.
- Dethleff, D., Rachold, V., Tintelnot, M., Antonow, M., **2000**. Sea-ice transport of riverine particles from the Laptev Sea to Fram Strait based on clay mineral studies. *Int. J. Earth Sci.* 89, 496–502.
- Dieckmann, G.S., Hellmer, H.H., **2003**. The importance of sea ice: an overview. In: Thomas, D.N., Dieckmann, G.S. (Eds.), *Sea Ice: An Introduction to Its Physics, Chemistry, Biology and Geology*. Blackwell Science Ltd, Oxford, UK.
- Dieckmann, G.S., Hellmer, H.H., **2008**. The Importance of Sea Ice: An Overview., In: Thomas, ed. Blackwell Science, Oxford.
- Dieckmann, G.S.; Thomas, D.N., **2010**. *Sea Ice: an introduction to its Physics*. Chem. Biol. Geol.

- Ding, Q., Schweiger, A., Heureux, M.L., Steig, E.J., Battisti, D.S., Johnson, N.C., Blanchard-wrigglesworth, E., Po-chedley, S., Zhang, Q., Harnos, K., Bushuk, M., Markle, B., Baxter, I., **2019**. loss in observations and model simulations. *Nat. Geosci.* 12.
- Dmitrenko, I. A., Kirillov, S. A., Serra, N., Koldunov, N. V., Ivanov, V. V., Schauer, U., Polyakov, I. V., Barber, D., Janout, M., Lien, V. S., Makhotin, M. and Aksenov, Y., **2014**. Heat loss from the Atlantic water layer in the northern Kara Sea: causes and consequences. *Ocean Sci.* 10, 719–730.
- Dmitrenko, Igor; Kirillov, S. A.; Rudels, B.; Babb, D. G. Perderson, L. T.; Rysgaard, S.; Kristoffersen, Y.; Barber, D.G., **2017**. Arctic Ocean outflow and glacier–ocean interactions modify waterover the Wandel Sea shelf (northeastern Greenland). *Ocean Sci.* 13, 1045–1060.
- Dupont, T.K., Alley, R.B., **2005**. Assessment of the importance of ice-shelf buttressing to ice-sheet flow. *Geophys. Res. Lett.* 32.
- Dyck, S., Tremblay, L.B., de Vernal, A., **2010**. Arctic sea-ice cover from the early Holocene: the role of atmospheric circulation patterns. *Quat. Sci. Rev.* 29, 3457–3467.
- Ebbesen, H., Hald, M., **2004**. Unstable Younger Dryas climate in the northeast North Atlantic. *Geology* 32, 673–676.
- Ehlers, J., Gibbard, P.L., **2007**. The extent and chronology of Cenozoic Global Glaciation. *Quat. Int.* 164–165, 6–20.
- Ehlers, B.; Jokat, W., **2013**. Paleo-bathymetry of the northern North Atlantic and consequences for the opening of the Fram Strait. *Mar. Geophys. Res.* 34, 25–43.
- Ehrmann, W. U.; Thiede, J., **1985**. History of mesozoic and cenozoic sediment fluxes to the North Atlantic Ocean. *Contrib. to Sediment. Geol.* 15.
- Eicken, H., Lensu, M., Leppäranta, M., Tucker III, W.B., Gow, A.J., Salmela, O., **1995**. Thickness, structure, and properties of level summer multiyear ice in the Eurasian sector of the Arctic Ocean. *J. Geophys. Res. Ocean.* 100, 22697–22710.
- Eicken, H., Gradinger, R., Gaylord, A., Mahoney, A., Rigor, I., Melling, H., **2005**. Sediment transport by sea ice in the Chukchi and Beaufort Seas: Increasing importance due to changing ice conditions? *Deep Sea Res. Part II Top. Stud. Oceanogr.* 52, 3281–3302.
- Enderlin, E.M., Howat, I.M., Jeong, S., Noh, M.-J., van Angelen, J.H., van den Broeke, M.R., **2014**. An improved mass budget for the Greenland ice sheet. *Geophys. Res. Lett.* 41, 866–872.
- Engen, Ø., Faleide, J.I., Dyreng, T.K., **2008**. Opening of the Fram Strait gateway: A review of plate tectonic constraints. *Tectonophysics* 450, 51–69.
- Evans, J., Dowdeswell, J.A., Grobe, H., Niessen, F., Stein, R., Hubberten, H.-W., Whittington, R.J., **2002**. Late Quaternary sedimentation in Kejser Franz Joseph Fjord and the continental margin of East Greenland. *Geol. Soc. London, Spec. Publ.* 203, 149–179.
- Evans, J., Ó Cofaigh, C., Dowdeswell, J.A., Wadhams, P., **2009**. Marine geophysical evidence for former expansion and flow of the Greenland Ice Sheet across the north-east Greenland continental shelf. *J. Quat. Sci.* 24, 279–293.
- Fahl, K.; Stein, R., **1997**. Modern organic carbon deposition in the Laptev Sea and the adjacent continental slope: surface water productivity vs. terrigenous input. *Org. Geochem.* 26, 379–390.
- Fahl, K., Stein, R., **1999**. Biomarkers as organic-carbon-source and environmental indicators in the Late Quaternary Arctic Ocean: problems and perspectives. *Mar. Chem.* 63, 293–309.
- Fahl, K.; Stein, R.; Gaye-Haake, B.; Gebhardt, c., Kodina, L.A., Unger, D., Ittekkot, V., **2003**. Biomarkers in surface sediments from the Ob and Yenisei estuaries and southern Kara Sea: Evidence for particulate organic carbon sources, pathways, and degradation. In: Stein, R., Fahl, K., Fütterer, D.K., Galimov, E.M., Stepanets, O.V. (Eds.), *Siberian*.
- Fahl, K., Stein, R., **2007**. Biomarker records, organic carbon accumulation, and river discharge in the Holocene southern Kara Sea (Arctic Ocean). *Geo-Marine Lett.* 27, 13–25.
- Fahl, K., Stein, R., **2012**. Modern seasonal variability and deglacial/Holocene change of central Arctic Ocean sea-ice cover: New insights from biomarker proxy records. *Earth Planet. Sci. Lett.* 351–352, 123–133.
- Fahnestock, M., Bindenschadler, R., Kwok, R., Jezek, K., **1993**. Greenland Ice Sheet Surface Properties and Ice Dynamics from ERS-1 SAR Imagery. *Science* (80). 262, 1530–1534.
- Fairbanks, R.G., **1989**. A 17,000-year glacio-eustatic sea level record: influence of glacial melting rates on the Younger Dryas event and deep-ocean circulation. *Nature* 342, 637–642.

- Fetterer, F., K. Knowles, W. N. Meier, M. Savoie, and A.K.W., **2017**. updated daily. Sea Ice Index, Version 3. Boulder, Colorado USA. NSIDC: National Snow and Ice Data Center. [March 2020].
- Foote, C.S., **1976**. CHAPTER 3 - Photosensitized Oxidation and Singlet Oxygen: Consequences in Biological Systems, in: Pryor, W.A.B.T.-F.R. in B. (Ed.). Academic Press, 85–133.
- Francis, J.A., Hunter, E., **2007**. Changes in the fabric of the Arctic's greenhouse blanket. *Environ. Res. Lett.* 2, 45011.
- Francis, J.A., Vavrus, S.J., **2015**. Evidence for a wavier jet stream in response to rapid Arctic warming. *Environ. Res. Lett.* 10, 14005.
- Francis, J.A., **2018**. Why Are Arctic Linkages to Extreme Weather Still up in the Air? *Bull. Am. Meteorol. Soc.* 98, 2551–2557.
- Funder, S., Goosse, H., Jepsen, H., Kaas, E., Kjær, K.H., Korsgaard, N.J., Larsen, N.K., Linderson, H., Lyså, A., Möller, P., Olsen, J., Willerslev, E., **2011**. A 10,000-Year Record of Arctic Ocean Sea-Ice Variability – View from the Beach. *Science* 333, 747–750.
- Gally, R. J.; Else, B.; Howell, S.; Lukovich, J.; Barber, D., **2012**. Landfast Sea Ice Conditions in the Canadian Arctic: 1983-2009. *Arctic* 65, 133–144.
- Gearing, P., Gearing, J.N., Lytle, T.F., Lytle, J.S., **1976**. Hydrocarbons in 60 northeast Gulf of Mexico shelf sediments: a preliminary survey. *Geochim. Cosmochim. Acta* 40, 1005–1017.
- Golden, K.M., Eicken, H., Heaton, A.L., Miner, J., Pringle, D.J., Zhu, J., **2007**. Thermal evolution of permeability and microstructure in sea ice. *Geophys. Res. Lett.* 34.
- Gordeev, V.V., Martin, J.M., Sidorov, I.S., Sidorova, M.V., **1996**. A reassessment of the Eurasian river input of water, sediment, major elements, and nutrients to the Arctic Ocean. *Am. J. Sci.* 296, 664–691.
- Grootes, P.M., Stuiver, M., White, J.W.C., Johnsen, S., Jouzel, J., **1993**. Comparison of oxygen isotope records from the GISP2 and GRIP Greenland ice cores. *Nature* 366, 552–554.
- Hald, M., Korsun, S., **1997**. Distribution of modern benthic foraminifera from fjords of Svalbard, European Arctic. *J. Foraminifer. Res.* 27, 101–122.
- Hald, M., Andersson, C., Ebbesen, H., Jansen, E., Klitgaard-Kristensen, D., Risebrobakken, B., Salomonsen, G.R., Samthein, M., Sejrup, H.P., Telford, R.J., **2007**. Variations in temperature and extent of Atlantic Water in the northern North Atlantic during the Holocene. *Quat. Sci. Rev.* 26, 3423–3440.
- He, J., Acharyya, K., Vidali, G., **2016**. Sticking of molecules on nonporous amorphous Watab, *Astrophys. J.* 823, 56.
- Heinemann, J., Noon, B., Willems, D., Budeski, K., Bothner, B., **2017**. Analysis of raw biofluids by mass spectrometry using microfluidic diffusion-based separation. *Anal. Methods* 9, 385–392.
- Heureux, A.M.C., Rickaby, R.E.M., **2015**. Refining our estimate of atmospheric CO₂ across the Eocene–Oligocene climatic transition. *Earth Planet. Sci. Lett.* 409, 329–338.
- Higgins, A.K., **1989**. North Greenland ice islands. *Polar Rec. (Gr. Brit.)* 25, 207–212.
- Higgins, K., **1991**. North Greenland Glacier Velocities and Calf Ice Production. *Polarforschung* 60, 1–23.
- Hirche, H.-J., Baumann, M.E.M., Kattner, G., Gradinger, R., **1991**. Plankton distribution and the impact of copepod grazing on primary production in Fram Strait, Greenland Sea. *J. Mar. Syst.* 2, 477–494.
- Hirche, H.-J., Hagen, W., Mumm, N., Richter, C., **1994**. The Northeast Water polynya, Greenland Sea. *Polar Biol.* 14, 491–503.
- Hjort, C., Funder, S., **1974**. The subfossil occurrence of *Mytilus edulis* L. in central East Greenland. *Boreas* 3, 23–33.
- Holland, D.M., Thomas, R.H., de Young, B., Ribergaard, M.H., Lyberth, B., **2008**. Acceleration of Jakobshavn Isbræ triggered by warm subsurface ocean waters. *Nat. Geosci.* 1, 659–664.
- Honda, M., Yamazaki, K., Nakamura, H., Takeuchi, K., **1999**. Dynamic and Thermodynamic Characteristics of Atmospheric Response to Anomalous Sea-Ice Extent in the Sea of Okhotsk. *J. Clim.* 12, 3347–3358.
- Hopkins, J., Henson, S.A., Painter, S.C., Tyrrell, T., Poulton, A.J., **2015**. Phenological characteristics of global coccolithophore blooms. *Global Biogeochem. Cycles* 29, 239–253.
- Hopkins, T.S., **1991**. The GIN Sea-A synthesis of its physical oceanography and literature review 1972-1985. *Earth Sci. Rev.* 30, 175–318.

- Hopkinson, B.M., Dupont, C.L., Allen, A.E., Morel, F.M.M., **2011**. Efficiency of the CO₂-concentrating mechanism of diatoms. *Proc. Natl. Acad. Sci.* 108, 3830–3837.
- Hörner, T., Stein, R., Fahl, K., Birgel, D., **2016**. Post-glacial variability of sea ice cover, river run-off and biological production in the western Laptev Sea (Arctic Ocean) - A high-resolution biomarker study. *Quat. Sci. Rev.* 143, 133–149.
- Hörner, T., Stein, R., Fahl, K., **2017**. Evidence for Holocene centennial variability in sea ice cover based on IP₂₅ biomarker reconstruction in the southern Kara Sea (Arctic Ocean). *Geo-Marine Lett.* 37, 515–526.
- Hu, F.S., Kaufman, D., Yoneji, S., Nelson, D., Shemesh, A., Huang, Y., Tian, J., Bond, G., Clegg, B., Brown, T., **2003**. Cyclic Variation and Solar Forcing of Holocene Climate in the Alaskan Subarctic. *Science* 301, 1890–1893.
- Hughes, N.E., Wilkinson, J.P., Wadhams, P., **2011**. Multi-satellite sensor analysis of fast-ice development in the Norske Øer Ice Barrier, northeast Greenland. *Ann. Glaciol.* 52, 151–160.
- Hurrell, J.W., **1995**. Decadal Trends in the North Atlantic Oscillation: Regional Temperatures and Precipitation. *Science* 269, 676–679.
- Ingleby, B., Huddleston, M., **2007**. Quality control of ocean temperature and salinity profiles – Historical and real-time data. *J. Mar. Syst.* 65, 158–175.
- Ito, E., Yu, Z., **1999**. Possible solar forcing of century-scale drought frequency in the northern Great Plains. *Geology* 27, 263–266.
- Jaffé, R., Wolff, G.A., Cabrera, A., Carvajal Chitty, H., **1995**. The biogeochemistry of lipids in rivers of the Orinoco Basin. *Geochim. Cosmochim. Acta* 59, 4507–4522.
- Jakobsson, M., **2002**. Hypsometry and volume of the Arctic Ocean and its constituent seas. *Geochemistry, Geophys. Geosystems* 3, 1–18.
- Jakobsson, M., Backman, J., Rudels, B., Nycander, J., Frank, M., Mayer, L., Jokat, W., Sangiorgi, F., O'Regan, M., Brinkhuis, H., King, J., Moran, K., **2007**. The early Miocene onset of a ventilated circulation regime in the Arctic Ocean. *Nature* 447, 986–990.
- Jakobsson, M., Mayer, L., Coakley, B., Dowdeswell, J.A., Forbes, S., Fridman, B., Hodnesdal, H., Noormets, R., Pedersen, R., Rebecco, M., Schenke, H.W., Zarayskaya, Y., Accettella, D., Armstrong, A., et al., **2012**. The International Bathymetric Chart of the Arctic Ocean (IBCAO) Version 3.0. *Geophys. Res. Lett.* 39.
- Jakobsson, M., Andreassen, K., Bjarnadóttir, L.R., Dove, D., Dowdeswell, J.A., England, J.H., Funder, S., Hogan, K., Ingólfsson, Ó., Jennings, A., Krog Larsen, N., Kirchner, N., Landvik, J.Y., et al., **2014**. Arctic Ocean glacial history. *Quat. Sci. Rev.* 92, 40–67.
- James, N.A., Matteson, D.S., **2013**. Ecp: an R package for nonparametric multiple change point Analysis of multivariate data. *J. Stat. Softw.* 62, 1–25.
- Jansen, E., Overpeck, J., Briffa, K., Duplessy, J.-C., Joos, F., Masson-Delmotte, V., Olago, D., Otto-Bliesner, B., Peltier, W., Rahmstorf, S., Ramesh, R., Raynaud, D., Rind, D., Solomina, O., Villalba, R., and Zhang, D., **2007**. Palaeoclimate, in: *Climate Change 2007: The Physical Science Basis*.
- Jayne, S.R., Marotzke, J., **1999**. A Destabilizing Thermohaline Circulation–Atmosphere–Sea Ice Feedback. *J. Clim.* 12, 642–651.
- Jennings, A.E., Weiner, N.J., **1996**. Environmental change in eastern Greenland during the last 1300 years: evidence from foraminifera and lithofacies in Nansen Fjord, 68°N. *The Holocene* 6, 179–191.
- Jennings, A.E., Knudsen, K.L., Hald, M., Hansen, C.V., Andrews, J.T., **2002**. A mid-Holocene shift in Arctic sea-ice variability on the East Greenland Shelf. *The Holocene* 12, 49–58.
- Jennings, A., Andrews, J., Wilson, L., **2011**. Holocene environmental evolution of the SE Greenland Shelf North and South of the Denmark Strait: Irminger and East Greenland current interactions. *Quat. Sci. Rev.* 30, 980–998.
- Jessen, S.P., Rasmussen, T.L., Nielsen, T., Solheim, A., **2010**. A new Late Weichselian and Holocene marine chronology for the western Svalbard slope 30,000–0 cal years BP. *Quat. Sci. Rev.* 29, 1301–1312.

- Johannessen, O.M., Bengtsson, L., Miles, M.W., Kuzmina, S.I., Semenov, V.A., Alekseev, G. V., Nagurnyi, A.P., Zakharov, V.F., Bobylev, L.P., Pettersson, L.H., Hasselmann, K., Cattle, H.P., **2004**. Arctic climate change: observed and modelled temperature and sea-ice variability. *Tellus A Dyn. Meteorol. Oceanogr.* 56, 328–341.
- Johnson, M., Niebauer, H.J., **1995**. The 1992 summer circulation in the Northeast Water Polynya from acoustic Doppler current profiler measurements. *J. Geophys. Res. Ocean.* 100, 4301–4307.
- Jones, P.D., Jonsson, T., Wheeler, D., **1997**. Extension to the North Atlantic oscillation using early instrumental pressure observations from Gibraltar and south-west Iceland. *Int. J. Climatol.* 17, 1433–1450.
- Joughin, I., Fahnestock, M., MacAyeal, D., Bamber, J.L., Gogineni, P., **2001**. Observation and analysis of ice flow in the largest Greenland ice stream. *J. Geophys. Res. Atmos.* 106, 34021–34034.
- Joughin, I., Smith, B.E., Howat, I.M., Scambos, T., Moon, T., **2010**. Greenland flow variability from ice-sheet-wide velocity mapping. *J. Glaciol.* 56, 415–430.
- Kanzow, T., **2017**. The Expedition PS100 of the Research Vessel POLARSTERN to the Greenland Sea and the Fram Strait in 2016. Reports on polar and marine research, Alfred Wegener Institute for Polar and Marine Research, Bremerhaven, No. 705.
- Kanzow, T., **2018**. The Expedition PS109 of the Research Vessel POLARSTERN to the Nordic Seas in 2017. Berichte zur Polar- und Meeresforschung = Reports on Polar and Marine Research, Alfred Wegener Institute for Polar and Marine Research, Bremerhaven. 715.
- Kaplan, M.R., Wolfe, A.P., **2006**. Spatial and temporal variability of Holocene temperature in the North Atlantic region. *Quat. Res.* 65, 223–231.
- Kapsch, M.-L., Graversen, R.G., Tjernström, M., Bintanja, R., **2016**. The Effect of Downwelling Longwave and Shortwave Radiation on Arctic Summer Sea Ice. *J. Clim.* 29, 1143–1159.
- Kashiwase, H., Ohshima, K.I., Nihashi, S., Eicken, H., **2017**. Evidence for ice-ocean albedo feedback in the Arctic Ocean shifting to a seasonal ice zone. *Sci. Rep.* 7, 8170.
- Kaufman, D.S., Ager, T.A., Anderson, N.J., Anderson, P.M., Andrews, J.T., Bartlein, P.J., Brubaker, L.B., Coats, L.L., Cwynar, L.C., Duvall, M.L., **2004**. Holocene thermal maximum in the western Arctic (0–180 W). *Quat. Sci. Rev.* 23, 529–560.
- Kaufman, D.S., Axford, Y.L., Henderson, A.C.G., McKay, N.P., Oswald, W.W., Saenger, C., Anderson, R.S., Bailey, H.L., Clegg, B., Gajewski, K., Hu, F.S., Jones, M.C., Massa, C., Routson, C.C., Werner, A., Wooller, M.J., Yu, Z., **2016**. Holocene climate changes in eastern Beringia (NW North America) – A systematic review of multi-proxy evidence. *Quat. Sci. Rev.* 147, 312–339.
- Kaur, S., Ehn, J.K., Barber, D.G., **2018**. Pan-arctic winter drift speeds and changing patterns of sea ice motion: 1979–2015. *Polar Rec. (Gr. Brit.)* 54, 303–311.
- Kay, J.E., Holland, M.M., Jahn, A., **2011**. Inter-annual to multi-decadal Arctic sea ice extent trends in a warming world. *Geophys. Res. Lett.* 38.
- Khan, S.A., Kjær, K.H., Bevis, M., Bamber, J.L., Wahr, J., Kjeldsen, K.K., Bjørk, A.A., Korsgaard, N.J., Stearns, L.A., van den Broeke, M.R., Liu, L., Larsen, N.K., Muresan, I.S., **2014**. Sustained mass loss of the northeast Greenland ice sheet triggered by regional warming. *Nat. Clim. Chang.* 4, 292.
- Kinnard, C.; Zdanowicz, C.M.; Fisher, D.A.; Isaksson, E.; de Vernal, A.; Thompson, L.G., **2011**. Reconstructed changes in Arctic sea ice over the past 1,450 years. *Nature* 479, 509–512.
- Kim, J.H., Gal, J.K., Jun, S.Y., Smik, L., Kim, D., Belt, S.T., Park, K., Shin, K.H., Nam, S. Il, **2019**. Reconstructing spring sea ice concentration in the Chukchi Sea over recent centuries: Insights into the application of the PIP₂₅ index. *Environ. Res. Lett.* 14.
- Kirillov, S., Dmitrenko, I., Rysgaard, S., Babb, D., Toudal Pedersen, L., Ehn, J., Bendtsen, J., Barber, D., **2017**. Storm-induced water dynamics and thermohaline structure at the tidewater Flade Isblink Glacier outlet to the Wandel Sea (NE Greenland). *Ocean Sci.* 13, 947–959.
- Kjeldsen, K.K., Korsgaard, N.J., Bjørk, A.A., Khan, S.A., Box, J.E., Funder, S., Larsen, N.K., Bamber, J.L., Colgan, W., van den Broeke, M., Siggaard-Andersen, M.-L., et al., **2015**. Spatial and temporal distribution of mass loss from the Greenland Ice Sheet since AD 1900. *Nature* 528, 396–400.

- Knies, J., Hald, M., Ebbesen, H., Mann, U., Vogt, C., **2003**. A deglacial – middle Holocene record of biogenic sedimentation and paleoproductivity changes from the northern Norwegian continental shelf. *Paleoceanography* 18, 1096.
- Knies, J., Gaina, C., **2008**. Middle Miocene ice sheet expansion in the Arctic: Views from the Barents Sea. *Geochemistry, Geophys. Geosystems* 9.
- Knies, J., Matthiessen, J., Vogt, C., Laberg, J.S., Hjelstuen, B.O., Smelror, M., Larsen, E., Andreassen, K., Eidvin, T., Vorren, T.O., **2009**. The Plio-Pleistocene glaciation of the Barents Sea–Svalbard region: a new model based on revised chronostratigraphy. *Quat. Sci. Rev.* 28, 812–829.
- Knies, J., Cabedo-Sanz, P., Belt, S.T., Baranwal, S., Fietz, S., Rosell-Melé, A., **2014**. The emergence of modern sea ice cover in the Arctic Ocean. *Nat. Commun.* 5, 5608.
- Knies, J., Pathirana, I., Cabedo-Sanz, P., Banica, A., Fabian, K., Rasmussen, T.L., Forwick, M., Belt, S.T., **2017**. Sea-ice dynamics in an Arctic coastal polynya during the past 6500 years. *Arktos* 3, 1.
- Knies, J., Köseoğlu, D., Rise, L., Baeten, N., Bellec, V.K., Bøe, R., Klug, M., Panieri, G., Jernas, P.E., Belt, S.T., **2018**. Nordic Seas polynyas and their role in preconditioning marine productivity during the Last Glacial Maximum. *Nat. Commun.* 9, 3959.
- Kobashi, T., Severinghaus, J.P., Brook, E.J., Barnola, J.M., Grachev, A.M., **2007**. Precise timing and characterization of abrupt climate change 8200 years ago from air trapped in polar ice. *Quat. Sci. Rev.* 26, 1212–1222.
- Koç, N., Jansen, E., Haflidason, H., **1993**. Paleoceanographic reconstructions of surface ocean conditions in the Greenland, Iceland and Norwegian Seas through the last 14 ka based on diatoms. *Quat. Sci. Rev.* 12, 115–140.
- Köhler, S. E. I.; Spielhagen, R.F., **1990**. Late Pleistocene paleo-oceanography of the Norwegian – Greenland Sea: Benthonic foraminiferal evidence, in: *Geologic History of the Polar Oceans: Arctic versus Antarctic*. 489–497.
- Kolling, H.M., **2017**. Decadal to centennial variability of (sub-) Arctic sea ice distribution and its paleoenvironmental significance, PhD thesis, University of Bremen.
- Kolling, H.M., Stein, R., Fahl, K., Perner, K., Moros, M., **2017**. Short-term variability in late Holocene sea ice cover on the East Greenland Shelf and its driving mechanisms. *Palaeogeogr. Palaeoclimatol. Palaeoecol.* 485, 336–350.
- Köseoğlu, D., Belt, S.T., Husum, K., Knies, J., **2018**. An assessment of biomarker-based multivariate classification methods versus the PIP₂₅ index for paleo Arctic sea ice reconstruction. *Org. Geochem.* 125, 82–94.
- Köseoğlu, D., Belt, S.T., Smik, L., Yao, H., Panieri, G., Knies, J., **2018**. Complementary biomarker-based methods for characterising Arctic sea ice conditions: A case study comparison between multivariate analysis and the PIP₂₅ index. *Geochim. Cosmochim. Acta* 222, 406–420.
- Köseoğlu, D., **2019**. Development of biomarker-based proxy methods for reconstructing the late Quaternary sea ice history in the Barents Sea.
- Köseoğlu, D., Belt, S.T., Knies, J., **2019**. Abrupt shifts of productivity and sea ice regimes at the western Barents Sea slope from the Last Glacial Maximum to the Bølling-Allerød interstadial. *Quat. Sci. Rev.* 222, 105903.
- Kozmenko, S., Teslya, A., Fedoseev, S., **2018**. Maritime economics of the Arctic: legal regulation of environmental monitoring. *IOP Conf. Ser. Earth Environ. Sci.* 180, 12009.
- Kremer, A., **2018**. The variability of sea ice in the Fram Strait throughout glacial-interglacial transitions of the Late Quaternary (MIS 11 to MIS 1). University of Bremen.
- Krieger, L., Floricioiu, D., Neckel, N., **2020**. Drainage basin delineation for outlet glaciers of Northeast Greenland based on Sentinel-1 ice velocities and TanDEM-X elevations. *Remote Sens. Environ.* 237, 111483.
- Krumpen, T., Belter, H.J., Boetius, A., Damm, E., Haas, C., Hendricks, S., Nicolaus, M., Nöthig, E., Paul, S., Peeken, I., Ricker, R., Stein, R., **2019**. Arctic warming interrupts the Transpolar Drift and affects long-range transport of sea ice and ice-rafted matter 1–9.
- Kucera, M., **2007**. Chapter Six Planktonic Foraminifera as Tracers of Past Oceanic Environments, in: Hillaire-Marcel, C., De Vernal, A.B.T.-D. in M.G. (Eds.), *Proxies in Late Cenozoic Paleoceanography*. Elsevier, 213–262.

- Kuklinski, P., Bader, B., **2007**. Diversity, structure and interactions of encrusting lithophyllic macrofaunal assemblages from Belgica Bank, East Greenland. *Polar Biol.* 30, 709–717.
- Kwok, R., Untersteiner, N., **2011**. The thinning of Arctic sea ice. *Phys. Today* 64, 36–41.
- Kwok, R., **2018**. Arctic sea ice thickness, volume, and multiyear ice coverage: losses and coupled variability (1958–2018). *Environ. Res. Lett.* 13, 105005.
- Laskar, J., Robutel, P., Joutel, F., Gastineau, M., Correia, A. C. M., Levrard, B., **2004**. A long-term numerical solution for the insolation quantities of the Earth. *A&A* 428, 261–285.
- Larsen, N.K., Levy, L.B., Carlson, A.E., Buizert, C., Olsen, J., Strunk, A., Bjørk, A.A., Skov, D.S., **2018**. Instability of the Northeast Greenland Ice Stream over the last 45,000 years. *Nat. Commun.* 9, 1872.
- Lawrence, D.M., Slater, A.G., Tomas, R.A., Holland, M.M., Deser, C., **2008**. Accelerated Arctic land warming and permafrost degradation during rapid sea ice loss. *Geophys. Res. Lett.* 35.
- Lecavalier, B.S., Fisher, D.A., Milne, G.A., Vinther, B.M., Tarasov, L., Huybrechts, P., Lacelle, D., Main, B., Zheng, J., Bourgeois, J., Dyke, A.S., **2017**. High Arctic Holocene temperature record from the Agassiz ice cap and Greenland ice sheet evolution. *Proc. Natl. Acad. Sci.* 114, 5952–5957.
- Lee, S.H., McRoy, C.P., Joo, H.M.I.N., Gradinger, R., Cui, X., Yun, M.I.S.U.N., Chung, K.H.O., Kang, S.-H., Kang, C.-K., Choy, E.U.N.J., Son, S., Carmack, E., Whitledge, T.E., **2011**. Holes in Progressively Thinning Arctic Sea Ice Lead to New Ice Algae Habitat. *Oceanography* 24, 302–308.
- Leu, E., Søreide, J.E., Hessen, D.O., Falk-Petersen, S., Berge, J., **2011**. Consequences of changing sea-ice cover for primary and secondary producers in the European Arctic shelf seas: Timing, quantity, and quality. *Prog. Oceanogr.* 90, 18–32.
- Liang, S., Zhao, X., Liu, S., Yuan, W., Cheng, X., Xiao, Z., Zhang, X., Liu, Q., Cheng, J., Tang, H., Qu, Yonghua, Bo, Y., Qu, Ying, Ren, H., Yu, K., Townshend, J., **2013**. A long-term Global Land Surface Satellite (GLASS) data-set for environmental studies. *Int. J. Digit. Earth* 6, 5–33.
- Limoges, A., Ribeiro, S., Weckström, K., Heikkilä, M., Zamelczyk, K., Andersen, T.J., Tallberg, P., Massé, G., Rysgaard, S., Nørgaard-Pedersen, N., Seidenkrantz, M.-S., **2018**. Linking the Modern Distribution of Biogenic Proxies in High Arctic Greenland Shelf Sediments to Sea Ice, Primary Production, and Arctic-Atlantic Inflow. *J. Geophys. Res. Biogeosciences* 123, 760–786.
- Lisiecki, L.E., Raymo, M.E., **2005**. A Pliocene-Pleistocene stack of 57 globally distributed benthic $\delta^{18}\text{O}$ records. *Paleoceanography* 20.
- Liu, Z., Pagani, M., Zinniker, D., DeConto, R., Huber, M., Brinkhuis, H., Shah, S.R., Leckie, R.M., Pearson, A., **2009**. Global Cooling During the Eocene-Oligocene Climate Transition. *Science* 323, 1187–1190.
- Liu, J., Curry, J.A., Wang, H., Song, M., Horton, R.M., **2012**. Impact of declining Arctic sea ice on winter snowfall. *Proc. Natl. Acad. Sci.* 109, 4074–4079.
- Ljungqvist, F.C., **2010**. A new reconstruction of temperature variability in the extra tropical northern Hemisphere during the last two millennia. *Geogr. Ann. Ser. A, Phys. Geogr.* 92, 339–351.
- Loeb, V., Siegel, V., Holm-Hansen, O., Hewitt, R., Fraser, W., Trivelpiece, W., Trivelpiece, S., **1997**. Effects of sea-ice extent and krill or salp dominance on the Antarctic food web. *Nature* 387, 897.
- Macdonald, R.W., Solomon, S.M., Cranston, R.E., Welch, H.E., Yunker, M.B., Gobeil, C., **1998**. A sediment and organic carbon budget for the Canadian Beaufort Shelf. *Mar. Geol.* 144, 255–273.
- Macdonald, R.W., Sakshaug, E., Stein, R., **2004**. The Arctic Ocean: Modern Status and Recent Climate Change. In: Stein, R., Macdonald, R.W. (Eds.), *The Organic Carbon Cycle in the Arctic Ocean*. Springer, Berlin, 6–21.
- MacGregor, J.A., Colgan, W.T., Fahnestock, M.A., Morlighem, M., Catania, G.A., Paden, J.D., Gogineni, S.P., **2016**. Holocene deceleration of the Greenland Ice Sheet. *Science* (80). 351, 590–593.
- Manabe, S., Stouffer, R.J., **1980**. Sensitivity of a global climate model to an increase of CO_2 concentration in the atmosphere. *J. Geophys. Res. Ocean.* 85, 5529–5554.
- Manabe, S., Spelman, M.J., Stouffer, R.J., **1992**. Transient Responses of a Coupled Ocean-Atmosphere Model to Gradual Changes of Atmospheric CO_2 . Part II: Seasonal Response. *J. Clim.* 5, 105–126.

- Marincovich, L., Gladenkov, A.Y., **1999**. Evidence for an early opening of the Bering Strait. *Nature* 397, 149–151.
- Maslanik, J.A., Fowler, C., Stroeve, J., Drobot, S., Zwally, J., Yi, D., Emery, W., **2007**. A younger, thinner Arctic ice cover: Increased potential for rapid, extensive sea-ice loss 34, 2004–2008.
- Massé, G.; Belt, S. t.; Crosta, X.; Schmidt, S.; Snape, I. et al., **2011**. Highly branched isoprenoids as proxies for variable sea ice conditions in the Southern Ocean. *Antarct. Sci.* 23, 487–498.
- Matthiessen, J., Knies, J., Nowaczyk, N.R., Stein, R., **2001**. Late Quaternary dinoflagellate cyst stratigraphy at the Eurasian continental margin, Arctic Ocean: indications for Atlantic water inflow in the past 150,000 years. *Glob. Planet. Change* 31, 65–86.
- Matthiessen, J., Knies, J., Vogt, C., Stein, R., **2009**. Pliocene palaeoceanography of the Arctic Ocean and subarctic seas. *Philos. Trans. R. Soc. A Math. Phys. Eng. Sci.* 367, 21–48.
- Mayer, C., Reeh, N., Jung-Rothenhäusler, F., Huybrechts, P., Oerter, H., **2000**. The subglacial cavity and implied dynamics under Nioghalvfjærdssjøen Glacier, NE-Greenland. *Geophys. Res. Lett.* 27, 2289–2292.
- Mayer, C., Schaffer, J., Hattermann, T., Floricioiu, D., Krieger, L., Dodd, P.A., Kanzow, T., Licciulli, C., Schannwell, C., **2018**. Large ice loss variability at Nioghalvfjærdssjøen Glacier, Northeast-Greenland. *Nat. Commun.* 9, 2768.
- Mayewski, P.A., Rohling, E.E., Curt Stager, J., Karlén, W., Maasch, K.A., Meeker, L.D., Meyerson, E.A., Gasse, F., van Kreveld, S., Holmgren, K., Lee-Thorp, J., Rosqvist, G., Rack, F., Staubwasser, M., Schneider, R.R., Steig, E.J., **2004**. Holocene climate variability. *Quat. Res.* 62, 243–255.
- McGregor, H. V, Evans, M.N., Gooose, H., Leduc, G., Martrat, B., Addison, J.A., Mortyn, P.G., Oppo, D.W., Seidenkrantz, M.-S., Sicre, M.-A., Phipps, S.J., Selvaraj, K., Thirumalai, K., Filipsson, H.L., Ersek, V., **2015**. Robust global ocean cooling trend for the pre-industrial Common Era. *Nat. Geosci.* 8, 671.
- McKay, N.P., Kaufman, D.S., Routson, C.C., Erb, M.P., Zander, P.D., **2018**. The Onset and Rate of Holocene Neoglacial Cooling in the Arctic. *Geophys. Res. Lett.* 45, 12, 412–487.
- Meier, W.N., Hovelsrud, G.K., van Oort, B.E.H., Key, J.R., Kovacs, K.M., Michel, C., Haas, C., Granskog, M.A., Gerland, S., Perovich, D.K., Makshtas, A., Reist, J.D., **2014**. Arctic sea ice in transformation: A review of recent observed changes and impacts on biology and human activity. *Rev. Geophys.* 52, 185–217.
- Meredith, M., M. Sommerkorn, S. Cassotta, C. Derksen, A. Ekaykin, A. Hollowed, G. Kofinas, A. Mackintosh, J. Melbourne-Thomas, M.M.C. Muelbert, G. Ottersen, H. Pritchard, and E.A.G.S., **2019**. Polar Regions. In: IPCC Special Report on the Ocean and Cryosphere in a Changing Climate
- Mernild, S.H., Seidenkrantz, M.-S., Chylek, P., Liston, G.E., Hasholt, B., **2011**. Climate-driven fluctuations in freshwater flux to Sermilik Fjord, East Greenland, during the last 4000 years. *The Holocene* 22, 155–164.
- Meyers, P.A., **1994**. Preservation of elemental and isotopic source identification of sedimentary organic matter. *Chem. Geol.* 114, 289–302.
- Meyers, S.R., **2012**. Seeing red in cyclic stratigraphy: Spectral noise estimation for astrochronology. *Paleoceanography* 27, 1–12.
- Miettinen, A., Koç, N., Husum, K., **2013**. Appearance of the Pacific diatom *Neodenticula seminae* in the northern Nordic Seas – An indication of changes in Arctic sea ice and ocean circulation. *Mar. Micropaleontol.* 99, 2–7.
- Miettinen, A., **2018**. Diatoms in Arctic regions: Potential tools to decipher environmental changes. *Polar Sci.* 18, 220–226.
- Miller, G.H., Alley, R.B., Brigham-Grette, J., Fitzpatrick, J.J., Polyak, L., Serreze, M.C., White, J.W.C., **2010**. Arctic amplification: Can the past constrain the future? *Quat. Sci. Rev.* 29, 1779–1790.
- Miller, G.H., Brigham-Grette, J., Alley, R.B., Anderson, L., Bauch, H.A., Douglas, M.S. V, Edwards, M.E., Elias, S.A., Finney, B.P., Fitzpatrick, J.J., Funder, S. V, Herbert, T.D., Hinzman, L.D., Kaufman, D.S., et al., **2010**. Temperature and precipitation history of the Arctic. *Quat. Sci. Rev.* 29, 1679–1715.

- Millot, R., Gaillardet, J. érôm., Dupré, B., Allègre, C.J., **2003**. Northern latitude chemical weathering rates: clues from the Mackenzie River Basin, Canada. *Geochim. Cosmochim. Acta* 67, 1305–1329.
- Moran, K., Backman, J., Brinkhuis, H., Clemens, S.C., Cronin, T., Dickens, G.R., Eynaud, F., Gattacceca, J., Jakobsson, M., Jordan, R.W., Kaminski, M., King, J., Koc, N., Krylov, A., Martinez, N., Matthiessen, J., McInroy, D., et al., **2006**. The Cenozoic palaeoenvironment of the Arctic Ocean. *Nature* 441, 601–605.
- Morlighem, M., Rignot, E., Mouginit, J., Seroussi, H., Larour, E., **2014**. Deeply incised submarine glacial valleys beneath the Greenland ice sheet. *Nat. Geosci.* 7, 418–422.
- Moros, M., Andrews, J.T., Eberl, D.D., Jansen, E., **2006**. Holocene history of drift ice in the northern North Atlantic: Evidence for different spatial and temporal modes. *Paleoceanography* 21.
- Mortyn, P.G., Martínez-Botí, M.A., **2008**. Planktonic foraminifera and their proxies for the reconstruction of surface-ocean climate parameters. *Contrib. to Sci.* 3, 371–383.
- Mote, T.L., **2007**. Greenland surface melt trends 1973–2007: Evidence of a large increase in 2007. *Geophys. Res. Lett.* 34.
- Mouginit, J., Rignot, E., Scheuchl, B., Fenty, I., Khazendar, A., Morlighem, M., Buzzi, A., Paden, J., **2015**. Fast retreat of Zachariæ Isstrøm, northeast Greenland. *Science* (80). 350, 1357–1361.
- Mouginit, J., Rignot, E., Bjørk, A.A., van den Broeke, M., Millan, R., Morlighem, M., Noël, B., Scheuchl, B., Wood, M., **2019**. Forty-six years of Greenland Ice Sheet mass balance from 1972 to 2018. *Proc. Natl. Acad. Sci.* 116, 9239–9244.
- Müller, J., Massé, G., Stein, R., Belt, S.T., **2009**. Variability of sea-ice conditions in the Fram Strait over the past 30,000 years. *Nat. Geosci.* 2, 772.
- Müller, J., Wagner, A., Fahl, K., Stein, R., Prange, M., Lohmann, G., **2011**. Towards quantitative sea ice reconstructions in the northern North Atlantic: A combined biomarker and numerical modelling approach. *Earth Planet. Sci. Lett.* 306, 137–148.
- Müller, J., Werner, K., Stein, R., Fahl, K., Moros, M., Jansen, E., **2012**. Holocene cooling culminates in sea ice oscillations in Fram Strait. *Quat. Sci. Rev.* 47, 1–14.
- Müller, J., Stein, R., **2014**. High-resolution record of late glacial and deglacial sea ice changes in Fram Strait corroborates ice-ocean interactions during abrupt climate shifts. *Earth Planet. Sci. Lett.* 403, 446–455.
- Münchow, A., Schaffer, J., Kanzow, T., **2020**. Ocean circulation connecting fram strait to glaciers off Northeast Greenland: Mean flows, topographic rossby waves, and their forcing. *J. Phys. Oceanogr.* 50, 509–530.
- Nam, S.-I., Stein, R., Grobe, H., Hubberten, H., **1995**. Late Quaternary glacial-interglacial changes in sediment composition at the East Greenland continental margin and their paleoceanographic implications. *Mar. Geol.* 122, 243–262.
- NASA Worldview. **2019**. <https://worldview.earthdata.nasa.gov/>, part of the NASA Earth Observing System Data and Information System (EOSDIS)
- Navarro-Rodriguez, A., Belt, S.T., Knies, J., Brown, T.A., **2013**. Mapping recent sea ice conditions in the Barents Sea using the proxy biomarker IP₂₅: implications for palaeo sea ice reconstructions. *Quat. Sci. Rev.* 79, 26–39.
- Nesje, A., Dahl, S.O., **1993**. Lateglacial and Holocene glacier fluctuations and climate variations in western Norway: A review. *Quat. Sci. Rev.* 12, 255–261.
- Nesje, A., Olaf Dahl, S., Andersson, C., Matthews, J.A., **2000**. The lacustrine sedimentary sequence in Sygneskardvatnet, western Norway: a continuous, high-resolution record of the Jostedalbreen ice cap during the Holocene. *Quat. Sci. Rev.* 19, 1047–1065.
- Nghiêm, S. V., Hall, D.K., Mote, T.L., Tedesco, M., Albert, M.R., Keegan, K., Shuman, C.A., DiGirolamo, N.E., Neumann, G., **2012**. The extreme melt across the Greenland ice sheet in 2012. *Geophys. Res. Lett.* 39.
- NGRIP-Members, **2004**. High-resolution record of Northern Hemisphere climate extending into the last interglacial period. *Nature* 431, 147–151.
- Nick, F.M., Vieli, A., Howat, I.M., Joughin, I., **2009**. Large-scale changes in Greenland outlet glacier dynamics triggered at the terminus. *Nat. Geosci.* 2, 110–114.
- Niederdrenk, A.L., Notz, D., **2018**. Arctic Sea Ice in a 1.5°C Warmer World, *Geophys. Res. Lett.*, 45, 1963–1971.

- Niessen, F., Hong, J.K., Hegewald, A., Matthiessen, J., Stein, R., Kim, H., Kim, S., Jensen, L., Jokat, W., Nam, S.-I., Kang, S.-H., **2013**. Repeated Pleistocene glaciation of the East Siberian continental margin. *Nat. Geosci.* 6, 842–846.
- Nordhaus, W., **2019**. Economics of the disintegration of the Greenland ice sheet.
- Nørgaard-Pedersen, N., Mikkelsen, N., Lassen, S.J., Kristoffersen, Y., Sheldon, E., **2007**. Reduced sea ice concentrations in the Arctic Ocean during the last interglacial period revealed by sediment cores off northern Greenland. *Paleoceanography* 22.
- Not, F., Siano, R., Kooistra, W.H.C.F., Simon, N., Vault, D., Probert, I., **2012**. Chapter One - Diversity and Ecology of Eukaryotic Marine Phytoplankton, in: Piganeau, G.B.T.-A. in B.R. (Ed.), *Genomic Insights into the Biology of Algae*. Academic Press, 1–53.
- Notz, D., Marotzke, J., **2012**. Observations reveal external driver for Arctic sea-ice retreat. *Geophys. Res. Lett.* 39.
- Notz, D., Stroeve, J., **2016**. Observed Arctic sea-ice loss directly follows anthropogenic CO₂ emission. *Science* 354, 747–750.
- Notz, D., Stroeve, J., **2018**. The Trajectory Towards a Seasonally Ice-Free Arctic Ocean. *Curr. Clim. Chang. Reports* 4, 407–416.
- NSIDC, Boulder, U.S.A., **2016**. http://nsidc.org/data/seaice_index/archives/.
- Ogi, M., Wallace, J.M., **2007**. Summer minimum Arctic sea ice extent and the associated summer atmospheric circulation. *Geophys. Res. Lett.* 34.
- Ogi, M., Yamazaki, K., Wallace, J.M., **2010**. Influence of winter and summer surface wind anomalies on summer Arctic sea ice extent. *Geophys. Res. Lett.* 37.
- Ogi, M., Rigor, I.G., **2013**. Trends in Arctic sea ice and the role of atmospheric circulation 101, 97–101.
- Overland, J.E., Wang, M., **2005**. The Arctic climate paradox: The recent decrease of the Arctic Oscillation. *Geophys. Res. Lett.* 32.
- Overland, J.E., Wang, M., **2010**. Large-scale atmospheric circulation changes are associated with the recent loss of Arctic sea ice. *Tellus A Dyn. Meteorol. Oceanogr.* 62, 1–9.
- Pados, T., Spielhagen, R.F., **2014**. Species distribution and depth habitat of recent planktic foraminifera in Fram Strait, Arctic Ocean. *Polar Res.* 33, 22483.
- Parkinson, C.L., Cavalieri, D.J., **2008**. Arctic sea ice variability and trends, 1979–2006. *J. Geophys. Res. Ocean.* 113.
- Parnell, A.C., Haslett, J., Allen, J.R.M., Buck, C.E., Huntley, B., **2008**. A flexible approach to assessing synchronicity of past events using Bayesian reconstructions of sedimentation history. *Quat. Sci. Rev.* 27, 1872–1885.
- Paulsen, M.L., Nielsen, S.E.B., Müller, O., Møller, E.F., Stedmon, C.A., Juul-Pedersen, T., Markager, S., Sejr, M.K., Delgado Huertas, A., Larsen, A., Middelboe, M., **2017**. Carbon Bioavailability in a High Arctic Fjord Influenced by Glacial Meltwater, NE Greenland. *Front. Mar. Sci.*
- Pedersen, R.A., Christensen, J.H., **2019**. Attributing Greenland Warming Patterns to Regional Arctic Sea Ice Loss. *Geophys. Res. Lett.* 46, 10495–10503.
- Peeken, I., Primpke, S., Beyer, B., Gütermann, J., Katlein, C., Krumpfen, T., Bergmann, M., Hehemann, L., Gerds, G., **2018**. Arctic sea ice is an important temporal sink and means of transport for microplastic. *Nat. Commun.* 9, 1505.
- Pendleton, S., Miller, G., Lifton, N., Young, N., **2019**. Cryosphere response resolves conflicting evidence for the timing of peak Holocene warmth on Baffin Island, Arctic Canada. *Quat. Sci. Rev.* 216, 107–115.
- Perner, K., Moros, M., Lloyd, J.M., Jansen, E., Stein, R. **2015**. Mid to Late Holocene strengthening of the East Greenland Current paralleled by increased Atlantic Intermediate Water outflow from the Arctic Ocean. *Quat. Sci. Rev.* 129, 296–307.
- Perovich, D.K., Richter-Menge, J.A., Jones, K.F., Light, B., **2008**. Sunlight, water, and ice: Extreme Arctic sea ice melt during the summer of 2007. *Geophys. Res. Lett.* 35, 2–5.
- Pieńkowski, A.J., Gill, N.K., Furze, M.F.A., Mugo, S.M., Marret, F., Perreux, A., **2016**. Arctic sea-ice proxies: Comparisons between biogeochemical and micropalaeontological reconstructions in a sediment archive from Arctic Canada. *The Holocene* 27, 665–682.
- Pistone, K., Eisenman, I., Ramanathan, V., **2014**. Observational determination of albedo decrease caused by vanishing Arctic sea ice. *Proc. Natl. Acad. Sci.* 111, 3322–3326.

- Polyak, L., Alley, R.B., Andrews, J.T., Brigham-Grette, J., Cronin, T.M., Darby, D.A., Dyke, A.S., Fitzpatrick, J.J., Funder, S., et al., **2010**. History of sea ice in the Arctic. *Quat. Sci. Rev.* 29, 1757–1778.
- Polyakov, I., V. A. Alexeev, I. M. Ashik, S. Bacon, A. Beszynska-Moller, E. C. Carmack, I. A. Dmitrenko, L. et al., **2011**. Fate of the early 2000's Arctic warm water pulse. *Bull. Am. Meteorol. Soc.* 92.
- Post, E., Bhatt, U.S., Bitz, C.M., Brodie, J.F., Fulton, T.L., Hebblewhite, M., Kerby, J., Kutz, S.J., Stirling, I., Walker, D.A., **2013**. Ecological Consequences of Sea-Ice Decline 341, 519–525.
- Proshutinsky, A., Dukhovskoy, D., Timmermans, M.-L., Krishfield, R., Bamber, J.L., **2015**. Arctic circulation regimes. *Philos. Trans. R. Soc. A Math. Phys. Eng. Sci.* 373, 20140160.
- Quillfeldt, C.H. von, **2000**. Common Diatom Species in Arctic Spring Blooms: Their Distribution and Abundance. *Bot. Mar.* 43, 499–516.
- Rachold V. and references therein, **2004**. Modern Terrigenous Organic Carbon Input to the Arctic Ocean. In: Stein R., MacDonald R.W. (eds) *The Organic Carbon Cycle in the Arctic Ocean*. Springer, Berlin, Heidelberg.
- Rahmstorf, S., Box, J.E., Feulner, G., Mann, M.E., Robinson, A., Rutherford, S., Schaffernicht, E.J., **2015**. Exceptional twentieth-century slowdown in Atlantic Ocean overturning circulation. *Nat. Clim. Chang.* 5, 475–480.
- Rampal, P., Weiss, J., Dubois, C., Campin, J.-M., **2011**. IPCC climate models do not capture Arctic sea ice drift acceleration: Consequences in terms of projected sea ice thinning and decline. *J. Geophys. Res. Ocean.* 116.
- Ran, L., Jiang, H., Knudsen, K.L., Eiriksson, J., Gu, Z., **2006**. Diatom response to the Holocene climatic optimum on the North Icelandic shelf. *Mar. Micropaleontol.* 60, 226–241.
- Randall, D., Curry, J., Battisti, D., Flato, G., Grumbine, R., Hakkinen, S., Martinson, D., Preller, R., Walsh, J., Weatherly, J., **1998**. Status of and Outlook for Large-Scale Modeling of Atmosphere–Ice–Ocean Interactions in the Arctic. *Bull. Am. Meteorol. Soc.* 79, 197–220.
- Rasmussen, S.O., Andersen, K.K., Svensson, A.M., Steffensen, J.P., Vinther, B.M., Clausen, H.B., Siggaard-Andersen, M.-L., Johnsen, S.J., Larsen, L.B., Dahl-Jensen, D., Bigler, et al., **2006**. A new Greenland ice core chronology for the last glacial termination. *J. Geophys. Res. Atmos.* 111.
- Rasmussen, S.O., Vinther, B.M., Clausen, H.B., Andersen, K.K., **2007**. Early Holocene climate oscillations recorded in three Greenland ice cores. *Quat. Sci. Rev.* 26, 1907–1914.
- Ravelo, A.C., Hillaire-Marcel, C., **2007**. Chapter Eighteen: The Use of Oxygen and Carbon Isotopes of Foraminifera in Paleoceanography, in: Hillaire–Marcel, C., De Vernal, A.B.T.-D. in M.G. (Eds.), *Proxies in Late Cenozoic Paleoceanography*. Elsevier, 735–764.
- Reeh, N., Thomsen, H.H., Olesen, O.B., Starzer, W., **1997**. Mass Balance of North Greenland. *Science* (80) 278, 205–209.
- Reeh, N., Madsen, S.N., Mohr, J.J., **1999**. Combining SAR interferometry and the equation of continuity to estimate the three-dimensional glacier surface-velocity vector. *J. Glaciol.* 45, 533–538.
- Reeh, N., Thomsen, H., Higgins, A., Weidick, A. **2001**. Sea ice and the stability of north and northeast Greenland floating glaciers. *Annals of Glaciology*, 33, 474–480.
- Reeh, N., **2004**. Holocene climate and fjord glaciations in Northeast Greenland: implications for IRD deposition in the North Atlantic. *Sediment. Geol.* 165, 333–342.
- Reeh, N., **2017**. Greenland Ice Shelves and Ice Tongues BT - Arctic Ice Shelves and Ice Islands, in: Copland, L., Mueller, D. (Eds.). Springer Netherlands, Dordrecht, 75–106.
- Reimer, P.J., and references therein, **2013**. IntCal13 and Marine13 Radiocarbon Age Calibration Curves 0–50,000 Years cal BP. *Radiocarbon* 55, 1869–1887.
- Reimnitz, E.; Kassens, H.; Eicken, H., **1995**. Sediment transport by Laptav Sea Ice. *Rep. Polar Res.* 176, 71–77.
- Renssen, H., Goosse, H., Muscheler, R., **2006**. Coupled climate model simulation of Holocene cooling events: solar forcing triggers oceanic feedback. *Clim. Past Discuss.* 2, 209–232.
- Renssen, H., Seppä, H., Heiri, O., Roche, D.M., Goosse, H., Fichet, T., **2009**. The spatial and temporal complexity of the Holocene thermal maximum. *Nat. Geosci.* 2, 411–414.

- Ribeiro, S., Sejr, M.K., Limoges, A., Heikkilä, M., Andersen, T.J., Tallberg, P., Weckström, K., Husum, K., Forwick, M., Dalsgaard, T., Massé, G., Seidenkrantz, M.-S., Rysgaard, S., **2017**. Sea ice and primary production proxies in surface sediments from a High Arctic Greenland fjord: Spatial distribution and implications for palaeoenvironmental studies. *Ambio* 46, 106–118.
- Ricker, R.; Girard-Ardhuin, F.; Krumpfen, T.; Lique, C., **2018**. Satellite-derived sea ice export and its impact on Arctic ice mass balance. *Cryosphere* 12, 3017–3032.
- Rignot, E.J., Gogineni, S.P., Krabill, W.B., Ekholm, S., **1997**. North and Northeast Greenland Ice Discharge from Satellite Radar Interferometry. *Science* (80) 276, 934–937.
- Rignot, E., Kanagaratnam, P., **2006**. Changes in the Velocity Structure of the Greenland Ice Sheet. *Science* (80) 311, 986–990.
- Rignot, E., Velicogna, I., van den Broeke, M.R., Monaghan, A., Lenaerts, J.T.M., **2011**. Acceleration of the contribution of the Greenland and Antarctic ice sheets to sea level rise. *Geophys. Res. Lett.* 38, L05503.
- Rignot, E., Mouginot, J., **2012**. Ice flow in Greenland for the International Polar Year 2008–2009. *Geophys. Res. Lett.* 39.
- Rigor, I., Colony, R., **1997**. Sea-ice production and transport of pollutants in the Laptev Sea, 1979–1993. *Sci. Total Environ.* 202, 89–110.
- Rigor, I.G., J.M. Wallace, and R.L. Colony, **2002**. Response of Sea Ice to the Arctic Oscillation, *J. Climate*, 15, 2648–2663,
- Rimbu, N., Lohmann, G., Kim, J.-H., Arz, H.W., Schneider, R., **2003**. Arctic/North Atlantic Oscillation signature in Holocene sea surface temperature trends as obtained from alkenone data. *Geophys. Res. Lett.* 30.
- Rinke, A., Maslowski, W., Dethloff, K., Clement, J., **2006**. Influence of sea ice on the atmosphere: A study with an Arctic atmospheric regional climate model. *J. Geophys. Res. Atmos.* 111.
- Robson, J.N., Rowland, S.J., **1986**. Identification of novel widely distributed sedimentary acyclic sesterterpenoids. *Nature* 324, 561–563.
- Robson, J.N., Rowland, S.J., **1988**. Biodegradation of highly branched isoprenoid hydrocarbons: A possible explanation of sedimentary abundance. *Org. Geochem.* 13, 691–695.
- Rogers, T.S., Walsh, J.E., Leonawicz, M., Lindgren, M., **2015**. Arctic sea ice: use of observational data and model hindcasts to refine future projections of ice extent. *Polar Geogr.* 38, 22–41.
- Rohling, E.J., Pälike, H., **2005**. Centennial-scale climate cooling with a sudden cold event around 8,200 years ago. *Nature* 434, 975.
- Rontani, J.-F., **2001**. Visible light-dependent degradation of lipidic phytoplanktonic components during senescence: a review. *Phytochemistry* 58, 187–202.
- Rontani, J.-F., Belt, S.T., Vaultier, F., Brown, T.A., **2011**. Visible light induced photo-oxidation of highly branched isoprenoid (HBI) alkenes: Significant dependence on the number and nature of double bonds. *Org. Geochem.* 42, 812–822.
- Rontani, J., Charrière, B., Sempéré, R., Doxaran, D., Vaultier, F., Vonk, J.E., Volkman, J.K., **2014**. Organic Geochemistry Degradation of sterols and terrigenous organic matter in waters of the Mackenzie Shelf, Canadian Arctic 75, 61–73.
- Rontani, J.F., Belt, S.T., Amiraux, R., **2018**. Biotic and abiotic degradation of the sea ice diatom biomarker IP₂₅ and selected algal sterols in near-surface Arctic sediments. *Org. Geochem.* 118, 73–88.
- Rowland, S.J., Robson, J.N., **1990**. The widespread occurrence of highly branched acyclic C₂₀, C₂₅ and C₃₀ hydrocarbons in recent sediments and biota –A review. *Mar. Environ. Res.* 30, 191–216.
- Rowland, S.J., Allard, W.G., Belt, S.T., Massé, G., Robert, J.-M., Blackburn, S., Frampton, D., Revill, A.T., Volkman, J.K., **2001**. Factors influencing the distributions of polyunsaturated terpenoids in the diatom, *Rhizosolenia setigera*. *Phytochemistry* 58, 717–728.
- Ruckstuhl, A.F., Jacobson, M.P., Field, R.W., Dodd, J.A., **2001**. Baseline subtraction using robust local regression estimation. *J. Quant. Spectrosc. Radiat. Transf.* 68, 179–193.
- Ruddiman, W.F., **2001**. *Earth's Climate: Past and Future*.
- Rudels, B., Quadfasel, D., **1991**. Convection and deep water formation in the Arctic Ocean-Greenland Sea System. *J. Mar. Syst.* 2, 435–450.

- Rudels, B., Anderson, L.G., Jones, E.P., **1996**. Formation and evolution of the surface mixed layer and halocline of the Arctic Ocean. *J. Geophys. Res. Ocean* 101, 8807–8821.
- Rudels, B., J. Friedrich, H., Quadfasel, D., **1999**. The Arctic Circumpolar Boundary Current. *Deep Sea Res. Part II Top. Stud. Oceanogr.* 46, 1023–1062.
- Rudels, B., Fahrbach, E., Meincke, J., Budéus, G., Eriksson, P., **2002**. The East Greenland Current and its contribution to the Denmark Strait overflow. *ICES J. Mar. Sci.* 59, 1133–1154.
- Rudels, B., Björk, G., Nilsson, J., Winsor, P., Lake, I., Nohr, C., **2005**. The interaction between waters from the Arctic Ocean and the Nordic Seas north of Fram Strait and along the East Greenland Current: Results from the Arctic Ocean-02 Oden expedition. *J. Mar. Syst.* 55, 1–30.
- Ryan, W.B.F., S.M. Carbotte, J.O. Coplan, S. O'Hara, A. Melkonian, R. Arko, R.A. Weissel, V. Ferrini, A. Goodwillie, F. Nitsche, J. Bonczkowski, and R. Zemsky. **2009**. Global Multi-Resolution Topography synthesis, *Geochem. Geophys. Geosyst.*, 10, Q03014
- Rysgaard, S., Glud, R.N., Sej, M.K., Bendtsen, J., Christensen, P.B., **2007**. Inorganic carbon transport during sea ice growth and decay: A carbon pump in polar seas. *J. Geophys. Res. Ocean.* 112.
- Sakshaug, E., **2004**. Primary and Secondary Production in the Arctic Seas BT - The Organic Carbon Cycle in the Arctic Ocean, in: Stein, R., MacDonald, R.W. (Eds.). Springer Berlin Heidelberg, Berlin, Heidelberg, 57–81.
- Sarnthein, M., Pflaumann, U., Weinelt, M., **2003**. Past extent of sea ice in the northern North Atlantic inferred from foraminiferal paleotemperature estimates. *Paleoceanography* 18.
- Sasgen, I., van den Broeke, M., Bamber, J.L., Rignot, E., Sørensen, L.S., Wouters, B., Martinec, Z., Velicogna, I., Simonsen, S.B., **2012**. Timing and origin of recent regional ice-mass loss in Greenland. *Earth Planet. Sci. Lett.* 333–334, 293–303.
- Schaffer, J., Kanzow, T., von Appen, W.-J., von Albedyll, L., Arndt, J.E., Roberts, D.H., **2020**. Bathymetry constrains ocean heat supply to Greenland's largest glacier tongue. *Nat. Geosci.* 13, 227–231.
- Schauer, U., Fahrbach, E., Osterhus, S., Rohardt, G., **2004**. Arctic warming through the Fram Strait: Oceanic heat transport from 3 years of measurements. *J. Geophys. Res. Ocean.* 109.
- Schlichtholz, P., Houssais, M.-N., **1999**. An inverse modeling study in Fram Strait. Part I: dynamics and circulation. *Deep Sea Res. Part II Top. Stud. Oceanogr.* 46, 1083–1135.
- Schlitzer, R. **2018**. Ocean Data View, <https://odv.awi.de>
- Schlüter, M., Sauter, E.J., Schäfer, A., Ritzrau, W., **2000**. Spatial budget of organic carbon flux to the seafloor of the northern North Atlantic (60°N–80°N). *Global Biogeochem. Cycles* 14, 329–340.
- Schneider, W., Budéus, G., **1994**. The North East Water polynya (Greenland Sea). *Polar Biol.* 14, 1–9.
- Schneider, W., Budéus, G., **1997**. Summary of the Northeast Water Polynya formation and development (Greenland Sea). *J. Mar. Syst.* 10, 107–122.
- Screen, J.A., Simmonds, I., **2010**. The central role of diminishing sea ice in recent Arctic temperature amplification. *Nature* 464, 1334.
- Sea, P., **2009**. The sea-level conundrum: case studies from. *J. Quat. Sci.* 22, 311–320.
- Seale, A., Christoffersen, P., Mugford, R.I., O'Leary, M., **2011**. Ocean forcing of the Greenland Ice Sheet: Calving fronts and patterns of retreat identified by automatic satellite monitoring of eastern outlet glaciers. *J. Geophys. Res. Earth Surf.* 116.
- Seidenkrantz, M.-S., **2013**. Benthic foraminifera as palaeo sea-ice indicators in the subarctic realm – examples from the Labrador Sea–Baffin Bay region. *Quat. Sci. Rev.* 79, 135–144.
- Sej, M.K., Stedmon, C.A., Bendtsen, J., Abermann, J., Juul-Pedersen, T., Mortensen, J., Rysgaard, S., **2017**. Evidence of local and regional freshening of Northeast Greenland coastal waters. *Sci. Rep.* 7, 13183.
- Sejrup, H.P., Lehman, S.J., Haflidason, H., Noone, D., Muscheler, R., Berstad, I.M., Andrews, J.T., **2010**. Response of Norwegian Sea temperature to solar forcing since 1000 A. D. *J. Geophys. Res.* 115, 1–10.
- Seppä, H., Birks, H.H., Birks, H.J.B., **2002**. Rapid climatic changes during the Greenland stadial 1 (Younger Dryas) to early Holocene transition on the Norwegian Barents Sea coast. *Boreas* 31, 215–225.

- Seroussi, H., Morlighem, M., Rignot, E., Larour, E., Aubry, D., Ben Dhia, H., Kristensen, S.S., **2011**. Ice flux divergence anomalies on 79 North Glacier, Greenland. *Geophys. Res. Lett.* 38.
- Serreze, M.C., Francis, J.A., **2006**. The Arctic Amplification Debate. *Clim. Change* 76, 241–264.
- Serreze, M. C.; Barrett, A. P.; Stroeve, J. C.; Kindig, D. N.; Holland, M.M., **2009**. The emergence of surface-based Arctic amplification. *Cryosph.* 3, 11–19.
- Serreze, M.C., Barry, R.G., **2011**. Processes and impacts of Arctic amplification: A research synthesis 77, 85–96.
- Serreze, M.C., Stroeve, J., **2015**. Arctic sea ice trends, variability and implications for seasonal ice forecasting. *Philos. Trans. R. Soc. A Math. Phys. Eng. Sci.* 373.
- Serreze, M.C., Stroeve, J., Barrett, A.P., Boisvert, L.N., **2016**. *J. Geophys. Res.: Atmospheres* 2, 463–485.
- Sévellec, F., Fedorov, A. V, Liu, W., **2017**. Arctic sea-ice decline weakens the Atlantic Meridional Overturning Circulation. *Nat. Clim. Chang.* 7, 604.
- Shakun, J.D., Carlson, A.E., **2010**. A global perspective on Last Glacial Maximum to Holocene climate change. *Quat. Sci. Rev.* 29, 1801–1816.
- Shepherd, A., and references therein, **2020**. Mass balance of the Greenland Ice Sheet from 1992 to 2018. *Nature* 579, 233–239.
- Shimada, K., Kamoshida, T., Itoh, M., Nishino, S., Carmack, E., McLaughlin, F., Zimmermann, S., Proshutinsky, A., **2006**. Pacific Ocean inflow: Influence on catastrophic reduction of sea ice cover in the Arctic Ocean. *Geophys. Res. Lett.* 33.
- Shokr, M.; Sinha, N., **2015**. *Sea Ice – Physics and Remote Sensing*. John Wiley & Sons, Ltd.
- Sigman, D.M., Jaccard, S.L., Haug, G.H., **2004**. Polar ocean stratification in a cold climate. *Nature* 428, 59–63.
- Signorini, S.R., McClain, C.R., **2009**. Environmental factors controlling the Barents Sea spring–summer phytoplankton blooms. *Geophys. Res. Lett.* 36, L10604.
- Simmonds, I., **2015**. Comparing and contrasting the behaviour of Arctic and Antarctic sea ice over the 35 year period 1979–2013. *Ann. Glaciol.* 56, 18–28.
- Skirbekk, K., Hald, M., Marchitto, T.M., Junttila, J., Klitgaard Kristensen, D., Aagaard Sørensen, S., **2016**. Benthic foraminiferal growth seasons implied from Mg/Ca-temperature correlations for three Arctic species. *Geochemistry, Geophys. Geosystems* 17, 4684–4704.
- Skoog, A., Lara, R., Kattner, G., **2001**. Spring–summer cycling of DOC, DON and inorganic N in a highly seasonal system encompassing the Northeast Water Polynya, 1993. *Deep Sea Res. Part I Oceanogr. Res. Pap.* 48, 2613–2629.
- Sluijs, A., Schouten, S., Pagani, M., Woltering, M., Brinkhuis, H., Damsté, J.S.S., Dickens, G.R., Huber, M., Reichart, G.-J., Stein, R., Matthiessen, J., Lourens, L.J., Pedentchouk, N., Backman, J., Moran, K., Scientists, the E. 302, **2006**. Subtropical Arctic Ocean temperatures during the Palaeocene/Eocene thermal maximum. *Nature* 441, 610–613.
- Sluijs, A., Röhl, U., Schouten, S., Brumsack, H.-J., Sangiorgi, F., Sinninghe Damsté, J.S., Brinkhuis, H., **2008**. Arctic late Paleocene–early Eocene paleoenvironments with special emphasis on the Paleocene-Eocene thermal maximum (Lomonosov Ridge, Integrated Ocean Drilling Program Expedition 302). *Paleoceanography* 23.
- Sluijs, A., Schouten, S., Donders, T.H., Schoon, P.L., Röhl, U., Reichart, G.-J., Sangiorgi, F., Kim, J.-H., Sinninghe Damsté, J.S., Brinkhuis, H., **2009**. Warm and wet conditions in the Arctic region during Eocene Thermal Maximum 2. *Nat. Geosci.* 2, 777–780.
- Smedsrud, L.H., Halvorsen, M.H., Stroeve, J.C., Zhang, R., Kloster, K., **2017**. Fram Strait sea ice export variability and September Arctic sea ice extent over the last 80 years. *The Cryosphere* 11, 65–79.
- Smik, L., Belt, S.T., Lieser, J.L., Armand, L.K., Leventer, A., **2016**. Distributions of highly branched isoprenoid alkenes and other algal lipids in surface waters from East Antarctica: Further insights for biomarker-based paleo sea-ice reconstruction. *Org. Geochem.* 95, 71–80.
- Smik, L., Cabedo-sanz, P., Belt, S.T., **2016**. Organic Geochemistry Semi-quantitative estimates of paleo Arctic sea ice concentration based on source-specific highly branched isoprenoid alkenes: A further development of the PIP₂₅ index. *Org. Geochem.* 92, 63–69.

- Smik, L., Cabedo-Sanz, P., Belt, S.T., **2016**. Semi-quantitative estimates of paleo Arctic sea ice concentration based on source-specific highly branched isoprenoid alkenes: A further development of the PIP₂₅ index. *Org. Geochem.* 92, 63–69.
- Smith, R.E.H., Cavaletto, J.F., Eadie, B.J., Gardner, W.S., **1993**. Growth and lipid composition of high Arctic ice algae during the spring bloom at Resolute, Northwest Territories, Canada. *Mar. Ecol. Prog. Ser.* 97, 19–29.
- Smith, S.D., Muench, R.D., Pease, C.H., **1990**. Polynyas and leads: An overview of physical processes and environment. *J. Geophys. Res. Ocean.* 95, 9461–9479.
- Sneed, W.A., Hamilton, G.S., **2016**. Recent changes in the Norske Øer Ice Barrier, coastal Northeast Greenland. *Ann. Glaciol.* 57, 47–55.
- Spielhagen, R.F., Werner, K., Sørensen, S.A., Zamelczyk, K., Kandiano, E., Budeus, G., Husum, K., Marchitto, T.M., Hald, M., **2011**. Enhanced Modern Heat Transfer to the Arctic by Warm Atlantic Water. *Science.* 331, 450–453.
- Spren, G., L. Kaleschke, and G. Heygster **2008**. Sea ice remote sensing using AMSR-E 89 GHz channels *J. Geophys. Res.* 113, C02S03.
- Stein, R., Grobe, H., Hubberten, H., Marienfeld, P., Nam, S., **1993**. Latest Pleistocene to Holocene changes in glaciomarine sedimentation in Scoresby Sund and along the adjacent East Greenland Continental Margin: Preliminary results. *Geo-Marine Lett.* 13, 9–16.
- Stein, R.; Schubert, C.; Vogt, C.; Fütterer, D., **1994a**. Stable isotope stratigraphy, sedimentation rates, and salinity changes in the Latest Pleistocene to Holocene eastern central Arctic Ocean. *Mar. Geol.* 119, 333–355.
- Stein, R., Nam, S.-I., Schubert, C., Vogt, C., Fütterer, D., Heinemeier, J. **1994b**. The Last Deglaciation Event in the Eastern Central Arctic Ocean. *Science* 264, 692–696.
- Stein, R. and Macdonald, R. W. **2004**. Geochemical Proxies Used for Organic Carbon Source Identification in Arctic Ocean Sediments, In: Stein, R. and Macdonald, R. W. (Eds.), *The Organic Carbon Cycle in the Arctic Ocean*. Springer-Verlag, Berlin.
- Stein, R.; Fahl, K., **2004**. The Kara Sea: Distribution, sources, variability and burial of organic carbon. In: Stein and Macdonald (Eds.), *The Arctic Ocean Organic Carbon Cycle: Present and Past*. Springer-Verlag, Berlin. 329–488.
- Stein, R., Boucsein, B., Meyer, H., **2006**. Anoxia and high primary production in the Paleogene central Arctic Ocean: First detailed records from Lomonosov Ridge. *Geophys. Res. Lett.* 33.
- Stein, R., **2008**. *Arctic Ocean Sediments: Processes, Proxies, and Paleoenvironment*. Elsevier, Amsterdam.
- Stein, R., Fahl, K., **2012**. A first southern Lomonosov Ridge (Arctic Ocean) 60 ka IP₂₅ sea-ice record. *Polarforschung* 82, 83–86.
- Stein, R.; Fahl, K.; Müller, J., **2012**. Proxy Reconstruction of Cenozoic Arctic Ocean Sea-Ice History – from IRD to IP₂₅. *Polarforschung* 82, 37–71.
- Stein, R., Blackman, D., Inagaki, F., & Larsen, H. -C. (Eds), **2014**. Earth and life processes discovered from seafloor environment – A decade of science achieved by the Integrated Ocean Drilling Program (IODP). In *Series Developments in Marine Geology*, (Vol. 7). Amsterdam/New York: Elsevier. 800.
- Stein, R., **2016**. The Expedition PS93.1 of the Research Vessel POLARSTERN to the Greenland Sea in 2015. *Berichte zur Polar- und Meeresforschung = Reports on Polar and Marine Research*, 695.
- Stein, R., Fahl, K., Schreck, M., Knorr, G., Niessen, F., Forwick, M., Gebhardt, C., Jensen, L., Kaminski, M., Kopf, A., Matthiessen, J., Jokat, W., Lohmann, G., **2016**. Evidence for ice-free summers in the late Miocene central Arctic Ocean. *Nat. Commun.* 7, 11148.
- Stein, R., Fahl, K., Gierz, P., Niessen, F., Lohmann, G., **2017a**. Arctic Ocean sea ice cover during the penultimate glacial and the last interglacial. *Nature Communications* 8, 373.
- Stein, R., Fahl, K., Schade, I., Manerung, A., Wassmuth, S., Niessen, F., Nam, S. II, **2017**. Holocene variability in sea ice cover, primary production, and Pacific-Water inflow and climate change in the Chukchi and East Siberian Seas (Arctic Ocean). *J. Quat. Sci.* 32, 362–379.
- Stein, R., **2019**. The Late Mesozoic-Cenozoic Arctic Ocean Climate and Sea Ice History: A Challenge for Past and Future Scientific Ocean Drilling. *Paleoceanogr. Paleoclimatology* 34, 1851–1894.

- Steinsund, P.I., Hald, M., **1994**. Recent calcium carbonate dissolution in the Barents Sea: Paleoceanographic applications. *Mar. Geol.* 117, 303–316.
- Stern, N., Taylor, C., **2007**. Climate Change: Risk, Ethics, and the Stern Review. *Science* (80). 317, 203–204.
- Stirling, I., **1980**. The Biological Importance of Polynyas in the Canadian Arctic. *Arctic* 33, 303–315.
- Stocker, T.F., Schmittner, A., **1997**. Influence of CO₂ emission rates on the stability of the thermohaline circulation. *Nature* 388, 862.
- Stocker, T.F., Allen, S.K., Bex, V., Midgley, P.M., **2013**. Climate Change 2013 The Physical Science Basis Working Group I Contribution to the Fifth Assessment Report of the Intergovernmental Panel on Climate Change Edited by.
- Straneo, F., Sutherland, D.A., Holland, D., Gladish, C., Hamilton, G.S., Johnson, H.L., Rignot, E., Xu, Y., Koppes, M., **2012**. Characteristics of ocean waters reaching Greenland's glaciers 53.
- Straneo, F., Cenedese, C., **2015**. The Dynamics of Greenland's Glacial Fjords and Their Role in Climate. *Ann. Rev. Mar. Sci.* 7, 89–112.
- Stroeve, J., Holland, M.M., Meier, W., Scambos, T., Serreze, M., **2007**. Arctic sea ice decline: Faster than forecast. *Geophys. Res. Lett.* 34, 1–5.
- Stroeve, J.C., Maslanik, J., Serreze, M.C., Rigor, I., Meier, W., Fowler, C., **2011**. Sea ice response to an extreme negative phase of the Arctic Oscillation during winter 2009/2010. *Geophys. Res. Lett.* 38.
- Stroeve, J.C., Serreze, M.C., Holland, M.M., Kay, J.E., Malanik, J., Barrett, A.P., **2012**. The Arctic's rapidly shrinking sea ice cover: A research synthesis. *Clim. Change* 110, 1005–1027.
- Stroeve, J.C., Markus, T., Boisvert, L., Miller, J., Barrett, A., **2014**. Changes in Arctic melt season and implications for sea ice loss. *Geophys. Res. Lett.* 41, 1216–1225.
- Stroeve, J., Notz, D., **2018**. Changing state of Arctic sea ice across all seasons. *Environ. Res. Lett.* 13, 103001.
- Stuart, K.M., Long, D.G., **2011**. Tracking large tabular icebergs using the SeaWinds Ku-band microwave scatterometer. *Deep Sea Res. Part II Top. Stud. Oceanogr.* 58, 1285–1300.
- Stuiver, M., Braziunas, T.F., **1993**. Sun, Ocean, climate and atmospheric ¹⁴CO₂: an evaluation of causal and spectral relationships. *The Holocene* 3, 289–305.
- Stuiver, M., Grootes, P.M., **2000**. GISP2 Oxygen Isotope Ratios. *Quat. Res.* 53, 277–284.
- Stuiver, M., Grootes, P.M., Braziunas, T.F., **1995**. The GISP2 $\delta^{18}\text{O}$ Climate Record of the Past 16,500 Years and the Role of the Sun, Ocean, and Volcanoes. *Quat. Res.* 44, 341–354.
- Stuiver, M.; Reimer, P. J.; Reimer, R.W., **2019**. CALIB 7.1 [WWW program] at. accessed 2019-8-14. <http://calib.org>.
- Sundqvist, H.S., Kaufman, D.S., McKay, N.P., Balascio, N.L., Briner, J.P., Cwynar, L.C., Sejrup, H.P., Seppä, H., Subetto, D.A., Andrews, J.T., Axford, Y., Bakke, J., Birks, et al., **2014**. Arctic Holocene proxy climate database – new approaches to assessing geochronological accuracy and encoding climate variables. *Clim. Past* 10, 1605–1631.
- Sun, L., Alexander, M., Deser, C., **2018**. Evolution of the Global Coupled Climate Response to Arctic Sea Ice Loss during 1990–2090 and Its Contribution to Climate Change. *J. Clim.* 31, 7823–7843.
- SWIPA, **2011**. Snow, Water, Ice and Permafrost in the Arctic: Climate Change and the Cryosphere Arctic Monitoring and Assessment Programme (AMAP), Oslo, Norway 538.
- Syring, N., Stein, R., Fahl, K., Vahlenkamp, M., Zehnich, M., Spielhagen, R.F., Niessen, F., **2020**. Holocene changes in sea-ice cover and polynya formation along the eastern North Greenland shelf: New insights from biomarker records. *Quat. Sci. Rev.* 231. 106173
- Szulejko, J.E., Kumar, P., Deep, A., Kim, K.-H., **2017**. Global warming projections to 2100 using simple CO₂ greenhouse gas modeling and comments on CO₂ climate sensitivity factor. *Atmos. Pollut. Res.* 8, 136–140.
- Tedesco, M., **2007**. a new record in 2007 for melting in Greenland. *Eos, Trans. Am. Geophys. Union* 88, 383.
- Tedesco, M., Fettweis, X., van den Broeke, M.R., van de Wal, R.S.W., Smeets, C.J.P.P., van de Berg, W.J., Serreze, M.C., Box, J.E., **2011**. The role of albedo and accumulation in the 2010 melting record in Greenland. *Environ. Res. Lett.* 6, 14005.

- Tedesco, M.; Alexander, P.; Box, J. E.; Cappelen, J.; Knudson, N. T.; Mote, T.; Steffen, K.; van de Wal, R. S. W.; Wahr, J.; Wouters, B., **2013**. [Arctic] Greenland ice sheet [in “State of the Climate in 2012”]. *Am. Meteorol. Soc.*
- Telesinski, M., Spielhagen, R. F. and Bauch, H.A., **2014**. Water mass evolution of the Greenland Sea since late glacial times. *Clim. Past* 10, 123–136.
- Thackeray, C.W., Hall, A. **2019**. An emergent constraint on future Arctic sea-ice albedo feedback. *Nat. Clim. Chang.* 9, 972–978.
- Thackeray, C.W., Hall, A., **2019**. albedo feedback. *Nat. Clim. Chang.* 9.
- Thomas, E.R., Wolff, E.W., Mulvaney, R., Steffensen, J.P., Johnsen, S.J., Arrowsmith, C., White, J.W.C., Vaughn, B., Popp, T., **2007**. The 8.2 ka event from Greenland ice cores. *Quat. Sci. Rev.* 26, 70–81.
- Thomas, D.N., Dieckmann, G.S., **2008**. Sea Ice: an introduction to its Physics, Chemistry, Biology and Geology, 1–22.
- Thomas, R., Frederick, E., Krabill, W., Manizade, S., Martin, C., **2009**. Recent changes on Greenland outlet glaciers. *J. Glaciol.* 55, 147–162.
- Thompson, D.W.J., Wallace, J.M., **2001**. Regional Climate Impacts of the Northern Hemisphere Annular Mode. *Science.* 293, 85–89.
- Thomson, D.J., **1982**. Spectrum estimation and harmonic analysis. *Proc. IEEE* 70, 1055–1096.
- Tilling, R.L., Ridout, A., Shepherd, A., Wingham, D.J., **2015**. Increased Arctic sea ice volume after anomalously low melting in 2013. *Nat. Geosci.* 8, 643–646.
- Topp, R., Johnson, M., **1997**. Winter intensification and water mass evolution from yearlong current meters in the Northeast Water Polynya. *J. Mar. Syst.* 10, 157–173.
- Tripati, A., Backman, J., Elderfield, H., Ferretti, P., **2005**. Eocene bipolar glaciation associated with global carbon cycle changes. *Nature* 436, 341–346.
- Tripati, A.K., Eagle, R.A., Morton, A., Dowdeswell, J.A., Atkinson, K.L., Bahé, Y., Dawber, C.F., Khadun, E., Shaw, R.M.H., Shorttle, O., Thanabalasundaram, L., **2008**. Evidence for glaciation in the Northern Hemisphere back to 44 Ma from ice-rafted debris in the Greenland Sea. *Earth Planet. Sci. Lett.* 265, 112–122.
- van den Broeke, M., Bamber, J., Ettema, J., Rignot, E., Schrama, E., van de Berg, W.J., van Meijgaard, E., Velicogna, I., Wouters, B., **2009**. Partitioning Recent Greenland Mass Loss. *Science* (80). 326, 984–986.
- Vinje, T., **1977**. Sea ice conditions in the European sector of the marginal seas of the Arctic, 1966e1975. *Norsk Polarinstitut Årbok* 1975, 163–174.
- Volkman, J.K., **1986**. A review of sterol markers for marine and terrigenous organic matter. *Org. Geochem.* 9, 83–99.
- Volkman, J.K., Barrett, S.M., Dunstan, G.A., Jeffrey, S.W., **1993**. Geochemical significance of the occurrence of dinosterol and other 4-methyl sterols in a marine diatom. *Org. Geochem.* 20, 7–15.
- Volkman, J.K., Barrett, S.M., Dunstan, G.A., **1994**. C₂₅ and C₃₀ highly branched isoprenoid alkenes in laboratory cultures of two marine diatoms. *Org. Geochem.* 21, 407–414.
- Volkman, J.K., Barrett, S.M., Blackburn, S.I., Mansour, M.P., Sikes, E.L., Gelin, F., **1998**. Microalgal biomarkers: A review of recent research developments. *Org. Geochem.* 29, 1163–1179.
- Volkman, R., **2000**. Planktic foraminifer ecology and stable isotope geochemistry in the Arctic Ocean: implications from water column and sediment surface studies for quantitative reconstructions of oceanic parameters. *Ber. Polarforsch.* 361, 61–86.
- Volkman, J.K., Revill, A.T., Holdsworth, D.G., Fredericks, D., **2008**. Organic matter sources in an enclosed coastal inlet assessed using lipid biomarkers and stable isotopes. *Org. Geochem.* 39, 689–710.
- Vonmoos, M., Beer, J., Muscheler, R., **2006**. Large variations in Holocene solar activity: Constraints from ¹⁰Be in the Greenland Ice Core Project ice core. *J. Geophys. Res. Sp. Phys.* 111, 1–14.
- Wadhams, P., **1981**. The ice cover in the Greenland and Norwegian seas. *Rev. Geophys.* 19, 345–393.
- Wadhams, P., Deacon, G.E.R., **1981**. Sea-ice topography of the Arctic Ocean in the region 70° W to 25° E. *Philos. Trans. R. Soc. London. Ser. A, Math. Phys. Sci.* 302, 45–85.

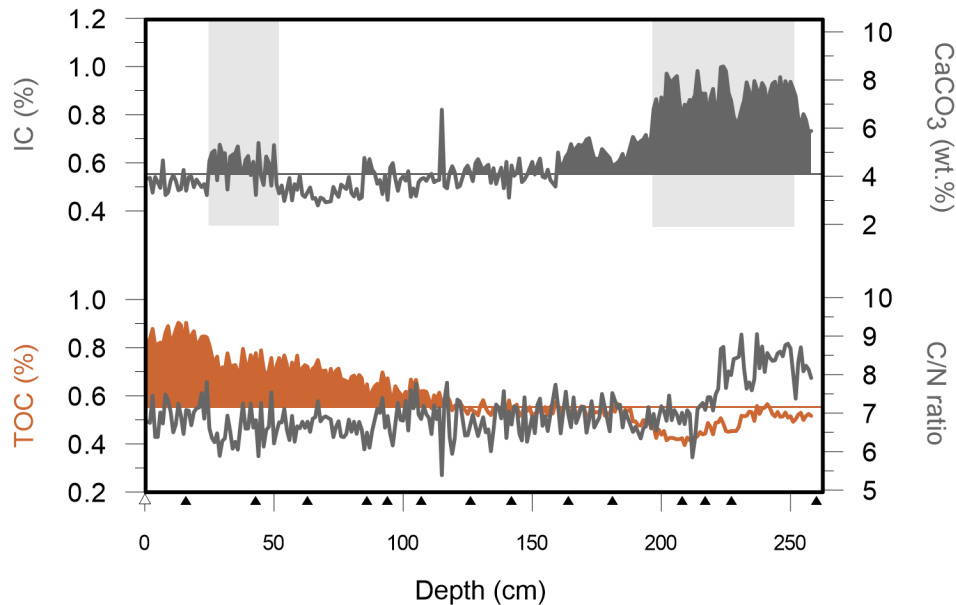
- Wadhams, P., **1992**. Sea ice thickness distribution in the Greenland Sea and Eurasian Basin, May 1987. *J. Geophys. Res. Ocean.* 97, 5331–5348.
- Wadhams, P., **2003**. How does Arctic Sea Ice Form and Decay [<https://www.pmel.noaa.gov.html>]. Arct. Theme Page. NOAA.
- Wallace, J. M.; Hobbs, P. V., **1977**. Atmosphere science - an introductory survey. *Atmos. Sci. - an Introd. Surv.* by Wallace, J. M.; Hobbs, P. V. New York, NY Acad. Press. 467
- Wallace, J.M., Gutzler, D.S., **1981**. Teleconnections in the Geopotential Height Field during the Northern Hemisphere Winter. *Mon. Weather Rev.* 109, 784–812.
- Walsh, J.E., Fetterer, F., Scott Stewart, J., Chapman, W.L., **2017**. A database for depicting Arctic sea ice variations back to 1850. *Geogr. Res.* 107, 89–107.
- Wang, J., Ikeda, M., **2000**. Arctic oscillation and Arctic sea-ice oscillation. *Geophys. Res. Lett.* 27, 1287–1290.
- Waniek, J.J., Holliday, N.P., Davidson, R., Brown, L., Henson, S.A., **2005**. Freshwater control of onset and species composition of Greenland shelf spring bloom. *MEPS* 288, 45–57.
- Wanner, H., Brönnimann, S., Casty, C., Gyalistras, D., Luterbacher, J., Schmutz, C., Stephenson, D.B., Xoplaki, E., **2001**. North Atlantic Oscillation – Concepts and Studies. *Surv. Geophys.* 22, 321–381.
- Wanner, H., Beer, J., Bütikofer, J., Crowley, T.J., Cubasch, U., Flückiger, J., Goosse, H., Grosjean, M., Joos, F., Kaplan, J.O., Küttel, M., Müller, S.A., Prentice, I.C., et al., **2008**. Mid- to Late Holocene climate change: an overview. *Quat. Sci. Rev.* 27, 1791–1828.
- Wanner, H., Solomina, O., Grosjean, M., Ritz, S.P., Jetel, M., **2011**. Structure and origin of Holocene cold events. *Quat. Sci. Rev.* 30, 3109–3123.
- Wassmann, P., Ratkova, T., Andreassen, I., Vernet, M., Pedersen, G., Rey, F., **1999**. Spring Bloom Development in the Marginal Ice Zone and the Central Barents Sea. *Mar. Ecol.* 20, 321–346.
- Wassmann, P.; Reigstad, M., **2011**. Future Arctic Ocean Seasonal Ice Zones and Implications for Pelagic–Benthic Coupling. *Oceanography* 24, 220–231.
- Weckström, K., Massé, G., Collins, L.G., Hanhijärvi, S., Bouloubassi, I., Sicre, M.-A., Seidenkrantz, M.-S., Schmidt, S., Andersen, T.J., Andersen, M.L., Hill, B., Kuijpers, A., **2013**. Evaluation of the sea ice proxy IP₂₅ against observational and diatom proxy data in the SW Labrador Sea. *Quat. Sci. Rev.* 79, 53–62.
- Weeks, W.F., **2010**. On Sea Ice. University of Alaska.
- Wendisch, M.; Brückner, M.; Burrows, J.P.; Crewell, S.; Dethloff, K.; Ebell, K.; Lüpkes, Ch.; Macke, A.; Notholt, J.; Quaas, J.; Rinke, A.; Tegen, I., **2017**. Introduction of the Transregional Collaborative Research Center TR 172: Arctic Amplification. *Wiss. Mitteil. Inst. f. Meteorol. Univ. Leipzig* 55.
- Werner, K., Spielhagen, R.F., Bauch, D., Hass, H.C., Kandiano, E., **2013**. Atlantic Water advection versus sea-ice advances in the eastern Fram Strait during the last 9 ka: Multiproxy evidence for a two-phase Holocene. *Paleoceanography* 28, 283–295.
- Werner, K., Müller, J., Husum, K., Spielhagen, R.F., Kandiano, E.S., Polyak, L., **2016**. Holocene sea subsurface and surface water masses in the Fram Strait – Comparisons of temperature and sea-ice reconstructions. *Quat. Sci. Rev.* 147, 194–209.
- Wickert, A.D., Anderson, R.S., Mitrovica, J.X., Naylor, S., Carson, E.C., **2019**. The Mississippi River records glacial-isostatic deformation of North America. *Sci. Adv.* 5, eaav2366.
- Williams, W.J., Carmack, E.C., **2015**. The ‘interior’ shelves of the Arctic Ocean: Physical oceanographic setting, climatology and effects of sea-ice retreat on cross-shelf exchange. *Prog. Oceanogr.* 139, 24–41.
- Wilson, N., Straneo, F., Heimbach, P., **2017**. Satellite-derived submarine melt rates and mass balance (2011–2015) for Greenland’s largest remaining ice tongues 2773–2782.
- Wilson, N.J., Straneo, F., **2015**. Water exchange between the continental shelf and the cavity beneath Nioghalvfjærdsbræ (79 North Glacier). *Geophys. Res. Lett.* 42, 7648–7654.
- Winkelmann, D., Jokat, W., Jensen, L., Schenke, H.W., **2010**. Submarine end moraines on the continental shelf off NE Greenland - Implications for Lateglacial dynamics. *Quat. Sci. Rev.* 29, 1069–1077.
- World Meteorological Organization **1970** WMO sea ice nomenclature. WMO Rep 259 TP 1

- World Meteorological Organization **1985** WMO sea ice nomenclature. WMO Rep 259 TP 145
- Wraige, E.J., Belt, S.T., Massé, G., Robert, J.-M., Rowland, S.J., **1998**. Variations in distributions of C₂₅ highly branched isoprenoid (HBI) alkenes in the diatom, *Haslea ostrearia*: influence of salinity. *Org. Geochem.* 28, 855–859.
- Wu, J., Stein, R., Fahl, K., Syring, N., Nam, S., Hefter, J., Mollenhauer, G., Geibert, W., **2020**. Deglacial to Holocene variability in surface water characteristics and major floods in the Beaufort Sea. *Commun. Earth & Science*, under review
- Xiao, X., Fahl, K., Stein, R., **2013**. Biomarker distributions in surface sediments from the Kara and Laptev seas (Arctic Ocean): Indicators for organic-carbon sources and sea-ice coverage. *Quat. Sci. Rev.* 79, 40–52.
- Xiao, X., Fahl, K., Müller, J., Stein, R., **2015**. Sea-ice distribution in the modern Arctic Ocean: Biomarker records from trans-Arctic Ocean surface sediments. *Geochim. Cosmochim. Acta* 155, 16–29.
- Xiao, X., Stein, R., Fahl, K., **2015**. MIS 3 to MIS 1 temporal and LGM spatial variability in Arctic Ocean sea ice cover: Reconstruction from biomarkers. *Paleoceanography* 30, 969–983.
- Xiao, X., Zhao, M., Knudsen, K.L., Sha, L., Eiríksson, J., Gudmundsdóttir, E., Jiang, H., Guo, Z., **2017**. Deglacial and Holocene sea-ice variability north of Iceland and response to ocean circulation changes. *Earth and Planetary Science Letters* 472, 14–24.
- Xu, D., Lu, H., Chu, G., Wu, N., Shen, C., Wang, C., Mao, L., **2014**. 500-year climate cycles stacking of recent centennial warming documented in an East Asian pollen record. *Sci. Rep.* 4, 3611.
- Yin, J., Overpeck, J.T., Griffies, S.M., Hu, A., Russell, J.L., Stouffer, R.J., **2011**. Different magnitudes of projected subsurface ocean warming around Greenland and Antarctica. *Nat. Geosci.* 4, 524–528.
- Young, N.E., Briner, J.P., Rood, D.H., Finkel, R.C., **2012**. Glacier Extent During the Younger Dryas and 8.2-ka Event on Baffin Island, Arctic Canada. *Science*. 337, 1330–1333.
- Young, N.E., Briner, J.P., Miller, G.H., Lesnek, A.J., Crump, S.E., Thomas, E.K., Pendleton, S.L., Cuzzone, J., Lamp, J., Zimmerman, S., Caffee, M., Schaefer, J.M., **2020**. Deglaciation of the Greenland and Laurentide ice sheets interrupted by glacier advance during abrupt coolings. *Quat. Sci. Rev.* 229.
- Yu, S.H., Colman, S.M., Lowell, T.V., Milne, G.A., Fisher, T.G., Breckenridge, A., Boyd, M., Teller, J.T., **2010**. Freshwater outburst from Lake Superior as a trigger for the cold event 9300 years ago. *Science* 328, 1262–1266.
- Yunker, M.B., Macdonald, R.W., Velthamp, D.J., Cretney, W.J., **1995**. Terrestrial and marine biomarkers in a seasonally ice-covered Arctic estuary – integration of multivariate and biomarker approaches. *Mar. Chem.* 49, 1–50.
- Zachos, J., Pagani, M., Sloan, L., Thomas, E., Billups, K., **2001**. Trends, Rhythms, and Aberrations in Global Climate 65 Ma to Present. *Science*. 292, 686–693.
- Zachos, J.C., Dickens, G.R., Zeebe, R.E., **2008**. An early Cenozoic perspective on greenhouse warming and carbon-cycle dynamics. *Nature* 451, 279–283.
- Zamani, B., Krumpfen, T., Smedsrud, L.H., Gerdes, R., **2019**. Fram Strait sea ice export affected by thinning: comparing high-resolution simulations and observations. *Clim. Dyn.* 53, 3257–3270.
- Zehnich, M., Spielhagen, R.F., Bauch, H.A., et al., **2020**. Environmental variability off NE Greenland (western Fram Strait) during the past 10,600 years. *The Holocene*.
doi:10.1177/0959683620950393
- Zhang, Y.G., Pagani, M., Liu, Z., **2014**. A 12-Million-Year Temperature History of the Tropical Pacific Ocean. *Science*. 344, 84–87.
- Zhao, C., Yu, Z., Ito, E., Zhao, Y., **2010**. Holocene climate trend, variability, and shift documented by lacustrine stable-isotope record in the northeastern United States. *Quat. Sci. Rev.* 29, 1831–1843.
- Zwally, H. J., M. B. Giovinetto, M. A. Beckley, and J.L.S., **2012**. Antarctic and Greenland Drainage Systems, GSFC. Cryospheric Sci. Lab.

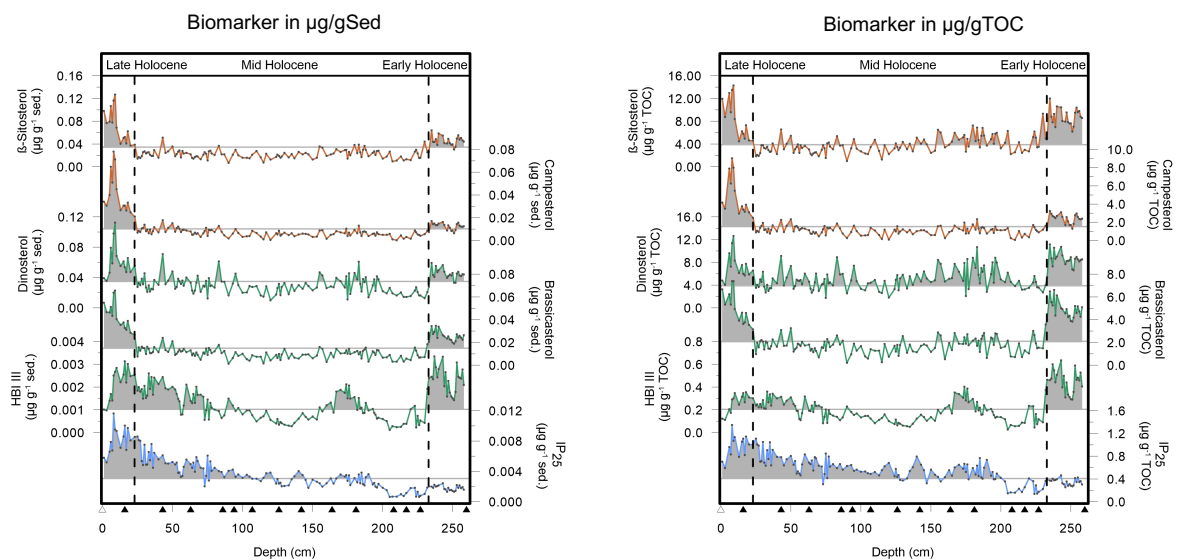
Appendix

Appendix A

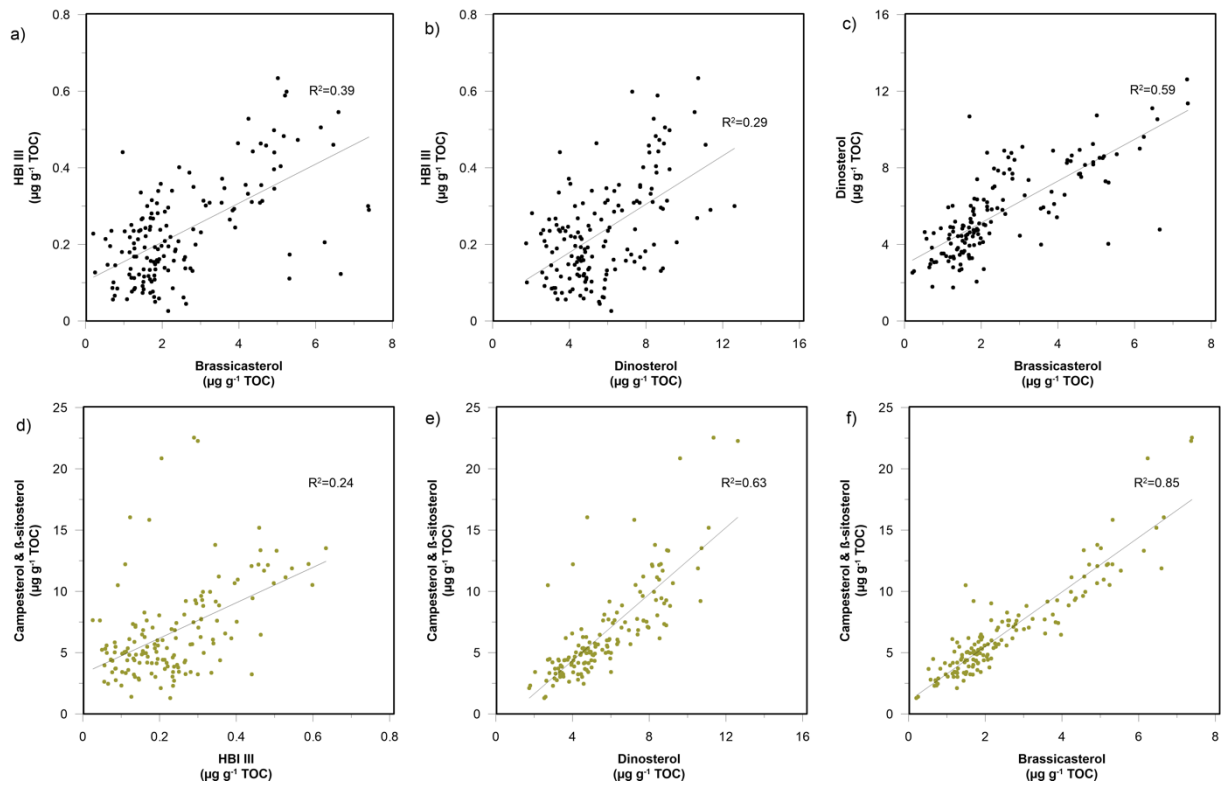
The generated data of Core PS93/025 (chapter 4) are published on the *Data Publisher for Earth & Environmental Science - PANGAEA* (doi: <https://doi.org/10.1594/PANGAEA.905516>).



A.1: Total organic carbon (%), C/N ratio, inorganic carbon (IC, %) and CaCO_3 (wt.%) against depth (cm). Grey bars mark maximum intervals in the CaCO_3 record. Black triangles mark position of corrected ^{14}C AMS dates.



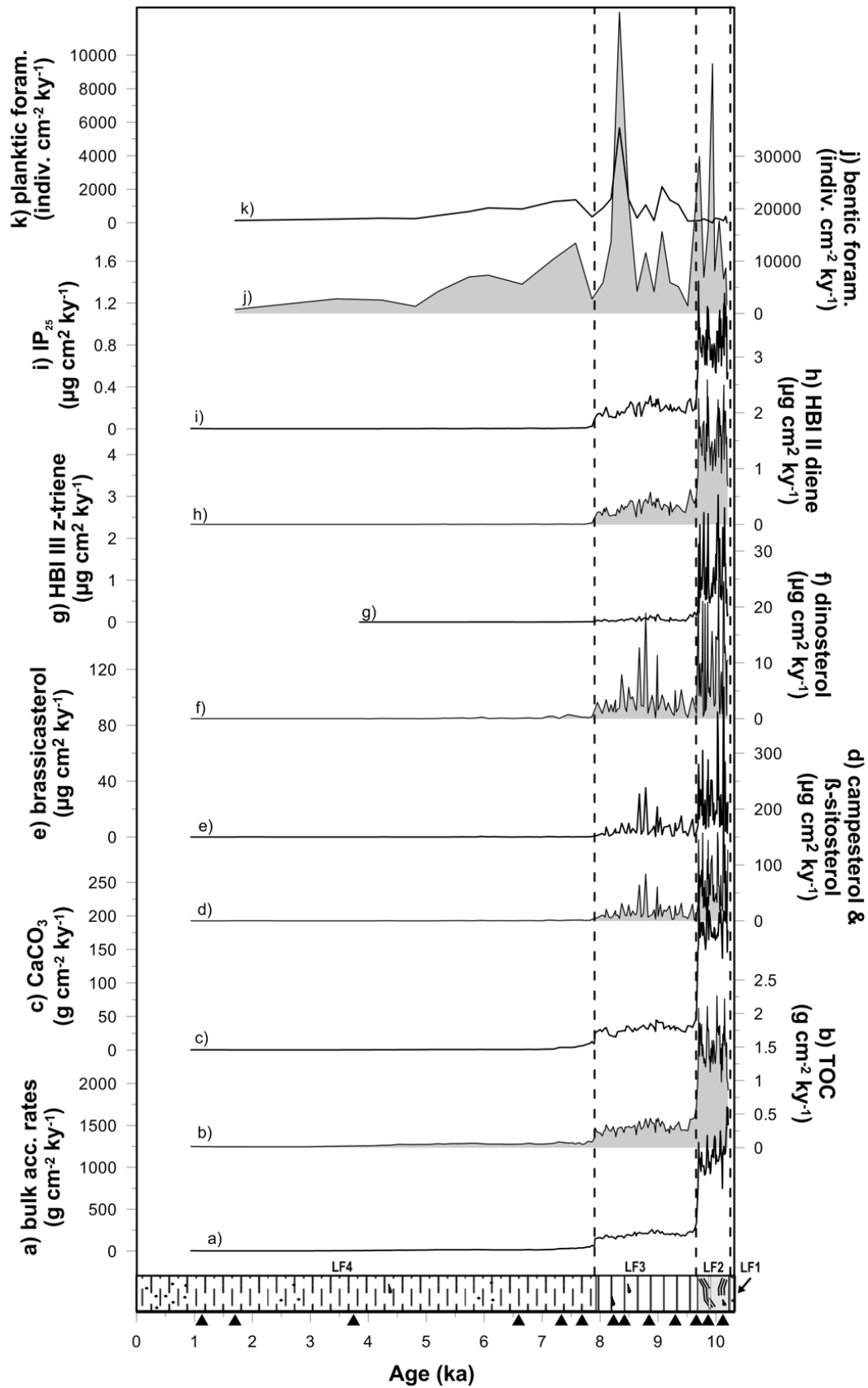
A.2: Lipid biomarker concentrations ($\mu\text{g g}^{-1}$ Sed, $\mu\text{g g}^{-1}$ TOC), including terrigenous biomarkers β -sitosterol and campesterol, phytoplankton biomarkers brassicasterol, dinosterol and HBI III triene and sea-ice associated biomarker IP_{25} against depth (cm). Grey shaded areas highlight maxima of these records. Black triangles mark position of corrected ^{14}C AMS dates.



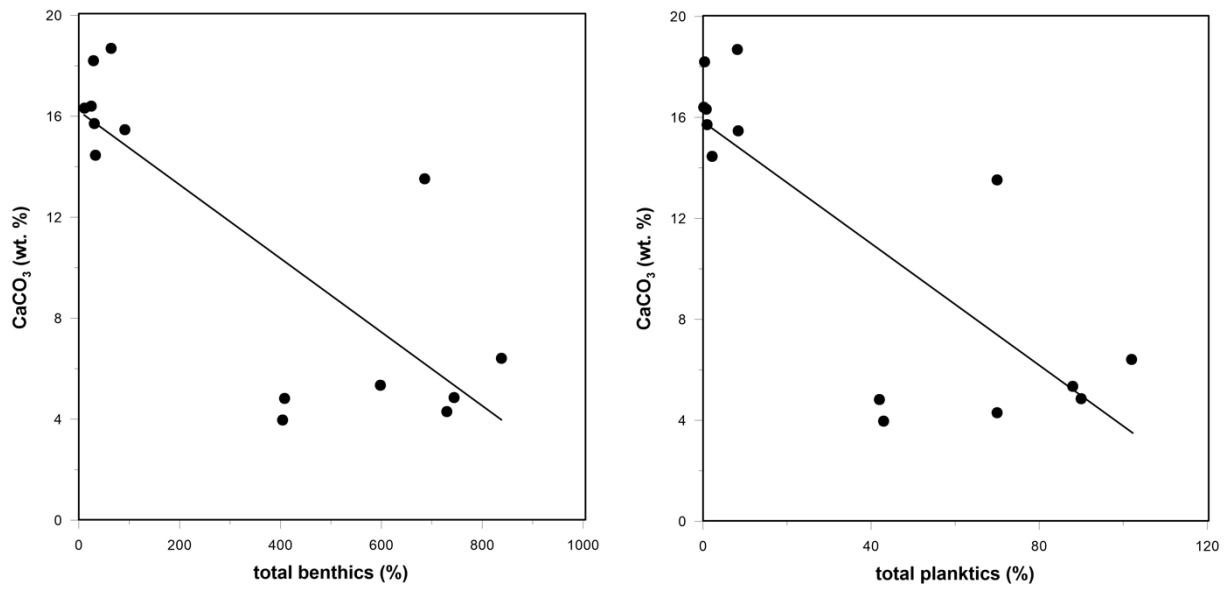
A.3: Source plots between phytoplankton marker against each other (black dots) and terrigenous biomarkers against phytoplankton biomarkers (green dots).

Appendix B

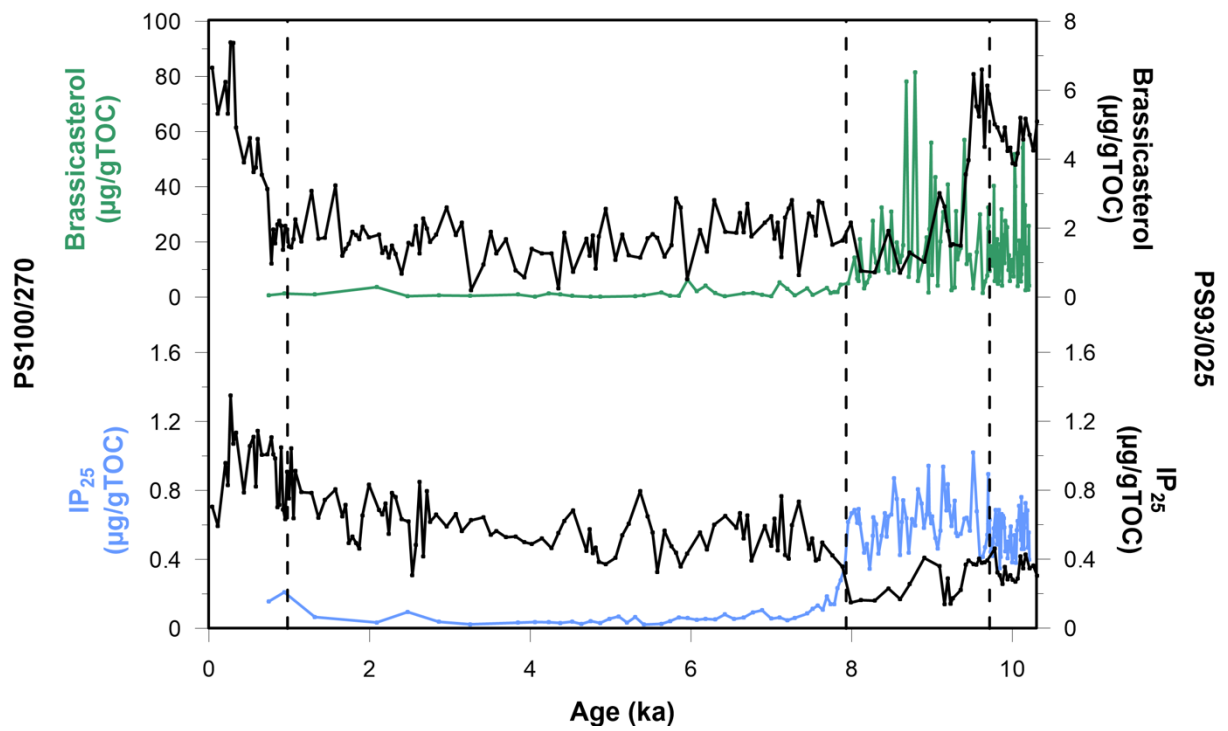
This Appendix contains various downcore data of organic bulk parameters, HBIs and specific sterols relevant to Chapter 5 of this thesis. These include organic bulk parameters, HBIs, specific sterol concentrations ($\mu\text{g g}^{-1}$ TOC), planktic and benthic foraminifers and will be accessible on *PANGAEA* as soon as the manuscript is published.



B.1: Accumulation rates ($\text{g cm}^{-2} \text{ky}^{-1}$, $\mu\text{g cm}^{-2} \text{ky}^{-1}$, $\text{indiv. cm}^{-2} \text{ky}^{-1}$) of total organic (TOC) and inorganic carbon (CaCO_3), terrigenous biomarkers (β -sitosterol, campesterol), phytoplankton biomarkers (brassicasterol, dinosterol, HBI III triene), sea-ice associated biomarker (IP_{25} , HBI II diene), planktic and benthic foraminifera, plotted against age (ka). Grey shaded areas highlight maxima of these records. Black triangles mark position of corrected ^{14}C AMS dates.



B.2: Carbonate (CaCO₃, wt.%) against total benthic foraminifera (%) and total planktic (%) foraminifers.



B.3: Comparison of biomarker records IP₂₅ and brassicasterol from the outer (PS93/025) and inner (PS100/270) Northeast Greenland continental shelf.

Tabel B.1: Organic bulk parameter

Cruise: PS100; Station: PS100/270; Lon [°E]: -18.14; Lat [°N]: 79.49; Water Depth: 424 m

| Depth | Age | Sed rate | TOC | Acc rate TOC | TC | IC | CaCO3 | Acc rate CaCO3 |
|-------|---------|----------|------|-------------------------|------|------|---------|-------------------------|
| [cm] | [ka BP] | [cm/ka] | [%] | [g/cm ² /ka] | [%] | [%] | [wt. %] | [g/cm ² /ka] |
| 1 | 0,75 | 5,24 | 0,44 | | | | | |
| 2 | 0,94 | 5,25 | 0,50 | 0,0181 | 1,35 | 0,85 | 7,10 | 0,060 |
| 4 | 1,32 | 5,20 | 0,47 | 0,0143 | 1,29 | 0,83 | 6,91 | 0,057 |
| 8 | 2,09 | 5,17 | 0,46 | 0,0126 | 1,03 | 0,57 | 4,77 | 0,027 |
| 10 | 2,48 | 5,15 | 0,43 | 0,0119 | | | | |
| 12 | 2,86 | 5,14 | 0,42 | 0,0120 | 0,94 | 0,52 | 4,33 | 0,023 |
| 14 | 3,25 | 6,71 | 0,48 | 0,0191 | 0,89 | 0,41 | 3,45 | 0,014 |
| 18 | 3,85 | 9,62 | 0,43 | 0,0259 | 0,90 | 0,47 | 3,91 | 0,018 |
| 20 | 4,06 | 11,36 | 0,37 | 0,0276 | | | | |
| 22 | 4,23 | 13,99 | 0,39 | 0,0350 | 0,86 | 0,48 | 3,97 | 0,019 |
| 24 | 4,38 | 13,89 | 0,39 | 0,0359 | 0,89 | 0,49 | 4,11 | 0,020 |
| 26 | 4,52 | 17,09 | 0,42 | 0,0492 | 0,86 | 0,44 | 3,70 | 0,016 |
| 28 | 4,64 | 17,09 | 0,42 | 0,0469 | 0,87 | 0,45 | 3,77 | 0,017 |
| 30 | 4,75 | 17,24 | 0,39 | 0,0457 | | | | |
| 32 | 4,87 | 17,24 | 0,38 | 0,0484 | 0,90 | 0,52 | 4,31 | 0,022 |
| 34 | 4,99 | 17,39 | 0,36 | 0,0465 | 0,90 | 0,54 | 4,46 | 0,024 |
| 36 | 5,10 | 19,23 | 0,34 | 0,0513 | 0,92 | 0,58 | 4,85 | 0,028 |
| 38 | 5,20 | 19,42 | 0,37 | 0,0586 | 0,95 | 0,58 | 4,82 | 0,028 |
| 40 | 5,31 | 18,87 | 0,35 | 0,0532 | | | | |
| 42 | 5,41 | 18,35 | 0,37 | 0,0593 | 0,89 | 0,52 | 4,33 | 0,022 |
| 46 | 5,63 | 18,52 | 0,38 | 0,0608 | 0,90 | 0,52 | 4,37 | 0,023 |
| 48 | 5,74 | 18,52 | 0,40 | 0,0637 | 0,91 | 0,52 | 4,30 | 0,022 |
| 50 | 5,85 | 18,02 | 0,36 | 0,0656 | | | | |
| 52 | 5,96 | 17,86 | 0,35 | 0,0588 | 0,96 | 0,61 | 5,10 | 0,031 |
| 54 | 6,07 | 17,70 | 0,34 | 0,0520 | 0,92 | 0,58 | 4,85 | 0,028 |
| 56 | 6,18 | 16,95 | 0,37 | 0,0534 | 0,94 | 0,56 | 4,68 | 0,026 |
| 58 | 6,30 | 16,95 | 0,36 | 0,0523 | 0,95 | 0,59 | 4,93 | 0,029 |
| 60 | 6,42 | 17,09 | 0,35 | 0,0495 | | | | |
| 62 | 6,54 | 16,95 | 0,35 | 0,0512 | 0,95 | 0,60 | 4,99 | 0,030 |
| 64 | 6,65 | 17,09 | 0,37 | 0,0531 | 1,01 | 0,64 | 5,34 | 0,034 |
| 66 | 6,77 | 17,54 | 0,36 | 0,0660 | 1,03 | 0,66 | 5,52 | 0,036 |
| 68 | 6,89 | 17,39 | 0,38 | 0,0529 | 1,03 | 0,66 | 5,49 | 0,036 |
| 70 | 7,00 | 19,23 | 0,32 | 0,0531 | | | | |
| 72 | 7,10 | 21,05 | 0,32 | 0,0577 | 1,20 | 0,88 | 7,34 | 0,065 |
| 74 | 7,20 | 21,05 | 0,32 | 0,0638 | 1,09 | 0,77 | 6,40 | 0,049 |
| 76 | 7,29 | 26,14 | 0,29 | 0,0849 | 1,83 | 1,54 | 12,86 | 0,199 |
| 80 | 7,45 | 28,57 | 0,22 | 0,0677 | | | | |
| 82 | 7,52 | 32,26 | 0,20 | 0,0713 | 1,54 | 1,33 | 11,12 | 0,148 |
| 84 | 7,58 | 32,26 | 0,17 | 0,0549 | 1,79 | 1,62 | 13,52 | 0,219 |
| 86 | 7,64 | 40,00 | 0,19 | 0,0737 | 2,03 | 1,84 | 15,35 | 0,283 |
| 88 | 7,69 | 40,82 | 0,13 | 0,0472 | 2,09 | 1,96 | 16,35 | 0,321 |
| 90 | 7,74 | 45,45 | 0,14 | 0,0583 | | | | |
| 92 | 7,78 | 52,63 | 0,18 | 0,0918 | 2,25 | 2,07 | 17,26 | 0,358 |
| 94 | 7,82 | 51,28 | 0,19 | 0,0915 | 2,55 | 2,36 | 19,66 | 0,464 |
| 96 | 7,86 | 76,92 | 0,12 | 0,0826 | 2,36 | 2,24 | 18,68 | 0,419 |
| 99 | 7,90 | 71,43 | 0,24 | 0,1386 | 2,13 | 1,89 | 15,74 | 0,297 |
| 100 | 7,91 | 195,12 | 0,20 | 0,2934 | 2,26 | 2,06 | 17,15 | 0,353 |
| 108 | 7,96 | 200,00 | 0,15 | 0,2279 | | | | |
| 117 | 8,00 | 222,22 | 0,14 | 0,2232 | 2,39 | 2,25 | 18,74 | 0,421 |
| 125 | 8,04 | 218,75 | 0,12 | 0,1750 | 2,31 | 2,19 | 18,25 | 0,400 |
| 132 | 8,07 | 222,22 | 0,15 | 0,2498 | 2,48 | 2,32 | 19,36 | 0,450 |
| 136 | 8,09 | 222,22 | 0,14 | 0,2604 | | | | |
| 140 | 8,10 | 230,77 | 0,18 | 0,3406 | 2,24 | 2,07 | 17,23 | 0,356 |
| 152 | 8,16 | 235,29 | 0,16 | 0,2593 | 1,78 | 1,62 | 13,52 | 0,219 |
| 160 | 8,19 | 228,57 | 0,14 | 0,2449 | | | | |
| 168 | 8,23 | 219,51 | 0,19 | 0,3111 | 1,65 | 1,46 | 12,18 | 0,178 |
| 177 | 8,27 | 200,00 | 0,14 | 0,2117 | 1,75 | 1,61 | 13,39 | 0,215 |
| 178 | 8,27 | 225,81 | 0,11 | 0,1632 | 1,69 | 1,58 | 13,17 | 0,208 |
| 185 | 8,30 | 212,12 | 0,16 | 0,2807 | 1,97 | 1,82 | 15,12 | 0,275 |
| 192 | 8,34 | 205,13 | 0,17 | 0,2996 | | | | |
| 200 | 8,37 | 200,00 | 0,17 | 0,3050 | 2,04 | 1,87 | 15,60 | 0,292 |
| 208 | 8,41 | 200,00 | 0,14 | 0,2254 | 2,34 | 2,20 | 18,31 | 0,402 |
| 212 | 8,43 | 208,33 | 0,18 | 0,3073 | 2,12 | 1,95 | 16,22 | 0,316 |
| 217 | 8,46 | 216,22 | 0,16 | 0,3017 | 2,38 | 2,22 | 18,51 | 0,411 |
| 225 | 8,50 | 218,75 | 0,16 | 0,3176 | 2,28 | 2,12 | 17,68 | 0,375 |
| 232 | 8,53 | 216,22 | 0,16 | 0,2971 | | | | |
| 240 | 8,56 | 216,22 | 0,16 | 0,3074 | 1,89 | 1,73 | 14,39 | 0,249 |
| 248 | 8,60 | 208,33 | 0,15 | 0,3340 | 1,87 | 1,73 | 14,40 | 0,249 |
| 253 | 8,63 | 214,29 | 0,10 | 0,1910 | 2,00 | 1,90 | 15,82 | 0,300 |
| 256 | 8,64 | 225,00 | 0,14 | 0,2933 | 1,88 | 1,73 | 14,45 | 0,251 |

| Depth | Age | Sed rate | TOC | Acc rate TOC | TC | IC | CaCO3 | Acc rate CaCO3 |
|-------|------------|----------|------|-------------------------|------|------|---------|-------------------------|
| [cm] | [ka BP] | [cm/ka] | [%] | [g/cm ² /ka] | [%] | [%] | [wt. %] | [g/cm ² /ka] |
| 265 | 8,68 | 218,75 | 0,18 | 0,3941 | 1,92 | 1,75 | 14,57 | 0,255 |
| 272 | 8,71 | 210,53 | 0,13 | 0,2742 | | | | |
| 280 | 8,75 | 205,13 | 0,14 | 0,3056 | 2,24 | 2,10 | 17,50 | 0,367 |
| 288 | 8,79 | 205,13 | 0,20 | 0,4324 | 2,06 | 1,86 | 15,46 | 0,287 |
| 296 | 8,83 | 219,51 | 0,14 | 0,2962 | 1,93 | 1,79 | 14,92 | 0,267 |
| 305 | 8,87 | 225,81 | 0,18 | 0,4367 | 2,17 | 1,98 | 16,53 | 0,328 |
| 312 | 8,90 | 242,42 | 0,14 | 0,3665 | | | | |
| 320 | 8,93 | 230,77 | 0,17 | 0,3636 | 2,05 | 1,88 | 15,71 | 0,296 |
| 326 | 8,96 | 222,22 | 0,10 | 0,2246 | 1,64 | 1,54 | 12,81 | 0,197 |
| 328 | 8,97 | 238,10 | 0,17 | 0,4215 | 2,39 | 2,22 | 18,47 | 0,409 |
| 333 | 8,99 | 230,77 | 0,16 | 0,3870 | 2,34 | 2,18 | 18,20 | 0,397 |
| 336 | 9,00 | 230,77 | 0,18 | 0,4407 | 2,19 | 2,01 | 16,72 | 0,336 |
| 345 | 9,04 | 233,33 | 0,15 | 0,3169 | | | | |
| 352 | 9,07 | 242,42 | 0,17 | 0,3897 | 2,28 | 2,11 | 17,57 | 0,371 |
| 360 | 9,10 | 235,29 | 0,17 | 0,3463 | 2,04 | 1,87 | 15,61 | 0,292 |
| 368 | 9,14 | 225,00 | 0,12 | 0,2402 | 2,16 | 2,04 | 17,00 | 0,347 |
| 377 | 9,18 | 227,27 | 0,14 | 0,2769 | 2,23 | 2,09 | 17,42 | 0,364 |
| 382 | 9,20 | 230,77 | 0,11 | 0,2138 | 2,26 | 2,15 | 17,96 | 0,387 |
| 385 | 9,21 | 218,75 | 0,17 | 0,3270 | 2,04 | 1,88 | 15,65 | 0,294 |
| 392 | 9,24 | 222,22 | 0,13 | 0,2786 | | | | |
| 400 | 9,28 | 222,22 | 0,13 | 0,2710 | 2,24 | 2,10 | 17,52 | 0,368 |
| 404 | 9,30 | 210,53 | 0,17 | 0,3214 | 2,07 | 1,89 | 15,78 | 0,299 |
| 408 | 9,32 | 214,29 | 0,16 | 0,3287 | 2,07 | 1,91 | 15,93 | 0,305 |
| 417 | 9,36 | 205,13 | 0,19 | 0,3838 | 2,10 | 1,91 | 15,94 | 0,305 |
| 425 | 9,40 | 200,00 | 0,14 | 0,2592 | 2,06 | 1,91 | 15,95 | 0,305 |
| 432 | 9,43 | 200,00 | 0,14 | 0,2606 | | | | |
| 440 | 9,47 | 195,12 | 0,14 | 0,2637 | 1,89 | 1,75 | 14,55 | 0,254 |
| 448 | 9,51 | 204,55 | 0,11 | 0,2511 | 2,07 | 1,96 | 16,32 | 0,320 |
| 457 | 9,56 | 210,53 | 0,18 | 0,4238 | 2,02 | 1,83 | 15,28 | 0,280 |
| 465 | 9,60 | 212,12 | 0,19 | 0,4250 | 1,99 | 1,80 | 14,97 | 0,269 |
| 472 | 9,63 | 235,29 | 0,17 | 0,4446 | | | | |
| 480 | 9,66 | 307,69 | 0,18 | 0,6091 | 1,92 | 1,73 | 14,44 | 0,250 |
| 488 | 9,69 | 700,00 | 0,14 | 1,0716 | 2,57 | 2,42 | 20,17 | 0,488 |
| 495 | 9,70 | 1000,00 | 0,14 | 1,5731 | 1,85 | 1,71 | 14,23 | 0,243 |
| 497 | 9,70 | 1142,86 | 0,16 | 2,0769 | 2,43 | 2,27 | 18,93 | 0,430 |
| 505 | 9,71 | 1000,00 | 0,14 | 1,5482 | 2,38 | 2,25 | 18,73 | 0,421 |
| 512 | 9,72 | 1000,00 | 0,13 | 1,3633 | | | | |
| 520 | 9,72 | 1000,00 | 0,17 | 1,8579 | 1,98 | 1,81 | 15,11 | 0,274 |
| 528 | 9,73 | 818,18 | 0,18 | 1,7794 | 2,23 | 2,05 | 17,07 | 0,350 |
| 537 | 9,74 | 800,00 | 0,16 | 1,5298 | 2,55 | 2,39 | 19,92 | 0,476 |
| 545 | 9,75 | 875,00 | 0,16 | 1,8412 | 2,09 | 1,94 | 16,15 | 0,313 |
| 552 | 9,76 | 727,27 | 0,13 | 1,3675 | | | | |
| 560 | 9,77 | 800,00 | 0,15 | 1,5391 | 2,18 | 2,03 | 16,90 | 0,343 |
| 568 | 9,78 | 818,18 | 0,14 | 1,4322 | 2,40 | 2,26 | 18,82 | 0,425 |
| 577 | 9,79 | 800,00 | 0,12 | 1,2603 | 2,26 | 2,13 | 17,79 | 0,380 |
| 585 | 9,80 | 777,78 | 0,15 | 1,3290 | 2,38 | 2,24 | 18,65 | 0,417 |
| 592 | 9,81 | 800,00 | 0,14 | 1,2564 | | | | |
| 600 | 9,82 | 727,27 | 0,13 | 1,2014 | 2,07 | 1,94 | 16,14 | 0,313 |
| 608 | 9,83 | 818,18 | 0,14 | 1,3679 | 2,15 | 2,01 | 16,75 | 0,337 |
| 617 | 9,84 | 1000,00 | 0,14 | 1,7440 | 2,26 | 2,11 | 17,62 | 0,373 |
| 625 | 9,85 | 1166,67 | 0,15 | 2,1079 | 2,13 | 1,98 | 16,52 | 0,327 |
| 632 | 9,86 | 1000,00 | 0,16 | 1,8229 | | | | |
| 640 | 9,87 | 930,23 | 0,14 | 1,7367 | 2,11 | 1,97 | 16,39 | 0,323 |
| 648 | 9,87 | 833,33 | 0,18 | 1,7671 | 2,15 | 1,98 | 16,47 | 0,325 |
| 657 | 9,88 | 833,33 | 0,12 | 1,3174 | 2,46 | 2,34 | 19,47 | 0,455 |
| 665 | 9,89 | 833,33 | 0,13 | 1,3602 | 2,52 | 2,38 | 19,85 | 0,473 |
| 672 | 9,90 | 833,33 | 0,12 | 1,1275 | | | | |
| 680 | 9,91 | 833,33 | 0,15 | 1,4783 | 2,36 | 2,21 | 18,38 | 0,405 |
| 688 | 9,92 | 833,33 | 0,11 | 1,2760 | 1,89 | 1,78 | 14,82 | 0,264 |
| 697 | 9,93 | 833,33 | 0,14 | 1,6008 | 2,01 | 1,87 | 15,56 | 0,291 |
| 705 | 9,94 | 833,33 | 0,12 | 1,4447 | 1,79 | 1,67 | 13,94 | 0,233 |
| 712 | 9,95 | 833,33 | 0,10 | 1,2511 | | | | |
| 720 | 9,96 | 833,33 | 0,14 | 1,5999 | 1,94 | 1,80 | 14,99 | 0,270 |
| 728 | 9,97 | 833,33 | 0,12 | 1,5236 | 1,77 | 1,66 | 13,82 | 0,229 |
| 737 | 9,98 | 833,33 | 0,09 | 1,2973 | 1,68 | 1,58 | 13,18 | 0,208 |
| 745 | 9,99 | 833,33 | 0,09 | 1,2566 | 1,58 | 1,48 | 12,35 | 0,183 |
| 752 | 10,00 | 833,33 | 0,13 | 1,3972 | | | | |
| 760 | 10,01 | 833,33 | 0,13 | 1,5222 | 1,91 | 1,78 | 14,85 | 0,265 |
| 768 | 10,02 | 833,33 | 0,21 | 2,2645 | 2,07 | 1,86 | 15,50 | 0,288 |
| 777 | 10,03 | 833,33 | 0,16 | 1,7250 | 2,11 | 1,95 | 16,24 | 0,317 |
| 785 | 10,04 | 833,33 | 0,17 | 1,7968 | 2,08 | 1,91 | 15,92 | 0,304 |
| 792 | 10,05 | 833,33 | 0,15 | 1,6804 | | | | |
| 800 | 10,06 | 833,33 | 0,16 | 1,8055 | 2,34 | 2,18 | 18,20 | 0,398 |

| Depth | Age | Sed rate | TOC | Acc rate TOC | TC | IC | CaCO3 | Acc rate CaCO3 |
|-------|---------|----------|------|-------------------------|------|------|---------|-------------------------|
| [cm] | [ka BP] | [cm/ka] | [%] | [g/cm ² /ka] | [%] | [%] | [wt. %] | [g/cm ² /ka] |
| 808 | 10,07 | 833,33 | 0,16 | 1,8218 | 2,13 | 1,97 | 16,41 | 0,323 |
| 817 | 10,08 | 833,33 | 0,09 | 1,2508 | 1,85 | 1,76 | 14,67 | 0,258 |
| 825 | 10,09 | 833,33 | 0,11 | 1,4792 | 1,95 | 1,84 | 15,31 | 0,281 |
| 832 | 10,09 | 833,33 | 0,09 | 0,9795 | | | | |
| 840 | 10,10 | 833,33 | 0,15 | 1,5524 | 2,01 | 1,86 | 15,49 | 0,288 |
| 847 | 10,11 | 833,33 | 0,15 | 1,1550 | 2,35 | 2,19 | 18,29 | 0,401 |
| 852 | 10,12 | 833,33 | 0,15 | 1,6908 | 2,08 | 1,93 | 16,10 | 0,311 |
| 860 | 10,13 | 833,33 | 0,13 | 1,5960 | 2,07 | 1,94 | 16,19 | 0,314 |
| 868 | 10,14 | 833,33 | 0,15 | 1,8143 | 2,13 | 1,99 | 16,56 | 0,329 |
| 872 | 10,14 | 833,33 | 0,13 | 1,5249 | | | | |
| 877 | 10,15 | 833,33 | 0,19 | 2,2204 | 2,20 | 2,01 | 16,72 | 0,335 |
| 885 | 10,16 | 833,33 | 0,14 | 1,6147 | 2,24 | 2,10 | 17,50 | 0,368 |
| 892 | 10,17 | 833,33 | 0,14 | 1,6124 | 2,22 | 2,08 | 17,35 | 0,361 |
| 900 | 10,18 | 833,33 | 0,10 | 1,3591 | 1,73 | 1,63 | 13,59 | 0,222 |
| 908 | 10,19 | 833,33 | 0,10 | 1,5614 | 1,90 | 1,80 | 14,97 | 0,269 |
| 912 | 10,19 | 833,33 | 0,06 | 1,0455 | | | | |
| 917 | 10,20 | 833,33 | 0,06 | 0,9931 | 1,08 | 1,02 | 8,53 | 0,087 |
| 925 | 10,21 | 833,33 | 0,06 | 0,9617 | 1,31 | 1,25 | 10,42 | 0,130 |
| 930 | 10,21 | 846,15 | 0,06 | 0,8587 | 1,63 | 1,57 | 13,09 | |

Table B.2: Highly branched isoprenoids (HBIs)

Cruise: PS100; Station: PS100/270; Lon [°E]: -18.14; Lat [°N]: 79.49; Water Depth: 424 m

| Depth | Age | IP ₂₅ /sed | IP ₂₅ /TOC | HBI II diene/sed | HBI II diene/TOC | HBI III z-triene/sed | HBI III z-triene/TOC | HBI III e-triene/sed | HBI III e-triene/TOC |
|-------|---------|-----------------------|-----------------------|------------------|------------------|----------------------|----------------------|----------------------|----------------------|
| [cm] | [ka BP] | [µg/g] | [µg/g] | [µg/g] | [µg/g] | [µg/g] | [µg/g] | [µg/g] | [µg/g] |
| 1 | 0,75 | 0,0007 | 0,16 | 0,0010 | 0,24 | | | | |
| 2 | 0,94 | 0,0011 | 0,21 | 0,0008 | 0,15 | | | | |
| 4 | 1,32 | 0,0003 | 0,07 | 0,0004 | 0,09 | | | | |
| 8 | 2,09 | 0,0002 | 0,03 | 0,0005 | 0,11 | | | | |
| 10 | 2,48 | 0,0004 | 0,10 | 0,0005 | 0,12 | | | | |
| 12 | 2,86 | 0,0002 | 0,04 | 0,0002 | 0,05 | | | | |
| 14 | 3,25 | 0,0001 | 0,02 | 0,0003 | 0,06 | | | | |
| 18 | 3,85 | 0,0001 | 0,03 | 0,0002 | 0,05 | 0,00006 | 0,01 | 0,00004 | 0,01 |
| 20 | 4,06 | 0,0001 | 0,04 | 0,0002 | 0,05 | | | | |
| 22 | 4,23 | 0,0001 | 0,04 | 0,0002 | 0,04 | | | | |
| 24 | 4,38 | 0,0001 | 0,03 | 0,0002 | 0,05 | | | | |
| 26 | 4,52 | 0,0002 | 0,04 | 0,0002 | 0,05 | | | | |
| 28 | 4,64 | 0,0001 | 0,03 | 0,0001 | 0,03 | | | | |
| 30 | 4,75 | 0,0002 | 0,04 | 0,0001 | 0,03 | | | | |
| 32 | 4,87 | 0,0001 | 0,03 | 0,0001 | 0,03 | | | | |
| 34 | 4,99 | 0,0002 | 0,06 | 0,0002 | 0,06 | | | 0,00006 | 0,02 |
| 36 | 5,10 | 0,0002 | 0,07 | 0,0001 | 0,04 | | | | |
| 38 | 5,20 | 0,0001 | 0,03 | 0,0001 | 0,04 | | | | |
| 40 | 5,31 | 0,0002 | 0,07 | 0,0004 | 0,11 | | | | |
| 42 | 5,41 | 0,0001 | 0,02 | 0,0001 | 0,03 | | | | |
| 46 | 5,63 | 0,0001 | 0,03 | 0,0002 | 0,04 | | | | |
| 48 | 5,74 | 0,0002 | 0,04 | 0,0002 | 0,06 | 0,00006 | 0,01 | 0,00005 | 0,01 |
| 50 | 5,85 | 0,0002 | 0,06 | 0,0001 | 0,04 | | | | |
| 52 | 5,96 | 0,0002 | 0,06 | 0,0003 | 0,08 | 0,00005 | 0,01 | 0,00007 | 0,02 |
| 54 | 6,07 | 0,0002 | 0,05 | 0,0002 | 0,05 | | | | |
| 56 | 6,18 | 0,0002 | 0,06 | 0,0003 | 0,07 | | | | |
| 58 | 6,30 | 0,0002 | 0,05 | 0,0002 | 0,05 | | | | |
| 60 | 6,42 | 0,0003 | 0,08 | 0,0002 | 0,06 | 0,00009 | 0,03 | 0,00009 | 0,03 |
| 62 | 6,54 | 0,0002 | 0,05 | 0,0003 | 0,08 | 0,00008 | 0,02 | 0,00008 | 0,02 |
| 64 | 6,65 | 0,0002 | 0,06 | 0,0003 | 0,08 | 0,00005 | 0,01 | 0,00008 | 0,02 |
| 66 | 6,77 | 0,0003 | 0,09 | 0,0003 | 0,08 | | | | |
| 68 | 6,89 | 0,0004 | 0,10 | 0,0005 | 0,14 | | | | |
| 70 | 7,00 | 0,0002 | 0,06 | 0,0002 | 0,05 | | | | |
| 72 | 7,10 | 0,0002 | 0,06 | 0,0002 | 0,07 | | | | |
| 74 | 7,20 | 0,0001 | 0,05 | 0,0002 | 0,06 | 0,00008 | 0,03 | 0,00003 | 0,01 |
| 76 | 7,29 | 0,0002 | 0,06 | 0,0003 | 0,09 | | | | |
| 80 | 7,45 | 0,0002 | 0,09 | | | | | | |
| 82 | 7,52 | 0,0002 | 0,11 | 0,0001 | 0,07 | | | | |
| 84 | 7,58 | 0,0002 | 0,13 | 0,0002 | 0,10 | | | | |
| 86 | 7,64 | 0,0002 | 0,11 | 0,0001 | 0,08 | | | | |
| 88 | 7,69 | 0,0002 | 0,18 | 0,0001 | 0,09 | | | | |

| Depth | Age | IP ₂₅ /sed | IP ₂₅ /TOC | HBI II diene/sed | HBI II diene/TOC | HBI III z-triene/sed | HBI III z-triene/TOC | HBI III e-triene/sed | HBI III e-triene/TOC |
|-------|---------|-----------------------|-----------------------|------------------|------------------|----------------------|----------------------|----------------------|----------------------|
| [cm] | [ka BP] | [µg/g] | [µg/g] | [µg/g] | [µg/g] | [µg/g] | [µg/g] | [µg/g] | [µg/g] |
| 90 | 7,74 | 0,0002 | 0,14 | 0,0001 | 0,11 | | | | |
| 92 | 7,78 | 0,0003 | 0,14 | 0,0003 | 0,14 | | | | |
| 94 | 7,82 | 0,0004 | 0,23 | 0,0005 | 0,26 | 0,00016 | 0,09 | 0,00021 | 0,11 |
| 96 | 7,86 | 0,0003 | 0,28 | 0,0004 | 0,32 | | | | |
| 100 | 7,91 | 0,0007 | 0,35 | 0,0009 | 0,48 | 0,00009 | 0,05 | 0,00012 | 0,06 |
| 108 | 7,96 | 0,0009 | 0,62 | 0,0014 | 0,95 | 0,00029 | 0,20 | 0,00035 | 0,24 |
| 117 | 8,00 | 0,0009 | 0,67 | 0,0014 | 1,01 | 0,00017 | 0,13 | 0,00025 | 0,18 |
| 125 | 8,04 | 0,0008 | 0,69 | 0,0011 | 0,93 | 0,00016 | 0,13 | 0,00025 | 0,21 |
| 132 | 8,07 | 0,0009 | 0,61 | 0,0018 | 1,14 | 0,00037 | 0,24 | 0,00046 | 0,29 |
| 136 | 8,09 | 0,0010 | 0,69 | 0,0012 | 0,85 | 0,00028 | 0,19 | 0,00035 | 0,24 |
| 140 | 8,10 | 0,0011 | 0,61 | 0,0016 | 0,90 | 0,00027 | 0,15 | 0,00040 | 0,23 |
| 152 | 8,16 | 0,0007 | 0,44 | 0,0010 | 0,61 | 0,00009 | 0,06 | 0,00013 | 0,08 |
| 160 | 8,19 | 0,0007 | 0,49 | 0,0009 | 0,64 | 0,00018 | 0,13 | 0,00018 | 0,13 |
| 168 | 8,23 | 0,0006 | 0,35 | 0,0010 | 0,55 | 0,00019 | 0,10 | 0,00019 | 0,10 |
| 177 | 8,27 | 0,0008 | 0,54 | 0,0011 | 0,80 | 0,00015 | 0,10 | 0,00019 | 0,14 |
| 178 | 8,27 | 0,0007 | 0,64 | 0,0011 | 0,96 | 0,00011 | 0,10 | 0,00013 | 0,12 |
| 185 | 8,30 | 0,0009 | 0,60 | 0,0015 | 0,99 | 0,00021 | 0,13 | 0,00029 | 0,18 |
| 192 | 8,34 | 0,0007 | 0,43 | 0,0012 | 0,70 | 0,00027 | 0,16 | 0,00025 | 0,15 |
| 200 | 8,37 | 0,0009 | 0,54 | 0,0019 | 1,16 | 0,00035 | 0,21 | 0,00040 | 0,24 |
| 208 | 8,41 | 0,0010 | 0,67 | 0,0017 | 1,17 | 0,00020 | 0,14 | 0,00027 | 0,19 |
| 212 | 8,43 | 0,0009 | 0,53 | 0,0019 | 1,06 | 0,00025 | 0,14 | 0,00028 | 0,16 |
| 217 | 8,46 | 0,0010 | 0,65 | 0,0016 | 1,01 | 0,00034 | 0,22 | 0,00041 | 0,26 |
| 225 | 8,50 | 0,0011 | 0,66 | 0,0019 | 1,16 | 0,00030 | 0,19 | 0,00028 | 0,17 |
| 232 | 8,53 | 0,0014 | 0,87 | 0,0023 | 1,45 | 0,00046 | 0,29 | 0,00041 | 0,25 |
| 240 | 8,56 | 0,0012 | 0,75 | 0,0022 | 1,34 | 0,00043 | 0,26 | 0,00041 | 0,25 |
| 248 | 8,60 | 0,0006 | 0,42 | 0,0011 | 0,76 | 0,00018 | 0,12 | 0,00014 | 0,10 |
| 253 | 8,63 | 0,0006 | 0,62 | 0,0007 | 0,70 | 0,00010 | 0,09 | 0,00014 | 0,13 |
| 256 | 8,64 | 0,0011 | 0,74 | 0,0016 | 1,12 | 0,00022 | 0,16 | 0,00022 | 0,15 |
| 265 | 8,68 | 0,0011 | 0,64 | 0,0020 | 1,15 | 0,00058 | 0,33 | 0,00049 | 0,28 |
| 272 | 8,71 | 0,0006 | 0,44 | 0,0009 | 0,71 | 0,00015 | 0,12 | 0,00020 | 0,16 |
| 280 | 8,75 | 0,0009 | 0,63 | 0,0018 | 1,27 | 0,00043 | 0,29 | 0,00042 | 0,29 |
| 288 | 8,79 | 0,0012 | 0,60 | 0,0021 | 1,05 | 0,00049 | 0,24 | 0,00042 | 0,21 |
| 296 | 8,83 | 0,0012 | 0,81 | 0,0018 | 1,27 | 0,00028 | 0,20 | 0,00024 | 0,17 |
| 305 | 8,87 | 0,0013 | 0,72 | 0,0024 | 1,33 | 0,00064 | 0,35 | 0,00051 | 0,28 |
| 312 | 8,90 | 0,0008 | 0,58 | 0,0013 | 0,92 | 0,00039 | 0,27 | 0,00037 | 0,26 |
| 320 | 8,93 | 0,0011 | 0,66 | 0,0019 | 1,12 | 0,00055 | 0,33 | 0,00043 | 0,25 |
| 326 | 8,96 | 0,0010 | 0,94 | 0,0014 | 1,34 | 0,00012 | 0,11 | 0,00014 | 0,14 |
| 328 | 8,97 | 0,0012 | 0,67 | 0,0019 | 1,10 | 0,00044 | 0,25 | 0,00056 | 0,32 |
| 333 | 8,99 | 0,0010 | 0,61 | 0,0017 | 1,05 | 0,00072 | 0,45 | 0,00073 | 0,46 |
| 336 | 9,00 | 0,0012 | 0,65 | 0,0019 | 1,06 | 0,00072 | 0,40 | 0,00069 | 0,39 |
| 345 | 9,04 | 0,0008 | 0,52 | 0,0015 | 1,00 | 0,00033 | 0,23 | 0,00029 | 0,19 |
| 352 | 9,07 | 0,0008 | 0,46 | 0,0011 | 0,66 | 0,00025 | 0,15 | 0,00023 | 0,14 |
| 360 | 9,10 | 0,0010 | 0,57 | 0,0018 | 1,05 | 0,00025 | 0,14 | 0,00024 | 0,14 |
| 368 | 9,14 | 0,0011 | 0,94 | 0,0017 | 1,42 | 0,00015 | 0,13 | 0,00020 | 0,16 |
| 377 | 9,18 | 0,0009 | 0,69 | 0,0015 | 1,13 | 0,00022 | 0,16 | 0,00022 | 0,16 |
| 382 | 9,20 | 0,0009 | 0,84 | 0,0008 | 0,77 | 0,00007 | 0,06 | 0,00009 | 0,08 |
| 385 | 9,21 | 0,0012 | 0,71 | 0,0020 | 1,24 | 0,00053 | 0,32 | 0,00043 | 0,26 |
| 392 | 9,24 | 0,0008 | 0,59 | 0,0011 | 0,81 | 0,00024 | 0,18 | 0,00020 | 0,15 |
| 400 | 9,28 | 0,0010 | 0,74 | 0,0014 | 1,06 | 0,00022 | 0,16 | 0,00034 | 0,26 |
| 404 | 9,30 | 0,0009 | 0,55 | 0,0016 | 0,93 | 0,00033 | 0,19 | 0,00033 | 0,19 |
| 408 | 9,32 | 0,0008 | 0,53 | 0,0017 | 1,07 | 0,00023 | 0,15 | 0,00026 | 0,17 |
| 417 | 9,36 | 0,0010 | 0,55 | 0,0016 | 0,85 | 0,00017 | 0,09 | 0,00022 | 0,11 |
| 426 | 9,40 | 0,0009 | 0,64 | 0,0015 | 1,01 | 0,00019 | 0,13 | 0,00017 | 0,12 |
| 432 | 9,43 | 0,0009 | 0,64 | 0,0012 | 0,89 | 0,00030 | 0,22 | 0,00035 | 0,26 |
| 440 | 9,47 | 0,0008 | 0,57 | 0,0012 | 0,82 | 0,00012 | 0,08 | 0,00014 | 0,10 |
| 448 | 9,51 | 0,0012 | 1,02 | 0,0018 | 1,59 | 0,00038 | 0,34 | 0,00034 | 0,30 |
| 457 | 9,56 | 0,0012 | 0,68 | 0,0027 | 1,48 | 0,00077 | 0,42 | 0,00064 | 0,36 |
| 465 | 9,60 | 0,0008 | 0,41 | 0,0020 | 1,06 | 0,00055 | 0,29 | 0,00043 | 0,23 |
| 472 | 9,63 | 0,0007 | 0,41 | 0,0015 | 0,85 | 0,00092 | 0,53 | 0,00079 | 0,45 |
| 480 | 9,66 | 0,0009 | 0,47 | 0,0015 | 0,84 | 0,00049 | 0,27 | 0,00035 | 0,19 |
| 488 | 9,69 | 0,0008 | 0,54 | 0,0012 | 0,83 | 0,00039 | 0,27 | 0,00048 | 0,33 |
| 495 | 9,70 | 0,0013 | 0,90 | 0,0016 | 1,12 | 0,00100 | 0,70 | 0,00108 | 0,76 |
| 497 | 9,70 | 0,0010 | 0,61 | 0,0017 | 1,09 | 0,00143 | 0,90 | 0,00137 | 0,86 |
| 505 | 9,71 | 0,0009 | 0,69 | 0,0017 | 1,25 | 0,00019 | 0,14 | 0,00040 | 0,29 |
| 512 | 9,72 | 0,0008 | 0,63 | 0,0015 | 1,13 | 0,00083 | 0,64 | 0,00088 | 0,68 |
| 520 | 9,72 | 0,0009 | 0,52 | 0,0016 | 0,94 | 0,00210 | 1,25 | 0,00185 | 1,11 |
| 528 | 9,73 | 0,0008 | 0,45 | 0,0017 | 0,96 | 0,00059 | 0,33 | 0,00059 | 0,33 |

| Depth | Age | IP ₂₅ /sed | IP ₂₅ /TOC | HBI II diene/sed | HBI II diene/TOC | HBI III z-triene/sed | HBI III z-triene/TOC | HBI III e-triene/sed | HBI III e-triene/TOC |
|-------|---------|-----------------------|-----------------------|------------------|------------------|----------------------|----------------------|----------------------|----------------------|
| [cm] | [ka BP] | [µg/g] | [µg/g] | [µg/g] | [µg/g] | [µg/g] | [µg/g] | [µg/g] | [µg/g] |
| 537 | 9,74 | 0,0008 | 0,48 | 0,0015 | 0,92 | 0,00112 | 0,70 | 0,00132 | 0,82 |
| 545 | 9,75 | 0,0007 | 0,42 | 0,0012 | 0,78 | 0,00070 | 0,45 | 0,00070 | 0,45 |
| 552 | 9,76 | 0,0007 | 0,50 | 0,0012 | 0,90 | 0,00076 | 0,57 | 0,00091 | 0,69 |
| 560 | 9,77 | 0,0009 | 0,58 | 0,0018 | 1,15 | 0,00134 | 0,88 | 0,00128 | 0,84 |
| 577 | 9,79 | 0,0009 | 0,69 | 0,0018 | 1,47 | 0,00257 | 2,07 | 0,00357 | 2,88 |
| 586 | 9,80 | 0,0008 | 0,53 | 0,0013 | 0,88 | 0,00075 | 0,51 | 0,00099 | 0,68 |
| 592 | 9,81 | 0,0007 | 0,49 | 0,0013 | 0,95 | 0,00099 | 0,72 | 0,00102 | 0,74 |
| 600 | 9,82 | 0,0008 | 0,60 | 0,0010 | 0,80 | 0,00057 | 0,44 | 0,00089 | 0,69 |
| 608 | 9,83 | 0,0009 | 0,69 | 0,0018 | 1,32 | 0,00131 | 0,95 | 0,00083 | 0,60 |
| 617 | 9,84 | 0,0005 | 0,35 | 0,0011 | 0,75 | 0,00046 | 0,32 | 0,00043 | 0,30 |
| 625 | 9,85 | 0,0008 | 0,55 | 0,0019 | 1,23 | 0,00105 | 0,69 | 0,00062 | 0,40 |
| 632 | 9,86 | 0,0007 | 0,42 | 0,0014 | 0,87 | 0,00150 | 0,96 | 0,00127 | 0,81 |
| 640 | 9,87 | 0,0010 | 0,66 | 0,0019 | 1,31 | 0,00215 | 1,49 | 0,00280 | 1,94 |
| 648 | 9,87 | 0,0010 | 0,58 | 0,0020 | 1,11 | 0,00086 | 0,49 | 0,00100 | 0,56 |
| 657 | 9,88 | 0,0008 | 0,65 | 0,0013 | 1,04 | 0,00049 | 0,40 | 0,00078 | 0,63 |
| 665 | 9,89 | 0,0009 | 0,64 | 0,0014 | 1,01 | 0,00045 | 0,34 | 0,00040 | 0,30 |
| 672 | 9,90 | 0,0007 | 0,58 | 0,0012 | 0,94 | 0,00064 | 0,52 | 0,00078 | 0,64 |
| 680 | 9,91 | 0,0007 | 0,45 | 0,0014 | 0,90 | 0,00058 | 0,39 | 0,00042 | 0,27 |
| 697 | 9,93 | 0,0007 | 0,50 | 0,0013 | 0,93 | 0,00083 | 0,58 | 0,00071 | 0,50 |
| 705 | 9,94 | 0,0005 | 0,41 | 0,0008 | 0,67 | 0,00050 | 0,42 | 0,00038 | 0,32 |
| 712 | 9,95 | 0,0005 | 0,49 | 0,0009 | 0,88 | 0,00090 | 0,87 | 0,00068 | 0,66 |
| 720 | 9,96 | 0,0007 | 0,46 | 0,0012 | 0,81 | 0,00116 | 0,81 | 0,00071 | 0,50 |
| 728 | 9,97 | 0,0006 | 0,53 | 0,0010 | 0,89 | 0,00071 | 0,61 | 0,00061 | 0,53 |
| 737 | 9,98 | 0,0006 | 0,59 | 0,0011 | 1,18 | 0,00064 | 0,68 | 0,00063 | 0,67 |
| 745 | 9,99 | 0,0004 | 0,44 | 0,0008 | 0,83 | 0,00051 | 0,54 | 0,00057 | 0,60 |
| 752 | 10,00 | 0,0005 | 0,38 | 0,0011 | 0,83 | 0,00156 | 1,16 | 0,00074 | 0,55 |
| 760 | 10,01 | 0,0006 | 0,43 | 0,0012 | 0,87 | 0,00088 | 0,66 | 0,00066 | 0,50 |
| 768 | 10,02 | 0,0009 | 0,41 | 0,0017 | 0,80 | 0,00219 | 1,04 | 0,00195 | 0,93 |
| 777 | 10,03 | 0,0009 | 0,54 | 0,0018 | 1,11 | 0,00182 | 1,14 | 0,00163 | 1,02 |
| 785 | 10,04 | 0,0008 | 0,48 | 0,0021 | 1,24 | 0,00283 | 1,69 | 0,00232 | 1,38 |
| 792 | 10,05 | 0,0006 | 0,38 | 0,0011 | 0,72 | 0,00169 | 1,09 | 0,00169 | 1,09 |
| 800 | 10,06 | 0,0009 | 0,57 | 0,0019 | 1,15 | 0,00094 | 0,59 | 0,00093 | 0,58 |
| 808 | 10,07 | 0,0010 | 0,62 | 0,0017 | 1,09 | 0,00173 | 1,09 | 0,00174 | 1,10 |
| 817 | 10,08 | 0,0005 | 0,62 | 0,0011 | 1,27 | 0,00042 | 0,48 | 0,00047 | 0,54 |
| 825 | 10,09 | 0,0008 | 0,71 | 0,0013 | 1,20 | 0,00066 | 0,58 | 0,00078 | 0,69 |
| 832 | 10,09 | 0,0005 | 0,62 | 0,0008 | 0,94 | 0,00048 | 0,55 | 0,00042 | 0,48 |
| 840 | 10,10 | 0,0008 | 0,51 | 0,0013 | 0,87 | 0,00067 | 0,45 | 0,00047 | 0,31 |
| 847 | 10,11 | 0,0012 | 0,76 | 0,0022 | 1,41 | 0,00206 | 1,34 | 0,00244 | 1,58 |
| 852 | 10,12 | 0,0007 | 0,46 | 0,0014 | 0,98 | 0,00195 | 1,34 | 0,00240 | 1,65 |
| 860 | 10,13 | 0,0009 | 0,64 | 0,0017 | 1,28 | 0,00113 | 0,85 | 0,00128 | 0,97 |
| 868 | 10,14 | 0,0010 | 0,66 | 0,0020 | 1,38 | 0,00107 | 0,73 | 0,00122 | 0,84 |
| 872 | 10,14 | 0,0006 | 0,46 | 0,0010 | 0,77 | 0,00127 | 0,97 | 0,00164 | 1,26 |
| 877 | 10,15 | 0,0011 | 0,58 | 0,0018 | 0,92 | 0,00236 | 1,23 | 0,00288 | 1,50 |
| 885 | 10,16 | 0,0009 | 0,65 | 0,0016 | 1,14 | 0,00122 | 0,88 | 0,00147 | 1,06 |
| 892 | 10,17 | 0,0010 | 0,73 | 0,0017 | 1,26 | 0,00115 | 0,85 | 0,00135 | 1,00 |
| 900 | 10,18 | 0,0006 | 0,65 | 0,0010 | 1,06 | 0,00032 | 0,33 | 0,00035 | 0,36 |
| 908 | 10,19 | 0,0007 | 0,68 | 0,0010 | 1,01 | 0,00052 | 0,50 | 0,00060 | 0,57 |
| 912 | 10,19 | 0,0003 | 0,47 | | | 0,00022 | 0,37 | | |
| 917 | 10,20 | 0,0003 | 0,48 | 0,0004 | 0,77 | 0,00009 | 0,15 | 0,00011 | 0,19 |
| 925 | 10,21 | 0,0003 | 0,56 | 0,0004 | 0,72 | 0,00011 | 0,20 | 0,00015 | 0,26 |
| 930 | 10,21 | 0,0002 | 0,40 | 0,0003 | 0,56 | 0,00014 | 0,24 | 0,00013 | 0,23 |

Table B.3: Accumulation rates HBIs
Cruise: PS100; Station: PS100/270; Lon [°E]: -18.14;
Lat [°N]: 79.49; Water Depth: 424 m

| Depth | Age | Acc rate IP ₂₅ | Acc rate HBI II diene | Acc rate HBI III z-triene | Acc rate HBI III e-triene |
|-------|---------|---------------------------|--------------------------|---------------------------|---------------------------|
| [cm] | [ka BP] | [µg/cm ² /ka] | [µg/cm ² /ka] | [µg/cm ² /ka] | [µg/cm ² /ka] |
| 1 | 0,75 | | | | |
| 2 | 0,94 | 0,0038 | 0,0028 | | |
| 4 | 1,32 | 0,0009 | 0,0013 | | |
| 8 | 2,09 | 0,0004 | 0,0013 | | |
| 10 | 2,48 | 0,0011 | 0,0015 | | |
| 12 | 2,86 | 0,0005 | 0,0006 | | |
| 14 | 3,25 | 0,0005 | 0,0011 | | |
| 18 | 3,85 | 0,0009 | 0,0014 | 0,0003 | 0,0003 |
| 20 | 4,06 | 0,0010 | 0,0013 | | |
| 22 | 4,23 | 0,0012 | 0,0015 | | |
| 24 | 4,38 | 0,0011 | 0,0018 | | |
| 26 | 4,52 | 0,0019 | 0,0024 | | |
| 28 | 4,64 | 0,0012 | 0,0014 | | |
| 30 | 4,75 | 0,0019 | 0,0014 | | |
| 32 | 4,87 | 0,0015 | 0,0016 | | |
| 34 | 4,99 | 0,0026 | 0,0029 | | 0,0008 |
| 36 | 5,10 | 0,0036 | 0,0022 | | |
| 38 | 5,20 | 0,0020 | 0,0022 | | |
| 40 | 5,31 | 0,0035 | 0,0058 | | |
| 42 | 5,41 | 0,0013 | 0,0016 | | |
| 46 | 5,63 | 0,0016 | 0,0026 | | |
| 48 | 5,74 | 0,0027 | 0,0036 | 0,0009 | 0,0008 |
| 50 | 5,85 | 0,0041 | 0,0025 | | |
| 52 | 5,96 | 0,0034 | 0,0045 | 0,0008 | 0,0011 |
| 54 | 6,07 | 0,0026 | 0,0025 | | |
| 56 | 6,18 | 0,0030 | 0,0036 | | |
| 58 | 6,30 | 0,0027 | 0,0028 | | |
| 60 | 6,42 | 0,0040 | 0,0032 | 0,0013 | 0,0013 |
| 62 | 6,54 | 0,0028 | 0,0039 | 0,0012 | 0,0012 |
| 64 | 6,65 | 0,0033 | 0,0045 | 0,0008 | 0,0011 |
| 66 | 6,77 | 0,0061 | 0,0053 | | |
| 68 | 6,89 | 0,0055 | 0,0075 | | |
| 70 | 7,00 | 0,0030 | 0,0029 | | |
| 72 | 7,10 | 0,0037 | 0,0038 | | |
| 74 | 7,20 | 0,0030 | 0,0035 | 0,0017 | 0,0007 |
| 76 | 7,29 | 0,0052 | 0,0076 | | |
| 80 | 7,45 | 0,0058 | | | |
| 82 | 7,52 | 0,0081 | 0,0047 | | |
| 84 | 7,58 | 0,0073 | 0,0055 | | |
| 86 | 7,64 | 0,0079 | 0,0055 | | |
| 88 | 7,69 | 0,0087 | 0,0041 | | |
| 90 | 7,74 | 0,0081 | 0,0061 | | |
| 92 | 7,78 | 0,0127 | 0,0133 | | |
| 94 | 7,82 | 0,0213 | 0,0235 | 0,0079 | 0,0103 |
| 96 | 7,86 | 0,0231 | 0,0261 | | |
| 100 | 7,91 | 0,1039 | 0,1402 | 0,0133 | 0,0179 |
| 108 | 7,96 | 0,1404 | 0,2174 | 0,0461 | 0,0554 |
| 117 | 8,00 | 0,1488 | 0,2254 | 0,0281 | 0,0408 |
| 125 | 8,04 | 0,1203 | 0,1627 | 0,0232 | 0,0373 |
| 132 | 8,07 | 0,1531 | 0,2857 | 0,0605 | 0,0735 |
| 136 | 8,09 | 0,1804 | 0,2223 | 0,0498 | 0,0624 |
| 140 | 8,10 | 0,2066 | 0,3080 | 0,0523 | 0,0771 |
| 152 | 8,16 | 0,1137 | 0,1592 | 0,0150 | 0,0212 |
| 160 | 8,19 | 0,1197 | 0,1560 | 0,0314 | 0,0309 |
| 168 | 8,23 | 0,1077 | 0,1703 | 0,0316 | 0,0318 |
| 177 | 8,27 | 0,1136 | 0,1696 | 0,0220 | 0,0291 |
| 178 | 8,27 | 0,1051 | 0,1569 | 0,0156 | 0,0189 |
| 185 | 8,30 | 0,1695 | 0,2781 | 0,0372 | 0,0516 |
| 192 | 8,34 | 0,1300 | 0,2085 | 0,0484 | 0,0443 |
| 200 | 8,37 | 0,1640 | 0,3526 | 0,0640 | 0,0730 |
| 208 | 8,41 | 0,1505 | 0,2643 | 0,0308 | 0,0421 |
| 212 | 8,43 | 0,1638 | 0,3249 | 0,0433 | 0,0495 |

| Depth | Age | Acc rate IP ₂₅ | Acc rate HBI II diene | Acc rate HBI III z-triene | Acc rate HBI III e-triene |
|-------|---------|---------------------------|--------------------------|---------------------------|---------------------------|
| [cm] | [ka BP] | [µg/cm ² /ka] | [µg/cm ² /ka] | [µg/cm ² /ka] | [µg/cm ² /ka] |
| 217 | 8,46 | 0,1960 | 0,3037 | 0,0649 | 0,0799 |
| 225 | 8,50 | 0,2097 | 0,3691 | 0,0588 | 0,0542 |
| 232 | 8,53 | 0,2583 | 0,4308 | 0,0857 | 0,0752 |
| 240 | 8,56 | 0,2305 | 0,4119 | 0,0813 | 0,0780 |
| 248 | 8,60 | 0,1416 | 0,2523 | 0,0415 | 0,0326 |
| 253 | 8,63 | 0,1178 | 0,1332 | 0,0179 | 0,0255 |
| 256 | 8,64 | 0,2181 | 0,3291 | 0,0456 | 0,0444 |
| 265 | 8,68 | 0,2521 | 0,4525 | 0,1292 | 0,1094 |
| 272 | 8,71 | 0,1203 | 0,1938 | 0,0320 | 0,0428 |
| 280 | 8,75 | 0,1938 | 0,3875 | 0,0901 | 0,0887 |
| 288 | 8,79 | 0,2576 | 0,4532 | 0,1026 | 0,0891 |
| 296 | 8,83 | 0,2393 | 0,3774 | 0,0587 | 0,0495 |
| 305 | 8,87 | 0,3157 | 0,5790 | 0,1533 | 0,1216 |
| 312 | 8,90 | 0,2133 | 0,3372 | 0,1003 | 0,0946 |
| 320 | 8,93 | 0,2401 | 0,4063 | 0,1184 | 0,0922 |
| 326 | 8,96 | 0,2114 | 0,3002 | 0,0255 | 0,0312 |
| 328 | 8,97 | 0,2810 | 0,4637 | 0,1053 | 0,1344 |
| 333 | 8,99 | 0,2354 | 0,4069 | 0,1747 | 0,1770 |
| 336 | 9,00 | 0,2858 | 0,4691 | 0,1764 | 0,1705 |
| 345 | 9,04 | 0,1662 | 0,3183 | 0,0713 | 0,0611 |
| 352 | 9,07 | 0,1799 | 0,2572 | 0,0572 | 0,0529 |
| 360 | 9,10 | 0,1960 | 0,3620 | 0,0498 | 0,0485 |
| 368 | 9,14 | 0,2251 | 0,3415 | 0,0306 | 0,0396 |
| 377 | 9,18 | 0,1897 | 0,3130 | 0,0441 | 0,0453 |
| 382 | 9,20 | 0,1785 | 0,1647 | 0,0134 | 0,0172 |
| 385 | 9,21 | 0,2323 | 0,4041 | 0,1042 | 0,0851 |
| 392 | 9,24 | 0,1652 | 0,2244 | 0,0501 | 0,0423 |
| 400 | 9,28 | 0,2004 | 0,2886 | 0,0439 | 0,0705 |
| 404 | 9,30 | 0,1778 | 0,3004 | 0,0623 | 0,0616 |
| 408 | 9,32 | 0,1755 | 0,3518 | 0,0486 | 0,0545 |
| 417 | 9,36 | 0,2103 | 0,3265 | 0,0338 | 0,0433 |
| 426 | 9,40 | 0,1689 | 0,2677 | 0,0344 | 0,0311 |
| 432 | 9,43 | 0,1673 | 0,2313 | 0,0570 | 0,0665 |
| 440 | 9,47 | 0,1496 | 0,2151 | 0,0223 | 0,0252 |
| 448 | 9,51 | 0,2563 | 0,3986 | 0,0844 | 0,0747 |
| 457 | 9,56 | 0,2875 | 0,6267 | 0,1789 | 0,1505 |
| 465 | 9,60 | 0,1727 | 0,4490 | 0,1224 | 0,0961 |
| 472 | 9,63 | 0,1842 | 0,3772 | 0,2352 | 0,2005 |
| 480 | 9,66 | 0,2859 | 0,5101 | 0,1617 | 0,1161 |
| 488 | 9,69 | 0,5809 | 0,8914 | 0,2892 | 0,3552 |
| 495 | 9,70 | 1,4092 | 1,7673 | 1,1043 | 1,2001 |
| 497 | 9,70 | 1,2573 | 2,2540 | 1,8591 | 1,7771 |
| 505 | 9,71 | 1,0606 | 1,9287 | 0,2208 | 0,4543 |
| 512 | 9,72 | 0,8612 | 1,5449 | 0,8781 | 0,9237 |
| 520 | 9,72 | 0,9637 | 1,7499 | 2,3260 | 2,0546 |
| 528 | 9,73 | 0,7921 | 1,7066 | 0,5861 | 0,5923 |
| 537 | 9,74 | 0,7312 | 1,4006 | 1,0668 | 1,2530 |
| 545 | 9,75 | 0,7755 | 1,4410 | 0,8209 | 0,8253 |
| 552 | 9,76 | 0,6853 | 1,2320 | 0,7863 | 0,9377 |
| 560 | 9,77 | 0,8922 | 1,7741 | 1,3526 | 1,2935 |
| 577 | 9,79 | 0,8664 | 1,8524 | 2,6138 | 3,6310 |
| 586 | 9,80 | 0,6915 | 1,1398 | 0,6682 | 0,8794 |
| 592 | 9,81 | 0,6116 | 1,1910 | 0,9069 | 0,9291 |
| 600 | 9,82 | 0,7179 | 0,9618 | 0,5336 | 0,8251 |
| 608 | 9,83 | 0,9410 | 1,8032 | 1,3023 | 0,8199 |
| 617 | 9,84 | 0,6090 | 1,3117 | 0,5588 | 0,5305 |
| 625 | 9,85 | 1,1669 | 2,5890 | 1,4459 | 0,8487 |
| 632 | 9,86 | 0,7573 | 1,5806 | 1,7470 | 1,4820 |
| 640 | 9,87 | 1,1494 | 2,2818 | 2,5844 | 3,3656 |
| 648 | 9,87 | 1,0336 | 1,9634 | 0,8582 | 0,9977 |
| 657 | 9,88 | 0,8572 | 1,3680 | 0,5274 | 0,8312 |
| 665 | 9,89 | 0,8697 | 1,3752 | 0,4583 | 0,4080 |
| 672 | 9,90 | 0,6589 | 1,0621 | 0,5885 | 0,7173 |
| 680 | 9,91 | 0,6615 | 1,3336 | 0,5692 | 0,4054 |
| 697 | 9,93 | 0,8046 | 1,4840 | 0,9304 | 0,7963 |
| 705 | 9,94 | 0,5872 | 0,9615 | 0,6099 | 0,4572 |

| Depth | Age | Acc rate IP ₂₅ | Acc rate HBI II diene | Acc rate HBI III z-triene | Acc rate HBI III e-triene |
|-------|---------|---------------------------|--------------------------|---------------------------|---------------------------|
| [cm] | [ka BP] | [µg/cm ² /ka] | [µg/cm ² /ka] | [µg/cm ² /ka] | [µg/cm ² /ka] |
| 712 | 9,95 | 0,6090 | 1,0983 | 1,0863 | 0,8199 |
| 720 | 9,96 | 0,7422 | 1,2929 | 1,2977 | 0,7972 |
| 728 | 9,97 | 0,8113 | 1,3544 | 0,9349 | 0,8017 |
| 737 | 9,98 | 0,7670 | 1,5264 | 0,8832 | 0,8635 |
| 745 | 9,99 | 0,5563 | 1,0457 | 0,6829 | 0,7565 |
| 752 | 10,00 | 0,5338 | 1,1560 | 1,6233 | 0,7748 |
| 760 | 10,01 | 0,6471 | 1,3194 | 1,0045 | 0,7560 |
| 768 | 10,02 | 0,9329 | 1,8228 | 2,3615 | 2,1103 |
| 777 | 10,03 | 0,9297 | 1,9234 | 1,9589 | 1,7576 |
| 785 | 10,04 | 0,8614 | 2,2329 | 3,0318 | 2,4796 |
| 792 | 10,05 | 0,6402 | 1,2031 | 1,8311 | 1,8392 |
| 800 | 10,06 | 1,0276 | 2,0840 | 1,0569 | 1,0472 |
| 808 | 10,07 | 1,1324 | 1,9909 | 1,9925 | 2,0059 |
| 817 | 10,08 | 0,7756 | 1,5835 | 0,5959 | 0,6725 |
| 825 | 10,09 | 1,0494 | 1,7693 | 0,8636 | 1,0198 |
| 832 | 10,09 | 0,6025 | 0,9172 | 0,5340 | 0,4682 |
| 840 | 10,10 | 0,7965 | 1,3486 | 0,6948 | 0,4862 |
| 847 | 10,11 | 0,8798 | 1,6275 | 1,5446 | 1,8292 |
| 852 | 10,12 | 0,7788 | 1,6519 | 2,2618 | 2,7912 |
| 860 | 10,13 | 1,0269 | 2,0491 | 1,3562 | 1,5435 |
| 868 | 10,14 | 1,1974 | 2,4955 | 1,3324 | 1,5278 |
| 872 | 10,14 | 0,7019 | 1,1669 | 1,4820 | 1,9173 |
| 877 | 10,15 | 1,2929 | 2,0388 | 2,7230 | 3,3253 |
| 885 | 10,16 | 1,0569 | 1,8434 | 1,4141 | 1,7040 |
| 892 | 10,17 | 1,1734 | 2,0257 | 1,3694 | 1,6154 |
| 900 | 10,18 | 0,8771 | 1,4390 | 0,4534 | 0,4949 |
| 908 | 10,19 | 1,0695 | 1,5704 | 0,7821 | 0,8969 |
| 912 | 10,19 | 0,4892 | | 0,3864 | |
| 917 | 10,20 | 0,4757 | 0,7696 | 0,1466 | 0,1880 |
| 925 | 10,21 | 0,5340 | 0,6930 | 0,1905 | 0,2510 |
| 930 | 10,21 | | | | |

Table B.4: Specific sterols

Cruise: PS100; Station: PS100/270; Lon [°E]: -18.14; Lat [°N]: 79.49; Water Depth: 424 m

| Depth | Age | Brassica /sed | Brassica /TOC | Campe /sed | Campe /TOC | beta-Sito /sed | beta-Sito /TOC | Dino /sed | Dino /TOC |
|-------|---------|---------------|---------------|------------|------------|----------------|----------------|-----------|-----------|
| [cm] | [ka BP] | [µg/g] | [µg/g] | [µg/g] | [µg/g] | [µg/g] | [µg/g] | [µg/g] | [µg/g] |
| 1 | 0,75 | 0,0030 | 0,69 | 0,0014 | 0,32 | 0,0061 | 1,40 | 1,7258 | 3,12 |
| 2 | 0,94 | 0,0064 | 1,27 | 0,0014 | 0,28 | 0,0149 | 2,97 | 1,0352 | 4,00 |
| 4 | 1,32 | 0,0043 | 0,93 | 0,0023 | 0,49 | 0,0108 | 2,32 | 0,9961 | 3,31 |
| 8 | 2,09 | 0,0167 | 3,62 | 0,0080 | 1,73 | 0,0401 | 8,70 | 1,8696 | 10,57 |
| 10 | 2,48 | 0,0015 | 0,35 | 0,0008 | 0,19 | 0,0038 | 0,89 | 1,0157 | 1,91 |
| 12 | 2,86 | 0,0027 | 0,64 | 0,0005 | 0,12 | 0,0042 | 1,00 | 0,5723 | 1,57 |
| 14 | 3,25 | 0,0023 | 0,48 | 0,0011 | 0,24 | 0,0044 | 0,92 | 0,3270 | 1,25 |
| 18 | 3,85 | 0,0040 | 0,92 | 0,0023 | 0,53 | 0,0133 | 3,07 | 0,4625 | 3,54 |
| 20 | 4,06 | 0,0006 | 0,15 | 0,0003 | 0,08 | 0,0012 | 0,33 | 0,1801 | 0,51 |
| 22 | 4,23 | 0,0051 | 1,31 | 0,0020 | 0,51 | 0,0134 | 3,46 | 1,1435 | 4,60 |
| 24 | 4,38 | 0,0039 | 0,98 | 0,0023 | 0,57 | 0,0114 | 2,89 | 0,8670 | 3,75 |
| 26 | 4,52 | 0,0017 | 0,40 | 0,0006 | 0,15 | 0,0030 | 0,73 | 0,2173 | 0,94 |
| 30 | 4,75 | 0,0004 | 0,11 | 0,0002 | 0,06 | 0,0011 | 0,27 | 0,4978 | 0,77 |
| 32 | 4,87 | 0,0005 | 0,12 | 0,0002 | 0,06 | 0,0033 | 0,86 | 0,0928 | 0,96 |
| 34 | 4,99 | | | | | 0,0026 | 0,72 | | |
| 36 | 5,10 | | | | | 0,0014 | 0,41 | | |
| 38 | 5,20 | | | 0,0009 | 0,23 | 0,0023 | 0,61 | 0,5293 | 1,14 |
| 40 | 5,31 | 0,0013 | 0,37 | 0,0006 | 0,17 | 0,0029 | 0,82 | 1,8873 | 2,71 |
| 42 | 5,41 | 0,0023 | 0,63 | 0,0017 | 0,44 | 0,0103 | 2,76 | 1,4716 | 4,23 |
| 46 | 5,63 | 0,0062 | 1,63 | 0,0032 | 0,85 | 0,0162 | 4,27 | 2,2678 | 6,53 |
| 48 | 5,74 | 0,0019 | 0,47 | 0,0018 | 0,45 | 0,0054 | 1,35 | 0,8204 | 2,17 |
| 50 | 5,85 | 0,0016 | 0,43 | 0,0016 | 0,45 | 0,0055 | 1,51 | 1,8917 | 3,40 |
| 52 | 5,96 | 0,0222 | 6,29 | 0,0106 | 2,99 | 0,0322 | 9,12 | 4,8009 | 13,92 |
| 54 | 6,07 | 0,0073 | 2,16 | 0,0019 | 0,56 | 0,0057 | 1,70 | 0,7126 | 2,41 |

| Depth | Age | Brassica /sed | Brassica /TOC | Campe /sed | Campe /TOC | beta-Sito /sed | beta-Sito /TOC | Dino /sed | Dino /TOC |
|-------|---------|---------------|---------------|------------|------------|----------------|----------------|-----------|-----------|
| [cm] | [ka BP] | [µg/g] | [µg/g] | [µg/g] | [µg/g] | [µg/g] | [µg/g] | [µg/g] | [µg/g] |
| 56 | 6,18 | 0,0153 | 4,08 | 0,0032 | 0,85 | 0,0092 | 2,45 | 1,0222 | 3,47 |
| 58 | 6,30 | 0,0051 | 1,40 | 0,0040 | 1,09 | 0,0135 | 3,72 | 2,0185 | 5,74 |
| 60 | 6,42 | 0,0010 | 0,28 | 0,0012 | 0,33 | 0,0029 | 0,82 | 1,2166 | 2,04 |
| 62 | 6,54 | | | 0,0027 | 0,78 | 0,0099 | 2,84 | 0,9489 | 3,79 |
| 64 | 6,65 | 0,0049 | 1,34 | 0,0046 | 1,25 | 0,0153 | 4,18 | 1,8361 | 6,02 |
| 66 | 6,77 | 0,0055 | 1,51 | 0,0064 | 1,75 | 0,0203 | 5,59 | 2,3369 | 7,93 |
| 68 | 6,89 | 0,0032 | 0,86 | 0,0017 | 0,46 | 0,0107 | 2,84 | 1,1266 | 3,97 |
| 70 | 7,00 | 0,0008 | 0,25 | 0,0004 | 0,12 | 0,0023 | 0,72 | 1,5205 | 2,24 |
| 72 | 7,10 | 0,0168 | 5,25 | 0,0128 | 3,99 | 0,0575 | 17,97 | 7,3933 | 25,37 |
| 74 | 7,20 | 0,0097 | 3,05 | 0,0079 | 2,48 | 0,0370 | 11,67 | 6,4082 | 18,08 |
| 76 | 7,29 | 0,0017 | 0,57 | 0,0009 | 0,32 | 0,0090 | 3,09 | 0,7921 | 3,88 |
| 80 | 7,45 | 0,0070 | 3,22 | 0,0050 | 2,27 | 0,0187 | 8,55 | 10,9246 | 19,48 |
| 82 | 7,52 | 0,0015 | 0,74 | 0,0003 | 0,15 | 0,0047 | 2,30 | | |
| 84 | 7,58 | | | | | 0,0049 | 2,87 | | |
| 86 | 7,64 | | | | | | | | |
| 88 | 7,69 | 0,0043 | 3,38 | 0,0047 | 3,76 | 0,0344 | 27,32 | 5,7240 | 33,05 |
| 90 | 7,74 | 0,0021 | 1,54 | 0,0016 | 1,17 | 0,0051 | 3,72 | 5,1284 | 8,85 |
| 92 | 7,78 | 0,0032 | 1,75 | 0,0014 | 0,80 | 0,0163 | 9,05 | 1,8014 | 10,86 |
| 94 | 7,82 | 0,0034 | 1,83 | 0,0036 | 1,91 | 0,0120 | 6,46 | 2,7776 | 9,24 |
| 96 | 7,86 | 0,0054 | 4,47 | 0,0048 | 3,91 | 0,0346 | 28,35 | 4,0920 | 32,44 |
| 100 | 7,91 | | | | | | | | |
| 108 | 7,96 | 0,0074 | 5,05 | 0,0029 | 1,98 | 0,0171 | 11,72 | 12,8017 | 24,52 |
| 117 | 8,00 | | | | | 0,0019 | 1,40 | | |
| 125 | 8,04 | 0,0167 | 14,28 | 0,0086 | 7,39 | 0,0623 | 53,39 | 5,3812 | 58,77 |
| 132 | 8,07 | 0,0103 | 6,65 | 0,0056 | 3,64 | 0,0451 | 29,17 | 8,0219 | 37,19 |
| 136 | 8,09 | 0,0084 | 5,84 | 0,0051 | 3,53 | 0,0212 | 14,64 | 9,9444 | 24,59 |
| 140 | 8,10 | 0,0369 | 20,95 | 0,0121 | 6,86 | 0,0893 | 50,73 | 10,0506 | 60,78 |
| 152 | 8,16 | 0,0049 | 3,15 | 0,0033 | 2,11 | 0,0306 | 19,56 | 4,7666 | 24,32 |
| 160 | 8,19 | 0,0075 | 5,33 | 0,0041 | 2,88 | 0,0160 | 11,34 | 10,3208 | 21,66 |
| 168 | 8,23 | 0,0142 | 7,60 | 0,0067 | 3,61 | 0,0430 | 23,06 | 4,0271 | 27,09 |
| 177 | 8,27 | 0,0389 | 27,73 | 0,0142 | 10,10 | 0,0999 | 71,19 | 15,7636 | 86,96 |
| 178 | 8,27 | 0,0193 | 17,33 | 0,0112 | 10,09 | 0,0616 | 55,41 | 7,2779 | 62,69 |
| 185 | 8,30 | 0,0195 | 12,48 | 0,0066 | 4,21 | 0,0508 | 32,47 | 5,9750 | 38,45 |
| 192 | 8,34 | 0,0162 | 9,54 | 0,0027 | 1,60 | 0,0132 | 7,76 | 6,3887 | 14,15 |
| 200 | 8,37 | 0,0547 | 32,53 | 0,0221 | 13,11 | 0,1283 | 76,24 | 25,9578 | 102,20 |
| 212 | 8,43 | 0,0177 | 10,10 | 0,0084 | 4,82 | 0,0467 | 26,68 | 6,4011 | 33,08 |
| 217 | 8,46 | 0,0138 | 8,79 | 0,0035 | 2,23 | 0,0394 | 25,16 | 4,1517 | 29,31 |
| 225 | 8,50 | 0,0502 | 31,04 | 0,0239 | 14,81 | 0,1152 | 71,24 | 17,7520 | 88,99 |
| 232 | 8,53 | 0,0156 | 9,70 | 0,0053 | 3,32 | 0,0274 | 17,06 | 11,8988 | 28,96 |
| 240 | 8,56 | 0,0322 | 19,78 | 0,0108 | 6,64 | 0,0736 | 45,21 | 12,7983 | 58,01 |
| 248 | 8,60 | 0,0187 | 12,71 | 0,0088 | 5,96 | 0,0384 | 26,12 | 6,7553 | 32,88 |
| 253 | 8,63 | 0,0155 | 15,02 | 0,0085 | 8,23 | 0,0541 | 52,28 | 7,6575 | 59,94 |
| 256 | 8,64 | 0,0267 | 18,74 | 0,0117 | 8,25 | 0,0741 | 52,07 | 12,4423 | 64,52 |
| 265 | 8,68 | 0,1377 | 78,21 | 0,0460 | 26,11 | 0,2311 | 131,28 | 32,2759 | 163,55 |
| 272 | 8,71 | 0,0095 | 7,32 | 0,0038 | 2,93 | 0,0196 | 15,01 | 8,5843 | 23,59 |
| 280 | 8,75 | 0,0230 | 15,89 | 0,0077 | 5,35 | 0,0516 | 35,68 | 7,3177 | 43,00 |
| 288 | 8,79 | 0,1670 | 81,50 | 0,0578 | 28,23 | 0,3081 | 150,34 | 43,7380 | 194,08 |
| 296 | 8,83 | 0,0082 | 5,78 | 0,0030 | 2,13 | 0,0271 | 19,04 | 3,2038 | 22,24 |
| 312 | 8,90 | 0,0208 | 14,49 | 0,0060 | 4,15 | 0,0272 | 18,95 | 11,4618 | 30,41 |
| 320 | 8,93 | 0,0368 | 21,65 | 0,0125 | 7,35 | 0,0826 | 48,59 | 6,1359 | 54,73 |
| 326 | 8,96 | 0,0016 | 1,59 | 0,0010 | 0,95 | 0,0151 | 14,61 | 0,6304 | 15,24 |
| 328 | 8,97 | 0,0431 | 24,64 | 0,0131 | 7,47 | 0,0793 | 45,38 | 3,5609 | 48,95 |
| 333 | 8,99 | 0,0898 | 55,93 | 0,0332 | 20,67 | 0,2044 | 127,38 | 29,2844 | 156,66 |
| 336 | 9,00 | 0,0144 | 8,03 | 0,0039 | 2,15 | 0,0274 | 15,29 | 3,5503 | 18,84 |
| 345 | 9,04 | 0,0647 | 43,49 | 0,0218 | 14,66 | 0,1252 | 84,17 | 8,8357 | 93,00 |
| 352 | 9,07 | 0,0071 | 4,22 | 0,0039 | 2,31 | 0,0154 | 9,20 | 10,9192 | 20,12 |
| 360 | 9,10 | 0,0345 | 20,14 | 0,0146 | 8,54 | 0,0808 | 47,20 | 9,4073 | 56,60 |
| 368 | 9,14 | 0,0367 | 30,75 | 0,0128 | 10,76 | 0,0761 | 63,83 | 6,1541 | 69,98 |
| 377 | 9,18 | 0,0374 | 27,64 | 0,0168 | 12,43 | 0,0957 | 70,79 | 10,3768 | 81,16 |
| 382 | 9,20 | 0,0434 | 40,80 | 0,0227 | 21,37 | 0,1233 | 115,87 | 10,3356 | 126,20 |
| 392 | 9,24 | 0,0033 | 2,45 | 0,0009 | 0,69 | 0,0063 | 4,72 | 3,7500 | 8,47 |
| 392 | 9,24 | 0,0033 | 2,45 | 0,0009 | 0,69 | 0,0063 | 4,72 | 3,7500 | 8,47 |
| 400 | 9,28 | 0,0045 | 3,42 | 0,0021 | 1,56 | 0,0169 | 12,72 | 2,0844 | 14,80 |
| 404 | 9,30 | 0,0533 | 31,13 | 0,0170 | 9,93 | 0,1184 | 69,13 | 15,6833 | 84,81 |
| 408 | 9,32 | 0,0212 | 13,62 | 0,0071 | 4,55 | 0,0430 | 27,61 | 3,6675 | 31,27 |
| 417 | 9,36 | 0,0339 | 17,76 | 0,0099 | 5,20 | 0,0529 | 27,74 | 5,2299 | 32,97 |

| Depth | Age | Brassica /sed | Brassica /TOC | Campe /sed | Campe /TOC | beta-Sito /sed | beta-Sito /TOC | Dino /sed | Dino /TOC |
|-------|---------|---------------|---------------|------------|------------|----------------|----------------|-----------|-----------|
| [cm] | [ka BP] | [µg/g] | [µg/g] | [µg/g] | [µg/g] | [µg/g] | [µg/g] | [µg/g] | [µg/g] |
| 426 | 9,40 | 0,0821 | 56,90 | 0,0305 | 21,15 | 0,1431 | 99,21 | 19,6235 | 118,83 |
| 432 | 9,43 | 0,0162 | 11,98 | 0,0045 | 3,34 | 0,0220 | 16,24 | 12,3938 | 28,64 |
| 440 | 9,47 | 0,0220 | 15,32 | 0,0053 | 3,69 | 0,0347 | 24,14 | 3,8700 | 28,01 |
| 448 | 9,51 | 0,0036 | 3,16 | 0,0014 | 1,23 | 0,0170 | 14,92 | 0,8445 | 15,77 |
| 457 | 9,56 | 0,0297 | 16,35 | 0,0109 | 5,99 | 0,0578 | 31,85 | 5,3134 | 37,16 |
| 465 | 9,60 | 0,0567 | 29,98 | 0,0173 | 9,12 | 0,1153 | 60,91 | 8,9542 | 69,87 |
| 472 | 9,63 | 0,0027 | 1,56 | 0,0010 | 0,56 | 0,0045 | 2,61 | 0,0000 | 2,61 |
| 472 | 9,63 | 0,0027 | 1,56 | 0,0010 | 0,56 | 0,0045 | 2,61 | 0,0000 | 2,61 |
| 480 | 9,66 | 0,0105 | 5,72 | 0,0023 | 1,28 | 0,0186 | 10,16 | 1,4988 | 11,66 |
| 488 | 9,69 | 0,0112 | 7,75 | 0,0016 | 1,11 | 0,0397 | 27,58 | 0,0000 | 27,58 |
| 495 | 9,70 | 0,0462 | 32,55 | 0,0181 | 12,74 | 0,1105 | 77,82 | 14,4035 | 92,23 |
| 497 | 9,70 | 0,0401 | 25,05 | 0,0175 | 10,94 | 0,0985 | 61,53 | 5,0296 | 66,56 |
| 505 | 9,71 | 0,0349 | 25,66 | 0,0128 | 9,38 | 0,0701 | 51,51 | 2,6355 | 54,15 |
| 512 | 9,72 | 0,0123 | 9,53 | 0,0048 | 3,69 | 0,0245 | 18,92 | 5,1971 | 24,12 |
| 512 | 9,72 | 0,0123 | 9,53 | 0,0048 | 3,69 | 0,0245 | 18,92 | 5,1971 | 24,12 |
| 520 | 9,72 | 0,0309 | 18,45 | 0,0124 | 7,44 | 0,0650 | 38,82 | 5,2795 | 44,10 |
| 528 | 9,73 | 0,0230 | 12,87 | 0,0099 | 5,53 | 0,0559 | 31,29 | 2,6377 | 33,93 |
| 537 | 9,74 | 0,0239 | 14,86 | 0,0104 | 6,44 | 0,0698 | 43,30 | 2,6073 | 45,91 |
| 545 | 9,75 | 0,0286 | 18,28 | 0,0129 | 8,23 | 0,0686 | 43,94 | 5,4236 | 49,37 |
| 552 | 9,76 | 0,0151 | 11,32 | 0,0076 | 5,69 | 0,0348 | 26,17 | 6,1509 | 32,32 |
| 560 | 9,77 | 0,0613 | 40,28 | 0,0263 | 17,25 | 0,1348 | 88,54 | 13,6763 | 102,21 |
| 568 | 9,78 | 0,0083 | 5,90 | 0,0025 | 1,75 | 0,0225 | 15,88 | 0,2991 | 16,18 |
| 577 | 9,79 | 0,0227 | 18,34 | 0,0059 | 4,79 | 0,0583 | 47,06 | 0,0000 | 47,06 |
| 585 | 9,80 | 0,0105 | 7,20 | 0,0039 | 2,67 | 0,0268 | 18,33 | 0,8873 | 19,21 |
| 592 | 9,81 | 0,0288 | 20,97 | 0,0098 | 7,13 | 0,0565 | 41,06 | 16,3842 | 57,45 |
| 600 | 9,82 | 0,0063 | 4,88 | 0,0036 | 2,75 | 0,0261 | 20,16 | 1,1728 | 21,33 |
| 608 | 9,83 | 0,0079 | 5,75 | 0,0030 | 2,15 | 0,0186 | 13,50 | 1,3747 | 14,87 |
| 625 | 9,85 | 0,0293 | 19,16 | 0,0128 | 8,35 | 0,0727 | 47,57 | 4,3624 | 51,93 |
| 632 | 9,86 | 0,0244 | 15,58 | 0,0113 | 7,23 | 0,0471 | 30,09 | 11,4325 | 41,52 |
| 640 | 9,87 | 0,0460 | 31,83 | 0,0173 | 11,99 | 0,1131 | 78,20 | 4,7631 | 82,96 |
| 648 | 9,87 | 0,0072 | 4,07 | 0,0030 | 1,72 | 0,0232 | 13,08 | 2,6598 | 15,74 |
| 657 | 9,88 | 0,0278 | 22,54 | 0,0124 | 10,07 | 0,0728 | 58,96 | 4,2282 | 63,19 |
| 665 | 9,89 | 0,0166 | 12,32 | 0,0085 | 6,33 | 0,0452 | 33,53 | 3,1596 | 36,69 |
| 672 | 9,90 | 0,0166 | 12,32 | 0,0085 | 6,33 | 0,0452 | 33,53 | 3,1596 | 36,69 |
| 680 | 9,91 | 0,0418 | 27,62 | 0,0201 | 13,28 | 0,0973 | 64,21 | 5,3073 | 69,52 |
| 697 | 9,93 | 0,0359 | 25,27 | 0,0145 | 10,21 | 0,0898 | 63,21 | 9,7680 | 72,98 |
| 712 | 9,95 | 0,0101 | 9,78 | 0,0045 | 4,32 | 0,0216 | 20,84 | 7,9813 | 28,82 |
| 720 | 9,96 | 0,0217 | 15,13 | 0,0104 | 7,27 | 0,0526 | 36,69 | 2,9302 | 39,62 |
| 728 | 9,97 | 0,0068 | 5,89 | 0,0028 | 2,44 | 0,0237 | 20,51 | 1,4606 | 21,97 |
| 737 | 9,98 | | | | | | | | |
| 745 | 9,99 | 0,0119 | 12,61 | 0,0040 | 4,20 | 0,0293 | 30,93 | 2,2029 | 33,13 |
| 752 | 10,00 | 0,0182 | 13,51 | 0,0074 | 5,50 | 0,0330 | 24,55 | 10,5424 | 35,10 |
| 768 | 10,02 | 0,0156 | 7,42 | 0,0020 | 0,93 | 0,0307 | 14,62 | 0,0000 | 14,62 |
| 777 | 10,03 | 0,0833 | 51,88 | 0,0280 | 17,48 | 0,1340 | 83,51 | 8,1938 | 91,70 |
| 785 | 10,04 | 0,0673 | 40,08 | 0,0251 | 14,94 | 0,1147 | 68,32 | 9,1220 | 77,45 |
| 792 | 10,05 | 0,0245 | 15,81 | 0,0116 | 7,48 | 0,0349 | 22,53 | 14,8836 | 37,42 |
| 800 | 10,06 | 0,0257 | 16,00 | 0,0084 | 5,21 | 0,0515 | 32,09 | 2,5208 | 34,62 |
| 808 | 10,07 | 0,0063 | 4,00 | 0,0025 | 1,61 | 0,0161 | 10,19 | 0,4591 | 10,65 |
| 817 | 10,08 | 0,0060 | 6,84 | 0,0045 | 5,16 | 0,0188 | 21,55 | 1,6460 | 23,20 |
| 825 | 10,09 | 0,0231 | 20,47 | 0,0105 | 9,33 | 0,0563 | 49,91 | 5,1205 | 55,03 |
| 832 | 10,09 | 0,0079 | 8,99 | 0,0051 | 5,88 | 0,0172 | 19,74 | 8,5666 | 28,31 |
| 840 | 10,10 | 0,0085 | 5,70 | 0,0064 | 4,31 | 0,0255 | 17,11 | 1,8841 | 18,99 |
| 847 | 10,11 | 0,0127 | 8,25 | 0,0023 | 1,48 | 0,0227 | 14,71 | 0,7507 | 15,46 |
| 852 | 10,12 | 0,0173 | 11,89 | 0,0060 | 4,11 | 0,0456 | 31,37 | 2,9831 | 34,35 |
| 860 | 10,13 | 0,0717 | 54,13 | 0,0334 | 25,26 | 0,1645 | 124,20 | 14,6624 | 138,86 |
| 868 | 10,14 | 0,0859 | 59,16 | 0,0420 | 28,94 | 0,2058 | 141,74 | 13,5272 | 155,26 |
| 872 | 10,14 | 0,0208 | 15,90 | 0,0089 | 6,81 | 0,0417 | 31,89 | 12,6369 | 44,53 |
| 877 | 10,15 | 0,0361 | 18,76 | 0,0159 | 8,27 | 0,0858 | 44,58 | 5,2924 | 49,88 |
| 885 | 10,16 | 0,0462 | 33,25 | 0,0186 | 13,35 | 0,1057 | 76,02 | 8,1374 | 84,15 |
| 892 | 10,17 | 0,0035 | 2,56 | 0,0018 | 1,35 | 0,0076 | 5,64 | 0,0000 | 5,64 |
| 900 | 10,18 | 0,0174 | 17,92 | 0,0095 | 9,83 | 0,0570 | 58,76 | 6,4641 | 65,22 |
| 908 | 10,19 | 0,0043 | 4,15 | 0,0017 | 1,63 | 0,0157 | 15,07 | 0,3758 | 15,45 |
| 912 | 10,19 | 0,0056 | 9,19 | 0,0027 | 4,47 | 0,0145 | 23,87 | 9,7753 | 33,65 |
| 917 | 10,20 | 0,0015 | 2,63 | 0,0008 | 1,31 | 0,0052 | 8,95 | 0,0000 | 8,95 |
| 925 | 10,21 | 0,0146 | 25,90 | 0,0109 | 19,42 | 0,0681 | 120,79 | 10,9404 | 131,73 |
| 930 | 10,21 | 0,0024 | 4,23 | 0,0015 | 2,67 | 0,0100 | 17,63 | 0,3049 | 17,94 |

Table B.5: Accumulation rates specific sterols

Cruise: PS100; Station: PS100/270; Lon [°E]: -18.14; Lat [°N]: 79.49; Water Depth: 424 m

| Depth | Age | Acc rate Brassicasterol | Acc rate Campesterol | Acc rate beta- Sitosterol | Acc rate Dinosterol |
|-------|---------|----------------------------|--------------------------|------------------------------|--------------------------|
| [cm] | [ka BP] | [µg/cm ² /ka] | [µg/cm ² /ka] | [µg/cm ² /ka] | [µg/cm ² /ka] |
| 1 | 0,75 | | | | |
| 2 | 0,94 | 0,023 | 0,005 | 0,054 | 0,019 |
| 4 | 1,32 | 0,013 | 0,007 | 0,033 | 0,014 |
| 8 | 2,09 | 0,046 | 0,022 | 0,110 | 0,024 |
| 10 | 2,48 | 0,004 | 0,002 | 0,011 | 0,012 |
| 12 | 2,86 | 0,008 | 0,001 | 0,012 | 0,007 |
| 14 | 3,25 | 0,009 | 0,005 | 0,018 | 0,006 |
| 18 | 3,85 | 0,024 | 0,014 | 0,080 | 0,012 |
| 20 | 4,06 | 0,004 | 0,002 | 0,009 | 0,005 |
| 22 | 4,23 | 0,046 | 0,018 | 0,121 | 0,040 |
| 24 | 4,38 | 0,035 | 0,021 | 0,104 | 0,031 |
| 26 | 4,52 | 0,020 | 0,008 | 0,036 | 0,011 |
| 30 | 4,75 | 0,005 | 0,003 | 0,012 | 0,023 |
| 32 | 4,87 | 0,006 | 0,003 | 0,042 | 0,004 |
| 34 | 4,99 | | | 0,033 | |
| 36 | 5,10 | | | 0,021 | |
| 38 | 5,20 | | 0,014 | 0,036 | 0,031 |
| 40 | 5,31 | 0,020 | 0,009 | 0,044 | 0,100 |
| 42 | 5,41 | 0,037 | 0,026 | 0,164 | 0,087 |
| 46 | 5,63 | 0,099 | 0,052 | 0,259 | 0,138 |
| 48 | 5,74 | 0,030 | 0,029 | 0,086 | 0,052 |
| 50 | 5,85 | 0,028 | 0,030 | 0,099 | 0,124 |
| 52 | 5,96 | 0,369 | 0,176 | 0,536 | 0,282 |
| 54 | 6,07 | 0,112 | 0,029 | 0,088 | 0,037 |
| 56 | 6,18 | 0,218 | 0,045 | 0,131 | 0,055 |
| 58 | 6,30 | 0,073 | 0,057 | 0,195 | 0,106 |
| 60 | 6,42 | 0,014 | 0,016 | 0,041 | 0,060 |
| 62 | 6,54 | 0,000 | 0,040 | 0,146 | 0,049 |
| 64 | 6,65 | 0,071 | 0,066 | 0,222 | 0,097 |
| 66 | 6,77 | 0,099 | 0,115 | 0,369 | 0,154 |
| 68 | 6,89 | 0,046 | 0,025 | 0,150 | 0,060 |
| 70 | 7,00 | 0,013 | 0,007 | 0,038 | 0,081 |
| 72 | 7,10 | 0,303 | 0,230 | 1,037 | 0,427 |
| 74 | 7,20 | 0,194 | 0,158 | 0,744 | 0,409 |
| 76 | 7,29 | 0,049 | 0,027 | 0,262 | 0,067 |
| 80 | 7,45 | 0,218 | 0,154 | 0,579 | 0,739 |
| 82 | 7,52 | 0,053 | 0,011 | 0,164 | |
| 84 | 7,58 | | | 0,158 | |
| 86 | 7,64 | | | | |
| 88 | 7,69 | 0,160 | 0,178 | 1,290 | 0,270 |
| 90 | 7,74 | 0,090 | 0,068 | 0,217 | 0,299 |
| 92 | 7,78 | 0,161 | 0,073 | 0,831 | 0,165 |
| 94 | 7,82 | 0,168 | 0,175 | 0,591 | 0,254 |
| 96 | 7,86 | 0,369 | 0,323 | 2,342 | 0,338 |
| 100 | 7,91 | | | | |
| 108 | 7,96 | 1,151 | 0,451 | 2,671 | 2,918 |
| 117 | 8,00 | | | 0,313 | |
| 125 | 8,04 | 2,498 | 1,293 | 9,342 | 0,942 |
| 132 | 8,07 | 1,661 | 0,909 | 7,286 | 2,004 |
| 136 | 8,09 | 1,521 | 0,919 | 3,813 | 2,589 |
| 140 | 8,10 | 7,135 | 2,336 | 17,278 | 3,423 |
| 152 | 8,16 | 0,816 | 0,546 | 5,071 | 1,236 |
| 160 | 8,19 | 1,305 | 0,704 | 2,777 | 2,527 |
| 168 | 8,23 | 2,363 | 1,122 | 7,174 | 1,253 |
| 177 | 8,27 | 5,871 | 2,139 | 15,074 | 3,338 |
| 178 | 8,27 | 2,827 | 1,646 | 9,040 | 1,187 |
| 185 | 8,30 | 3,504 | 1,181 | 9,115 | 1,677 |
| 192 | 8,34 | 2,859 | 0,480 | 2,325 | 1,914 |
| 200 | 8,37 | 9,920 | 3,999 | 23,251 | 7,917 |
| 212 | 8,43 | 3,105 | 1,481 | 8,199 | 1,967 |
| 217 | 8,46 | 2,652 | 0,672 | 7,591 | 1,252 |
| 225 | 8,50 | 9,860 | 4,703 | 22,627 | 5,638 |
| 232 | 8,53 | 2,880 | 0,986 | 5,067 | 3,535 |
| 240 | 8,56 | 6,081 | 2,043 | 13,898 | 3,935 |
| 248 | 8,60 | 4,246 | 1,989 | 8,724 | 2,256 |
| 253 | 8,63 | 2,867 | 1,572 | 9,983 | 1,462 |
| 256 | 8,64 | 5,498 | 2,420 | 15,276 | 3,650 |

| Depth | Age | Acc rate Brassicasterol | Acc rate Campesterol | Acc rate beta- Sitosterol | Acc rate Dinosterol |
|--------------|------------|---|---|---|---|
| [cm] | [ka BP] | [$\mu\text{g}/\text{cm}^2/\text{ka}$] | [$\mu\text{g}/\text{cm}^2/\text{ka}$] | [$\mu\text{g}/\text{cm}^2/\text{ka}$] | [$\mu\text{g}/\text{cm}^2/\text{ka}$] |
| 265 | 8,68 | 30,819 | 10,289 | 51,732 | 12,719 |
| 272 | 8,71 | 2,006 | 0,802 | 4,115 | 2,354 |
| 280 | 8,75 | 4,857 | 1,634 | 10,904 | 2,236 |
| 288 | 8,79 | 35,245 | 12,206 | 65,013 | 18,914 |
| 296 | 8,83 | 1,713 | 0,632 | 5,639 | 0,949 |
| 312 | 8,90 | 5,312 | 1,522 | 6,946 | 4,201 |
| 320 | 8,93 | 7,870 | 2,672 | 17,667 | 2,231 |
| 326 | 8,96 | 0,357 | 0,213 | 3,281 | 0,142 |
| 328 | 8,97 | 10,387 | 3,147 | 19,132 | 1,501 |
| 333 | 8,99 | 21,647 | 8,000 | 49,298 | 11,334 |
| 336 | 9,00 | 3,540 | 0,947 | 6,738 | 1,565 |
| 345 | 9,04 | 13,785 | 4,646 | 26,675 | 2,800 |
| 352 | 9,07 | 1,644 | 0,901 | 3,585 | 4,255 |
| 360 | 9,10 | 6,976 | 2,956 | 16,344 | 3,258 |
| 368 | 9,14 | 7,385 | 2,585 | 15,329 | 1,478 |
| 377 | 9,18 | 7,653 | 3,441 | 19,602 | 2,874 |
| 382 | 9,20 | 8,724 | 4,568 | 24,773 | 2,210 |
| 392 | 9,24 | 0,682 | 0,192 | 1,315 | 1,045 |
| 392 | 9,24 | 0,682 | 0,192 | 1,315 | 1,045 |
| 400 | 9,28 | 0,927 | 0,422 | 3,446 | 0,565 |
| 404 | 9,30 | 10,008 | 3,192 | 22,221 | 5,041 |
| 408 | 9,32 | 4,475 | 1,494 | 9,073 | 1,205 |
| 417 | 9,36 | 6,815 | 1,997 | 10,647 | 2,007 |
| 426 | 9,40 | 15,100 | 5,612 | 26,326 | 5,207 |
| 432 | 9,43 | 3,122 | 0,871 | 4,233 | 3,229 |
| 440 | 9,47 | 4,040 | 0,973 | 6,368 | 1,021 |
| 448 | 9,51 | 0,793 | 0,310 | 3,747 | 0,212 |
| 457 | 9,56 | 6,931 | 2,540 | 13,498 | 2,252 |
| 465 | 9,60 | 12,743 | 3,878 | 25,890 | 3,806 |
| 472 | 9,63 | 0,693 | 0,251 | 1,160 | |
| 472 | 9,63 | 0,693 | 0,251 | 1,160 | |
| 480 | 9,66 | 3,482 | 0,782 | 6,186 | 0,913 |
| 488 | 9,69 | 8,308 | 1,195 | 29,550 | |
| 495 | 9,70 | 51,211 | 20,048 | 122,422 | 22,658 |
| 497 | 9,70 | 52,035 | 22,718 | 127,792 | 10,446 |
| 505 | 9,71 | 39,730 | 14,526 | 79,747 | 4,080 |
| 512 | 9,72 | 12,989 | 5,032 | 25,794 | 7,085 |
| 512 | 9,72 | 12,989 | 5,032 | 25,794 | 7,085 |
| 520 | 9,72 | 34,279 | 13,814 | 72,131 | 9,809 |
| 528 | 9,73 | 22,903 | 9,842 | 55,682 | 4,693 |
| 537 | 9,74 | 22,730 | 9,853 | 66,244 | 3,989 |
| 545 | 9,75 | 33,660 | 15,152 | 80,909 | 9,986 |
| 552 | 9,76 | 15,485 | 7,778 | 35,792 | 8,411 |
| 560 | 9,77 | 62,001 | 26,542 | 136,268 | 21,049 |
| 568 | 9,78 | 8,444 | 2,500 | 22,739 | 0,428 |
| 577 | 9,79 | 23,115 | 6,035 | 59,311 | |
| 585 | 9,80 | 9,569 | 3,548 | 24,355 | 1,179 |
| 592 | 9,81 | 26,353 | 8,961 | 51,592 | 20,585 |
| 600 | 9,82 | 5,859 | 3,298 | 24,221 | 1,409 |
| 608 | 9,83 | 7,869 | 2,940 | 18,465 | 1,880 |
| 625 | 9,85 | 40,387 | 17,598 | 100,263 | 9,196 |
| 632 | 9,86 | 28,406 | 13,178 | 54,852 | 20,841 |
| 640 | 9,87 | 55,276 | 20,817 | 135,806 | 8,272 |
| 648 | 9,87 | 7,191 | 3,039 | 23,118 | 4,700 |
| 657 | 9,88 | 29,694 | 13,271 | 77,676 | 5,570 |
| 665 | 9,89 | 16,753 | 8,605 | 45,609 | 4,298 |
| 672 | 9,90 | 15,338 | 7,878 | 41,756 | 3,935 |
| 680 | 9,91 | 40,828 | 19,640 | 94,921 | 7,846 |
| 697 | 9,93 | 40,447 | 16,351 | 101,190 | 15,636 |
| 712 | 9,95 | 12,230 | 5,403 | 26,077 | 9,986 |
| 720 | 9,96 | 24,211 | 11,623 | 58,703 | 4,688 |
| 728 | 9,97 | 8,970 | 3,725 | 31,244 | 2,225 |
| 737 | 9,98 | | | | |
| 745 | 9,99 | 15,842 | 5,275 | 38,864 | 2,768 |
| 752 | 10,00 | 18,882 | 7,688 | 34,306 | 14,730 |
| 768 | 10,02 | 16,812 | 2,112 | 33,118 | |
| 777 | 10,03 | 89,498 | 30,146 | 144,046 | 14,134 |
| 785 | 10,04 | 72,013 | 26,853 | 122,766 | 16,391 |
| 792 | 10,05 | 26,569 | 12,577 | 37,867 | 25,010 |
| 800 | 10,06 | 28,886 | 9,407 | 57,945 | 4,551 |
| 808 | 10,07 | 7,282 | 2,932 | 18,570 | 0,836 |
| 817 | 10,08 | 8,560 | 6,450 | 26,961 | 2,059 |
| 825 | 10,09 | 30,278 | 13,799 | 73,825 | 7,574 |

| Depth | Age | Acc rate Brassicasterol | Acc rate Campesterol | Acc rate beta- Sitosterol | Acc rate Dinosterol |
|-------|---------|---|---|---|---|
| [cm] | [ka BP] | [$\mu\text{g}/\text{cm}^2/\text{ka}$] | [$\mu\text{g}/\text{cm}^2/\text{ka}$] | [$\mu\text{g}/\text{cm}^2/\text{ka}$] | [$\mu\text{g}/\text{cm}^2/\text{ka}$] |
| 832 | 10,09 | 8,809 | 5,757 | 19,338 | 8,391 |
| 840 | 10,10 | 8,852 | 6,691 | 26,561 | 2,925 |
| 847 | 10,11 | 9,525 | 1,705 | 16,990 | 0,867 |
| 852 | 10,12 | 20,098 | 6,949 | 53,041 | 5,044 |
| 860 | 10,13 | 86,383 | 40,318 | 198,221 | 23,401 |
| 868 | 10,14 | 107,339 | 52,513 | 257,155 | 24,542 |
| 872 | 10,14 | 24,243 | 10,391 | 48,632 | 19,271 |
| 877 | 10,15 | 41,653 | 18,352 | 98,993 | 11,751 |
| 885 | 10,16 | 53,681 | 21,557 | 122,744 | 13,140 |
| 892 | 10,17 | 4,120 | 2,181 | 9,091 | |
| 900 | 10,18 | 24,361 | 13,359 | 79,854 | 8,785 |
| 908 | 10,19 | 6,484 | 2,541 | 23,533 | 0,587 |
| 912 | 10,19 | 9,606 | 4,671 | 24,961 | 10,220 |
| 917 | 10,20 | 2,611 | 1,303 | 8,885 | |
| 925 | 10,21 | 24,905 | 18,679 | 116,167 | 10,522 |

Appendix C

This Appendix contains various data of organic bulk parameter, HBI and specific sterols relevant to Chapter 6 of this thesis. These include organic bulk parameters, HBIs, specific sterol concentrations ($\mu\text{g g}^{-1}$ TOC) and planktic and benthic foraminifers.

Table C.1: Surface Samples off Northeast Greenland - HBIs

| Station | Lat | Lon | TOC | IP ₂₅ | IP ₂₅ | HBI II diene | HBI II diene | HBI III z- triene | HBI III z- triene |
|--------------|-------|--------|------|-------------------------------|-------------------------------|-------------------------------|-------------------------------|-------------------------------|-------------------------------|
| | [°N] | [°E] | (%) | ($\mu\text{g}/\text{gSed}$) | ($\mu\text{g}/\text{gTOC}$) | ($\mu\text{g}/\text{gSed}$) | ($\mu\text{g}/\text{gTOC}$) | ($\mu\text{g}/\text{gSed}$) | ($\mu\text{g}/\text{gTOC}$) |
| PS109/19-02 | 80,15 | -7,95 | 0,47 | 0,0695 | 13,59 | 0,1180 | 23,08 | 0,0233 | 4,55 |
| PS109/105-01 | 78,47 | -18,56 | 0,51 | 0,0380 | 11,38 | 0,0509 | 15,25 | 0,0116 | 3,47 |
| PS109/115-02 | 78,03 | -16,54 | 0,33 | 0,0435 | 6,57 | 0,0554 | 8,38 | 0,0114 | 1,72 |
| PS109/125-01 | 77,80 | -13,63 | 0,66 | 0,0263 | 5,54 | 0,0444 | 9,37 | 0,0059 | 1,25 |
| PS109/129-01 | 77,91 | -13,18 | 0,24 | 0,0239 | 9,90 | 0,0384 | 15,91 | 0,0047 | 1,95 |
| PS109/139-01 | 76,80 | -8,63 | 0,56 | 0,0155 | 3,31 | 0,0268 | 5,70 | 0,0053 | 1,12 |
| PS109/36-02 | 76,80 | -8,63 | 0,47 | 0,1074 | 19,24 | 0,1801 | 32,27 | 0,0319 | 5,71 |
| PS109/46-02 | 80,15 | -17,70 | 0,46 | 0,1010 | 22,17 | 0,0469 | 10,30 | 0,0075 | 1,65 |
| PS109/76-01 | 79,62 | -19,29 | 0,56 | 0,0307 | 5,50 | 0,0278 | 4,98 | 0,0069 | 1,23 |
| PS109/85-02 | 79,56 | -19,23 | 0,13 | 0,0294 | 23,44 | 0,0300 | 23,93 | 0,0052 | 4,10 |
| PS109/93-02 | 79,19 | -17,12 | 0,55 | 0,0343 | 6,25 | 0,0465 | 8,46 | 0,0085 | 1,54 |
| PS115.1/4-2 | 76,39 | -4,80 | 0,57 | 0,0008 | 0,14 | 0,0008 | 0,15 | 0,0007 | 0,12 |
| PS115.1/6-1 | 78,44 | -8,96 | 0,78 | 0,0024 | 0,30 | 0,0036 | 0,45 | 0,0004 | 0,05 |
| PS115.1/7-1 | 78,46 | -10,53 | 0,73 | 0,0026 | 0,35 | 0,0037 | 0,50 | 0,0004 | 0,06 |
| PS115.1/9-4 | 78,93 | -11,76 | 0,91 | 0,0041 | 0,45 | 0,0057 | 0,62 | 0,0009 | 0,10 |
| PS115.1/11-1 | 78,93 | -11,74 | 0,26 | 0,0020 | 0,77 | 0,0024 | 0,90 | 0,0008 | 0,29 |
| PS115.1/17-2 | 82,18 | -10,51 | 0,40 | 0,0009 | 0,22 | 0,0007 | 0,17 | 0,0001 | 0,02 |
| PS115.1/18-1 | 82,11 | -11,24 | 0,25 | 0,0006 | 0,24 | 0,0005 | 0,20 | 0,0000 | 0,01 |
| PS115.1/19-2 | 81,96 | -12,65 | 0,46 | 0,0018 | 0,38 | 0,0016 | 0,35 | 0,0001 | 0,02 |
| PS115.1/21-2 | 82,00 | -13,23 | 0,49 | 0,0020 | 0,40 | 0,0021 | 0,43 | 0,0002 | 0,03 |
| PS115.1/22-2 | 82,28 | -9,47 | 0,56 | 0,0007 | 0,13 | 0,0007 | 0,13 | 0,0000 | 0,01 |
| PS115.1/26-1 | 82,50 | -11,49 | 0,46 | 0,0007 | 0,16 | 0,0006 | 0,12 | 0,0001 | 0,02 |
| PS115.1/47-2 | 84,24 | -29,60 | 0,32 | 0,0002 | 0,06 | 0,0002 | 0,06 | | |
| PS115.1/48-2 | 83,12 | -20,54 | 0,32 | 0,0010 | 0,32 | 0,0009 | 0,29 | 0,0001 | 0,03 |
| PS115.1/50-2 | 80,89 | -3,49 | 0,55 | 0,0028 | 0,50 | 0,0044 | 0,80 | 0,0004 | 0,07 |
| PS115.1/51-2 | 80,48 | -8,49 | 0,89 | 0,0063 | 0,71 | 0,0107 | 1,21 | 0,0010 | 0,11 |
| PS115.1/52-2 | 80,35 | -6,84 | 0,47 | 0,0016 | 0,35 | 0,0018 | 0,39 | 0,0004 | 0,09 |

Table C.2: Surface Samples off Northeast Greenland – specific sterols

| Station | Lat | Lon | Brassica | Brassica | Campe | Campe | β-Sito | β-Sito | Dino | Dino |
|--------------|------|-------|-----------|-----------|-----------|-----------|-----------|-----------|-----------|-----------|
| | [°N] | [°E] | (µg/gSed) | (µg/gTOC) | (µg/gSed) | (µg/gTOC) | (µg/gSed) | (µg/gTOC) | (µg/gSed) | (µg/gTOC) |
| PS109/ 19-2 | 80,1 | -8,0 | 0,37 | 34,86 | 0,41 | 38,72 | 0,74 | 70,22 | 0,50 | 47,24 |
| PS109/105-1 | 78,5 | -18,6 | 0,12 | 34,93 | 0,04 | 12,81 | 0,29 | 87,25 | 0,07 | 21,29 |
| PS109/115-2 | 78,0 | -16,5 | 0,11 | 17,15 | 0,05 | 7,54 | 0,69 | 104,96 | 0,05 | 6,95 |
| PS109/125-1 | 77,8 | -13,6 | 0,13 | 26,62 | 0,05 | 11,01 | 1,21 | 256,20 | 0,05 | 10,43 |
| PS109/129-1 | 77,9 | -13,2 | 0,09 | 39,01 | 0,06 | 25,98 | 0,80 | 331,04 | 0,03 | 14,26 |
| PS109/139-1 | 76,8 | -8,6 | 0,34 | 66,09 | 0,23 | 45,80 | 0,95 | 185,23 | 0,09 | 18,34 |
| PS109/36-2 | 76,8 | -8,6 | 0,28 | 50,95 | 0,16 | 28,63 | 0,36 | 64,18 | 0,11 | 19,29 |
| PS109/46-2 | 80,1 | -17,7 | 0,21 | 46,22 | 0,06 | 13,30 | 0,28 | 61,46 | 0,07 | 14,86 |
| PS109/76-1 | 79,6 | -19,3 | 0,10 | 17,83 | 0,04 | 6,92 | 0,17 | 31,20 | 0,05 | 8,48 |
| PS109/85-2 | 79,6 | -19,2 | 0,09 | 68,88 | 0,03 | 25,17 | 0,17 | 133,09 | 0,04 | 33,36 |
| PS109/93-2 | 79,2 | -17,1 | 0,06 | 10,81 | 0,03 | 6,02 | 0,19 | 35,29 | 0,04 | 7,41 |
| PS115.1/4-2 | 76,4 | -4,8 | 0,31 | 54,68 | 0,07 | 12,31 | 0,60 | 105,66 | 0,08 | 14,58 |
| PS115.1/6-1 | 78,4 | -9,0 | 0,26 | 33,22 | 0,16 | 20,75 | 0,51 | 65,42 | 0,08 | 9,90 |
| PS115.1/7-1 | 78,5 | -10,5 | 0,16 | 21,11 | 0,12 | 15,74 | 0,89 | 121,18 | 0,04 | 5,78 |
| PS115.1/9-4 | 78,9 | -11,8 | 0,25 | 26,83 | 0,21 | 22,88 | 0,59 | 64,65 | 0,08 | 8,94 |
| PS115.1/11-1 | 78,9 | -11,7 | 0,18 | 69,58 | 0,11 | 41,66 | 0,30 | 115,10 | 0,05 | 20,14 |
| PS115.1/17-2 | 82,2 | -10,5 | 0,05 | 12,05 | 0,03 | 7,43 | 0,18 | 43,96 | 0,01 | 3,56 |
| PS115.1/18-1 | 82,1 | -11,2 | 0,04 | 17,23 | 0,02 | 9,06 | 0,12 | 45,87 | 0,01 | 2,69 |
| PS115.1/19-2 | 82,0 | -12,7 | 0,09 | 18,95 | 0,05 | 10,28 | 0,18 | 39,01 | 0,03 | 5,87 |
| PS115.1/21-2 | 82,0 | -13,2 | 0,26 | 52,29 | 0,12 | 23,91 | 0,33 | 67,59 | 0,04 | 7,22 |
| PS115.1/22-2 | 82,3 | -9,5 | 0,03 | 5,11 | 0,02 | 3,30 | 0,13 | 23,79 | 0,01 | 1,85 |
| PS115.1/26-1 | 82,5 | -11,5 | 0,05 | 11,02 | 0,02 | 5,03 | 0,23 | 50,01 | 0,01 | 2,02 |
| PS115.1/47-2 | 84,2 | -29,6 | 0,03 | 8,96 | 0,02 | 4,89 | 0,13 | 39,67 | 0,01 | 2,94 |
| PS115.1/48-2 | 83,1 | -20,5 | 0,11 | 33,05 | 0,05 | 17,13 | 0,23 | 72,63 | 0,02 | 7,14 |
| PS115.1/50-2 | 80,9 | -3,5 | 0,16 | 28,20 | 0,10 | 18,33 | 0,37 | 66,55 | 0,04 | 6,92 |
| PS115.1/51-2 | 80,5 | -8,5 | 0,32 | 35,72 | 0,21 | 23,33 | 0,53 | 60,20 | 0,09 | 9,90 |
| PS115.1/52-2 | 80,3 | -6,8 | 0,06 | 12,80 | 0,04 | 8,05 | 0,30 | 65,22 | 0,03 | 6,72 |

Table C.3: Surface Samples off Northeast Greenland – PIP₂₅ indices

| Station | Lat | Lon | P _B IP ₂₅ | P _D IP ₂₅ | P _M IP ₂₅ |
|--------------|-------|--------|---------------------------------|---------------------------------|---------------------------------|
| | [°N] | [°E] | | | |
| PS109/ 19-02 | 80,15 | -7,95 | 0,72 | 0,41 | 0,41 |
| PS109/105-01 | 78,47 | -18,56 | 0,68 | 0,56 | 0,43 |
| PS109/115-02 | 78,03 | -16,54 | 0,71 | 0,69 | 0,47 |
| PS109/125-01 | 77,80 | -13,63 | 0,57 | 0,56 | 0,50 |
| PS109/129-01 | 77,91 | -13,18 | 0,62 | 0,63 | 0,54 |
| PS109/139-01 | 76,80 | -8,63 | 0,24 | 0,30 | 0,40 |
| PS109/36-02 | 76,80 | -8,63 | 0,71 | 0,71 | 0,44 |
| PS109/46-02 | 80,15 | -17,70 | 0,76 | 0,78 | 0,76 |
| PS109/76-01 | 79,62 | -19,29 | 0,67 | 0,61 | 0,51 |
| PS109/85-02 | 79,56 | -19,23 | 0,69 | 0,63 | 0,57 |
| PS109/93-02 | 79,19 | -17,12 | 0,79 | 0,67 | 0,48 |
| PS115.1/4-2 | 76,39 | -4,80 | 0,02 | 0,02 | 0,21 |
| PS115.1/6-1 | 78,44 | -8,96 | 0,06 | 0,07 | 0,57 |
| PS115.1/7-1 | 78,46 | -10,53 | 0,10 | 0,13 | 0,58 |
| PS115.1/9-4 | 78,93 | -11,76 | 0,10 | 0,11 | 0,51 |
| PS115.1/11-1 | 78,93 | -11,74 | 0,07 | 0,08 | 0,38 |
| PS115.1/17-2 | 82,18 | -10,51 | 0,11 | 0,13 | 0,73 |
| PS115.1/18-1 | 82,11 | -11,24 | 0,08 | 0,18 | 0,82 |
| PS115.1/19-2 | 81,96 | -12,65 | 0,12 | 0,14 | 0,82 |
| PS115.1/21-2 | 82,00 | -13,23 | 0,05 | 0,12 | 0,74 |
| PS115.1/22-2 | 82,28 | -9,47 | 0,14 | 0,15 | 0,79 |
| PS115.1/26-1 | 82,50 | -11,49 | 0,09 | 0,16 | 0,70 |
| PS115.1/47-2 | 84,24 | -29,60 | 0,04 | 0,05 | 1,00 |
| PS115.1/48-2 | 83,12 | -20,54 | 0,06 | 0,10 | 0,73 |
| PS115.1/50-2 | 80,89 | -3,49 | 0,10 | 0,15 | 0,61 |
| PS115.1/51-2 | 80,48 | -8,49 | 0,11 | 0,15 | 0,59 |
| PS115.1/52-2 | 80,35 | -6,84 | 0,15 | 0,11 | 0,47 |

Table C.4: HBIs

Cruise: PS109; Station: PS109/46; Lon [°E]: -17.72; Lat [°N]: 80.13; Water Depth: 206 m

| Depth | IP ₂₅ /sed | IP ₂₅ /TOC | HBI II diene/sed | HBI II diene/TOC | HBI III z-triene/sed | HBI III z-triene/TOC |
|-------|-----------------------|-----------------------|------------------|------------------|----------------------|----------------------|
| [cm] | [µg/g] | [µg/g] | [µg/g] | [µg/g] | [µg/g] | [µg/g] |
| 1 | 0,0153 | 2,95 | 0,0069 | 1,34 | 0,00101 | 0,19 |
| 2 | 0,0072 | 1,70 | 0,0046 | 1,09 | 0,00053 | 0,13 |
| 3 | 0,0040 | 1,04 | 0,0037 | 0,96 | 0,00046 | 0,12 |
| 4 | 0,0023 | 0,62 | 0,0020 | 0,55 | 0,00023 | 0,06 |
| 5 | 0,0017 | 0,46 | 0,0021 | 0,54 | 0,00022 | 0,06 |
| 6 | 0,0013 | 0,40 | 0,0012 | 0,35 | 0,00014 | 0,04 |
| 7 | 0,0009 | 0,26 | 0,0010 | 0,29 | 0,00006 | 0,02 |
| 8 | 0,0004 | 0,14 | 0,0006 | 0,18 | 0,00005 | 0,02 |
| 9 | 0,0004 | 0,11 | 0,0004 | 0,12 | 0,00003 | 0,01 |
| 10 | 0,0008 | 0,22 | 0,0008 | 0,23 | 0,00010 | 0,03 |
| 11 | 0,0002 | 0,05 | 0,0002 | 0,06 | | |
| 12 | 0,0001 | 0,04 | 0,0002 | 0,05 | | |
| 13 | 0,0002 | 0,05 | 0,0002 | 0,06 | 0,00006 | 0,02 |
| 14 | 0,0002 | 0,05 | 0,0002 | 0,05 | 0,00020 | 0,05 |
| 15 | 0,0002 | 0,06 | 0,0003 | 0,09 | 0,00005 | 0,01 |
| 16 | 0,0003 | 0,07 | 0,0003 | 0,08 | | |
| 17 | 0,0002 | 0,05 | 0,0003 | 0,08 | | |
| 18 | 0,0002 | 0,06 | 0,0003 | 0,09 | 0,00005 | 0,01 |
| 19 | 0,0002 | 0,05 | 0,0003 | 0,07 | | |
| 20 | 0,0001 | 0,04 | 0,0002 | 0,05 | 0,00008 | 0,02 |
| 21 | 0,0000 | 0,00 | 0,0000 | 0,00 | | |
| 22 | 0,0002 | 0,05 | 0,0002 | 0,05 | | |
| 23 | 0,0001 | 0,04 | 0,0002 | 0,06 | | |
| 24 | 0,0001 | 0,04 | 0,0001 | 0,03 | 0,00002 | 0,01 |
| 25 | 0,0001 | 0,03 | 0,0002 | 0,06 | | |
| 26 | 0,0002 | 0,05 | 0,0002 | 0,07 | | |
| 27 | 0,0001 | 0,03 | 0,0001 | 0,04 | | |
| 28 | 0,0002 | 0,06 | 0,0003 | 0,08 | 0,00005 | 0,02 |
| 29 | 0,0001 | 0,04 | 0,0002 | 0,06 | | |
| 30 | 0,0001 | 0,04 | 0,0002 | 0,05 | | |
| 31 | 0,0002 | 0,05 | 0,0003 | 0,08 | | |
| 32 | 0,0002 | 0,05 | 0,0003 | 0,08 | | |
| 33 | 0,0002 | 0,07 | 0,0003 | 0,08 | | |

Table C.5: Specific sterols

Cruise: PS109; Station: PS109/46; Lon [°E]: -17.72; Lat [°N]: 80.13; Water Depth: 206 m

Cruise: PS109; Station: PS109/46

| Depth | Brassica/sed | Brassica/TOC | Campe/sed | Campe/TOC | beta-Sito/sed | beta-Sito/TOC | Dino/sed | Dino/TOC |
|-------|--------------|--------------|-----------|-----------|---------------|---------------|----------|----------|
| [cm] | [µg/g] | [µg/g] | [µg/g] | [µg/g] | [µg/g] | [µg/g] | [µg/g] | [µg/g] |
| 1 | 0,1098 | 21,18 | 0,0303 | 5,84 | 0,1945 | 37,52 | 0,0632 | 12,20 |
| 2 | 0,0249 | 5,88 | 0,0083 | 1,97 | 0,0505 | 11,90 | 0,0230 | 5,43 |
| 3 | 0,0154 | 3,97 | 0,0072 | 1,86 | 0,0271 | 6,99 | 0,0176 | 4,54 |
| 4 | 0,0063 | 1,71 | 0,0034 | 0,92 | 0,0165 | 4,46 | 0,0125 | 3,38 |
| 5 | 0,0000 | 0,01 | 0,0000 | 0,01 | 0,0001 | 0,02 | 0,0001 | 0,02 |
| 6 | 0,0029 | 0,88 | 0,0013 | 0,38 | 0,0085 | 2,60 | 0,0057 | 1,75 |
| 8 | 0,0012 | 0,38 | 0,0004 | 0,12 | 0,0036 | 1,12 | 0,0026 | 0,79 |
| 9 | 0,0008 | 0,25 | 0,0008 | 0,25 | 0,0040 | 1,19 | 0,0023 | 0,67 |
| 10 | 0,0019 | 0,54 | 0,0019 | 0,53 | 0,0055 | 1,54 | 0,0074 | 2,06 |
| 11 | 0,0006 | 0,17 | 0,0006 | 0,16 | 0,0017 | 0,46 | 0,0023 | 0,62 |
| 12 | 0,0006 | 0,17 | 0,0003 | 0,10 | 0,0024 | 0,69 | 0,0032 | 0,92 |
| 13 | 0,0009 | 0,23 | 0,0008 | 0,20 | 0,0029 | 0,77 | 0,0037 | 0,97 |
| 14 | 0,0007 | 0,19 | 0,0006 | 0,15 | 0,0017 | 0,45 | 0,0034 | 0,93 |
| 15 | 0,0008 | 0,21 | 0,0008 | 0,20 | 0,0027 | 0,71 | 0,0050 | 1,32 |
| 16 | 0,0006 | 0,15 | 0,0005 | 0,12 | 0,0019 | 0,48 | 0,0021 | 0,52 |
| 17 | 0,0009 | 0,23 | 0,0011 | 0,28 | 0,0031 | 0,77 | 0,0034 | 0,84 |
| 18 | 0,0008 | 0,20 | 0,0005 | 0,13 | 0,0028 | 0,76 | 0,0033 | 0,88 |
| 19 | 0,0006 | 0,16 | 0,0005 | 0,13 | 0,0015 | 0,42 | 0,0019 | 0,53 |
| 20 | 0,0005 | 0,13 | 0,0006 | 0,16 | 0,0022 | 0,64 | 0,0036 | 1,01 |
| 21 | 0,0007 | 0,21 | 0,0007 | 0,21 | 0,0017 | 0,51 | 0,0011 | 0,31 |
| 22 | 0,0004 | 0,11 | 0,0006 | 0,17 | 0,0024 | 0,71 | 0,0034 | 1,00 |
| 23 | 0,0006 | 0,20 | 0,0002 | 0,06 | 0,0017 | 0,52 | 0,0011 | 0,35 |
| 24 | 0,0004 | 0,12 | 0,0003 | 0,08 | 0,0017 | 0,49 | 0,0022 | 0,65 |
| 25 | 0,0008 | 0,24 | 0,0005 | 0,15 | 0,0032 | 0,92 | 0,0033 | 0,95 |

| Depth | Brassica/sed | Brassica/TOC | Campe/sed | Campe/TOC | beta-Sito/sed | beta-Sito/TOC | Dino/sed | Dino/TOC |
|-------|--------------|--------------|-----------|-----------|---------------|---------------|----------|----------|
| [cm] | [µg/g] | [µg/g] | [µg/g] | [µg/g] | [µg/g] | [µg/g] | [µg/g] | [µg/g] |
| 26 | 0,0005 | 0,13 | 0,0005 | 0,13 | 0,0015 | 0,45 | 0,0028 | 0,82 |
| 27 | 0,0006 | 0,17 | 0,0006 | 0,18 | 0,0018 | 0,56 | 0,0033 | 1,01 |
| 28 | 0,0004 | 0,12 | 0,0004 | 0,12 | 0,0020 | 0,61 | 0,0008 | 0,24 |
| 29 | 0,0005 | 0,16 | 0,0009 | 0,27 | 0,0021 | 0,63 | 0,0038 | 1,12 |
| 30 | 0,0006 | 0,19 | 0,0009 | 0,25 | 0,0033 | 0,99 | 0,0040 | 1,21 |
| 31 | 0,0006 | 0,18 | 0,0008 | 0,22 | 0,0022 | 0,64 | 0,0030 | 0,88 |
| 32 | 0,0007 | 0,20 | 0,0002 | 0,06 | 0,0015 | 0,45 | 0,0027 | 0,77 |
| 33 | 0,0007 | 0,20 | 0,0008 | 0,21 | 0,0030 | 0,81 | 0,0044 | 1,20 |

Table C.6: Highly branched isoprenoids

Cruise: PS109/76; Station: PS109/76; Lon [°E]: -19.28; Lat [°N]: 79.629; Water Depth: 367 m

| Depth | IP ₂₅ /sed | IP ₂₅ /TOC | HBI II diene/sed | HBI II diene/TOC | HBI III z-triene/sed | HBI III z-triene/TOC |
|-------|-----------------------|-----------------------|------------------|------------------|----------------------|----------------------|
| [cm] | [µg/g] | [µg/g] | [µg/g] | [µg/g] | [µg/g] | [µg/g] |
| 1 | 0,0047 | 2,60 | 0,0026 | 1,43 | 0,00026 | 0,14 |
| 2 | 0,0014 | 0,99 | 0,0011 | 0,76 | 0,00005 | 0,04 |
| 3 | 0,0012 | 1,02 | 0,0009 | 0,80 | 0,00006 | 0,05 |
| 4 | 0,0010 | 0,94 | 0,0006 | 0,55 | 0,00006 | 0,05 |
| 5 | 0,0009 | 0,83 | 0,0009 | 0,85 | 0,00005 | 0,05 |
| 6 | 0,0006 | 0,59 | 0,0004 | 0,43 | 0,00002 | 0,02 |
| 7 | 0,0005 | 0,46 | 0,0003 | 0,31 | 0,00004 | 0,04 |
| 8 | 0,0007 | 0,74 | 0,0007 | 0,77 | 0,00002 | 0,03 |
| 9 | 0,0005 | 0,53 | 0,0006 | 0,64 | 0,00005 | 0,05 |
| 10 | 0,0007 | 0,72 | 0,0007 | 0,78 | 0,00007 | 0,08 |
| 11 | 0,0006 | 0,62 | 0,0006 | 0,64 | 0,00010 | 0,11 |
| 12 | 0,0005 | 0,68 | 0,0004 | 0,48 | 0,00006 | 0,07 |
| 13 | 0,0009 | 1,08 | 0,0008 | 0,95 | 0,00008 | 0,10 |
| 14 | 0,0006 | 0,83 | 0,0006 | 0,74 | 0,00015 | 0,20 |
| 15 | 0,0006 | 0,62 | 0,0004 | 0,47 | 0,00012 | 0,13 |
| 16 | 0,0005 | 0,53 | 0,0005 | 0,58 | 0,00014 | 0,16 |
| 17 | 0,0004 | 0,49 | 0,0004 | 0,52 | 0,00005 | 0,07 |
| 18 | 0,0006 | 0,82 | 0,0006 | 0,76 | 0,00006 | 0,08 |
| 19 | 0,0006 | 0,66 | 0,0007 | 0,79 | 0,00008 | 0,09 |
| 20 | 0,0007 | 0,76 | 0,0007 | 0,82 | 0,00012 | 0,14 |
| 21 | 0,0008 | 0,88 | 0,0006 | 0,74 | 0,00007 | 0,08 |
| 22 | 0,0009 | 1,01 | 0,0010 | 1,18 | 0,00008 | 0,09 |
| 23 | 0,0009 | 1,08 | 0,0008 | 1,00 | 0,00004 | 0,05 |
| 24 | 0,0007 | 0,75 | 0,0007 | 0,72 | 0,00004 | 0,04 |
| 25 | 0,0007 | 0,73 | 0,0007 | 0,66 | 0,00007 | 0,07 |
| 26 | 0,0006 | 0,59 | 0,0007 | 0,74 | 0,00005 | 0,05 |
| 27 | 0,0004 | 0,50 | 0,0005 | 0,53 | 0,00009 | 0,10 |
| 28 | 0,0007 | 0,76 | 0,0007 | 0,79 | 0,00013 | 0,14 |
| 29 | 0,0006 | 0,55 | 0,0005 | 0,49 | 0,00012 | 0,12 |
| 30 | 0,0005 | 0,55 | 0,0006 | 0,64 | 0,00013 | 0,14 |
| 31 | 0,0005 | 0,47 | 0,0006 | 0,57 | 0,00011 | 0,11 |
| 32 | 0,0004 | 0,46 | 0,0004 | 0,47 | 0,00010 | 0,12 |
| 33 | 0,0002 | 0,31 | 0,0003 | 0,37 | 0,00009 | 0,11 |
| 34 | 0,0002 | 0,33 | 0,0003 | 0,46 | 0,00007 | 0,10 |
| 35 | 0,0002 | 0,35 | 0,0003 | 0,42 | 0,00007 | 0,11 |
| 36 | 0,0003 | 0,36 | 0,0002 | 0,29 | 0,00004 | 0,06 |

Table C.7: Specific sterols

Cruise: PS109/76; Station: PS109/76; Lon [°E]: -19.28; Lat [°N]: 79.629; Water Depth: 367 m

| Depth | Brassica/sed | Brassica/TOC | Campe/sed | Campe/TOC | beta-Sito/sed | beta-Sito/TOC | Dino/sed | Dino/TOC |
|-------|--------------|--------------|-----------|-----------|---------------|---------------|----------|----------|
| [cm] | [µg/g] | [µg/g] | [µg/g] | [µg/g] | [µg/g] | [µg/g] | [µg/g] | [µg/g] |
| 1 | 0,0413 | 23,00 | 0,0169 | 9,44 | 0,1063 | 59,19 | 0,0309 | 17,22 |
| 2 | 0,0055 | 3,97 | 0,0024 | 1,69 | 0,0162 | 11,60 | 0,0055 | 3,94 |
| 3 | 0,0059 | 5,07 | 0,0030 | 2,59 | 0,0171 | 14,79 | 0,0050 | 4,36 |
| 4 | 0,0062 | 5,71 | 0,0042 | 3,89 | 0,0200 | 18,54 | 0,0081 | 7,47 |
| 5 | 0,0096 | 8,83 | 0,0070 | 6,43 | 0,0349 | 32,11 | 0,0107 | 9,84 |
| 6 | 0,0051 | 5,47 | 0,0025 | 2,65 | 0,0183 | 19,55 | 0,0056 | 5,94 |
| 7 | 0,0052 | 5,10 | 0,0034 | 3,35 | 0,0195 | 18,94 | 0,0058 | 5,60 |
| 8 | 0,0046 | 4,94 | 0,0027 | 2,88 | 0,0157 | 16,81 | 0,0070 | 7,57 |
| 9 | 0,0042 | 4,36 | 0,0019 | 1,97 | 0,0126 | 13,13 | 0,0049 | 5,05 |
| 10 | 0,0064 | 6,99 | 0,0039 | 4,26 | 0,0257 | 28,04 | 0,0096 | 10,51 |
| 11 | 0,0042 | 4,34 | 0,0027 | 2,84 | 0,0155 | 16,12 | 0,0072 | 7,44 |

| Depth | Brassica/sed | Brassica/TOC | Campe/sed | Campe/TOC | beta-Sito/sed | beta-Sito/TOC | Dino/sed | Dino/TOC |
|-------|--------------|--------------|-----------|-----------|---------------|---------------|----------|----------|
| [cm] | [µg/g] | [µg/g] | [µg/g] | [µg/g] | [µg/g] | [µg/g] | [µg/g] | [µg/g] |
| 12 | 0,0035 | 4,32 | 0,0018 | 2,26 | 0,0135 | 16,76 | 0,0057 | 7,00 |
| 13 | 0,0042 | 5,00 | 0,0038 | 4,54 | 0,0173 | 20,69 | 0,0066 | 7,82 |
| 14 | 0,0039 | 5,23 | 0,0046 | 6,08 | 0,0141 | 18,72 | 0,0045 | 6,03 |
| 15 | 0,0051 | 5,43 | 0,0052 | 5,57 | 0,0212 | 22,73 | 0,0063 | 6,76 |
| 16 | 0,0046 | 5,21 | 0,0029 | 3,26 | 0,0147 | 16,62 | 0,0059 | 6,71 |
| 17 | 0,0027 | 3,75 | 0,0013 | 1,81 | 0,0095 | 13,20 | 0,0042 | 5,86 |
| 18 | 0,0056 | 7,45 | 0,0030 | 4,01 | 0,0171 | 22,89 | 0,0081 | 10,93 |
| 19 | 0,0055 | 6,04 | 0,0038 | 4,20 | 0,0189 | 20,78 | 0,0047 | 5,20 |
| 20 | 0,0104 | 11,62 | 0,0063 | 6,98 | 0,0272 | 30,34 | 0,0044 | 4,95 |
| 21 | 0,0067 | 7,84 | 0,0042 | 4,87 | 0,0209 | 24,38 | 0,0087 | 10,19 |
| 22 | 0,0038 | 4,38 | 0,0020 | 2,25 | 0,0126 | 14,42 | 0,0076 | 8,70 |
| 23 | 0,0038 | 4,68 | 0,0024 | 2,96 | 0,0136 | 16,88 | 0,0070 | 8,73 |
| 24 | 0,0052 | 5,57 | 0,0031 | 3,36 | 0,0177 | 18,91 | 0,0072 | 7,73 |
| 25 | 0,0078 | 7,84 | 0,0056 | 5,61 | 0,0253 | 25,42 | 0,0074 | 7,43 |
| 26 | 0,0054 | 5,56 | 0,0024 | 2,43 | 0,0165 | 17,00 | 0,0044 | 4,54 |
| 27 | 0,0084 | 9,88 | 0,0034 | 3,95 | 0,0222 | 26,12 | 0,0087 | 10,22 |
| 28 | 0,0058 | 6,12 | 0,0037 | 3,87 | 0,0166 | 17,51 | 0,0076 | 8,08 |
| 29 | 0,0060 | 6,00 | 0,0031 | 3,11 | 0,0156 | 15,50 | 0,0054 | 5,40 |
| 30 | 0,0054 | 5,83 | 0,0030 | 3,25 | 0,0154 | 16,49 | 0,0059 | 6,38 |
| 31 | 0,0041 | 4,17 | 0,0021 | 2,18 | 0,0110 | 11,30 | 0,0046 | 4,68 |
| 32 | 0,0036 | 4,11 | 0,0008 | 0,88 | 0,0084 | 9,53 | 0,0028 | 3,18 |
| 33 | 0,0037 | 4,76 | 0,0020 | 2,60 | 0,0087 | 11,13 | 0,0039 | 4,96 |
| 34 | 0,0022 | 3,23 | 0,0012 | 1,80 | 0,0056 | 8,40 | 0,0023 | 3,36 |
| 35 | 0,0030 | 4,62 | 0,0013 | 1,97 | 0,0071 | 10,86 | 0,0023 | 3,48 |
| 36 | 0,0019 | 2,65 | 0,0014 | 2,00 | 0,0058 | 8,15 | 0,0024 | 3,34 |

Table C.8: Highly branched isoprenoids

Cruise: PS109; Station: PS109/105; Lon [°E]: -18.56; Lat [°N]: 78.47; Water Depth: 441 m

| Depth | IP ₂₅ /sed | IP ₂₅ /TOC | HBI II diene/sed | HBI II diene/TOC | HBI III z-triene/sed | HBI III z-triene/TOC |
|-------|-----------------------|-----------------------|------------------|------------------|----------------------|----------------------|
| [cm] | [µg/g] | [µg/g] | [µg/g] | [µg/g] | [µg/g] | [µg/g] |
| 1 | 0,0049 | 1,33 | 0,0064 | 1,75 | 0,00084 | 0,23 |
| 4 | 0,0008 | 0,52 | 0,0010 | 0,66 | 0,00013 | 0,09 |
| 5 | 0,0004 | 0,31 | 0,0004 | 0,32 | 0,00000 | 0,00 |
| 6 | 0,0003 | 0,29 | 0,0002 | 0,20 | 0,00010 | 0,11 |
| 7 | 0,0002 | 0,23 | 0,0002 | 0,19 | | |
| 8 | 0,0002 | 0,21 | 0,0002 | 0,24 | | |
| 9 | 0,0003 | 0,26 | 0,0003 | 0,30 | | |
| 10 | 0,0003 | 0,26 | 0,0003 | 0,23 | | |
| 11 | 0,0004 | 0,24 | 0,0004 | 0,26 | 0,00015 | 0,10 |
| 12 | 0,0003 | 0,22 | 0,0004 | 0,26 | 0,00007 | 0,05 |
| 13 | 0,0003 | 0,27 | 0,0004 | 0,35 | 0,00015 | 0,12 |
| 15 | 0,0004 | 0,28 | 0,0006 | 0,40 | 0,00018 | 0,11 |
| 16 | 0,0004 | 0,25 | 0,0006 | 0,38 | 0,00021 | 0,13 |
| 17 | 0,0004 | 0,21 | 0,0005 | 0,27 | 0,00014 | 0,08 |
| 18 | 0,0005 | 0,29 | 0,0006 | 0,32 | 0,00027 | 0,16 |
| 19 | 0,0005 | 0,26 | 0,0007 | 0,37 | 0,00015 | 0,08 |
| 20 | 0,0005 | 0,30 | 0,0007 | 0,40 | 0,00021 | 0,13 |
| 21 | 0,0006 | 0,33 | 0,0009 | 0,49 | 0,00032 | 0,18 |
| 22 | 0,0006 | 0,34 | 0,0009 | 0,50 | 0,00050 | 0,28 |
| 23 | 0,0008 | 0,49 | 0,0012 | 0,73 | 0,00072 | 0,43 |
| 24 | 0,0008 | 0,51 | 0,0013 | 0,78 | 0,00052 | 0,32 |
| 25 | 0,0008 | 0,46 | 0,0013 | 0,75 | 0,00045 | 0,26 |
| 26 | 0,0005 | 0,27 | 0,0008 | 0,42 | 0,00022 | 0,11 |
| 27 | 0,0006 | 0,33 | 0,0008 | 0,45 | 0,00023 | 0,13 |
| 28 | 0,0005 | 0,29 | 0,0008 | 0,42 | 0,00021 | 0,11 |
| 29 | 0,0007 | 0,46 | 0,0011 | 0,74 | 0,00031 | 0,21 |
| 30 | 0,0007 | 0,50 | 0,0011 | 0,78 | 0,00027 | 0,18 |
| 31 | 0,0004 | 0,24 | 0,0006 | 0,36 | 0,00012 | 0,07 |
| 32 | 0,0004 | 0,27 | 0,0005 | 0,34 | 0,00011 | 0,07 |
| 33 | 0,0004 | 0,38 | 0,0008 | 0,66 | 0,00022 | 0,19 |
| 34 | 0,0004 | 0,39 | 0,0006 | 0,62 | 0,00016 | 0,16 |
| 35 | 0,0004 | 0,42 | 0,0005 | 0,56 | 0,00016 | 0,16 |
| 36 | 0,0004 | 0,36 | 0,0006 | 0,51 | 0,00013 | 0,11 |
| 34 | 0,0002 | 0,33 | 0,0003 | 0,46 | 0,00007 | 0,10 |
| 35 | 0,0002 | 0,35 | 0,0003 | 0,42 | 0,00007 | 0,11 |
| 36 | 0,0003 | 0,36 | 0,0002 | 0,29 | 0,00004 | 0,06 |

Table C.9: Specific sterols

Cruise: PS109; Station: PS109/105; Lon [°E]: -18.56; Lat [°N]: 78.47; Water Depth: 441 m

| Depth | Brassica/sed | Brassica/TOC | Campe/sed | Campe/TOC | beta-Sito/sed | beta-Sito/TOC | Dino/sed | Dino/TOC |
|-------|--------------|--------------|-----------|-----------|---------------|---------------|----------|----------|
| [cm] | [µg/g] | [µg/g] | [µg/g] | [µg/g] | [µg/g] | [µg/g] | [µg/g] | [µg/g] |
| 1 | 0,0254 | 6,93 | 0,0090 | 2,45 | 0,0763 | 20,81 | 0,0122 | 3,34 |
| 4 | 0,0024 | 1,52 | 0,0017 | 1,08 | 0,0068 | 4,42 | 0,0030 | 1,91 |
| 5 | 0,0015 | 1,26 | 0,0007 | 0,59 | 0,0040 | 3,25 | 0,0024 | 1,95 |
| 7 | 0,0012 | 1,41 | 0,0007 | 0,81 | 0,0029 | 3,25 | 0,0016 | 1,78 |
| 8 | 0,0008 | 0,86 | 0,0009 | 1,01 | 0,0027 | 3,01 | 0,0014 | 1,54 |
| 9 | 0,0016 | 1,57 | 0,0009 | 0,86 | 0,0034 | 3,28 | 0,0030 | 2,88 |
| 10 | 0,0019 | 1,72 | 0,0010 | 0,92 | 0,0040 | 3,70 | 0,0024 | 2,18 |
| 11 | 0,0023 | 1,53 | 0,0015 | 0,98 | 0,0062 | 4,05 | 0,0043 | 2,83 |
| 12 | 0,0032 | 2,18 | 0,0021 | 1,45 | 0,0063 | 4,29 | 0,0038 | 2,59 |
| 13 | 0,0023 | 1,83 | 0,0014 | 1,16 | 0,0052 | 4,22 | 0,0017 | 1,37 |
| 14 | 0,0020 | 1,32 | 0,0012 | 0,76 | 0,0049 | 3,19 | 0,0022 | 1,45 |
| 15 | 0,0023 | 1,44 | 0,0017 | 1,05 | 0,0053 | 3,26 | 0,0014 | 0,87 |
| 16 | 0,0033 | 2,03 | 0,0019 | 1,16 | 0,0065 | 4,03 | 0,0031 | 1,91 |
| 17 | 0,0057 | 3,36 | 0,0006 | 0,36 | 0,0029 | 1,69 | 0,0003 | 0,16 |
| 18 | 0,0034 | 1,99 | 0,0021 | 1,21 | 0,0061 | 3,54 | 0,0043 | 2,50 |
| 19 | 0,0039 | 2,20 | 0,0030 | 1,69 | 0,0099 | 5,59 | 0,0071 | 4,00 |
| 20 | 0,0045 | 2,62 | 0,0024 | 1,43 | 0,0095 | 5,58 | 0,0032 | 1,86 |
| 21 | 0,0041 | 2,34 | 0,0025 | 1,44 | 0,0081 | 4,61 | 0,0041 | 2,31 |
| 22 | 0,0058 | 3,30 | 0,0027 | 1,54 | 0,0111 | 6,29 | 0,0072 | 4,09 |
| 23 | 0,0071 | 4,29 | 0,0028 | 1,69 | 0,0110 | 6,59 | 0,0098 | 5,92 |
| 24 | 0,0066 | 4,07 | 0,0030 | 1,83 | 0,0131 | 8,04 | 0,0076 | 4,68 |
| 25 | 0,0082 | 4,77 | 0,0029 | 1,70 | 0,0098 | 5,68 | 0,0040 | 2,32 |
| 26 | 0,0034 | 1,80 | 0,0020 | 1,05 | 0,0079 | 4,12 | 0,0052 | 2,72 |
| 27 | 0,0039 | 2,22 | 0,0025 | 1,39 | 0,0090 | 5,03 | 0,0058 | 3,27 |
| 28 | 0,0038 | 2,05 | 0,0024 | 1,32 | 0,0077 | 4,21 | 0,0052 | 2,82 |
| 29 | 0,0068 | 4,45 | 0,0037 | 2,40 | 0,0094 | 6,18 | 0,0075 | 4,89 |
| 30 | 0,0037 | 2,53 | 0,0024 | 1,63 | 0,0075 | 5,05 | 0,0044 | 3,00 |
| 31 | 0,0028 | 1,64 | 0,0015 | 0,90 | 0,0047 | 2,77 | 0,0052 | 3,04 |
| 32 | 0,0025 | 1,54 | 0,0018 | 1,09 | 0,0061 | 3,77 | 0,0030 | 1,84 |
| 33 | 0,0039 | 3,35 | 0,0020 | 1,75 | 0,0061 | 5,21 | 0,0029 | 2,46 |
| 34 | 0,0047 | 4,60 | 0,0030 | 2,89 | 0,0073 | 7,08 | 0,0024 | 2,34 |
| 35 | 0,0042 | 4,36 | 0,0028 | 2,94 | 0,0065 | 6,74 | 0,0037 | 3,81 |
| 36 | 0,0026 | 2,29 | 0,0020 | 1,77 | 0,0046 | 4,03 | 0,0019 | 1,71 |